ISSN-e 2594-0317

JOURNAL *of the* MEXICAN CHEMICAL SOCIETY

(J. Mex. Chem. Soc.)
Former Revista de la Sociedad Química de México (Rev. Soc. Quím. Mex.)

Regular Issue

J. Mex. Chem. Soc.
Volume 69
Issue 4
October-December
Year 2025

Quarterly publication
www.jmcs.org.mx
Mexico City

ISSN-e 2594-0317

JOURNAL *of the* MEXICAN CHEMICAL SOCIETY

(J. Mex. Chem. Soc.)
Former Revista de la Sociedad Química de México (Rev. Soc. Quím. Mex.)

Regular Issue

J. Mex. Chem. Soc.
Volume 69
Issue 4
October-December
Year 2025

Quarterly publication
www.jmcs.org.mx
Mexico City

J. Mex. Chem. Soc. **2024**, *69(4)*
Regular Issue

ISSN-e 2594-0317

The *Sociedad Química de México* was founded in 1956 as a non-profit association to promote the development of the professionals and students of chemistry in education, research, services and industry, and for the diffusion of chemical knowledge. The *Sociedad Química de México* organizes annually the *Mexican Congress of Chemistry* and the *National Congress of Chemical Education*, both congresses include activities of current interest for professionals and students of the chemical sciences. It grants annually the "*Andrés Manuel del Río*" *National Award of Chemistry* in the Academic area (field of research and field of education) and in the Technological area (field of technological development). It also grants each year the *Rafael Illescas Frisbie Best Bachelor, Master and Doctoral Thesis in Chemical Sciences Awards* and the biennial *Award of the Sociedad Química de México in honor of the Doctor Mario J. Molina, directed to the professionals in Chemistry Sciences*.

The *Journal of the Mexican Chemical Society* (*J. Mex. Chem. Soc*) is the official journal of the *Sociedad Química de México*, it was published as *Revista de la Sociedad Química de México* (*Rev. Soc. Quím. Mex.*) from 1957 to 2003, changing its name in 2004. The Journal of the Mexican Chemical Society (J. Mex. Chem. Soc.) is a scientific, blind, peer reviewed, and open access, free of charge publication that covers all areas of chemistry and its sub-disciplines (i.e. medicinal chemistry, natural products, electrochemistry, material science, computational chemistry, organic chemistry, bioinorganic chemistry, etc). It is devoted to facilitating the worldwide advancement of our understanding of chemistry. It will primarily publish original contributions of research in all branches of the theory and practice of chemistry in its broadest context as well as critical reviews in active areas of chemical research where the author has published significant contributions. The J. Mex. Chem. Soc. is a quarterly publication in which language of submission and publication is English. To be suitable for publication in J. Mex. Chem. Soc., manuscripts must describe novel aspects of chemistry, high quality of results and discussion an excellent bibliographic support, and contribute to the development of the field. Routine or incremental works are not suitable for publication in J. Mex. Chem. Soc. Authors are encouraged to send contributions in electronic form. Our online submission system guides you stepwise through the process of entering your article details and uploading your files. The *Sociedad Química de México* also publishes since 2007 articles of general interest in the *Boletín de la Sociedad Química de México*.

La *Sociedad Química de México* fue fundada en 1956 como una agrupación sin fines de lucro para promover el desarrollo de los profesionales y estudiantes de la química en las áreas educativa, investigación, servicios e industria, y para difundir el conocimiento de la química. La *Sociedad Química de México* organiza anualmente el *Congreso Mexicano de Química* y el *Congreso Nacional de Educación Química*, en los cuales se desarrollan diversas actividades de interés para los profesionales y estudiantes de las ciencias químicas. Asimismo, otorga anualmente el *Premio Nacional de Química "Andrés Manuel del Río"* en el área Académica (campos de docencia e investigación) y en el área Tecnológica (campo de Desarrollo Tecnológico). También otorga anualmente el *Premio a las Mejores Tesis de Licenciatura, Maestría y Doctorado en Ciencias Químicas, Rafael Illescas Frisbie*. De manera bienal otorga el *Premio de la Sociedad Química de México en Honor al Doctor Mario J. Molina, dirigido a los profesionistas de las Ciencias Químicas*.

El *Journal of the Mexican Chemical Society* (*J. Mex. Chem. Soc.*), es la revista oficial de la *Sociedad Química de México*. Desde 1957 y hasta 2003 fue publicada como *Revista de la Sociedad Química de México* (*Rev. Soc. Quím. Mex.*), cambiando su nombre en 2004. Es una publicación trimestral que tiene como objetivo coadyuvar al avance del entendimiento de la química; las instrucciones para los autores aparecen en cada fascículo. La *Sociedad Química de México* también publica desde 2007 artículos de interés general en el *Boletín de la Sociedad Química de México*

Journal of the Mexican Chemical Society
(*J. Mex. Chem. Soc.*)

ISSN-e: 2594-0317
ISSN 1870-249X

former

Revista de la Sociedad Química de México
(*Rev. Soc. Quím. Mex.*) ISSN 0583-7693

Journal of the Mexican Chemical Society (*J. Mex. Chem. Soc.*)
Quarterly publication.
Editor-in-Chief: Prof. Alberto Vela Amieva

Indexed Journal

Certificate of reserved rights granted by the Instituto Nacional del Derecho de Autor (INDAUTOR): 04-2005-052710530600-102
Certificate of lawful title and content: Under procedure
Postal registration of printed matter deposited by editors or agents granted by SEPOMEX: IM09-0312

The Figures/schemes quality and the general contents of this publication including referencing, are full responsability of the authors.

Edited and distributed by Sociedad Química de México, A.C.
Barranca del Muerto 26, Col. Crédito Constructor,
Del. Benito Juárez, C.P. 03940, Mexico City.
Phone: +5255 56626837; +5255 56626823
Contact: soquimex@sqm.org.mx
https://www.sqm.org.mx

Editorial assistance: jmcs@sqm.org.mx
https://www.jmcs.org.mx

J. Mex. Chem. Soc. **2025**, *69(4)*
Regular Issue

ISSN-e 2594-0317

Table of Contents

Articles

continues...

* The asterisk indicates the name of the author to whom inquiries about the paper should be addressed.

J. Mex. Chem. Soc. **2025**, *69(4)*
Regular Issue

ISSN-e 2594-0317

Table of Contents

continues...

* The asterisk indicates the name of the author to whom inquiries about the paper should be addressed.

J. Mex. Chem. Soc. **2025**, *69(4)*
Regular Issue

ISSN-e 2594-0317

Table of Contents

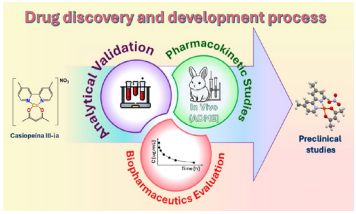

Reviews

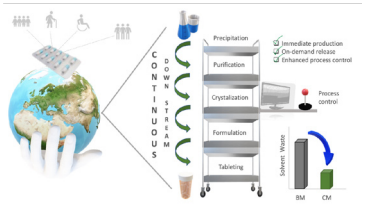

* The asterisk indicates the name of the author to whom inquiries about the paper should be addressed.

Article

J. Mex. Chem. Soc. **2025**, *69*(4)
Regular Issue

ISSN-e 2594-0317

In silico Exploration of Leads from Lichen Derived Salazinic Acid, Sekikaic Acid and Usnic Acid Targeting HER2 in Breast Cancer

Miah Roney[1,2], Amit Dubey[3], Mohd Fadhlizil Fasihi Mohd Aluwi[1,2]*

[1]Faculty of Industrial Sciences and Technology, Universiti Malaysia Pahang Al-Sultan Abdullah, Lebuhraya Persiaran Tun Khalil Yaakob, Kuantan, Pahang, Malaysia.
[2]Centre for Bio-aromatic Research, Universiti Malaysia Pahang Al-Sultan Abdullah, Lebuhraya Persiaran Tun Khalil Yaakob, Kuantan, Pahang, Malaysia.
[3]Center for Global Health Research, Saveetha Medical College and Hospitals, Saveetha Institute of Medical and Technical Sciences, Chennai, Tamil Nadu, India.

***Corresponding author:** Mohd Fadhlizil Fasihi Mohd Aluwi, email: fasihi@umpsa.edu.my

Received December 5th, 2023; Accepted October 17th, 2024.

DOI: http://dx.doi.org/10.29356/jmcs.v69i4.2175

Abstract. One of the most common cancers that strikes women is breast cancer (BC). Twenty percent of cases of BC are caused by human epidermal growth factor receptor-2 (HER2), which may be a target for the development of BC medicines. Consequently, the main goal was to find a BC inhibitor by using pass prediction and in silico docking techniques. Usnic acid may be used as a potential HER2 inhibitor, according to in silico study results, and compounds with high binding free energies may have significant anti-BC effects, making them promising candidates for further therapeutic development. Usnic acid was shown to have an inhibitory effect against HER2 of -8.9 kcal/mol, which was comparable to the reference substance (co-crystal; -9.7 kcal/mol). Additionally, because the probability active (Pa) value of usnic acid is greater than 0.700, it possesses a broad spectrum of anti-neoplastic properties against BC. The main substance in the present study that can suppress BC has been shown to be usnic acid, an active lichen extract. The present computational findings will be validated in a wet lab using both *in vitro* and *in vivo* tests.
Keywords: Breast cancer; usnic acid; HER2; docking; PASS prediction.

Resumen. Uno de los cánceres más comunes que afecta a las mujeres es el cáncer de mama (CM). El veinte por ciento de los casos de BC son causados por el receptor 2 del factor de crecimiento epidérmico humano (HER2), que puede ser un objetivo para el desarrollo de medicamentos contra la BC. En consecuencia, el objetivo principal era encontrar un inhibidor de BC mediante el uso de predicción de pases y técnicas de acoplamiento in silico. El ácido úsnico puede usarse como un posible inhibidor de HER2, según los resultados de un estudio in silico, y los compuestos con altas energías libres de unión pueden tener importantes efectos anti-BC, lo que los convierte en candidatos prometedores para un mayor desarrollo terapéutico. Se demostró que el ácido úsnico tiene un efecto inhibidor contra HER2 de -8.9 kcal/mol, comparable al de la sustancia de referencia (cocristal; -9.7 kcal/mol). Además, debido a que el valor de probabilidad activa (Pa) del ácido úsnico es superior a 0.700, posee un amplio espectro de propiedades antineoplásicas contra BC. Se ha demostrado que la principal sustancia en el presente estudio que puede suprimir la BC es el ácido úsnico, un extracto activo de liquen. Los presentes hallazgos computacionales se validarán en un laboratorio húmedo mediante pruebas tanto *in vitro* como *in vivo*.
Palabras clave: Cáncer de mama; ácido úsnico;HER2; acoplamiento; predicción PASS.

J. Mex. Chem. Soc. **2025**, *69*(4)
Regular Issue

ISSN-e 2594-0317

Introduction

The most common cancer in women to be diagnosed is breast cancer (BC), which also happens to be the second largest cause of cancer-related mortality in this population. BC can now be identified and diagnosed with much greater accuracy. There is a correlation between a high-fat diet, excessive alcohol consumption, and inactivity in relation to BC [1]. Reducing morbidity and mortality could be aided by the removal of these variables. Early tumour diagnosis may be aided by breast self-examination, mammography, ultrasound, and magnetic resonance imaging [2]. Lung cancer has been overtaken by BC (11.7 %) as the most common cancer diagnosed in women. Lung cancer (11.4 %), colorectal (10.0 %), prostate (7.3 %), and stomach (5.6 %) follow. About 2.1 million women are impacted by BC annually, and it is the primary cause of cancer-related deaths in women. BC accounted for about 15 % of all female cancer deaths in 2020, affecting 2.3 million women worldwide and resulting in 685,000 fatalities [1].

Human epidermal growth factor receptor 2 (HER2) is a member of the epidermal growth factor family (ErbB family) that consists of four transmembrane tyrosine kinase receptors: ErbB1 (EGFR/HER1), ErbB2 (HER2), ErbB3 (HER3), and ErbB4 (HER4) [3]. Overexpression of HER2 has been associated with adenocarcinomas, including those of the breast, ovaries, endometrium, cervix, and lung. HER2 is therefore an important target for a number of cancer therapeutic modalities [1]. Fifteen to twenty percent of BC cases had overexpression of the HER2 gene, which is typically associated with a high degree of biological and clinical disease aggression [4]. Many malignancies' biology is significantly influenced by HER2 [5]. In addition, novel HER2-targeted medications have been thoroughly investigated recently and have demonstrated improved results [1]. The development of active dimers is stabilised by ligand binding to the extracellular domain of ErbB receptors, which are ordinarily inactive monomers (Fig. 1). Dimerization causes kinase domain activation, which in turn causes transphosphorylation of tyrosine residues within the domains. It can happen between two distinct ErbB receptors or between two domains of the same receptor.

Tyrosine residue phosphorylation generates binding sites for effector or adaptor proteins with phosphotyrosine-binding domains and Src-homology (SH2) [6]. Two significant signalling pathways that are triggered by ErbB receptors are phosphatidylinositol-3-kinase (PI3K) and mitogen-activated protein kinase (MAPK) (Fig. 1). These pathways cause gene transcription, which produces proteins involved in cell division, migration, proliferation, and death [3].

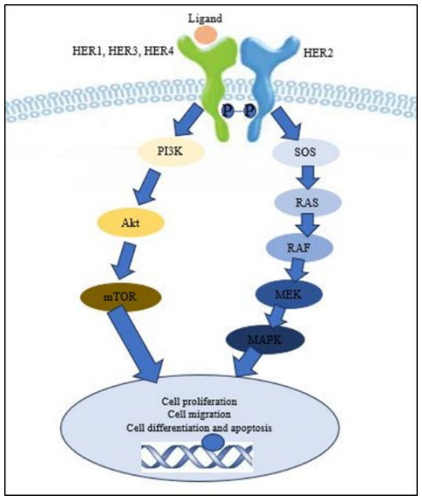

Fig. 1. The Human epidermal growth factor receptor 2 (HER2) pathway. The generation of active HER2 heterodimers is stabilised by ligand binding to the extracellular domain of HER1/3/4.

The finest sources of therapeutic compounds are natural items. Because medicinal plants feature intriguing secondary metabolites that may have undiscovered anticancer properties, there has been a surge in scientific interest in these plants within the last several decades [7]. One of these is lichen, which is a symbiotic

J. Mex. Chem. Soc. **2025**, *69*(4)
Regular Issue

ISSN-e 2594-0317

relationship between fungus and algae. There are around 20,000 types of lichen on the globe. A vast variety of primary (intracellular) and secondary (extracellular) chemicals are produced by their chemistry. Amino acids, polyols, carotenoids, polysaccharides, and vitamins are examples of primary metabolites. Lichen acids, or secondary metabolites generated by the lichen's fungal partner, comprise most of the organic chemicals present in lichens. More than 850 secondary metabolites have been found in lichens thus far, and research has demonstrated that these chemicals are produced by lichens under duress and are crucial for the self-defence of slow-growing lichens [8].

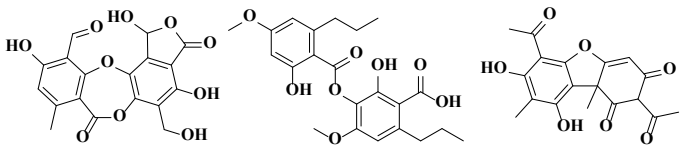

Fig. 2. Structure of selected secondary metabolites of Lichen.

A wide range of secondary metabolites, including those with antibacterial, antiviral, antitumor, antioxidant, antihervivor, insecticidal, allelochemical, and allergenic properties, are produced by lichen [9]. The fresh thallus of the natural lichens *Ramalina celastri*, *Ramalina nervulosa*, and *Ramalina pacifica* produce usnic acid, salazinic acid, and sekikaic acid, respectively [10]. Based on the evidence by Morris Kupchan and Kopperman (1975), we postulated that the secondary metabolites (salazinic acid, sekikaic acid, and usnic acid; Fig. 2) may interact with BC's HER2 receptor in light of lichens' anti-cancer properties [11]. Therefore, the primary emphasis of this work was on computer-aided drug design processes such as molecular docking, PASS prediction methods, and e-pharmacophore to find a potential natural antagonist against the HER2 protein in order to cure BC.

Methodology

Molecular docking

The compounds were docked with the receptor separately using the CB-Dock (cavity-detection-guided blind docking) protein-ligand docking technique [12]. The ChemSketch tool was used to create compound structures, which were then saved in the .mol format. The RCSB Protein Data Bank provided the target protein for docking, which had a resolution of less than 2.25 Å, a R value of less than 0.260, and a PDB ID (PDB ID: 3PP0) [13]. According to Liu *et al*., the CB-Dock method accurately locates the binding zone, ascertains the size and location of the centre, modifies the size of the docking region in response to the molecule input, and then uses AutoDock Vina version 1.1.2 to dock [14]. A PBD file for the receptor and a .mol file for the ligands were entered prior to docking. Each of the several top cavities that were automatically selected throughout this process and used for additional research (cavity sorting) underwent molecular docking.

Prediction of anticancer activity

Using a web server called the PASS-Way2Drug server, the in-silico prediction of usnic acid's anticancer characteristics was investigated further. P values for the similarity measures are provided by the PASS (Prediction of Activity Spectra for Substances), which is based on the likelihood of anticancer activity being highly or less likely [15]. At a false-positive rate of 0.05, it may get 65% positive findings. We sourced the necessary entries from the PubChem service as it necessitates the canonical Simplified Molecular Input Line Entry String (SMILES) of substances to be examined [16].

E-pharmacophore analysis

The energetic (e)-pharmacophore technique now incorporates both structure- and ligand-based approaches. The pharmacophore sites of UA, such as hydrogen bond acceptor (A), hydrogen bond donor (D),

J. Mex. Chem. Soc. **2025**, *69*(4)
Regular Issue

ISSN-e 2594-0317

hydrophobic group (H), positively ionizable (P), negatively ionizable (N), and aromatic ring (R), were identified using the phase v 3.4 module in Schrödinger [17].

Results

Molecular docking

Table 1. Molecular docking analysis of lichen derived salazinic acid, sekikaic acid, usnic acid and reference compound (co-crystal ligand) with the HER2 receptor of breast cancer (PDB ID: 3PP0).

Compound Name	Cavity Size	Vina Score	Bound Amino Acids
Co-crystal (Control)	4513	-9.7	Met774, Arg784, Thr862, Thr798, Gln799, Asn850, Arg849, Ser728, Cys805 (H-B), Ala771, Glu770, Met774, Leu769, Leu785, Phe864, Thr798, Ala751, Lys753, Leu852, Val734, Leu726 (C-H)
Salazinic Acid	4513	-7.7	Leu726, Cys805, Arg849, Gly804, Thr862 (H-B), Leu726, Met801, Ala751, Leu852, Val734 (C-H), Lys753 (ionic)
Sekikaic Acid	4513	-8.1	Thr862, Ala730, Asp863, Arg849, Cys805, Ser728, Asp808 (H-B), Ala751, Leu800, Leu726, Val734, Leu852 (C-H), Lys753 (ionic)
Usnic Acid	4513	-8.9	Thr862, Cys805, Asp808, Thr798 (H-B), Val734, Thr862, Leu852, Met801, Leu726 (C-H), Lys753 (ionic)

The current work attempted to generate lead targeting HER2 by comparing docking scores and subsequently the interactions with the co-crystal ligand from lichen-derived salazinic acid, sekikaic acid, and usnic acid to inhibit BC. Table 1 lists the docking scores of the chosen lichen and the reference ligand (co-crystal). The reference chemical showed a -9.7 kcal/mol docking score. It is well understood that a higher affinity for the target receptor is indicated by a lower docking score. Docking scores of -7.7, -8.1, and -8.9 kcal/mol were observed for the salazinic acid, usnic acid, and sedikaic acid that were extracted from lichens, respectively. Docking studies indicate that usnic acid may function as an HER2 receptor inhibitor.

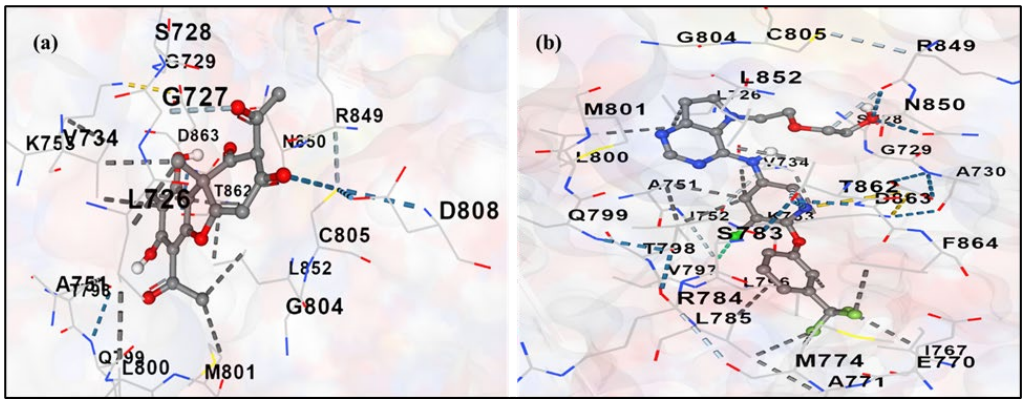

Fig. 3. Molecular docking interactions analysis of lichen derived **(a)** usnic acid and **(b)** reference compound (co-crystal ligand) with the HER2 receptor of breast cancer (PDB ID: 3PP0).

J. Mex. Chem. Soc. **2025**, *69*(4)
Regular Issue

ISSN-e 2594-0317

Fig. 3**(b)** shows that the reference compound showed nine hydrogen bonds (H-B) with residues of Met774, Arg784, Thr862, Thr798, Gln799, Asn850, Arg849, Ser728, and Cys805, whereas the usnic acid showed four H-B with residues of Thr862, Cys805, Asp808, and Thr798 (Fig. 3**(a)**). The possible anticancer effects of usnic acid have been thoroughly investigated, especially in relation to breast cancer [18–20]. It has been shown that usnic acid causes apoptosis via a ROS-dependent mitochondrial route, therefore inhibiting the survival of human breast cancer MCF-7 cells in a concentration- and time-dependent manner [21]. To increase usnic acid's anticancer efficacy and selectivity, compounds such as isoxazole and pyrazole derivatives have been created. It has been demonstrated that these compounds cause breast cancer cells to undergo cell cycle arrest, apoptosis, and paraptosis-like cell death [22]. Furthermore, the docking score of usnic acid in the BCL2, PI3KCA, and PI3KCG proteins was -36.51, -44.59, and -41.93 kcal/mol, respectively [23]. Human BC MCF-7 cell viability was reduced by usnic acid in a concentration- and time-dependent way [24]. Moreover, usnic acid suppresses VEGFR2-mediated AKT and ERK1/2 signalling pathways, which in turn decreases BC angiogenesis and growth [25]. These academic works further supported our conclusions.

Prediction of anticancer activity

Using the PASS Online programme (http://www.way2drug.com/passonline), the possible BC inhibitor, usnic acid, was subjected to biological activity analysis after docking [26]. We only forecasted the anticancer activity in which the antineoplastic property—the primary parameter—was taken into account using PASS Online. The PASS Online server forecasts the biological activities of various substances and displays the outcomes as indicators of biological activity or inactivity. The likelihood of either biological activity (Pa) or biological inactivity (Pi) is present [16]. Table 2 lists the UA's expected antineoplastic characteristics. Pa values of usnic acid were greater than Pi for antineoplastic characteristics, indicating a higher likelihood of biological activity as opposed to inactivity. It is noteworthy that the Pa value of usnic acid was significantly higher than the Pi value. This indicates that there is a higher chance that usnic acid will block BC.

Table 2. Anti-cancer predictions of Usnic acid using the Pass server.

Compound Name	Bioactivity	Pa	Pi
Usnic acid	Antineoplastic (breast cancer)	0.710	0.005

E-Pharmacophore Analysis

By preserving the activity criterion in the range of 6.5 to 7.9, the data set was split into regions that were actively, moderately, and inactively occupied. Due to the usnic acid binding domain's strong survival value, the generic pharmacophore hypotheses were added among its four properties, as illustrated in Fig. 4. The e-pharmacophore also reveals that usnic acid is composed of seven acquired acceptors (A1 to A7), two obtained donors (D8 and D9), two obtained hydrophobics (H10 and H11), and one obtained aromatic ring (R12).

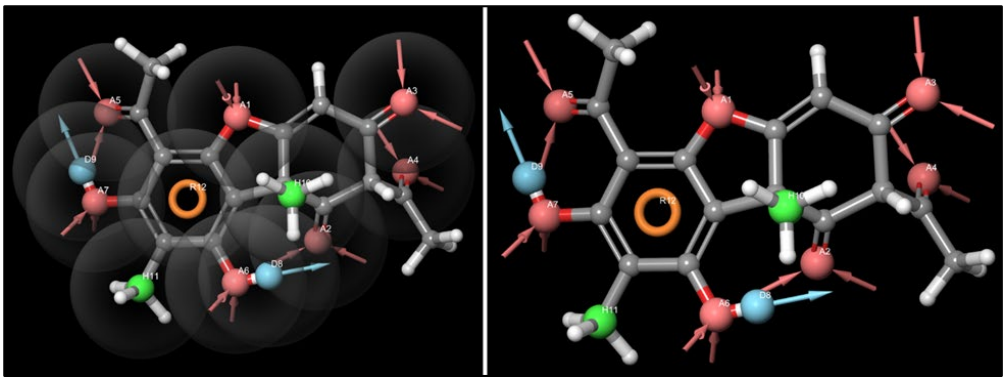

Fig. 4. Pharmacophore hypothesis of Usnic acid. A denotes hydrogen bond acceptor in pink color, D denotes hydrogen bond donor in blue, H denotes hydrophobic in green color and R denotes aromatic rings in brown color from docked phytochemicals.

J. Mex. Chem. Soc. **2025**, *69*(4)
Regular Issue

ISSN-e 2594-0317

Discussion

One of the most prevalent malignant illnesses in the world is cancer, with BC ranking as the second most common cause of death for women. According to the World Health Organisation (WHO), were an estimated 2.3 million women diagnosed with breast cancer and 670 000 deaths globally in 2022 [27]. Age, a personal or family history of BC, radiation, inborn errors, and obesity are among the most significant risk factors for BC. According to a case study conducted in Mexico City, women who are obese, overweight, or nursing have an increased chance of developing BC [28]. In the ongoing search for more secure and potent medication choices, innovative chemopreventive and anticancer therapy strategies are frequently highlighted. Various types of natural and synthetic chemicals have already been used to investigate a large number of molecular targets of distinct cellular processes during tumour formation. On the other hand, because cancer cells are immortal, many scientists are interested in finding new techniques to cause cancer cells to undergo apoptosis in order to create anticancer medications. Many new substances and anticancer medications can dramatically and occasionally precisely cause apoptosis in a range of cancer cells [29]. Currently, one of the most actively researched areas in BC research is tailored therapies, which can target certain targets. Following the oestrogen receptor-α, the human epidermal growth factor receptor 2 (HER2) is a tyrosine kinase protein that is frequently targeted in BC. HER2-positive tumours make up around 18–20 % of all other BC and are often more aggressive than HER2-negative tumours [30]. Thus, it is essential to treat BC and stop the spread of malignant cells by suppressing HER2 expression and activity [31].

The most popular methods of treating BC have been linked to several drawbacks. According to Muhammad *et al*., they primarily include stem cell and dendritic cell-based immunotherapy, radiation, chemotherapy, and surgery [32]. Therefore, the development of novel drugs to treat BC is crucial. Massive global research is being conducted by scientists to both prevent and treat BC. The invention of synthetic medications started as a result of the rapid breakthroughs in technology, and the long-term use of medicinal plants was forgotten. But over the past several decades, the promise of phytomedicine has drawn more attention due to the serious side effects that such synthetic medications induce [33]. Natural goods are a reliable source of pharmaceuticals. Among them, lichen demonstrated a wide range of biological properties, including the ability to fight cancer [34, 35]. Given that lichens have anti-cancer properties, we speculate that salazinic acid, sekikaic acid, and usnic acid—all derived from lichens—would be effective BC agents.

Theoretical and computational techniques employed in *in silico* drug creation can be utilised to find new hits or leads against certain biologically active macromolecules. In order to find, create, and evaluate medications and related physiologically active compounds, computer-aided drug design (CADD) techniques, including virtual screening, molecular docking, and dynamic simulation methods, are now being utilised. A compound's biological activity may be assessed anytime it attaches to a target macromolecule and sets off a particular reaction. In traditional drug development, determining a compound's binding capability required extensive *in vitro* and *in vivo* testing, which was time-consuming and expensive. However, using a molecular docking technique simplifies this process quickly [36]. Additionally, pharmacology is using the e-pharmacophore modelling approach to quickly create new medications [37]. The terms Pa (probability for active molecules) and Pi (probability for inactive molecules) define the measurement data that PASS provides. In order for a molecule to be classified as potential, its Pa and Pi values need to be between 0.00 and 1.00, with $Pa + Pi \neq 1$. In this case, the chosen pharmacological molecule's biological activities are considered likely if $Pa > Pi$ [26]. Thus, the primary emphasis of this work was on computer-aided drug design processes such as e-pharmacophore methods, pass prediction, and molecular docking to find a potential natural antagonist against the HER2 protein in order to cure BC.

Salazinic acid, sekikaic acid, and usnic acid produced from lichens have docking scores of -7.7, -8.1, and -8.9 kcal/mol, respectively. Usnic acid was regarded as the lead chemical based on the highest docking score. Four hydrogen connections were observed between usnic acid and the residues of Thr862, Cys805, Asp808, and Thr798. In addition, this molecule exhibited ionic connections with the Lys753 residue, which enhances the inhibitory effect, and hydrophobic contacts with Val734, Thr862, Leu852, Met801, and Leu726. The PASS prediction was evaluated using the Pass online biological activity prediction tool based on the structure of usnic acid. Table 2 indicates that usnic acid has potential pharmacological effects ($Pa > Pi$), which may include BC prevention. A lead molecule's activity is considered experimental if $Pa > Pi$. Pa values of 0.5 to 0.6 demonstrate considerable pharmacological potential, whereas $Pa > 0.6$ suggests a significant possibility

J. Mex. Chem. Soc. **2025**, *69*(4)
Regular Issue

ISSN-e 2594-0317

of pharmacological potential [38]. It was predicted that usnic acid will function as an anti-cancer agent against BC with a Pa of >0.7 and a Pi of <0.005. The generic pharmacophore hypotheses were added to the usnic acid binding domain's four features due to its significant survival value, as shown in Fig. 4. Usnic acid is likewise made up of seven acquired acceptors (A1 to A7), two obtained donors (D8 and D9), two obtained hydrophobics (H10 and H11), and one acquired aromatic ring (R12), according to the e-pharmacophore.

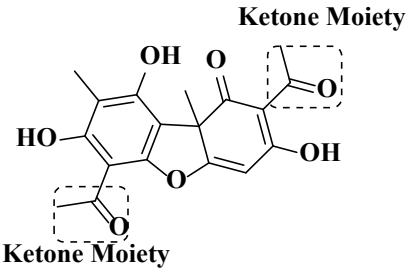

Fig. 5. Ketone moiety in usnic acid structure.

Usnic acid is a secondary metabolite of biologically active lichens that is well known as an antibiotic but also endowed with several other interesting properties [39]. In addition, usnic acid is structurally unique and has two ketone moieties, which could undergo further modification. For instance, the ketone moiety (Fig. 5) is potentially to be used in structural modifications such as the formation of new C-C and C-N bonds through the Claisen-Schmidt condensation reaction and the Michael addition reaction, respectively. Furthermore, α,β-unsaturated compounds like chalcone could be synthesised from the reaction of the usnic acid ketone moiety and benzaldehyde. In this study, usnic acid showed anti-BC activity against the HER2 receptor. Based on the results and discussion, we hypothesised that usnic acid derivatives could be good inhibitors of BC.

Conclusions

In silico research can save a great deal of time and money by avoiding the need for experiments before they begin. In addition to computational tests, *in silico* methods can aid in the prediction of the likely active medication. The best compound (usnic acid) was predicted using docking and Pass prediction algorithms in the current study, which may open the door to the creation of novel, safer drugs for BC. We were able to identify usnic acid as a BC inhibitor against the HER2 receptor with the use of the *in silico* platform. To further assess usnic acid as a BC inhibitor, more wet-lab research is needed.

Acknowledgments

The authors would like to thank the Ministry of Higher Education for providing financial support under the Fundamental Research Grant Scheme (FRGS) No. FRGS/1/2019/STG01/UMP/02/4 (University Reference: RDU1901160) and Universiti Malaysia Pahang Al-Sultan Abdullah for lab facilities.

References

1. Sohrab, S.S.; Kamal, M.A. *Life*. **2022**, *12*, 1729.
2. Kolak, A.; Kamińska, M.; Sygit, K.; Budny, A.; Surdyka, D.; Kukiełka-Budny, B.; Burdan, F. *Ann. Agric. Environ. Med*. **2017**, *24*.

J. Mex. Chem. Soc. **2025**, *69*(4)
Regular Issue

ISSN-e 2594-0317

3. Ottini, L.; Capalbo, C.; Rizzolo, P.; Silvestri, V.; Bronte, G.; Rizzo, S.; Russo, A. *Breast Cancer: Targets Ther*. **2010**, 45-58.
4. Slamon, D.J.; Clark, G.M.; Wong, S.G.; Levin, W.J.; Ullrich, A.; McGuire, W.L. *Science*. **1987**, *235*, 177-182.
5. Tarantino, P.; Curigliano, G.; Tolaney, S.M. *Cancer Discovery*. **2022**, *12*, 2026-2030.
6. Baselga, J.; Swain, S.M. *Nat. Rev. Cancer*. **2009**, *9*, 463-475.
7. Shams ul Hassan, S.; Abbas, S.Q.; Hassan, M.; Jin, H.Z. *Anti-Cancer Agents Med. Chem*. **2022**, *22*, 731-746.
8. Candan, M.; Yılmaz, M.; Tay, T.; Erdem, M.; Türk, A.Ö. *Zeitschrift für Naturforschung C*. **2007**, *62*, 619-621.
9. Bhattacharyya, S.; Deep, P.R.; Singh, S.; Nayak, B. *Am. J. PharmTech Res*. **2016**, *6*, 1-7.
10. Verma, N.; Behera, B.C.; Sharma, B.O. *Hacettepe Journal of Biology and Chemistry*. **2012**, *40*, 7-21.
11. Morris Kupchan, S.; Kopperman, H.L. *Experientia*. **1975**, *31*, 625-625.
12. Roney, M.; Singh, G.; Huq, A.M.; Forid, M.S.; Ishak, W.M.B.W.; Rullah, K.; Tajuddin, S.N. *Mol. Biotechnol*. **2023**, 1-11.
13. Aertgeerts, K.; Skene, R.; Yano, J.; Sang, B.C.; Zou, H.; Snell, G.; Sogabe, S. *J. Biol. Chem*. **2011**, *286*, 18756-18765.
14. Liu, Y.; Grimm, M.; Dai, W.T.; Hou, M.C.; Xiao, Z.X.; Cao, Y. *Acta Pharmacol. Sin*. **2020**, *41*, 138-144.
15. Filimonov, D.A.; Lagunin, A.A.; Gloriozova, T.A.; Rudik, A.V.; Druzhilovskii, D.S.; Pogodin, P.V.; Poroikov, V.V. *Chem. Heterocycl. Compd*. **2014**, *50*, 444-457.
16. Qais, F.A.; Alomar, S.Y.; Imran, M.A.; Hashmi, M.A. *Molecules*. **2022**, *27*, 5793.
17. Rani, A.C.; Kalaimathi, K.; Jayasree, S.; Prabhu, S.; Vijayakumar, S.; Ramasubbu, R.; Priya, N.S. *Chem. Afr*. **2022**, 1-14.
18. Kiliç, N.; Islakoğlu, Y.Ö.; Büyük, İ.; Gür-Dedeoğlu, B.; Cansaran-Duman, D. D. *Anti-Cancer Agents Med. Chem.* **2019**, *19*, 1463-1472.
19. Özben, R.Ş.; Cansaran-Duman, D. *Human Experimen. Toxicol.* **2020**, *39*, 1497-1506.
20. Cansaran-Duman, D.; Tanman, Ü.; Yangın, S.; Atakol, O. *Cytotechnol.* **2020**, *72*, 855-872.
21. Zuo, S.T.; Wang, L.P.; Zhang, Y.; Zhao, D.N.; Li, Q.S.; Shao, D.; Fang, X.D. *RSC Adv.* **2015**, *5*, 153-162.
22. Pyrczak-Felczykowska, A.; Reekie, T.A.; Jąkalski, M.; Hać, A.; Malinowska, M.; Pawlik, A.; Herman-Antosiewicz, A. *Int. J. Mol. Sci.* **2022**, *23*, 1802.
23. Wong, K.K.V.; Roney, M.; Uddin, N.; Imran, S.; Gazali, A.M.; Zamri, N.; Aluwi, M.F.F.M. *J. Biomol. Struct. Dyn*. **2023**, 1-14.
24. Zuo, S.T.; Wang, L.P.; Zhang, Y.; Zhao, D.N.; Li, Q.S.; Shao, D.; Fang, X.D. *RSC Advances*. **2015**, *5*, 153-162.
25. Song, Y.; Dai, F.; Zhai, D.; Dong, Y.; Zhang, J.; Lu, B.; Yi, Z. *Angiogenesis*. **2012**, *15*, 421-432.
26. Roney, M.; Issahaku, A.R.; Govinden, U.; Gazali, A.M.; Aluwi, M.F.F.M.; Zamri, N.B. *J. Biomol. Struct. Dyn*. **2023**, 1-14.
27. https://www.who.int/news-room/fact-sheets/detail/breast-cancer, accessed in August 2025.
28. Cordero, M.J.A.; Villar, N.M.; Sánchez, M.N.; Pimentel-Ramírez, M.L.; García-Rillo, A.; Valverde, E.G. *Nutr. Hosp.* **2015**, *31*, 371-379.
29. Al-Khodairy, F.M.; Khan, M.K.A.; Kunhi, M.; Pulicat, M.S.; Akhtar, S.; Arif, J.M. *Am. J. Bioinform. Res*. **2013**, *3*, 62-71.
30. Yousuf, Z.; Iman, K.; Iftikhar, N.; Mirza, M.U. *Breast Cancer: Targets Ther*. **2017**, 447-459.
31. Ashtekar, S.S.; Bhatia, N.M.; Bhatia, M.S. *Int. J. Pept. Res. Ther*. **2019**, *25*, 659-667.
32. Muhammad, A.; Katsayal, B.S.; Forcados, G.E.; Malami, I.; Abubakar, I.B.; Kandi, A.I.; Umar, Z.W.S. *In Silico Pharmacology*. **2020**, *8*, 1-13.
33. Shrihastini, V.; Muthuramalingam, P.; Adarshan, S.; Sujitha, M.; Chen, J.T.; Shin, H.; Ramesh, M. *Cancers*. **2021**, *13*, 6222.
34. Tripathi, A.H.; Negi, N.; Gahtori, R.; Kumari, A.; Joshi, P.; Tewari, L.M.; Upadhyay, S.K. *Anti-Cancer Agents Med. Chem*. **2022**, *22*, 115-142.
35. Nguyen, T.T.; Yoon, S.; Yang, Y.; Lee, H.B.; Oh, S.; Jeong, M.H.; Kim, H. *PloS one*. **2014**, *9*, e111575.

J. Mex. Chem. Soc. **2025**, *69*(4)
Regular Issue

ISSN-e 2594-0317

36. Opo, F.A.D.M.; Rahman, M.M.; Ahammad, F.; Ahmed, I.; Bhuiyan, M.A.; Asiri, A.M. *Sci. Rep*. **2021**, *11*, 4049.
37. Uddin, M.J.; Ali Reza, A.S.M.; Abdullah-Al-Mamun, M.; Kabir, M.S.; Nasrin, M.S.; Akhter, S.; Rahman, M.A. *Front. Pharmacol*. **2018**, *9*, 246.
38. James, N.; Surana, R.; Thigale, I.; Preethi, B.; Shanthi, V.; Ramanathan, K. *Indian J. Pharm. Educ. Res.* **2018**, *52*, 707-717.
39. Roney, M.; Huq, A.M.; Rullah, K.; Hamid, H.A.; Imran, S.; Islam, M.A.; Mohd Aluwi, M.F.F. *J. Comput. Biophys. Chem*. **2021**, *20*, 797-814.

Article

J. Mex. Chem. Soc. **2025**, *69*(4)
Regular Issue

ISSN-e 2594-0317

In silico Computational Study of Cinnamon (*Cinnamomum verum*) Bioactive Compounds as Cancer-Immunotherapy Drug Candidate Targeting RAS-JAK-ERK Signaling Pathway to Inhibit the Programmed Death Protein Ligand 1 (PD-L1) Expression

Wira Eka Putra[1*], Sustiprijatno[2], Arief Hidayatullah[3], Diana Widiastuti[4], Muhammad Fikri Heikal[5]

[1]Biotechnology Study Program, Department of Applied Sciences, Faculty of Mathematics and Natural Sciences, Universitas Negeri Malang, East Java, Indonesia.
[2]Research Center for Applied Botany, National Research and Innovation Agency, West Java, Indonesia.
[3]Health Governance Initiative, United Nations Development Programme Indonesia, Eijkman-RSCM Building, Jakarta, Indonesia.
[4]Department of Chemistry, Faculty of Mathematics and Natural Science, Universitas Pakuan, West Java, Indonesia.
[5]Department of Biology, Faculty of Mathematics and Natural Sciences, Universitas Negeri Malang, East Java, Indonesia.

***Corresponding author:** Wira Eka Putra, email: wira.putra.fmipa@um.ac.id

Received March 20th, 2024; Accepted October 17th, 2024.

DOI: http://dx.doi.org/10.29356/jmcs.v69i4.2241

Abstract. Immunotherapy is the current and an alternative therapy option for cancer. Targeting PD-L1 expression provides one approach for limiting cancer progression. Cinnamon is a plant with medicinal properties that is also commonly used as a spice. Previous study indicates that cinnamon has multiple therapeutic effects because it is utilized to treat a variety of diseases. The purpose of this research is to examine the potential of bioactive compounds derived from cinnamon as potential cancer immunotherapy agents through the inhibition of PD-L1 expression. In the present investigation, *in silico* approaches were used, which included molecular docking and predicting the biological activity of cinnamon bioactive compounds. According to the findings, the active compound of cinnamon was effective and had the potential to inhibit the JAK protein, but not RAS or ERK. Furthermore, according to the biological activity predictions, cinnamon bioactive compounds contribute as cancer fighting agents by having high Pa values for several parameters such as antineoplastic, apoptosis agonist, BRAF expression inhibitor, JAK2 expression inhibitor, and Myc inhibitor also low Pa values for M-CSF agonists. Finally, more detailed research on cinnamon bioactive compounds, particularly caryophyllene, is required.
Keywords: Cancer-immunotherapy; ERK; JAK; PD-L1; RAS.

Resumen. La inmunoterapia es la opción terapéutica alternativa actual para el cáncer. Usar como blanco la expresión de PD-L1 ofrece un enfoque para limitar la progresión del cáncer. La canela es una planta con propiedades medicinales que también se usa comúnmente como especia. Estudios previos indican que la canela tiene múltiples efectos terapéuticos, ya que se utiliza para tratar diversas enfermedades. El propósito de esta investigación es examinar el potencial de los compuestos bioactivos derivados de la canela como posibles agentes de inmunoterapia contra el cáncer mediante la inhibición de la expresión de PD-L1. En la presente investigación, se utilizaron enfoques *in silico*, que incluyeron el acoplamiento molecular y la predicción de la actividad biológica de los compuestos bioactivos de la canela. Según los hallazgos, el compuesto activo de la

J. Mex. Chem. Soc. **2025**, *69*(4)
Regular Issue

ISSN-e 2594-0317

canela fue eficaz y tenía el potencial de inhibir la proteína JAK, pero no RAS ni ERK. Además, según las predicciones de la actividad biológica, los compuestos bioactivos de la canela contribuyen como agentes anticancerígenos al presentar altos valores de Pa para diversos parámetros, como antineoplásico, agonista de la apoptosis, inhibidor de la expresión de BRAF, inhibidor de la expresión de JAK2 e inhibidor de Myc, así como bajos valores de Pa para agonistas del M-CSF. Finalmente, se requiere una investigación más detallada sobre los compuestos bioactivos de la canela, en particular el cariofileno.
Palabras clave: Inmunoterapia contra el cáncer; ERK; JAK; PD-L1; RAS.

Introduction

Nearly 2 million new cancer diagnoses and approximately six hundred thousand cancer deaths are expected in the United States in 2023 [1]. According to the recent study, lung cancer will still be the primary cause of cancer-related mortality in 2040, accounting for 63,000 deaths, while breast cancer will account for 364,000 cases of cancer overall [2]. Ironically about 35 % of global cancer-related mortality can be attributed to lifestyle-related risk factors that are conceivably modifiable. These risks include smoking, alcohol intake, infections, parasites, exposure to UV radiation, and nutritional factors [3]. For instance, a study showed the excessive caloric consumption and insufficient physical activity are linked to elevated adipose tissue accumulation, which ultimately results in overweight, obesity, and cancer [4].

The classifications of cancer treatment are divided into conventional and advanced categories. Presently, established conventional treatment modalities, including surgery, chemotherapy, and radiotherapy, continue to be employed. However, noteworthy progressions in recent years have been observed in the form of targeted therapies, nanoparticles, hormonal therapy and stem cell therapy. Currently, oncology techniques have their emphasis on the creation of safe and efficient cancer treatments [5,6].

Immune checkpoint inhibitors are examples of immunotherapy, a type of cancer treatment that uses immune system components to combat tumor cells [7]. In various cancer cases, immunotherapy—either by itself or in conjunction with conventional approaches such radiation and chemotherapy—has shown favorable outcomes when utilized alongside standard care. PD-1 inhibitors, PD-L1 inhibitors, and CTLA-4 inhibitors are three distinct classes of immune checkpoint inhibitors that have been used to treat different kinds of cancer. However, only a small percentage of individuals recover from this treatment. A number of variables determine immunotherapy outcomes, including tumor mutational burden, PD-L1 expression, hypoxia, extracellular matrix, and molecular and cellular characterization within the tumor microenvironment [7,8]

In order to decrease T cell activation and the immunological response of T cells specific to antigens, tumors overstimulate the PD-1/L1 signaling pathway. Apart from PD-L1 expression, cancer cells also trigger intrinsic cellular signals that improve cancer cell survival, control stress reactions, and strengthen tumor resistance to pro-apoptotic agents like interferons [7]. A study showed the stimulation of interferon could increasing the expression of PD-L1 through JAK/STAT signaling pathway [9]. Another study in cholangiocarcinoma cell lines showed that PD-L1 expression is modulated via ERK signaling [10]. Thus, by blocking the signaling pathways that involved in PD-L1 expression might contribute in the anti-tumor surveillance system. Recently, some immune checkpoint inhibitors have been proposed for targeting PD-1/PD-L1, however, unfortunately, some additional adverse events also appears which need serious attention to solve [11,12].

Recently, medicinal plants and their bioactive components have gained popularity as immunomodulation and complementary cancer treatments [13-18]. Numerous clinical investigations have found that medicinal plants improve survival, immunological regulation, and quality of life [19,20]. On a large scale, cinnamon can be found in tropical regions. Cinnamon is widely utilized on a daily basis throughout the globe and is regarded as one of the most essential spices. Importantly, cinnamon has antioxidant, anti-inflammatory, antidiabetic, antibacterial, anti-obesity, and anticancer properties [21,22]. Interestingly, a study showed that cinnamon extract inhibit the melanoma cell lines progression by reducing some factors related to the angiogenesis. Moreover, the study also demonstrated that cinnamon extract increase the activity of CD8+ T cells which were known for its anti-tumor activity [23]. In light of the aforementioned, the intent of this study

J. Mex. Chem. Soc. **2025**, *69*(4)
Regular Issue

ISSN-e 2594-0317

is to determine the potential of bioactive compounds found in cinnamon as a cancer immunotherapy drugs candidate by blocking PD-L1 expression.

Experimental

Data retrieval and preparation

Bioactive compounds that widely found in cinnamon were occupied in this study [24]. The chemical structure of bioactive compounds was retrieved from The PubChem database (https://pubchem.ncbi.nlm.nih.gov/). About nine bioactive compounds (Fig. 1) including camphor (CID. 2537); caryophyllene (CID. 5281515); caryophyllene oxide (CID. 1742210); cinnamaldehyde (CID. 637511); eugenol (CID. 3314); trans-alpha-bergamotene (CID. 6429302); trans-cinnamyl acetate (CID. 5282110); α-bergamotene (CID. 86608); and α-copaene (CID. 442355) were retrieved together with three control drugs including RAS inhibitor/ Tipifarnib (CID. 159324); JAK inhibitor/ Ruxolitinib (CID. 25126798); and ERK inhibitor/ GDC-0994 (CID. 154702204). In order to provide target proteins, homology modelling approach was applied. The sequences of target protein were retrieved from UniProt (https://www.uniprot.org/) and the 3D structure of target proteins was built through SWISS-MODEL (https://swissmodel.expasy.org/) as our previous study [25-27]. The detailed UniProt ID and protein template of each target proteins are RAS (UniProt ID. P01112/ template 4q21.1.A); JAK (UniProt ID. P23458/ template 7t6f.1.A); and ERK (UniProt ID. P28482/ template 4qtb.1.A).

Molecular docking and data visualization

Molecular docking was performed by using PyRx (https://pyrx.sourceforge.io/) software [28,29]. Prior to docking process, the whole structure of each target proteins was aimed by bioactive compounds and control drug. The center coordinates for each target protein (Å) are RAS (X= 57.1120; Y= 71.3046; Z= 40.5094); JAK (X= 178.123; Y= 198.282; Z= 171.913); and ERK (X= 33.2178; Y= 46.6949; Z= 56.9310). Molecular coverage area (Å) for each target proteins are RAS (X= 39.8465; Y= 43.3056; Z= 42.5991); JAK (X= 85.5510; Y= 72.0893; Z= 148.8165); and ERK (X= 60.5657; Y= 47.6961; Z= 69.0495). After molecular docking was performed, the data visualization then was conducted by using Biovia Discovery Studio (https://discover.3ds.com/) software. Several parameters including protein – ligand interaction, amino acids residues, H-bond, and hydrophobicity were visualized and analyzed [30,31].

Biological activity prediction

Biological activity prediction was performed on bioactive compounds derived from cinnamon through the Way2Drug (https://www.way2drug.com/PassOnline/index.php) webserver. The purpose of this prediction was to determine the effectiveness as well as the potential of the active compound derived from cinnamon with regarding a variety of distinct biological activities. Some parameters were evaluated including antineoplastic, apoptosis agonist, BRAF expression inhibitor, JAK2 expression inhibitor, Myc inhibitor, M-CSF agonist.

Results and discussion

It has been widely known that, the expressed PD-L1 on cancer cells interacts to the PD-1 on immune cells promotes cancer progression and cancer immune escape. Therefore, the recent immunotherapy strategy is to block the PD-1/ PD-L1 interaction which in turn could optimize the T cells function, reducing the regulatory T cells activity, and other immune mechanisms in eliminating cancer cells [32,33]. Another strategy which might work is to limiting the PD-L1 expression on the cancer cells by targeting RAS-JAK-ERK signaling pathways [34,35]. In this present study, we evaluated the therapeutic properties of cinnamon bioactive compounds through computational assessment and biological activity prediction.

According to the results of molecular docking, the bioactive components from cinnamon were found to be in the same position as the control drugs across the RAS, JAK, and ERK target proteins (Fig. 2). This suggests that these active compounds have a similar ability to interact at the same active site on target proteins

J. Mex. Chem. Soc. **2025**, *69*(4)
Regular Issue

ISSN-e 2594-0317

as the control drug [36,37]. Interestingly, a binding affinity value was established based on the results of molecular docking, which determines whether the active component from Cinnamon has greater potential than the control drugs. Three substances, trans-cinnamyl acetate, trans-alpha-bergamotene, and caryophyllene oxide, were found to have binding affinity values of -6.9, -6.2, and -6.1 kcal/mol for the RAS protein target. However, the stated binding affinity value is still less effective when compared to the control drug, Tipifarnib, which has a binding affinity value of -8.5 kcal/mol.

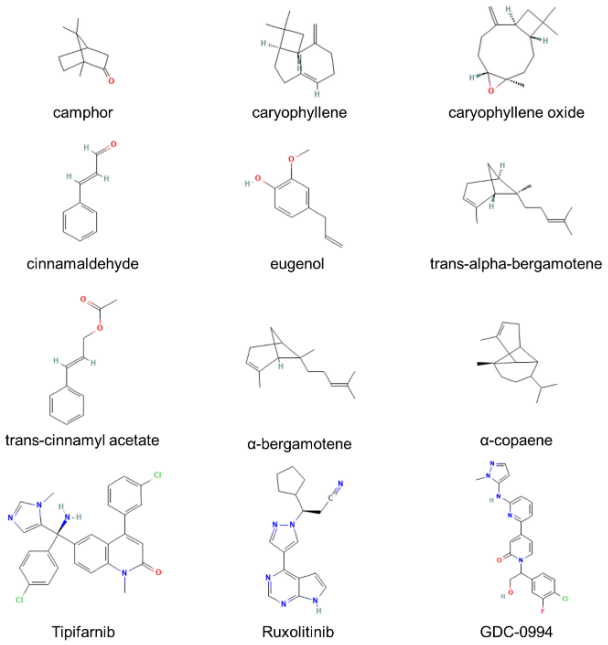

Fig. 1. The 2D structure of ligands used for targeting the RAS, JAK, and ERK protein.

Furthermore, binding affinity values for the JAK protein target were -7.0, -6.9, and -6.7 kcal/mol for three substances, namely caryophyllene, caryophyllene oxide, and α-copaene. Surprisingly, it was discovered that caryophyllene had a higher binding affinity value than the control drug while caryophyllene oxide had the same binding affinity value as the control medication, Ruxolitinib, with a value of -6.9 kcal/mol. Finally, for the ERK protein target, binding affinity values of -7.9, -7.5, and -7.3 kcal/mol were reported for three compounds, namely caryophyllene oxide, caryophyllene, and α-copaene. Similarly to the RAS protein target, the binding affinity value obtained for the ERK protein target is still less favorable when compared to the control medication, GDC-0994, which has a value of -9.4 kcal/mol. Based on the findings from previous studies, it is known that if a molecule has a rising negative binding affinity value, it has a higher proclivity to interact with the target protein [38,39]. As a result, it was discovered in this study that the caryophyllene that interacts with the JAK protein has greater potential than the control drugs due to the fact that has a lower binding affinity value.

J. Mex. Chem. Soc. **2025**, *69*(4)
Regular Issue

ISSN-e 2594-0317

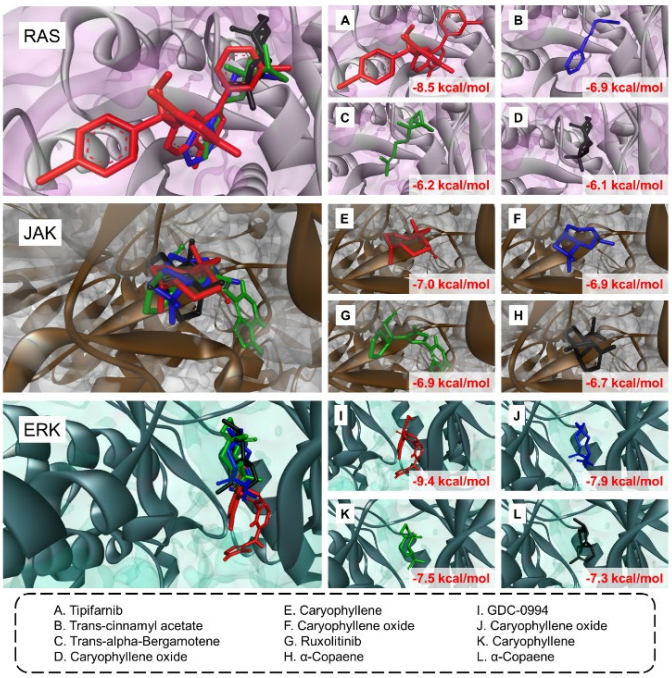

Fig. 2. The 3D structure visualization of protein – ligand complexes after molecular docking. There are three target proteins related to the PDL1 generation signaling including RAS (upper panel), JAK (middle panel), and ERK (lower panel). The number shown in the figure represent the binding affinity value from each ligand to the target protein.

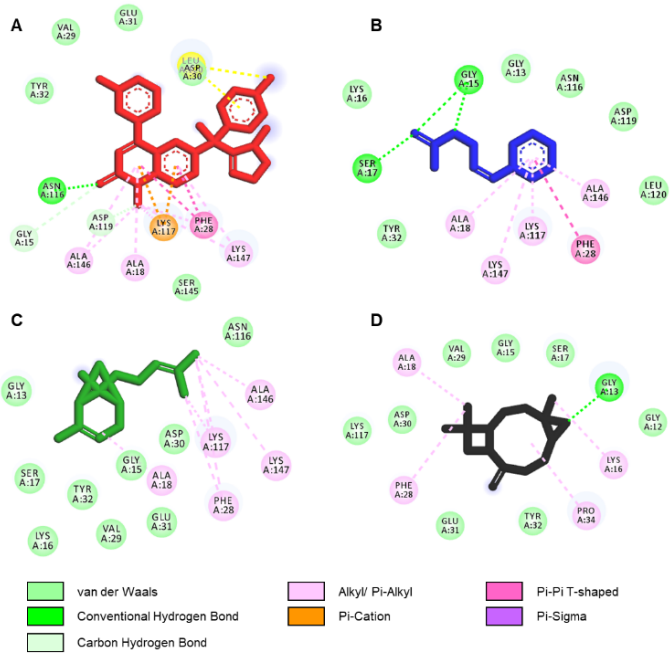

Fig. 3. The 2D structure visualization of ligand interaction to RAS protein after molecular docking. The order of ligand showed in the figure based on the lowest binding affinity score; **(A)** Tipifarnib, **(B)** Trans-cinnamyl acetate, **(C)** Trans-alpha-Bergamotene, and **(D)** Caryophyllene oxide.

J. Mex. Chem. Soc. **2025**, *69*(4)
Regular Issue

ISSN-e 2594-0317

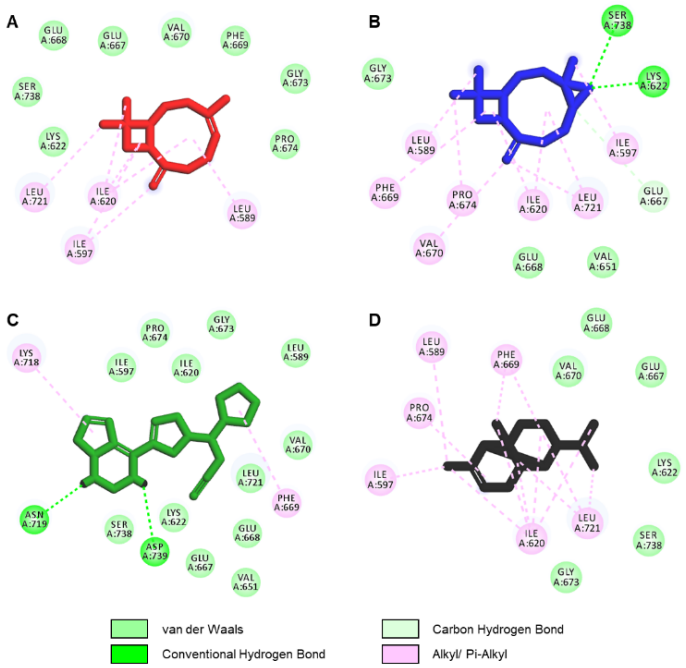

Fig. 4. The 2D structure visualization of ligand interaction to JAK protein after molecular docking. The order of ligand showed in the figure based on the lowest binding affinity score; **(A)** Caryophyllene, **(B)** Caryophyllene oxide, **(C)** Ruxolitinib, and **(D)** α-Copaene.

Furthermore, an overview of the chemical interactions established, and the amino acid residues contained in these interactions is given based on 2D imaging of the protein-ligand complex. Van der Waals, conventional hydrogen bond, carbon hydrogen bond, alkyl/pi-alkyl, pi-cation, pi-pi T-shaped, and pi-sigma chemical interactions have been observed in the RAS protein target (Fig. 3). Meanwhile, various chemical interactions were founded in the JAK protein target, including van der Waals, conventional hydrogen bond, carbon hydrogen bond, and alkyl/pi-alkyl (Fig. 4). Finally, numerous chemical interactions were formed on the ERK protein target, including van der Waals, conventional hydrogen bond, carbon hydrogen bond, unfavorable donor-donor, pi-cation/ pi-anion, pi-sulfur, alkyl/ pi-alkyl, pi-pi T-shaped, and pi-sigma (Fig. 5). Noncovalent interactions, such as electrostatic interactions, salt bridges, or hydrogen bonds, are commonly employed by bioactive compounds and small molecules to bind to proteins [40]. The type of interaction between ligand and protein is particularly essential in drug discovery and development research. The interactions that occur can be beneficial or detrimental. For example, the interaction formed between the ligand and protein can increase the ligand's activity and performance against the target protein, or conversely, it can reduce the effectiveness of the ligand's work and increase the occurrence of side effects [41,42]. Furthermore, each complex of protein-ligand interactions encompasses various amino acid residues. The presence of amino acid residues is particularly crucial in drug discovery and development research since it may determine the strength and weakness of interactions, folding, rigidity, and flexibility of complexes [43,44].

J. Mex. Chem. Soc. **2025**, *69*(4)
Regular Issue

ISSN-e 2594-0317

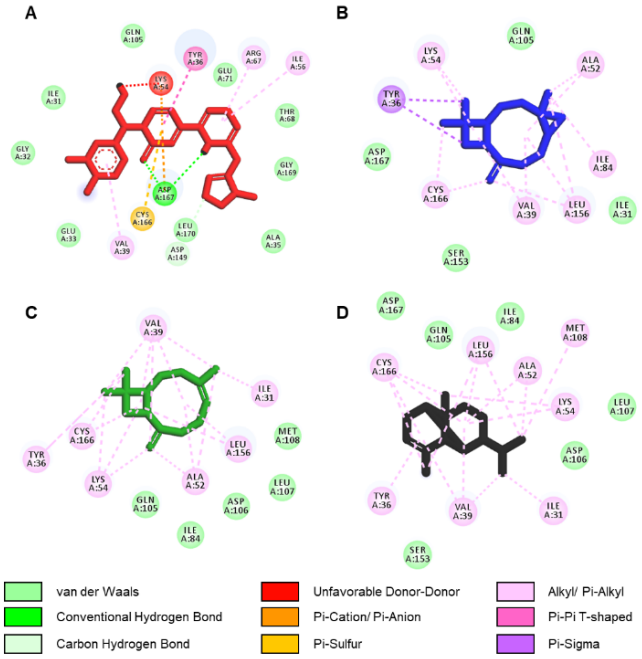

Fig. 5. The 2D structure visualization of ligand interaction to ERK protein after molecular docking. The order of ligand showed in the figure based on the lowest binding affinity score; **(A)** GDC-0994, **(B)** Caryophyllene oxide, **(C)** Caryophyllene, and **(D)** α-Copaene.

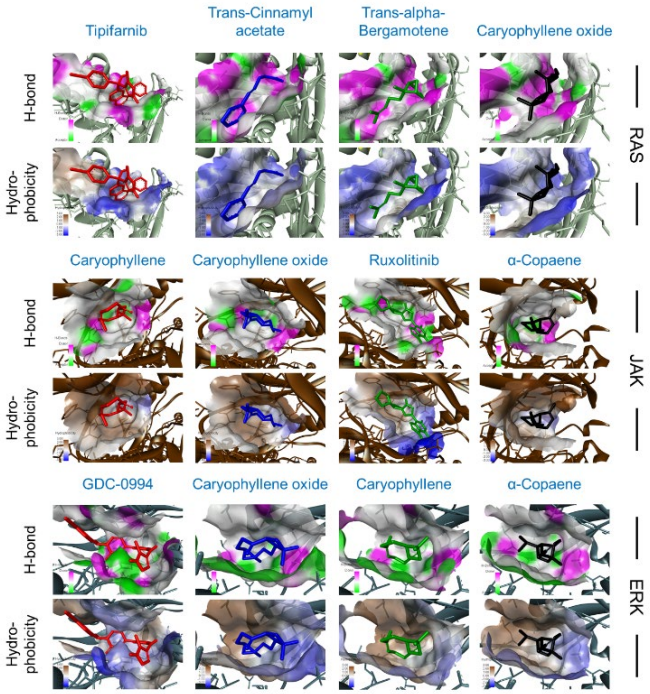

Fig. 6. The physic-chemistry properties of protein – ligand complexes including H-bond and hydrophobicity. RAS (upper panel), JAK (middle panel), and ERK (lower panel).

J. Mex. Chem. Soc. **2025**, *69*(4)
Regular Issue

ISSN-e 2594-0317

In addition, we attempted to investigate and demonstrate the appearance of protein-ligand interactions with H-bond composition and hydrophobicity features (Fig. 6). Commonly, in the interaction of protein-drugs, H-bonds play a critical role. For example, the strength of the H-bond in an interaction influences drug release. A number of variables influence the strength of the H-bond, including the sort of amino acid residue located in the active site and the amount of hydrogen acceptors and donors. The experimental application of hydrogen bonding interactions in drug research has yielded promising outcomes in terms of changing medicinal properties, effectivity of recognition, and drug delivery [45-47]. Thus, in this present study, we assumed that the hydrogen bond in the complex of protein – ligand might become favorable factors that improve the activity of cinnamon bioactive compounds during protein – ligand interaction. It has widely known that hydrophobic forces affect biology and pharmacological activity. In protein structures with open conformations, weak intermolecular interactions like hydrogen bonding and hydrophobic interactions stabilize energetically-favored ligands. More important, precision hydrophobicity measurements and hydrophobic interaction estimations may significantly impact protein folding and side chain orientation models. Improved modeling and depiction of hydrophobic interactions may assist to elucidate biological phenomena like efflux-induced medication resistance [48,49].

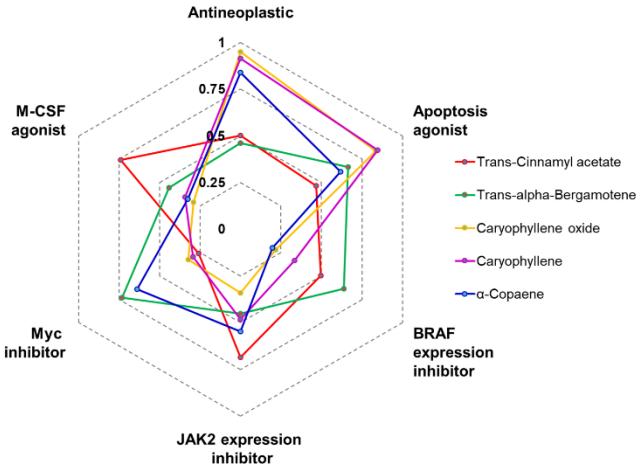

Fig. 7. The biological activities prediction of *Cinamon* bioactive compounds. The predicted biological activities measured are related to the anti-cancer progression which include antineoplastic, apoptosis agonist, BRAF expression inhibitor, JAK2 expression inhibitor, Myc inhibitor, and M-CSF agonist.

Moreover, we predicted the biological activity of bioactive compounds derived from cinnamon (Fig. 7). By employing this biological activity prediction method, it is possible to ascertain the propensities and potential of these active compounds as viable substitute therapies for specific diseases. Several parameters with anti-cancer hallmarks were employed in this work, including antineoplastic, apoptosis agonist, BRAF expression inhibitor, JAK2 expression inhibitor, Myc inhibitor, and M-CSF agonist [50,51]. A number of compounds with prominent potential for various parameters were obtained according to our *in silico* study. Caryophyllene oxide, caryophyllene, and α-copaene, for example, have a high antineoplastic potential. Caryophyllene and caryophyllene oxide are powerful apoptosis inducers. Trans-alpha-bergamotene and trans-cinnamyl acetate have the ability to suppress BRAF expression. JAK2 expression inhibitors comprise trans-cinnamyl acetate, α-copaene, and caryophyllene. Trans-alpha-bergamotene and α-copaene have the potential to be dominant as Myc inhibitors, while very few substances operate as M-CSF agonists, with only trans-cinnamyl acetate having a high Pa value when compared to other drugs which indicates the other compounds exerts the anti-M-CSF activation properties.

J. Mex. Chem. Soc. **2025**, *69*(4)
Regular Issue

ISSN-e 2594-0317

Conclusions

In accordance with the results of biological activity predictions, it was discovered that cinnamon's active compounds contribute as cancer fighting agents by having high Pa values for several parameters such as antineoplastic, apoptosis agonist, BRAF expression inhibitor, JAK2 expression inhibitor, and Myc inhibitor also low Pa values contrary to M-CSF agonists. On top of that, molecular docking experiments revealed that caryophyllene compounds have higher binding affinity for JAK as a protein target than other compounds, including control drugs. Even though the cinnamon compounds did not possess more affinity for binding than the control drugs on the RAS and ERK protein, a larger investigation such as structure modification and molecular dynamic simulations remains required.

Acknowledgments

We thank Biocomputational Laboratory, Department of Biology, Brawijaya University for providing the research facility for this study.

References

1. Siegel, R. L.; Miller, K. D.; Wagle, N. S.; Jemal, A. *CA Cancer J. Clin.* **2023**, *73*, 17–48.
2. Rahib, L.; Wehner, M. R.; Matrisian, L. M.; Nead, K. T. *JAMA Netw. Open.* **2021**, *4*, e214708.
3. Lewandowska, A. M.; Rudzki, M.; Rudzki, S.; Lewandowski, T.; Laskowska, B. *Ann. Agric. Environ. Med.* **2019**, *26*, 1–7.
4. Akinyemiju, T.; Wiener, H.; Pisu, M. *BMC Cancer.* **2017**, *17*, 597.
5. Debela, D. T.; Muzazu, S. G.; Heraro, K. D.; Ndalama, M. T.; Mesele, B. W.; Haile, D. C.; Kitui, S. K.; Manyazewal, T. *SAGE Open Med.* **2021**, *9*, 20503121211034308.
6. Stub, T.; Quandt, S. A.; Arcury, T. A.; Sandberg, J. C.; Kristoffersen, A. E. *BMC Health Serv. Res.* **2018**, *18*, 854.
7. Makuku, R.; Khalili, N.; Razi, S.; Keshavarz-Fathi, M.; Rezaei, N. J. *Immunol. Res.* **2021**, *2021*, 6661406.
8. Shiravand, Y.; Khodadadi, F.; Kashani, S. M. A.; Hosseini-Fard, S. R.; Hosseini, S.; Sadeghirad, H.; Ladwa, R.; O'Byrne, K.; Kulasinghe, A. *Curr. Oncol.* **2022**, *29*, 3044–3060.
9. Zhao, T.; Li, Y.; Zhang, J.; Zhang, B. *Oncol. Lett.* **2020**, *20*, 1127–1134.
10. Gao, Z.; Chen, J. F.; Li, X. G.; Shi, Y. H.; Tang, Z.; Liu, W. R.; Zhang, X.; Huang, A.; Luo, X. M.; Gao, Q.; Shi, G. M.; Ke, A. W.; Zhou, J.; Fan, J.; Fu, X. T.; Ding, Z. B. *Cancer Cell Int.* **2022**, *22*, 1–12.
11. Su, C.; Wang, H.; Liu, Y.; Guo, Q.; Zhang, L.; Li, J.; Zhou, W.; Yan, Y.; Zhou, X.; Zhang, J. *Front. Oncol.* **2020**, *10*, 554313.
12. Martins, F.; Sofiya, L.; Sykiotis, G. P.; Lamine, F.; Maillard, M.; Fraga, M.; Shabafrouz, K.; Ribi, C.; Cairoli, A.; Guex-Crosier, Y.; Kuntzer, T.; Michielin, O.; Peters, S.; Coukos, G.; Spertini, F.; Thompson, J. A.; Obeid, M. *Nat. Rev. Clin. Oncol.* **2019**, *16*, 563–580.
13. Putra, W. E.; Mentari, A. M. L. S.; Ratnasari, D.; Chairunniza, D.; Hidayatullah, A.; Rifa'i, M. *FABAD J. Pharm. Sci.* **2024**, *49*, 91–110.
14. Li, T. F.; Hwang, I. H.; Tsai, C. H.; Hwang, S. J.; Wu, T. P.; Chen, F. P. J. *Chin. Med. Assoc.* **2023**, *86*, 767–774.
15. Putra, W. E.; Agusinta, A. K.; Ashar, M. S. A. A.; Manullang, V. A.; Rifa'i, M. K. *Int. J. Mod. Sci.* **2023**, *9*, 1–14.
16. Amrati, F. E.; Bourhia, M.; Slighoua, M.; Mohammad, S. A.; Alzahrani, A.; Ullah, R.; Bari, A.; Bousta, D. *Saudi Pharm. J.* **2021**, *29*, 1185–1204.
17. Putra, W. E.; Maulana, A. R.; Ramadhan, A. T. K.; Rifa'i, M. *J. Herbmed Pharmacol.* **2020**, *9*, 408–411.

J. Mex. Chem. Soc. **2025**, *69*(4)
Regular Issue

ISSN-e 2594-0317

18. Putra, W. E.; Rifa'i, M. *Adv. Pharm. Bull.* **2019**, *9*, 619–623.
19. Xiang, Y.; Guo, Z.; Zhu, P.; Chen, J.; Huang, Y. *Cancer Med.* **2019**, *8*, 1958–1975.
20. Yin, S. Y.; Wei, W. C.; Jian, F. Y.; Yang, N. S. *Evid. Based Complement. Alternat. Med.* **2013**, *2013*, 302426.
21. Rao, P. V.; Gan, S. H. *Evid. Based Complement. Alternat. Med.* **2014**, *2014*, 642942.
22. Gruenwald, J.; Freder, J.; Armbruester, N. *Crit. Rev. Food Sci. Nutr*. **2010**, *50*, 822–834.
23. Kwon, H. K.; Jeon, W. K.; Hwang, J. S.; Lee, C. G.; So, J. S.; Park, J. A.; Ko, B. S.; Im, S. H. *Cancer Lett.* **2009**, *278*, 174–182.
24. Arora, S.; Gusain, M. P.; Gunupuru, R.; Kaushik, R.; Sinha, P.; Kumar, D. *Eur. J. Mol. Clin. Med.* **2021**, *8*, 1–15.
25. Hidayatullah, A.; Putra, W. E.; Sustiprijatno; Widiastuti, D.; Salma, W. O.; Heikal, M. F. *Trends Sci.* **2023**, *20*, 1–12.
26. Putra, W. E. *FTSTJ*. **2018**, *3*, 682–685.
27. Putra, W. E.; Agustin, F.; Rochmatika, L.; Salma, W. O. Malays. J. *Biochem. Mol. Biol.* **2019**, *1*, 152–154.
28. Hidayatullah, A.; Putra, W. E.; Sustiprijatno; Permatasari, G. W.; Salma, W. O.; Widiastuti, D.; Susanto, H.; Muchtaromah, B.; Sari, D. R. T.; Ningsih, F. N.; Heikal, M. F.; Yusuf, A. M. R.; Arizona, A. S. *Chiang Mai Univ. J. Nat. Sci.* **2021**, *20*, 1–20.
29. Putra, W. E.; Salma, W. O.; Rifa'i, M. *Nat. Prod. Sci*. **2019**, *25*, 215–221.
30. Hidayatullah, A.; Putra, W. E.; Salma, W. O.; Muchtaromah, B.; Permatasari, G. W.; Susanto, H.; Widiastuti, D.; Kismurtono, M. *Chiang Mai Univ. J. Nat. Sci.* **2021**, *20*, 1–17.
31. Putra, W. E.; Waffareta, E.; Ardiana, O.; Januarisasi, I. D.; Soewondo, A.; Rifa'i, M. *Biosci. Res.* **2017**, *14*, 201–213.
32. Yi, M.; Niu, M.; Xu, L.; Luo, S.; Wu, K. J. *Hematol. Oncol.* **2021**, *14*, 10.
33. Dong, Y.; Sun, Q.; Zhang, X. *Oncotarget*. **2017**, *8*, 2171–2186.
34. Zerdes, I.; Matikas, A.; Bergh, J.; Rassidakis, G. Z.; Foukakis, T. *Oncogene.* **2018**, *37*, 4639–4661.
35. Bardhan, K.; Anagnostou, T.; Boussiotis, V. A. *Front. Immunol.* **2016**, *7*, 550.
36. McDonald, J.; Lambert, D. G. *BJA Educ.* **2022**, *22*, 20–25.
37. Dror, R. O.; Pan, A. C.; Arlow, D. H.; Borhani, D. W.; Maragakis, P.; Shan, Y.; Xu, H.; Shaw, D. E. *Proc. Natl. Acad. Sci. U.S.A.* **2011**, *108*, 13118–13123.
38. Terefe, E. M.; Ghosh, A. *Bioinform. Biol. Insights.* **2022**, *16*, 11779322221125605.
39. Owoloye, A. J.; Ligali, F. C.; Enejoh, O. A.; Musa, A. Z.; Aina, O.; Idowu, E. T.; Oyebola, K. M. *PLoS One.* **2022**, *17*, e0268269.
40. Pichler, W. J.; Adam, J.; Watkins, S.; Wuillemin, N.; Yun, J.; Yerly, D. *Int. Arch. Allergy Immunol.* **2015**, *168*, 13–24.
41. Cascorbi, I. *Dtsch. Arztebl. Int.* **2012**, *109*, 546–555.
42. van Roon, E. N.; Flikweert, S.; le Comte, M.; Langendijk, P. N.; Kwee-Zuiderwijk, W. J.; Smits, P.; Brouwers, J. R. *Drug Saf.* **2005**, *28*, 1131–1139.
43. Alekseeva, I. V.; Kuznetsova, A. A.; Bakman, A. S.; Fedorova, O. S.; Kuznetsov, N. A. *Biochim. Biophys. Acta Gen. Subj.* **2020**, *1864*, 129718.
44. Kulandaisamy, A.; Lathi, V.; ViswaPoorani, K.; Yugandhar, K.; Gromiha, M. M. *Int. J. Biol. Macromol.* **2017**, *94*, 438–444.
45. Luo, Z.; Liu, C.; Quan, P.; Yang, D.; Zhao, H.; Wan, X.; Fang, L. *Acta Pharm. Sin. B.* **2020**, *10*, 928–945.
46. Hutchins, K. M. R. *Soc. Open Sci.* **2018**, *5*, 180564.
47. Chen, D.; Oezguen, N.; Urvil, P.; Ferguson, C.; Dann, S. M.; Savidge, T. C. *Sci. Adv*. **2016**, *2*, e1501240.
48. Patil, R.; Das, S.; Stanley, A.; Yadav, L.; Sudhakar, A.; Varma, A. K. *PLoS One.* **2010**, *5*, e12029.
49. Sarkar, A.; Kellogg, G. E. *Curr. Top. Med. Chem.* **2010**, *10*, 67–83.
50. Hanahan, D. *Cancer Discov.* **2022**, *12*, 31–46.
51. Ravi, S.; Alencar, A. M., Jr.; Arakelyan, J.; Xu, W.; Stauber, R.; Wang, C. I.; Papyan, R.; Ghazaryan, N.; Pereira, R. M. *Cureus.* **2022**, *14*, e24803.

Article

J. Mex. Chem. Soc. **2025**, *69*(4)
Regular Issue

ISSN-e 2594-0317

Targeted transcriptomics of the Mexican prickly poppy (*Argemone mexicana* L.) reveals diverse proteins related to benzylisoquinoline alkaloid biosynthesis

José Germán Serrano-Gamboa[1,§], Jorge Froylán Xool-Tamayo[1,2,§], Lloyd Loza-Muller[1], Yahaíra J. Tamayo-Ordóñez[1,3], Felipe Vázquez-Flota[1]*

[1]Unidad de Biología Integrativa, Centro de Investigación Científica de Yucatán, Calle 43 No. 130 Chuburná 97205, Mérida, Yucatán, México.
[2]Current address: División de Biología Experimental y Aplicada, Centro de Investigación Científica y de Educación Superior de Ensenada, Carretera Ensenada-Tijuana No. 3918 Zona Playitas 22860, Ensenada BC México.
[3]Current address: Facultad de Ciencias Químicas, Universidad Autónoma de Coahuila, Ing J. Cárdenas Valdez S/N República 25280, Saltillo Coahuila México.

[§]*These authors contributed equally*

***Corresponding author:** Felipe Vázquez-Flota, email: felipe@cicy.mx

Received February 19th, 2024; Accepted November 11th, 2024.

DOI: http://dx.doi.org/10.29356/jmcs.v69i4.2223

Abstract. A transcriptomic approach was employed to describe a set of putatively protein-coding sequences involved in the biosynthesis of berberine and sanguinarine, the two major benzylisoquinoline alkaloids (BIA) from *Argemone mexicana* (L.; Papaveraceae). A robust *de novo* assembled transcriptome was obtained from developing seedlings. Initial screening identified 514 unigenes, from eight different Pfam domains, such as Cyt-P450 dependent proteins, which are recurrently involved in BIA biosynthesis. Additional annotation by KEGG Orthology and Gene Ontology supported putative participation of the selected proteins in alkaloid biosynthesis. Moreover, *in silico* structure prediction of sanguinarine reductase (SanR), dihydrobenzophenantridine oxidase (DHBO) and tetrahydroprotoberberine oxidase (STOX), involved in the last reactions of sanguinarine and berberine biosynthesis, fitted to those of previously characterized proteins from related species, and thus, further supporting proper annotation. Hence, the pipeline analysis presented can provide a comprehensive description of the biosynthetic potential of this plant through functionality associated to its transcripts.
Keywords: *Argemone mexicana*; benzylisoquinoline alkaloids; cytochrome P450; dihydrobenzophenantridine oxidase; sanguinarine reductase; tetrahydroprotoberberine oxidase; transcriptomics.

Resumen. Un acercamiento transcriptómico se empleó para predecir un conjunto de secuencias condificantes para proteínas presuntamente involucradas en la biosíntesis de dos de los principales alcaloides bencilisoquinlínicos (ABI) en *Argemone mexicana* (L.; Papaveraceae). Un transcriptoma robusto, se obtuvo de plántulas en desarrollo. Un cribaje inicial identificó 514 unigenes de ocho dominios Pfam diferentes, incluyendo proteínas dependientes del CitP450, que participan en muchas reacciones en la biosíntesis de ABI. Anotaciones adicionales siguiendo la ortología KEGG y Gene Ontology sugirió la participación de un grupo de proteínas en la biosíntesis de alcaloides. Más aún, el modelaje estructural *in silico* de la sanguinarina reductasa (SanR), dihidrobenzophenantridina oxidasa (DHBO) y tetrahidroprotoberberine oxidase (STOX), responsables de las últimas reacciones de la síntesis de sanguinarina y berberina encajaron los previamente descritos para estas enzimas en otras especies relacionadas, confirmando la asignación recibida en la anotación. De este modo, el

J. Mex. Chem. Soc. **2025**, *69*(4)
Regular Issue

ISSN-e 2594-0317

análisis bioinformático realizado puede ser útil para la descripción detallada del potencial biosintético de esta planta a través de la caracterización funcional de los candidatos seleccionados.
Palabras clave: *Argemone mexicana*; alcaloides bencilisoquinolínicos; citocromo P450; dihidrobenzofenantridina oxidasa; sanguinarina reductasa; tetrahydroprotoberberina oxidasa; transcriptómica.

Introduction

Argemone mexicana L., commonly known as Mexican prickly poppy, cardosanto or chicalote, belongs to the Papaveraceae family. It is widely spread through tropical and subtropical ecosystems and often used in traditional medicine. Ancient Mesoamerican cultures used it against parasitic and microbial infections [1–3]. However, it is also a poisonous plant, particularly for the presence of alkaloids in its seeds [4]. Although it accumulates more than 20 alkaloids, berberine, a protoberberine, and sanguinarine, a benzophenanthridine, represent the most prominent ones [5,6]. Sanguinarine has potent antiviral and cytotoxic effects [7,8], whereas berberine displays important antidiabetic effects on hyperglycemic rats [9]. Moreover, recent studies have demonstrated that berberine ameliorates the inflammatory response in severely affected COVID-19 patients [10]. Hence, a growing interest exists in obtaining both these alkaloids. Unfortunately, only low quantities of them could be recovered directly from plant tissues, so other viable alternatives are under analysis. Although their chemical synthesis or semi-synthesis has been explored, the presence of multiple chiral centers makes large-scale production economically unfeasible [11,12]. Metabolic engineering represents an interesting approach for the up-yield production of plant specialized metabolites (PSM), especially in non-model species. However, this approach requires an extensive knowledge of the genes involved in the metabolic pathways of interest, not only for the biosynthetic process, but also for its regulation and intermediary transport [13]. In this sense, high throughput technologies ("omic" sciences) constitute a valuable tool for the exploration, analysis and application of the vast gene pool (genomics, transcriptomics) and molecular diversity (metabolomics) related to PSM [14,15]. Next generation sequencing technologies, along with current methods for functional annotation, offer comprehensive tools to predict and characterize proteins, within reasonably closeness to the actual *in vivo* functions, offering a wide range of resources to be applied in alkaloid engineering research [16]. In this study, a high sensitivity bioinformatic method was used to identify a set of unique protein-coding sequences involved in BIA biosynthesis, within an *A. mexicana* transcriptomic dataset in the absence of a reference genome.

Experimental

Plant material

In vitro plantlets were obtained from seeds that were collected and disinfested as previously described [17]. Developing seedlings were harvested after the emergence of the first pair of true leaves (non-cotyledonary) and formation of secondary roots (ca. 20 days after germination). Both sanguinarine and berberine are actively synthetized at these developmental phases [17]. Plantlets were sectioned into shoots (hypocotyl and leaflets) and radicles (main and lateral roots). Fresh tissues were quickly processed in a ribonuclease-free environment and immediately subjected to the extraction process to avoid important changes at the transcriptional level.

RNA isolation and sequencing

Total RNA was extracted using the Spectrum Plant Total RNA kit (Sigma-Aldrich, St Louis MO), followed by DNA decontamination with Turbo DNA-free kit (Invitrogen, Waltham MA), according to the manufacturer's protocols. Samples containing 5 µg of total RNA were preserved in RNAstable matrix (Biomatrica, San Diego CA) until analysis. RNA NGS was performed using an Ion torrent semiconductor sequencing platform by an external service provider. Prior to library preparation, RNA quality was verified by capillary electrophoresis on the RNA 6000 pico gel matrix (Agilent Technologies, Santa Clara CA), loaded on the Agilent 2100 Bioanalyzer. At this step, only two samples with an RNA Integrity Number (RIN) above 8

J. Mex. Chem. Soc. **2025**, *69*(4)
Regular Issue

ISSN-e 2594-0317

were selected for further processing. These QC-passed samples (one from root and other from aerial tissues) were purified and polyadenylated mRNA enriched with Dynabeads mRNA DIRECT Micro Purification kit (Ambion Austin TX). cDNA synthesis was conducted with Total RNA-Seq Kit v2 (Thermo Fisher Scientific, Watham MA), using strand-compatible Ion Torrent sequencing adapters. RNA sequencing template was prepared with the Ion PI Hi-Q OT2 200 Kit to deliver into the Ion Proton™ System (Thermo Fisher Scientific), with a sequencing depth about 30 million reads and a length up to 200 bp fragment reads.

Transcriptome processing and assembling

Raw reads were examined and filtered with the FastQC tool [18]. Low complexity sequences and those with a length below 20 bp and/or with a Phred score <23 were discarded. Next, all read sets were trimmed and filtered with FASTX [19] to eliminate adapters and artifacts. In order to obtain a robust reference transcriptome in terms of tissue representability, a de novo assembly of pooled read sets was conducted with Oases RNA-seq assembler [20] configured to a k-mer of 27, after assaying different values (19, 21, 27 and 29). The assembly's completeness was assessed with the Benchmarking Universal Single-Copy Orthologue (BUSCO) tool v5.7.1 [21], using the eudicots odb10 dataset in transcriptome mode. Additionally, N50 and N90 statistics were calculated employing a custom script.

Functional annotation

All the analyzed sequences were retrieved from the above described XT1 *A. mexicana* assembled transcriptome. The XT1 transcriptome was deposited as a Transcriptome Shotgun Assembly (TSA) project, publicly available at NCBI Sequence Read Archive (SRA) under the run accessions SRR18335407 and SRR18335408. Bioproject: PRJNA814261. Biosample: SAMN26542188.

In order to predict proteins encoded by the XT1 reference transcriptome, open reading frame (ORF) calling was performed with the TransDecoder module of Trinity suite [22], using default parameters. Translated transcriptomes (longest_orfs.pep files) were header-formatted and indexed with SAMtools [23], in conjunction with BEDtools [24] that was used to manipulate and extract sequence subsets for further analysis. The predicted coding sequences (CDS) were analyzed using HMMER3 [25] versus the Pfam-A database [26] by hmmscan searches for domain composition.

Best-hit results (cutoff e-value < 0.001) were screened for Pfam domains related to BIAs biosynthesis. Protein families retrieved included pyridoxal-dependent decarboxylases, pathogenesis-related Bet v 1, mycolic acid cyclopropane synthetase, berberine and berberine like, O-methyltransferase, Cytochrome P450, NAD(P)H-binding domain and FAD binding domain proteins, corresponding to PF00282, PF00407, PF02353, PF08031, PF00891, PF00067, PF13460 and PF01565 records, respectively [27–30].

Function of the Pfam selected CDS was further confirmed by local alignment against the NCBI RefSeq non-redundant (nr) protein database (February 12, 2022 release) using DIAMOND v2.0.14 [31]. In addition, sequences were re-annotated using the Kyoto Encyclopedia of Genes and Genomes (KEGG) Ortholog family (KOfam) assignment, based on Hidden Markov Model (HMM) profiles [32]. Metabolic assignments of CDS were reconstructed and visualized, employing KEGG mapper [32]. Finally, Gene Ontology (GO) terms of annotated proteins were obtained at the PANNZER2 web server [34]. Visualization of GO terms were conducted with REVIGO [35].

Selection and analysis of protein-coding sequences

Annotated sequences related to BIA biosynthesis were manually filtered to remove duplicates and incompletes. DBOX [EC. 1.3.1.12] and SanR [EC. 1.3.1.107], corresponding to last step in sanguinarine biosynthesis and dihydrosanguinarine interconversion, were selected for subsequent analysis, due to the lack of reports in *A. mexicana*. Multiple Sequence Alignments (MSA) were obtained with ClustalW, followed by a phylogenetic analysis of maximum likelihood and JTT matrix-based evolutionary model [36]. All these processes were conducted using MEGA X software [37]. For the above, the query sequences of previously characterized enzymes in related species were obtained from public databases. *Papaver somniferum* ADOX5, ADOX7 and ADOX8 (NCBI accessions: AGL44334.1, AGL44335.1 and AGL44336.1), respectively, were included for DBOX, as well as a FAD linked oxidase from Macleaya cordata (OVA00265.1) and the (S)-tetrahydroprotoberberine oxidase from *A. mexicana* (ADY15027.1). In the case of SanR, the UNIPROT record A0A6J0ZSP7, two sequences from *Papaver somniferum* (XP_026412126.1 and XP_026397103.1) and one

J. Mex. Chem. Soc. **2025**, *69*(4)
Regular Issue

ISSN-e 2594-0317

from Eschscholzia californica (ADE41047.1) were included. The selected A. mexicana SanR candidates (AmSanR1 and AmSanR2) were submitted to in silico 3D structural analysis using PHYRE2 (http://www.sbg.bio.ic.ac.uk/phyre2/) [38] and the 3D viewer FirstGlance (http://firstglance.jmol.org).

Results and discussion

Transcriptome overview

A total of 75,378 CDS, corresponding to at least 100 amino acid length putative proteins (PP), were extracted from 97,592 *de novo* assembled transcripts from the *A. mexicana* seedling XT-1 transcriptome. Comparison to Pfam and nr data bases assigned functional groups to over 70 % of these PP. in contrast, KEGG and GO only assigned functional groups to 32 and 49 % of them, respectively (Table 1; Fig 1 and 2). KEGG identified 24,364 *Argemone* PP, and 1,063 of them were assigned catalytic functions. Those PP were distributed among 479 metabolic pathways; it is noteworthy to point out that they were involved in amino acid biosynthesis and cofactors, as well as carbon metabolism (131, 100 and 104 hits, respectively; Fig. 1). Interestingly, up to 30 PP were related to isoquinoline alkaloid biosynthesis (map: 00950; Fig. 1). KEGG comparison also revealed *Argemone* PP involved in the processing of environmental and genetic information, cellular processes, and organismal systems (Supplementary file 1; Fig. S1).

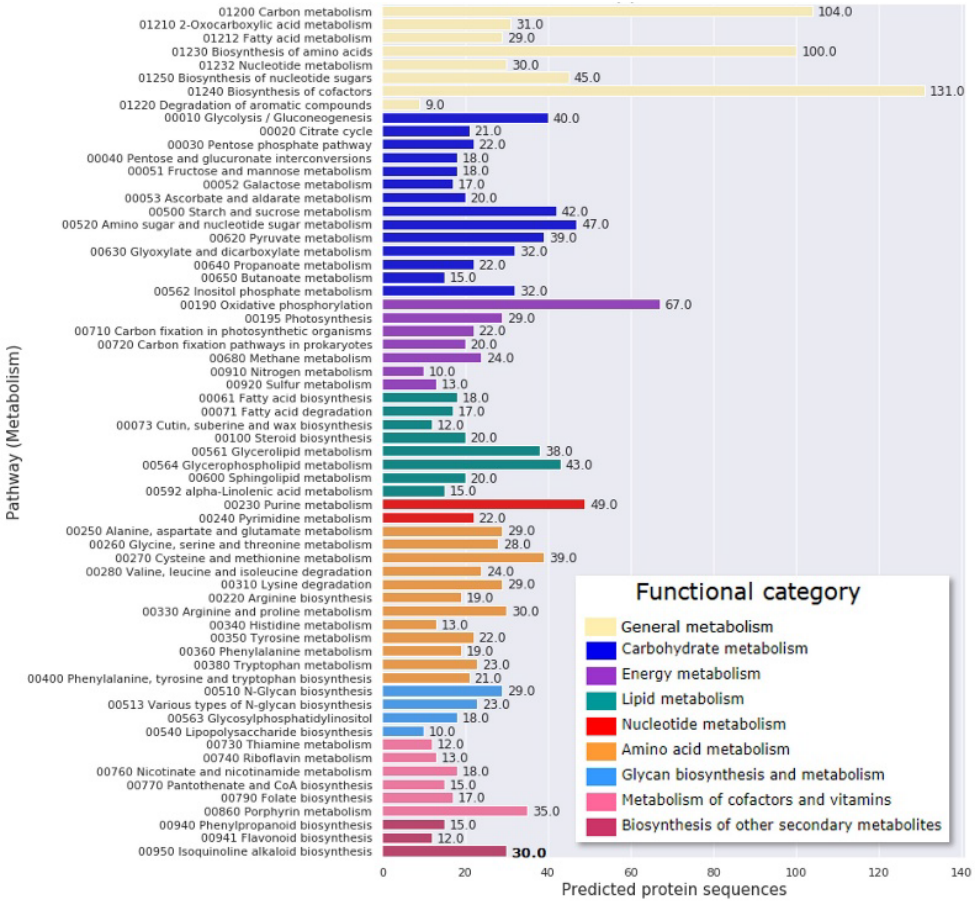

Fig. 1. Reconstruction of the metabolic pathways represented in the XT1 *A. mexicana* transcriptome by KEGG mapper. Number of putative proteins identified of the different categories are indicated at the end of each bar.

J. Mex. Chem. Soc. **2025**, *69*(4)
Regular Issue

ISSN-e 2594-0317

Table 1. Summary of XT1 sequencing, assembly statistics, and functional annotation features.

Aerial body post QC reads	17 011 810
Root system post QC reads	17 757 669
Percentage of assembled reads	63.31%
Assembled contigs/transcripts	97 592
Largest contig/transcript size	1 0951 nt
N50 contig size	1 409 nt
N90 contig size	375 nt
Total BUSCO groups searched	2 326
Complete BUSCOs	1 853 (80%)
Putative proteins from unigenes*	75 378
Pfam annotated	54 867 (72.79%)
nr annotated	61 969 (82.21%)
KEGG annotated (KOfam)	24 364 (32.32%)
GO annotated	37 241 (49.4%)

*Number of predicted protein-coding sequences using TransDecoder.LongOrfs algorithm that identifies ORFs that are at least 100 amino acids long.

GO annotation assigned 37,241 PP into three major categories (Fig. 2**(A)**). Most of GO terms related to berberine and sanguinarine biosynthesis, such as tyrosine decarboxylase (GO:0004837), (S)-coclaurine-N-methyltransferase (GO:0030794) and (S)-tetrahydroprotoberberine N-methyltransferase (GO:0030782) activities, were highly represented within the recognized molecular functions, and this was consistent with assignments made by Pfam and KEGG. Likewise, coincidences were also detected in terms associated to plant growth regulators, such as receptors for ethylene (GO:0038199) and auxins (GO:0038198) (Fig. 2**(B)**).

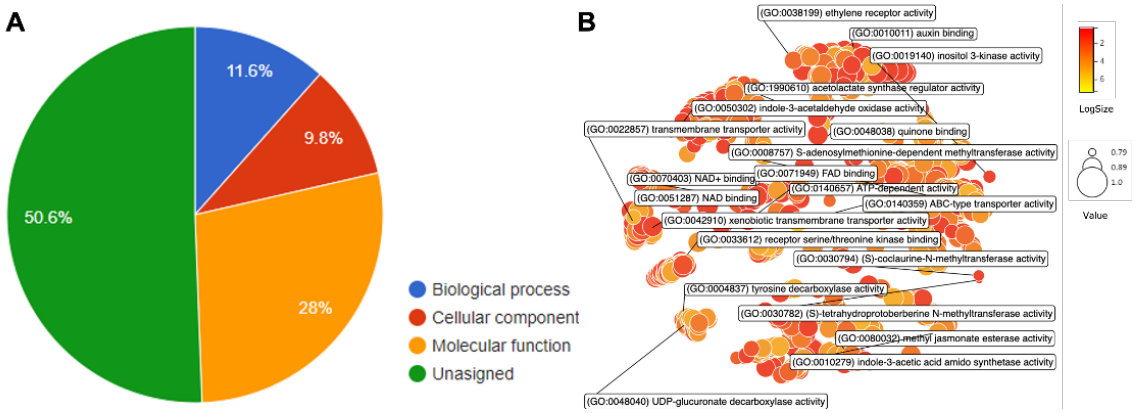

Fig. 2. GO annotation of XT1 transcriptome. **(A)** GO major category classification of protein-coding sequences. **(B)** Revigo visualization of the molecular function terms. Labeled bubbles in B include terms representative for specialized metabolism, amino acid biosynthesis and growth regulators.

J. Mex. Chem. Soc. **2025**, *69*(4)
Regular Issue

ISSN-e 2594-0317

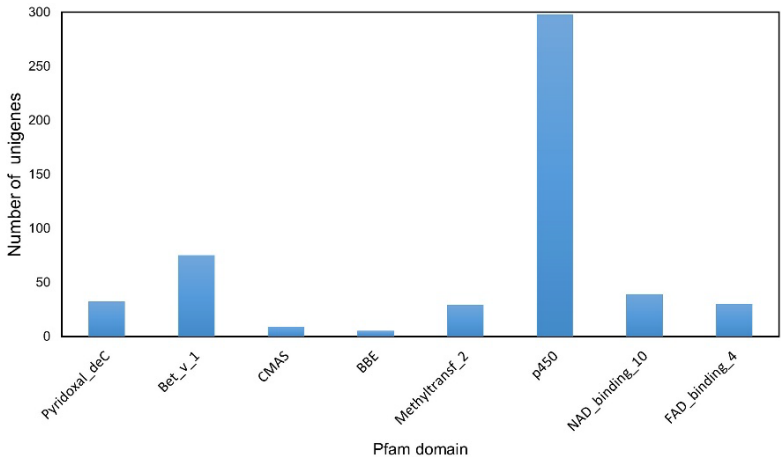

Fig. 3. Pfam classification of proteins involved in BIAs biosynthesis identified in the XT-1 *A. mexicana* transcriptome. **Pyridoxal_deC**, Pyridoxal-dependent aminoacid decarboxylase; **Bet_v_1**, Pathogenesis-related protein Bet v 1 Family; **CMAS**, Mycolic acid cyclopropane synthetase; **BBE**, Berberine and berberine like; Methyltransf_2, O-methyltransferase; **p450**, Cytochrome P450; **NAD_binding_10**, NAD(P)H-binding; **FAD_binding_4**, FAD binding domain.

BIA related proteins in XT1 transcriptome

A total of 514 unigenes encoding putative BIA biosynthetic enzymes were identified within the Pfam screened transcriptome (Fig. 3). This set, together with sequences related to the secondary metabolism identified by KEGG and GO functional annotations, were analyzed by BLAST to further confirm their identity (Supplementary file 2; Dataset S1). The larger group corresponded to Cytochrome P450 proteins (CYPs) followed by Pathogenesis-related protein 10/Bet v 1, from the major allergen protein family (PR10/Bet v1-like), which shares homology with norcoclaurine synthase (NCS).

Interestingly, candidates for the complete biosynthetic routes for both berberine and sanguinarine were reconstructed from the assembled transcriptome by phylogenetic analysis (Supplementary file 1; Fig. S2). The related Pfam records, identified as described in Materials and Methods (see Functional Annotation), are displayed in Fig. 4 and Table 2, which also lists the enzyme acronyms and EC numbers. The first set of reactions involves the transformation of two tyrosine units into the three-hydroxylated intermediary norcoclaurine, with the participation of TyDC and NCS (Table 2; Fig. 4). The next track of reactions consists in the transformation of norcoclaurine into reticuline. This requires the addition of three methyl groups: two on hydroxyl substitutions and one on the heterocyclic N of the structure. Further closing of the reticuline methylene bridge, performed by BBE, produces scoulerine, the last common intermediary for sanguinarine and berberine synthesis (Table 2; Fig. 4). Sanguinarine synthesis from scoulerine proceeds via a dehydro- intermediary and requires the formation of two methylendioxy bridges, followed by oxidation and hydroxylation, as depicted in Fig. 4. This requires the involvement of CheSyn (CYP719A14), StySyn (CYP719A13), TNMT, MSH and PH6. Final steps consist in the interconversion of dihydrosanguinarine and sanguinarine with the participation of SanR and DBOX (Fig. 4). On the other hand, berberine synthesis from scoulerine initiates with a methylation, followed by the formation of the corresponding methylendioxy bridge and further oxidation (Fig. 4). These reactions are performed by SOMT, CDS (CYP719A13) and STOX (Table 2) [6]. In this way, developing *A. mexicana* seedlings possess the complete set of enzymes involved in the synthesis of BIAs from both, the benzophenanthridine and protoberberine, groups. This suggests that genes involved in coordinating the operation of both branches are also present in the XT-1 transcriptome. RPKM values (see Supplementary) indicated a lower BIA gene expression in aerial parts (maximum 200 RPKM) than roots (Fig. S3**(a)**), which is consisted with previous observations in is *Argemone* developing seedlings [5,17]. However, general transcriptional activity in aerial tissue seems considerable, as suggested by a selected photosynthetic marker (ribulose bisphosphate carboxylase oxidase small subunit; RuBisCO; rbcs; Fig. S3**(a)**). Higher BIA gene expression in roots was confirmed by RT-qPCR analysis of a group of selected genes (Fig. S3**(b)**) which showed a similar trend.

J. Mex. Chem. Soc. **2025**, *69*(4)
Regular Issue

ISSN-e 2594-0317

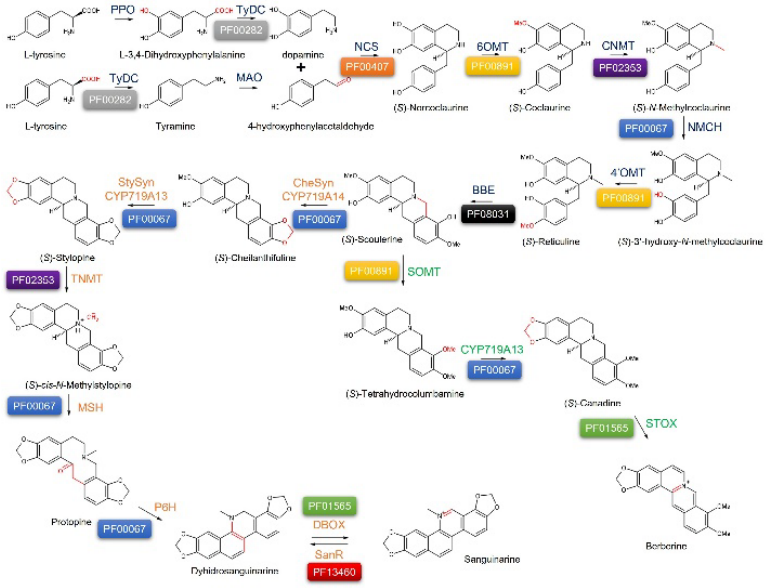

Fig. 4. Schematic representation of sanguinarine and berberine biosynthetic pathways in *A. mexicana*. Colored boxes indicate the Pfam record associated to the functional domain of the different enzymes. **PPO**, Polyphenol oxidase; **TyDC**, tyrosine/DOPA decarboxylase; **MAO**, Monoamine oxidase; **NCS**, norcoclaurine synthase; **6OMT**, norcoclaurine *6-O*-methyltransferase; **CNMT**, coclaurine *N*-methyltransferase; **NMCH**, *N*-methylcoclaurine 3'-hydroxylase; **4'OMT**, *3'*-hydroxy-*N*-methylcoclaurine *4'-O*-methyltransferase; **BBE**, berberine bridge enzyme; **CheSyn/CYP719A14**, cheilanthifoline synthase; **CYP719A13**, trifunctional (S)-stylopine synthase/(S)-nandinine synthase/(S)-canadine synthase; **TNMT**, tetrahydroprotoberberine *N*-methyltransferase; **MSH**, *N*-methyl-stylopine 14-hydroxylase; P6H, protopine 6-hydroxylase; **DBOX**, dihydrobenzophenanthridine oxidase; **SanR**, sanguinarine reductase; **SOMT**, scoulerine 9-*O*-methyltransferase; **STOX**, tetrahydroprotoberberine oxidase.

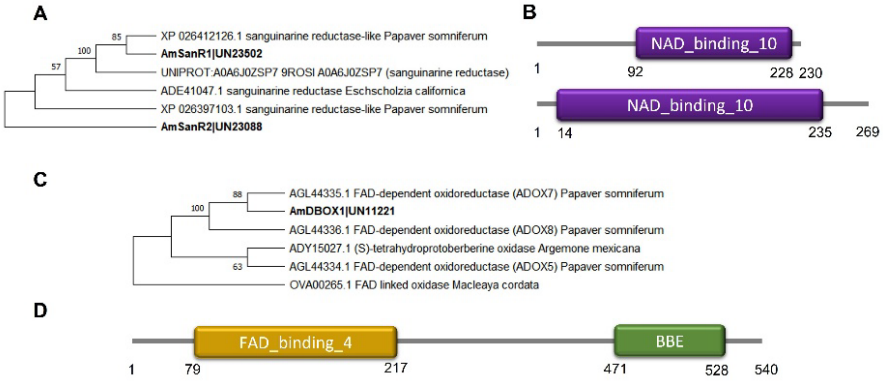

Fig. 5. *In silico* analysis of the putative SanR (AmSanR) and DBOX (AmDBOX) retrieved from the XT1 *A. mexicana* transcriptome. **(A)** Maximum likelihood phylogenetic tree of sanguinarine reductase related sequences. **(B)** Domain architecture scheme of UN23502 and UN23088 transcripts encoding a putative SanR isoforms (AmSanR1 and AmSanR2). **(C)** Maximum likelihood phylogenetic tree of dihydrobenzophenantridine oxidase related sequences. **(D)** Domain architecture scheme of UN11221 transcript encoding a putative DBOX (AmDBOX1). Bootstrap frequencies for each clade are percentages of 1000 iterations. Species and associated GenBank accession numbers for phylogenetic tree construction are indicated in each taxon name. Numbers at the bottom of the predicted architectures indicate the domain position in amino acids.

J. Mex. Chem. Soc. **2025**, *69*(4)
Regular Issue

ISSN-e 2594-0317

Table 2. BIA biosynthetic enzymes identified in XT1 transcriptome.

Enzyme (Abbreviation)	**Pathway**	**Transcript ID (Length of predicted coding product in amino acids)**	**Best hit accession and/or reference**
Tyrosine/DOPA decarboxylase (TyDC)	Common	UN06517 (532) UN06518 (532) UN07029 (537)	ACJ76782.1
Norcoclaurine synthase (NCS)	Common	UN18055 (351) UN06380 (274)	ACO90257.2 [51] ACJ76785.1
Norcoclaurine *6-O*-methyltransferase (6OMT)	Common	UN45871 (137)	XP_026447518.1
Coclaurine *N*-methyltransferase (CNMT)	Common	UN22975 (365) UN19321 (322)	XP_017224815.1 ANY58190.1
N-methylcoclaurine 3'-hydroxylase (NMCH)	Common	UN16831 (488) UN13116 (513) UN10440 (368)	XP_010253990.1
3'-hydroxy-*N*-methylcoclaurine *4'-O*-methyltransferase (4'OMT)	Common	UN18945 (356)	XP_026440860.1
Berberine bridge enzyme (BBE)	Common	UN14424 (548)	ACJ76783.1
Cheilanthifoline synthase (CheSyn/CYP719A14)	Sanguinarine	UN16884 (405)	B1NF20.1
Trifunctional (S)-stylopine synthase/(S)-nandinine synthase/(S)-canadine synthase (CYP719A13)	Sanguinarine and/or berberine	UN11761 (504)	B1NF19.1 [45]
Tetrahydroprotoberberine *N*-methyltransferase (TNMT)	Sanguinarine	UN14356 (362) UN15660 (387)	XP_026421878.1
N-methyl-stylopine 14-hydroxylase (MSH)	Sanguinarine	UN08536 (465)	OVA14716.1
Protopine 6-hydroxylase (P6H)	Sanguinarine	UN04162 (511)	XP_026456227.1
Dihydrobenzophenanthridine oxidase (DBOX)	Sanguinarine	UN11221 (540)	AGL44334.1[44]
Sanguinarine reductase (SanR)	Sanguinarine	UN23502 (230) UN23088 (269)	ADE41047 [41] XP_026397103.1
Scoulerine 9-*O*-methyltransferase (SOMT)	Berberine	UN12378 (371)	ALY11061.1
Tetrahydroprotoberberine oxidase (STOX)	Berberine	UN10862 (454)	ADY15027.1 [52]

J. Mex. Chem. Soc. **2025**, *69*(4)
Regular Issue

ISSN-e 2594-0317

Phylogenetic analysis and protein structure modelling of DBOX and SanR

Interconversion of sanguinarine to dihydrosanguinarine is carried out by the pair SanR/DBOX and plays a critical role in protecting plant cells from the possible toxic effects caused by an excessive accumulation of sanguinarine [39]. Although these enzymes have been described in other species, such as *E. californica* [39], these ones in *A. mexicana* have been not reported. Candidates for AmSanR and AmDBOX were identified in the XT-1 transcriptome. For AmSanR, two proteins; AmSanR-1 and -2 were selected due to their phylogenetic proximity to PsSanR1 (XP_026397103.1) and EcSanR1 (ADE41047) (Fig. 5**(A)**). Both PP presented the required domains for binding of NAD(P)$^+$ and for reductase activity (Fig. 5**(B)**). Interestingly, despite being only 230 and 269 residues long, respectively, both AmSanR-1 and -2 corresponded to complete proteins, as revealed by the pairwise comparison to other SanR and for the presence of the untranslatable regions (UTRs) at both ends of the original transcripts (UN23502 and UN23088). These results suggest that AmSanR1 and -2 represent possible isoforms, as it could be deduced from multiple alignment and protein *in silico* modeling (Fig. 6). On the other hand, the complete AmDBOX1 coding sequence, belonging to the UN11221 transcript, was 540 amino acids long and displayed 50 and 68 % identity to the *P. somniferum* DBOX (PsADOX5) and PsADOX7, respectively (Fig. 5**(C)**). The predicted architecture of AmDBOX1 included the typical structural DBOX features, such as the FAD-binding pocket and the catalytic BBE-like domain (Fig. 5**(D)**).

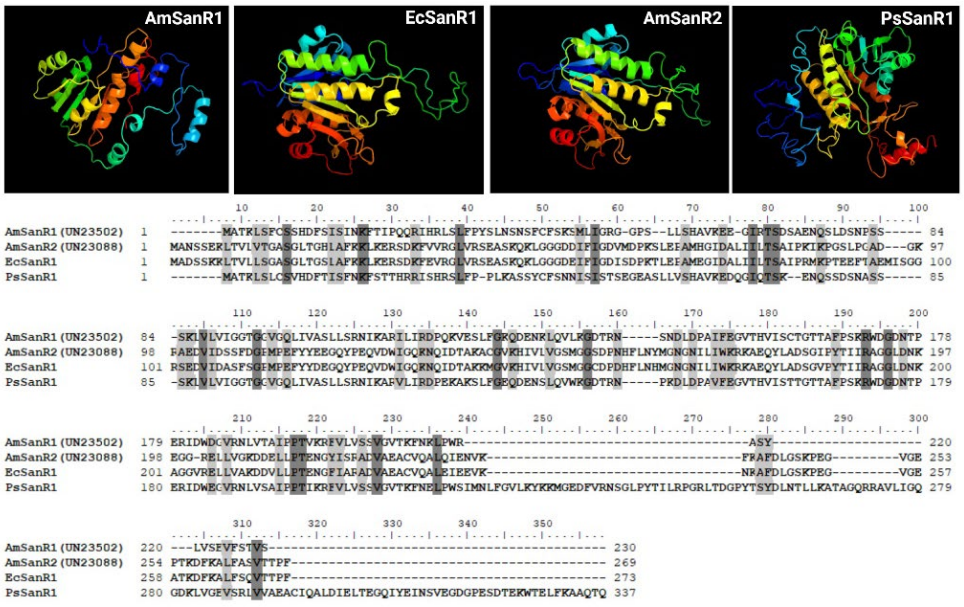

Fig. 6. AmSanR1 and AmSanR2 alignment and 3D structure. The 3D structure can be visualized at the top panel. The alignment of both sequences with that of the PsSanR1 and EcSanR1 can be visualized at the lower panel which indicates the divergent and conserved residues between them. The 3D structure and alignment were realized through PHYRE2 and BioEdit respectively. The caption was created with BioRender.com.

Conclusions

In exploring an *A. mexicana* trancriptomic data set by homology of protein domains using the hidden Markov models, Pfam classification and predictive structural modeling allowed the identification of strong candidates of coding sequences involved in the complete BIA biosynthetic pathway in *A. mexicana*, a non-model plant species used in traditional medicine. Hence, this approach may be applied in similar studies, such as the identification of regulatory proteins or those involved in metabolite transportation.

J. Mex. Chem. Soc. **2025**, *69*(4)
Regular Issue

ISSN-e 2594-0317

Acknowledgments

We thank Ing. L.A. Puc-Canul for providing support for the use of the supercomputing infrastructure (HOBON server; CICY). In addition, the authors thank Dr. M.L. Miranda-Ham for her critical review and Dr. A. Muñoz-Sánchez and MSc. M. Monforte-González for technical support during different stages of this work.

This work was supported by CONAHCYT (National Council for Humanities, Science and Technology, Mexico), grants CB-2016-0285887 and CBF 2023-2024-1879. JGS-G is awarded a research assistance scholarship from SNI/CONACYT. LLM was recipient of a postdoctoral scholarship from CONAHCYT (514907/289293).

References

1. Gbesso, G. H. F.; Gbesso, F. K.; Adoukonou, R. C. F.; Akabassi, G. C.; Padonou, E. A.; Tente, A. B. H. *Ethnobot. Res. Appl.* **2021**, *21,* 1–11. DOI: https://doi.org/10.32859/era.21.20.1-11
2. Priya, C. L.; Rao, Kokati V. B. *Int. J. Pharm. Sci. Res.* **2012**, *36,* 2143–48. DOI: http://dx.doi.org/10.13040/IJPSR.0975-8232.3(7).2143-48
3. Rubio-Pina, J.; Vazquez-Flota, F. *Curr. Top. Med. Chem.* **2013**, *13,* 2200–2207. DOI: https://doi.org/10.2174/15680266113139990152
4. Babu, C. K.; Khanna, S. K.; Das, M. *Antioxid. Redox Signaling.* **2007**, *9,* 515–525. DOI: https://doi.org/10.1089/ars.2006.1492
5. Vázquez-Flota, F; Rubio-Piña, J.; Xool-Tamayo, J.; Vergara-Olivares, M.; Tamayo-Ordoñez, Y.; Monforte-González, M.; Guízar-González, C.; Mirón-López, G. *Rev. Fitotec. Mex.* **2018**, *41,* 13–21. DOI: https://doi.org/10.35196/rfm.2018.1.13-21
6. Laines-Hidalgo, J. I.; Muñoz-Sánchez, J. A.; Loza-Müller, L.; Vázquez-Flota, F. *Molecules,* **2022**, *27, 1378.* DOI: https://doi.org/10.3390/molecules27041378
7. Chang, Y. C.; Chang, F. R.; Khalil, A. T.; Hsieh, P. W.; Wu, Y. C. *Zeitschrift für Naturforschung C.* **2003**, *58,* 521–526. DOI: https://doi.org/10.1515/znc-2003-7-813
8. Gali, K.; Ramakrishnan, G.; Kothai, R.; Jaykar, B. *Int. J. Pharmtech. Res.* **2011**, *3,*1329–1333.
9. Nayak, P.; Kar, D. M.; Maharana, L. *Pharmacologyonline*. **2011**, *1, 889–903.*
10. Zhang, B. Y.; Chen, M.; Chen, X. C.; Cao, K.; You, Y.; Qian, Y. J.; Yu, W. K. *Br. J. Surg.* **2021**, *108,* e9–e11. DOI: https://doi.org/10.1093/bjs/znaa021
11. Namdeo, A. G.; Jadhav, T. A.; Rai, P. K.; Gavali, S.; Mahadik, K. *Phcog. Rev*. **2007**, *1, 227–231.*
12. Isah, T.; Umar, S.; Mujib, A.; Sharma, M. P.; Rajasekharan, P. E.; Zafar, N.; Frukh, A. *Plant Cell Tiss. Organ Cult.* **2018**, *132,* 239–265. DOI: https://doi.org/10.1007/s11240-017-1332-2
13. Yadav, A. N.; Kour, D.; Rana, K. L.; Yadav, N.; Singh, B.; Chauhan, V. S.; Rastegari, A. A.; Hesham, A. E.; Gupta, V. K., in: *New and Future Developments in Microbial Biotechnology and Bioengineering: Microbial Secondary Metabolites Biochemistry and Applications*. Chapter 20, Vijai Kumar Gupta and Anita Pandey, Elsevier, **2019**, 279-320. DOI: https://doi.org/10.1016/B978-0-444-63504-4.00020-7
14. Dasgupta, A.; Chowdhury, N.; De, R. K. *Comput. Methods Programs Biomed*. **2020**, *192,* 105436. DOI: https://doi.org/10.1016/j.cmpb.2020.105436
15. Marchev, A. S.; Yordanova, Z. P.; Georgiev, M. I. *Crit. Rev. Biotechnol*. **2020**, *40,* 443–458. DOI: https://doi.org/10.1080/07388551.2020.1731414
16. Yamada, Y.; Sato, F. *Biomolecules.* **2021***, 11,* 1719. DOI: https://doi.org/10.3390/biom11111719
17. Xool-Tamayo, J.; Serrano-Gamboa, G.; Monforte-González, M.; Mirón-López, G.; Vázquez-Flota, F. *Biotechnol. Lett.* **2017**, *39,* 323–330. DOI: https://doi.org/10.1007/s10529-016-2250-9
18. http://www.bioinformatics.babraham.ac.uk/projects/fastqc, accessed in October 2023.
19. http://hannonlab.cshl.edu/fastx_toolkit, accessed in January 2024

J. Mex. Chem. Soc. **2025**, *69*(4)
Regular Issue

ISSN-e 2594-0317

20. Schulz, M. H.; Zerbino, D. R.; Vingron, M.; Birney, E. *Bioinformatics*. **2012**, *28,* 1086–1092. DOI: https://doi.org/10.1093/bioinformatics/bts094
21. Simão, F.A.; Waterhouse, R.M.; Ioannidis, P.; Kriventseva, E. V.; Zdobnov, E.M. *Bioinformatics*, **2015**, *31*, 3210-3212. DOI: https://doi.org/10.1093/bioinformatics/btv351
22. Grabherr, M. G.; Haas, B. J.; Yassour, M.; Levin, J. Z.; Thompson, D. A.; Amit, I.; Adiconis, X.; Fan, L.; Raychowdhury, R.; Zeng, Q.; Chen, Z.; Mauceli, E.; Hacohen, N.; Gnirke, A.; Rhind, N.; di Palma, F.; Birren, B. W.; Nusbaum, C.; Lindblad-Toh, K.; Friedman, N.; Regev, A. *Nat. Biotechnol.* **2011**, *29,* 644–652. DOI: https://doi.org/10.1038/nbt.1883
23. Danecek, P.; Bonfield, J. K.; Liddle, J.; Marshall, J.; Ohan, V.; Pollard, M. O.; Whitwham, A.; Keane, T.; McCarthy, S. A.; Davies, R. M.; Li, H. *GigaScience*. **2021**, *10,* giab008. DOI: https://doi.org/10.1093/gigascience/giab008
24. Quinlan, A. R.; Hall, I. M. *Bioinformatics*. **2010**, *26,* 841–842. DOI: https://doi.org/10.1093/bioinformatics/btq033
25. Eddy, S. R. *PLoS Computational Biology*. **2011**, *7,* e1002195. DOI: https://doi.org/10.1371/journal.pcbi.1002195
26. Mistry, J.; Chuguransky, S.; Williams, L.; Qureshi, M.; Salazar, G. A.; Sonnhammer, E. L. L.; Tosatto, S. C. E.; Paladin, L.; Raj, S.; Richardson, L. J.; Finn, R. D.; Bateman, A. *Nucleic Acids Res.* **2021**, *49,* D412–D419. DOI: https://doi.org/10.1093/nar/gkaa913
27. Dastmalchi, M.; Park, M. R.; Morris, J. S.; Facchini, P. *Phytochem. Rev*. **2018**, *17,* 249–277. DOI: https://doi.org/10.1007/s11101-017-9519-z
28. Gracz-bernaciak, J.; Mazur, O.; Nawrot, R. *Int. J. Mol. Sci.* **2021**, *22,* 12427. DOI: https://doi.org/10.3390/ijms222212427
29. Facchini, P. J.; Morris, J. S. *Front. Plant Sci*. **2019**, *10,* 1058. DOI: https://doi.org/10.3389/fpls.2019.01058
30. Zhong, F.; Huang, L.; Qi, L.; Ma, Y.; Yan, Z. *Plant Mol. Biol.* **2020**, *102,* 477–499. DOI: https://doi.org/10.1007/s11103-019-00959-y
31. Buchfink, B.; Reuter, K.; Drost, H.-G. *Nat. Methods*. **2021**, *18,* 366–368. DOI: https://doi.org/10.1038/s41592-021-01101-x
32. Aramaki, T.; Blanc-Mathieu, R.; Endo, H.; Ohkubo, K.; Kanehisa, M.; Goto, S.; Ogata, H. *Bioinformatics*. **2020**, *36, 2251–2252*. DOI: https://doi.org/10.1093/bioinformatics/btz859
33. Kanehisa, M.; Sato, Y. *Protein Sci*. **2020**, *29, 28–35*. DOI: https://doi.org/10.1002/pro.3711
34. Törönen, P.; Medlar, A.; Holm, L. *Nucleic Acids Res*. **2018**, *46,* W84–W88. DOI: https://doi.org/10.1093/nar/gky350
35. Jones D.T.; Taylor W.R. *FEBS Lett* **1994**, *339,* 269–275. DOI:10.1016/0014-5793(94)80429-X.
36. Supek, F.; Bošnjak, M.; Škunca, N.; Šmuc, T. *PLoS ONE*. **2011**, *6,* e21800. DOI: https://doi.org/10.1371/journal.pone.0021800
37. Kumar, S.; Stecher, G.; Li, M.; Knyaz, C.; Tamura, K. *Mol. Biol. Evol.* **2018**, *35,* 1547–1549. DOI: https://doi.org/10.1093/molbev/msy096
38. Kelley, L. A.; Mezulis, S.; Yates, C. M.; Wass, M. N.; Sternberg, M. J. E. *Nat. Protoc.* **2015**, *10,* 845–858. DOI: https://doi.org/10.1038/nprot.2015.053
39. Vogel, M.; Lawson, M.; Sippl, W.; Conrad, U.; Roos, W. *J. Biol. Chem.* **2010**, *285,* 18397–18406. DOI: https://doi.org/10.1074/jbc.M109.088989
40. Deng, X.; Zhao, L.; Fang, T.; Xiong, Y.; Ogutu, C.; Yang, D.; Vimolmangkang, S.; Liu, Y.; Han, Y. *Hortic. Res.* **2018**, *5,* 29. DOI: https://doi.org/10.1038/s41438-018-0035-0
41. Hagel, J. M.; Morris, J. S.; Lee, E.-J.; Desgagné-Penix, I.; Bross, C. D.; Chang, L.; Chen, X.; Farrow, S. C.; Zhang, Y.; Soh, J.; Sensen, C. W.; Facchini, P. J. *BMC Plant Biol.* **2015**, *15,* 227. DOI: https://doi.org/10.1186/s12870-015-0596-0
42. Pei, L.; Wang, B.; Ye, J.; Hu, X.; Fu, L.; Li, K.; Ni, Z.; Wang, Z.; Wei, Y.; Shi, L.; Zhang, Y.; Bai, X.; Jiang, M.; Wang, S.; Ma, C.; Li, S.; Liu, K.; Li, W.; Cong, B. *Hortic. Res.* **2021**, *8,* 5. DOI: https://doi.org/10.1038/s41438-020-00435-5

J. Mex. Chem. Soc. **2025**, *69*(4)
Regular Issue

ISSN-e 2594-0317

43. Morris, J. S.; Caldo, K. M. P.; Liang, S.; Facchini, P. J. *ChemBioChem*. **2021**, *22,* 264–287. DOI: https://doi.org/10.1002/cbic.202000354
44. Hagel, J. M.; Beaudoin, G. A. W.; Fossati, E.; Ekins, A.; Martin, V. J. J.; Facchini, P. J. *J. Biol. Chem.* **2012**, *287, 42972–42983*. DOI: https://doi.org/10.1074/jbc.M112.420414
45. Díaz Chávez, M. L.; Rolf, M.; Gesell, A.; Kutchan, T. M. *Arch. Biochem. Biophys.* **2011**, *507,* 186–193. DOI: https://doi.org/10.1016/j.abb.2010.11.016
46. Leong, B. J.; Last, R. L. *Curr. Opin. Struct. Biol.* **2017**, *47, 105–112.* DOI: https://doi.org/10.1016/j.sbi.2017.07.005
47. Waki, T.; Takahashi, S.; Nakayama, T. *BioEssays*. **2021**, *43,* 2000164. DOI: https://doi.org/10.1002/bies.202000164
48. Loza-Muller, L.; Shitan, N.; Yamada, Y.; Vázquez-Flota, F. *Planta*. **2021**, *254,* 122. DOI: https://doi.org/10.1007/s00425-021-03780-4
49. Kato, N.; Dubouzet, E.; Kokabu, Y.; Yoshida, S.; Taniguchi, Y.; Dubouzet, J. G.; Yazaki, K.; Sato, F. *Plant Cell Physiol*. **2007**, *48,* 8–18. DOI: https://doi.org/10.1093/pcp/pcl041
50. Yamada, Y.; Kokabu, Y.; Chaki, K.; Yoshimoto, T.; Ohgaki, M.; Yoshida, S.; Kato, N.; Koyama, T.; Sato, F. *Plant Cell Physiol*. **2011**, *52,* 1131–1141. DOI: https://doi.org/10.1093/pcp/pcr062

Article

J. Mex. Chem. Soc. **2025**, *69*(4)
Regular Issue

ISSN-e 2594-0317

Regioselective Functionalization and Diels–Alder Cycloadditions of Exocyclic Dienes in Five-membered Heterocycles

Gustavo A. Monroy-Flores[1], Pablo Montoya[1], Ailyn N. García-González[1], Carlos H. Escalante[1], R. Uri Gutiérrez[1], R. Israel Hernández[1], Aydeé Fuentes-Benítes[1,2], Edson Barrera,[1] Omar Gómez-García[1], Francisco Delgado[1], Joaquín Tamariz[1,*]

[1]Departamento de Química Orgánica, Escuela Nacional de Ciencias Biológicas, Instituto Politécnico Nacional. Prol. Carpio y Plan de Ayala, S/N, 11340 México, D.F. México.
[2]Departamento de Química Orgánica, Facultad de Química, Universidad Autónoma del Estado de México, Paseo Colón/Paseo Tollocan S/N, 50000 Toluca, Estado de México, México.

***Corresponding author:** Joaquín Tamariz, email: jtamarizm@ipn.mx; jtamarizm@gmail.com

Received March 20th, 2024; Accepted October 17th, 2024.

DOI: http://dx.doi.org/10.29356/jmcs.v69i4.2343

Abstract. An acid-catalyzed regioselective addition of diverse nucleophiles to *exo*-oxazolidin-2-one dienes was presently carried out, leading to a series of functionalized 4-oxazolin-2-ones. The direct formylation of 4-methyl-4-oxazolin-2-ones provided the corresponding 5-formyl-4-oxazolin-2-ones, which were applied in the construction of the 4,5-dihydrobenzo[*d*]oxazolones through a Staunton-Weinreb annulation process. The reactivity of symmetrical and unsymmetrical *exo*-imidazolidin-2-one dienes was studied in Diels–Alder cycloadditions with dienophiles *N*-phenylmaleimide and benzyne. The aromatization of the [4+2] adducts led to the polycyclic benzo- and naphtho[*d*]imidazol-2-ones, which have potential pharmacological activity.
Keywords: 4,5-dimethylene-2-oxazolidinone dienes; 5-functionalized 4-oxazolin-2-ones; 4,5-dimethylene-2-imidazolidinone dienes; Staunton-Weinreb annulation; Diels–Alder reaction.

Resumen. Se describe la adición regioselectiva catalizada por ácido de diversos nucleófilos a los dienos *exo*-oxazolidinonas que conduce a una serie de 4-oxazolin-2-onas funcionalizadas. La formilación directa de 4-metil-4-oxazolidin-2-onas proporcionó las 5-formil-4-oxazolin-2-onas correspondientes, las cuales se emplearon en la construcción de las 4,5-dihidrobenzo[*d*]oxazolonas mediante un proceso de anillación de Staunton-Weinreb. Se estudió la reactividad de dienos *exo*-imidazolidin-2-onas simétricos y no simétricos en cicloadiciones de Diels-Alder con los dienófilos *N*-fenilmaleimida y bencino. La aromatización de los aductos [4+2] condujo a los benzo- y nafto[*d*]imidazol-2-onas policíclicas como compuestos con actividad farmacológica potencial.
Palabras clave: Dienos 4,5-dimetilen-2-oxazolidinonas; 4-oxazolin-2-onas 5-funcionalizadas; dienos 4,5-dimetilen-2-imidazolidinonas; anillación de Staunton-Weinreb; reacción de Diels–Alder.

Introduction

Conjugated dienes constitute a seminal molecular building block due to their potential use in the construction of six-membered rings through a concerted [4+2] Diels–Alder addition [1]. Moreover, they may have an important role in the regio- and stereoselective synthesis of highly functionalized double bonds [2]. Since the Diels–Alder reaction is relevant from a theoretical [3] and synthetic viewpoint [4], a diversity of dienes has been designed and synthesized, including outer-ring *o*-carbodimethylenes [5]. There has been considerable interest in

J. Mex. Chem. Soc. **2025**, *69*(4)
Regular Issue

ISSN-e 2594-0317

the preparation of *exo*-heterocyclic dienes for the study of their reactivity [5b,5c,6], given that their heteroatoms increase such reactivity and allow for much greater versatility in the functionalization of the cycloadducts.

Over the years, our group has described the regio- and stereoselective one-pot synthesis of novel *N*-substituted *exo*-2-oxazolidinone dienes **1**–**3** [7] via a base-assisted condensation of α-diketones **4** and isocyanates **5** (Scheme 1). This method has been adopted for the synthesis of 1,4-disubstituted exocyclic dienes [8] and heterocycle-fused *endo*-cyclohexenic dienes [9], which undergo regioselective Diels–Alder cycloadditions to monosubstituted dienophiles with electron-withdrawing groups. The corresponding adducts were useful precursors for preparing 2-(3*H*)-benzoxazolones **6** [10], which were involved in a general approach for the formation of the carbazole scaffold **7** [11], being applicable in the total synthesis of natural carbazoles [12]. Furthermore, dienes **1**-**3** have been efficient substrates for the synthesis of $Fe(CO)_3$ complexes and their conversion into conjugated enamido-enol $Fe(CO)_3$ complexes [13], or new polycyclic oxazol-2-one derivatives, in the latter case by reacting them with Fischer (arylalkynyl)(alkoxy)carbenes [14].

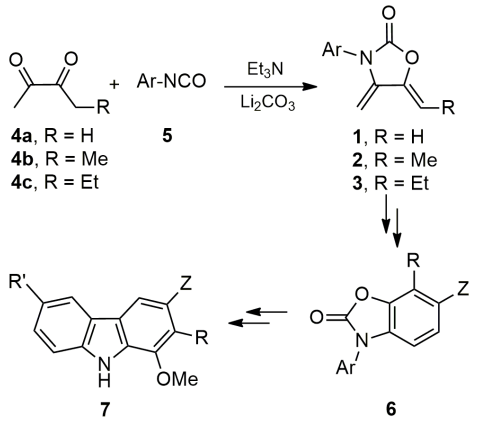

Scheme 1. Synthesis of *exo*-2-oxazolidinone dienes **1**–**3** and their conversion into carbazoles **7**.

A single-step and regioselective procedure was developed by our group to prepare 4-oxazolin-2-ones **9** and 4-methylidene-2-oxazolidinones **10** through a solvent-free condensation between isocyanates **5** and α-ketols **8**, carried out under conventional heating or microwave (MW)-assisted thermal conditions (Scheme 2) [15,16]. Both heterocycles served as a building block for the divergent synthesis of propellane compounds [9], α-hydroxyamides [16], aza-polycyclic compounds [17], enantiopure heterocyclic frameworks [18], natural pyridocarbazoles [19], and functionalized indoles [20].

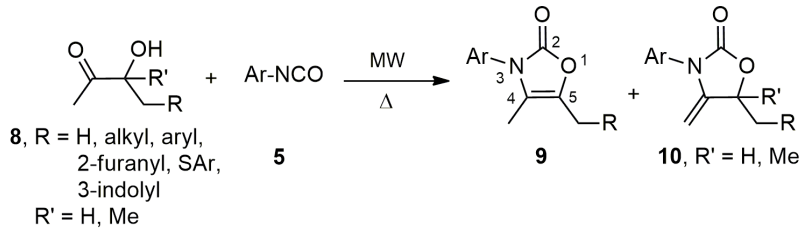

Scheme 2. Preparation of 4-oxazolin-2-ones **9** and 4-methylidene-2-oxazolidinones **10**.

Due to the synthetic potential and versatility of 4-oxazolin-2-ones **9**, a new approach for their formation is presently explored, starting from *N*-substituted *exo*-2-oxazolidinone dienes **1** and **2** and proceeding to a Brønsted acid-promoted addition of a variety of nucleophiles to generate a series of 4-methyl-5-substituted 4-oxazolin-2-ones.

Moreover, novel *exo*-imidazolidin-2-one dienes **15** and **16** were synthesized as part of our ongoing research on the elaboration of new *exo*-heterocyclic dienes and the examination of their reactivity in Diels–Alder reactions (Scheme 3) [21,22]. Symmetrical N,N'-substituted dienes **15** were prepared through two routes.

J. Mex. Chem. Soc. **2025**, *69*(4)
Regular Issue

ISSN-e 2594-0317

The first one was based on the reaction of α-iminoketones **11**–**12** with isocyanates **5** under basic conditions [21] and the second on a bis-condensation of α-bis-imino compounds **13** with triphosgene (**14**) [22]. The first approach was applied in the case of unsymmetrical dienes **16**, utilizing α-iminoketones **12** and isocyanates **5** substituted by different aryl rings [21]. The Diels–Alder addition of dienes **15** with symmetrical or unsymmetrical dienophiles afforded the respective adducts **17**, which underwent a subsequent aromatization to give to benzimidazol-2-ones **18** (Scheme 3) [21,22]. The processes with unsymmetrical dienes and dienophiles resulted in a mixture of regioisomers, except when catalysis was performed with a Lewis acid [22].

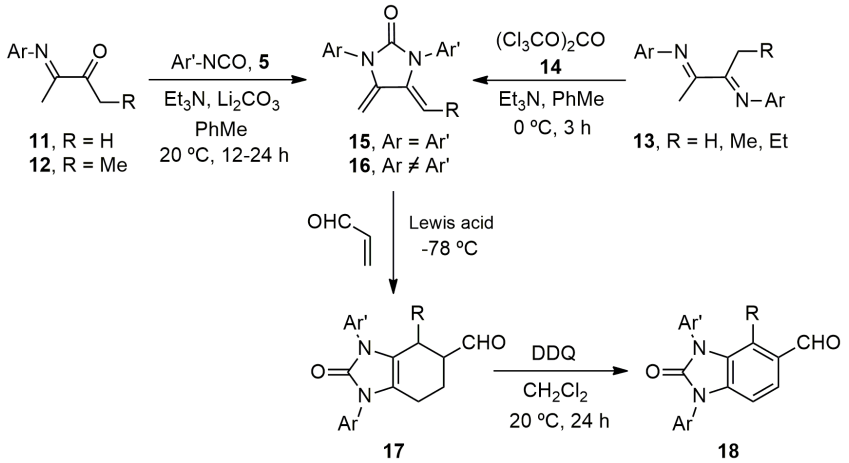

Scheme 3. Synthesis of *exo*-imidazolidin-2-one dienes **15** and **16** as precursors of benzimidazol-2-ones **18**.

Owing to the pharmacological value of benzimidazol-2-ones as potent antagonists of neurokinin NK_1 [23], calcitonin gene-related peptide (CGRP) [24], 5-HT_4 [25], and progesterone [26] receptors, and as anticancer agents [27], a variety of tricyclic benzo[*d*]imidazol-2-ones are herein synthesized through the Diels–Alder cycloadditions of dienes **15** and **16** with symmetrical dienophiles such as *N*-phenylmaleimide (**19**) and benzyne (**20**).

Experimental

General

Melting points were determined with a capillary Krüss KSP 1N melting point apparatus. The IR spectra were recorded on Perkin-Elmer 2000 and Smiths Detection IlluminatIR (ATR) spectrophotometers. ^{1}H (300, 500, or 600 MHz) and ^{13}C (75.4, 125, or 150 MHz) NMR spectra were recorded on Varian Mercury (300 MHz), Varian VNMR System (500 MHz), and Bruker 600AVANCE III (600 MHz) spectrometers, with TMS and $CDCl_3$ as internal standards. Assignment of the NMR signals was made by HMQC, HSQC, and HMBC 2D methods. Mass spectra (MS) were obtained in the electron impact (EI) (70 eV) mode on Thermo Polaris Q-Trace GC Ultra and Hewlett-Packard 5971A spectrometers. High-resolution mass spectra (HRMS) were captured in the ionization mode on Jeol JSM-GcMateII and Bruker MicrOTOF-Q II spectrometers. MW irradiation was generated in a CEM MW reactor. Analytical thin-layer chromatography was carried out on 0.25 plates coated with silica gel 60 F254 (E. Merck), which were visualized by a long- and short-wavelength UV lamp. Flash column chromatography was performed over silica gel (230-400 mesh, Natland International Co.). All air moisture sensitive reactions were carried out under N_2 atmosphere with oven-dried glassware. Triethylamine (TEA) was distilled on NaOH. Toluene and MeOH were freshly distilled over sodium, and DMF, DMSO, and CH_2Cl_2 over 4Å molecular sieves and then over CaH_2. Li_2CO_3 was dried overnight at 200 °C prior to use. All other reagents were employed without further purification. Compounds **1a**–**c**, **2a**–**c**, **15a**, **16a**–**b**, **16d**, and **32a**–**c** were prepared as reported [7,10,15,21,22].

J. Mex. Chem. Soc. **2025**, *69*(4)
Regular Issue

ISSN-e 2594-0317

5-(Methoxymethyl)-4-methyl-3-phenyloxazol-2(3*H*)-one (22a). In a round-bottom flask (100 mL) equipped with a magnetic stirring bar, **1a** (0.121 g, 0.65 mmol), MeOH (1.58 g, 49.4 mmol), and HCl (38 %) (0.061 g, 0.63 mmol) were mixed under N_2 atmosphere at rt. The mixture was stirred for 1 h, dissolved in CH_2Cl_2 (10 mL), and washed in an aqueous saturated solution of $NaHCO_3$ (2 x 5 mL) and water (2 x 5 mL). The organic layer was dried with Na_2SO_4 and the solvent was removed under vacuum. The residue was purified by column chromatography over silica gel (30 g/g crude, hexane/EtOAc, 8:2) resulting in **22a** (0.131 g, 92%) as a yellow oil. R*f* 0.32 (hexane/EtOAc, 7:3). IR (film): $\bar{\upsilon}$ = 1759, 1598, 1505, 1380, 1191, 1096, 1045, 983, 767, 715, 695 cm^{-1}. ^{1}H NMR (500 MHz, $CDCl_3$): δ 1.95 (s, 3H, C*H*$_3$-C4), 3.42 (s, 3H, C*H*$_3$O), 4.26 (s, 2H, C*H*$_2$OMe), 7.27–7.31 (m, 2H, H-2'), 7.37–7.43 (m, 1H, H-4'), 7.45–7.50 (m, 2H, H-3'). ^{13}C NMR (125 MHz, $CDCl_3$): δ 8.8 (*C*H$_3$-C4), 58.1 (*C*H$_3$O), 63.1 (*C*H$_2$OMe), 122.9 (C-4), 126.9 (C-2'), 128.5 (C-4'), 129.4 (C-3'), 132.5 (C-5), 133.3 (C-1'), 154.2 (C-2). HRMS (EI, [M$^+$]): *m/z* calcd for $C_{12}H_{13}NO_3$: 219.0895; found: 219.0901.

5-(Methoxymethyl)-4-methyl-3-(*p*-tolyl)oxazol-2(3*H*)-one (22b). Following the method for preparing **22a**, a mixture of **1b** (0.050 g, 0.25 mmol), MeOH (1.58 g, 49.4 mmol), and HCl (38 %) (0.053 g, 0.55 mmol) generated **22b** (0.048 g, 83%) as a yellow oil. R*f* 0.21 (hexane/EtOAc, 7:3). IR (film): $\bar{\upsilon}$ = 2927, 1755, 1699, 1516, 1452, 1380, 1282, 1244, 1170, 1094, 1045, 985, 820, 756, 723 cm^{-1}. ^{1}H NMR (500 MHz, $CDCl_3$): δ 1.94 (br s, 3H, C*H*$_3$-C4), 2.40 (br s, 3H, C*H*$_3$Ar), 3.42 (s, 3H, C*H*$_3$O), 4.26 (br s, 2H, C*H*$_2$OMe), 7.16–7.19 (m, 2H, H-2'), 7.26–7.29 (m, 2H, H-3'). ^{13}C NMR (125 MHz, $CDCl_3$): δ 8.8 (*C*H$_3$-C4), 21.1 (*C*H$_3$Ar), 58.1 (*C*H$_3$O), 63.2 (*C*H$_2$OMe), 123.1 (C-4), 126.9 (C-2'), 130.1 (C-3'), 130.7 (C-1'), 132.4 (C-5), 138.7 (C-4'), 154.4 (C-2). HRMS (EI, [M$^+$]): *m/z* calcd for $C_{13}H_{15}NO_3$: 233.1052; found: 233.1054.

5-(Methoxymethyl)-3-(4-methoxyphenyl)-4-methyloxazol-2(3*H*)-one (22c). Following the method for preparing **22a**, a mixture of **1c** (0.050 g, 0.23 mmol), MeOH (1.58 g, 49.4 mmol), and HCl (38 %) (0.052 g, 0.54 mmol) gave **22c** (0.048 g, 84%) as a yellow oil. R*f* 0.13 (hexane/EtOAc, 7:3). IR (film): $\bar{\upsilon}$ = 2933, 1756, 1516, 1444, 1383, 1299, 1250, 1168, 1094, 1044, 984, 835, 757 cm^{-1}. ^{1}H NMR (500 MHz, $CDCl_3$): δ 1.92 (br s, 3H, C*H*$_3$-C4), 3.42 (s, 3H, C*H*$_3$O), 3.83 (s, 3H, C*H*$_3$OAr), 4.25 (br s, 2H, C*H*$_2$OMe), 6.96–6.70 (m, 2H, H-3'), 7.19–7.23 (m, 2H, H-2'). ^{13}C NMR (125 MHz, $CDCl_3$): δ 8.8 (*C*H$_3$-C4), 55.6 (*C*H$_3$O), 58.2 (*C*H$_3$OAr), 63.2 (*C*H$_2$OMe), 114.8 (C-3'), 123.3 (C-4), 126.0 (C-1'), 128.5 (C-2'), 132.3 (C-5), 154.6 (C-2), 159.7 (C-4'). HRMS (EI, [M$^+$]): *m/z* calcd for $C_{13}H_{15}NO_4$: 249.1001; found: 249.1004.

(4-Methyl-2-oxo-3-phenyl-2,3-dihydrooxazol-5-yl)methyl acetate (23a). In a round-bottom flask (100 mL) equipped with a magnetic stirring bar, **1a** (0.029 g, 0.16 mmol) and glacial AcOH (1.05 g, 17.5 mmol) in CH_2Cl_2 (2 mL) were mixed under N_2 atmosphere at rt and stirred for 24 h. The mixture was dissolved in CH_2Cl_2 (5 mL) and washed in an aqueous saturated solution of $NaHCO_3$ (3 x 5 mL). The organic layer was dried with Na_2SO_4 and the solvent was removed under vacuum. The residue was purified by column chromatography over silica gel (30 g/g crude, hexane/EtOAc, 8:2) to provide **23a** (0.037 g, 95%) as a yellow oil. R*f* 0.25 (hexane/EtOAc, 7:3). IR (film): $\bar{\upsilon}$ = 2928, 1765, 1743, 1598, 1505, 1380, 1365, 1220, 1047, 1022, 986, 768, 712, 695 cm^{-1}. ^{1}H NMR (500 MHz, $CDCl_3$): δ 1.98 (br s, 3H, C*H*$_3$-C4), 2.11 (s, 3H, C*H*$_3$CO$_2$), 4.91 (br s, 2H, C*H*$_2$OAc), 7.28–7.31 (m, 2H, H-2"), 7.39–7.44 (m, 1H, H-4"), 7.45–7.50 (m, 2H, H-3"). ^{13}C NMR (125 MHz, $CDCl_3$): δ 8.9 (*C*H$_3$-C4), 20.8 (*C*H$_3$CO$_2$), 55.0 (*C*H$_2$OAc), 124.4 (C-4'), 126.9 (C-2"), 128.7 (C-4"), 129.5 (C-3"), 130.5 (C-5'), 133.1 (C-1"), 154.0 (C-2'), 170.7 (CH$_3$*C*O$_2$). HRMS (EI, [M$^+$]): *m/z* calcd for $C_{13}H_{13}NO_4$: 247.0845; found: 247.0845.

(4-Methyl-2-oxo-3-(*p*-tolyl)-2,3-dihydrooxazol-5-yl)methyl acetate (23b). Following the method for preparing **23a**, a mixture of **1b** (0.050 g, 0.25 mmol) and glacial AcOH (1.05 g, 17.5 mmol) in CH_2Cl_2 (4 mL) afforded **23b** (0.053 g, 81 %) as a yellow oil. R*f* 0.28 (hexane/EtOAc, 7:3). IR (film): $\bar{\upsilon}$ = 1770, 1744, 1519, 1398, 1364, 1220, 1046, 1022, 988, 820, 756 cm^{-1}. ^{1}H NMR (500 MHz, $CDCl_3$): δ 1.97 (br s, 3H, C*H*$_3$-C4), 2.11 (s, 3H, C*H*$_3$CO$_2$), 2.39 (br s, 3H, C*H*$_3$Ar), 4.91 (br s, 2H, C*H*$_2$OAc), 7.15–7.19 (m, 2H, H-2"), 7.25–7.30 (m, 2H, H-3"). ^{13}C NMR (125 MHz, $CDCl_3$): δ 8.9 (*C*H$_3$-C4), 20.8 (*C*H$_3$CO$_2$), 21.1 (*C*H$_3$Ar), 55.1 (*C*H$_2$OAc), 124.6 (C-4'), 126.8 (C-2"), 130.2 (C-3"), 130.4 (C-5'), 130.5 (C-1"), 138.9 (C-4"), 154.2 (C-2'), 170.7 (CH$_3$*C*O$_2$). HRMS (EI, [M$^+$]): *m/z* calcd for $C_{14}H_{15}NO_4$: 261.1001; found: 261.1000.

(3-(4-Methoxyphenyl)-4-methyl-2-oxo-2,3-dihydrooxazol-5-yl)methyl acetate (23c). Following the method for preparing **23a**, a mixture of **1c** (0.050 g, 0.23 mmol) and glacial AcOH (1.05 g, 17.5 mmol) in CH_2Cl_2 (4 mL) furnished **23c** (0.037 g, 59 %) as a yellow oil. R*f* 0.13 (hexane/EtOAc, 7:3). IR (film): $\bar{\upsilon}$ = 2937, 1766, 1744, 1516,

J. Mex. Chem. Soc. **2025**, *69*(4)
Regular Issue

ISSN-e 2594-0317

1443, 1398, 1365, 1300, 1249, 1221, 1169, 1046, 1025, 987, 837, 757 cm^{-1}. ^1H NMR (500 MHz, $CDCl_3$): δ 1.95 (br s, 3H, C*H*$_3$-C4), 2.11 (s, 3H, C*H*$_3$CO$_2$), 3.84 (s, 3H, C*H*$_3$OAr), 4.91 (br s, 2H, C*H*$_2$OAc), 6.96–7.00 (m, 2H, H-3"), 7.18–7.22 (m, 2H, H-2"). ^{13}C NMR (125 MHz, $CDCl_3$): δ 8.8 (*C*H$_3$-C4), 20.8 (*C*H$_3$CO$_2$), 55.1 (*C*H$_2$OAc), 55.5 (*C*H$_3$OAr), 114.8 (C-3"), 124.7 (C-4'), 125.8 (C-1"), 128.4 (C-2"), 130.3 (C-5'), 154.4 (C-2'), 159.7 (C-4"), 170.7 (CH$_3$*C*O$_2$). HRMS (EI, [M^+]): *m/z* calcd for $C_{14}H_{15}NO_5$: 277.0950; found: 277.0949.

5-(((4-Chlorophenyl)thio)methyl)-4-methyl-3-phenyloxazol-2(3*H*)-one (24a). In a round-bottom flask (100 mL) equipped with a magnetic stirring bar, **1a** (0.06 g, 0.32 mmol), **21c** (0.089 g, 0.62 mmol), and H_3PO_4 (85 %) (0.036 g, 0.31 mmol) in CH_2Cl_2 (5 mL) were mixed under N_2 atmosphere at rt and stirred for 24 h. The mixture was dissolved in CH_2Cl_2 (10 mL) and washed in an aqueous saturated solution of $NaHCO_3$ (2 x 5 mL). The organic layer was dried with Na_2SO_4 and the solvent was removed under vacuum. The residue was purified by column chromatography over silica gel (30 g/g crude, hexane/EtOAc, 85:15) to obtain **24a** (0.063 g, 60%) as a yellow solid. R*f* 0.38 (hexane/EtOAc, 7:3); mp 106–108 °C. IR (film): ῡ = 1756, 1698, 1597, 1504, 1476, 1382, 1272, 1186, 1095, 1040, 1012, 981, 819, 766, 709, 604 cm^{-1}. ^1H NMR (500 MHz, $CDCl_3$): δ 1.59 (br s, 3H, C*H*$_3$-C4), 3.85 (br s, 2H, C*H*$_2$S), 7.19–7.22 (m, 2H, H-2'), 7.28–7.32 (m, 2H, H-3"), 7.37–7.42 (m, 3H, H-4', H-2"), 7.44–7.49 (m, 2H, H-3'). ^{13}C NMR (125 MHz, $CDCl_3$): δ 8.6 (*C*H$_3$-C4), 30.2 (*C*H$_2$S), 121.3 (C-4), 126.9 (C-2'), 128.6 (C-4'), 129.2 (C-3"), 129.5 (C-3'), 131.2 (C-5), 132.8 (C-1"), 133.3 (C-1'), 134.2 (C-4"), 134.3 (C-2"), 154.0 (C-2). HRMS (ESI, [M + H]$^+$): *m/z* calcd for $C_{17}H_{15}ClNO_2S$: 332.0512; found: 332.0465.

5-(((4-Chlorophenyl)thio)methyl)-4-methyl-3-(*p*-tolyl)oxazol-2(3*H*)-one (24b). Following the method for preparing **24a**, a mixture of **1b** (0.040 g, 0.20 mmol), **21c** (0.056 g, 0.39 mmol), and H_3PO_4 (85 %) (0.028 g, 0.24 mmol) in CH_2Cl_2 (5 mL) yielded **24b** (0.052 g, 75%) as a yellow solid. R*f* 0.44 (hexane/EtOAc, 7:3); mp 103–104 °C. IR (KBr): ῡ = 1751, 1694, 1516, 1478, 1387, 1270, 1191, 1092, 1039, 1011, 988, 817, 755 cm^{-1}. ^1H NMR (600 MHz, $CDCl_3$): δ 1.57 (br s, 3H, C*H*$_3$-C4), 2.38 (br s, 3H, C*H*$_3$Ar), 3.85 (br s, 2H, C*H*$_2$S), 7.07–7.10 (m, 2H, H-2'), 7.24–7.27 (m, 2H, H-3'), 7.28–7.31 (m, 2H, H-3"), 7.38–7.41 (m, 2H, H-2"). ^{13}C NMR (150 MHz, $CDCl_3$): δ 8.5 (*C*H$_3$-C4), 21.1 (*C*H$_3$Ar), 30.2 (*C*H$_2$S), 121.4 (C-4), 126.7 (C-2'), 129.1 (C-3"), 130.1 (C-3'), 130.6 (C-1'), 130.9 (C-5), 132.8 (C-1"), 134.1 (C-4"), 134.3 (C-2"), 138.7 (C-4'), 154.1 (C-2). HRMS (EI, [M^+]): *m/z* calcd for $C_{18}H_{16}ClNO_2S$: 345.0590; found: 345.0589.

5-(((4-Chlorophenyl)thio)methyl)-3-(4-methoxyphenyl)-4-methyloxazol-2(3*H*)-one (24c). Following the method for preparing **24a**, a mixture of **1c** (0.040 g, 0.18 mmol), **21c** (0.054 g, 0.37 mmol), and H_3PO_4 (85 %) (0.029 g, 0.25 mmol) in CH_2Cl_2 (3 mL) generated **24c** (0.049 g, 74%) as a yellow solid. R*f* 0.38 (hexane/EtOAc, 7:3); mp 84–86 °C. IR (film): ῡ = 2930, 1759, 1698, 1515, 1476, 1387, 1300, 1251, 1169, 1095, 1036, 1012, 983, 832, 755 cm^{-1}. ^1H NMR (500 MHz, $CDCl_3$): δ 1.55 (br s, 3H, C*H*$_3$-C4), 3.82 (s, 3H, C*H*$_3$O), 3.84 (br s, 2H, C*H*$_2$S), 6.94–6.98 (m, 2H, H-3'), 7.10–7.14 (m, 2H, H-2'), 7.28–7.31 (m, 2H, H-3"), 7.37–7.41 (m, 2H, H-2"). ^{13}C NMR (125 MHz, $CDCl_3$): δ 8.5 (*C*H$_3$-C4), 30.2 (*C*H$_2$S), 55.5 (*C*H$_3$O), 114.8 (C-3'), 121.6 (C-4), 125.9 (C-1'), 128.3 (C-2'), 129.1 (C-3"), 130.8 (C-5), 132.9 (C-1"), 134.1 (C-4"), 134.3 (C-2"), 154.3 (C-2), 159.6 (C-4'). HRMS (EI, [M^+]): *m/z* calcd for $C_{18}H_{16}ClNO_3S$: 361.0539; found: 361.0535.

5-(4-Hydroxybenzyl)-4-methyl-3-(*p*-tolyl)oxazol-2(3*H*)-one (25a). In a round-bottom flask (100 mL) equipped with a magnetic stirring bar, **1a** (0.06 g, 0.32 mmol), **21d** (0.06 g, 0.64 mmol), and H_3PO_4 (85 %) (0.062 g, 0.54 mmol) in CH_2Cl_2 (5 mL) were mixed under N_2 atmosphere at rt and stirred for 24 h. The mixture was dissolved in CH_2Cl_2 (10 mL) and washed in an aqueous saturated solution of $NaHCO_3$ (2 x 5 mL) and EtOAc (2 x 5 mL). The organic layer was dried with Na_2SO_4 and the solvent was removed under vacuum. The residue was purified by column chromatography over silica gel (30 g/g crude, hexane/EtOAc, 7:3), resulting in **25a** (0.058 g, 64 %) as a yellow oil. R*f* 0.21 (hexane/EtOAc, 7:3). IR (film): ῡ = 3328, 1737, 1699, 1614, 1597, 1515, 1504, 1388, 1265, 1227, 1171, 1044, 986, 833, 766, 695 cm^{-1}. ^1H NMR (600 MHz, $CDCl_3$): δ 1.86 (br s, 3H, C*H*$_3$-C4), 3.67 (br s, 2H, C*H*$_2$Ar), 6.77–6.79 (m, 2H, H-3"), 7.03–7.07 (m, 2H, H-2"), 7.26–7.28 (m, 2H, H-2'), 7.35–7.38 (m, 1H, H-4'), 7.42–7.46 (m, 2H, H-3'). ^{13}C NMR (150 MHz, $CDCl_3$): δ 8.7 (*C*H$_3$-C4), 30.0 (*C*H$_2$Ar), 115.6 (C-3"), 118.5 (C-4), 126.9 (C-2'), 127.6 (C-1"), 128.5 (C-4'), 129.39 (C-2"), 129.43 (C-3'), 133.3 (C-1'), 135.6 (C-5), 155.0 (C-2), 155.5 (C-4"). HRMS (ESI, [M + H]$^+$): *m/z* calcd for $C_{17}H_{15}NO_3$: 282.1130; found: 282.1072.

5-(4-Hydroxybenzyl)-4-methyl-3-(*p*-tolyl)oxazol-2(3*H*)-one (25b). Following the method for preparing **25a**, a mixture of **1b** (0.080 g, 0.40 mmol), **21d** (0.075 g, 0.80 mmol), and H_3PO_4 (85 %) (0.077 g, 0.67 mmol) in CH_2Cl_2

J. Mex. Chem. Soc. **2025**, *69*(4)
Regular Issue

ISSN-e 2594-0317

(5 mL) gave **25b** (0.081 g, 69 %) as a yellow solid. R*f* 0.21 (hexane/EtOAc, 7:3); mp 218–220 °C. IR (KBr): $\bar{\upsilon}$ = 3256, 1733, 1695, 1614, 1515, 1452, 1393, 1276, 1261, 1234, 1173, 994, 825, 758 cm^{-1}. ^1H NMR (600 MHz, $CDCl_3$): δ 1.88 (br s, 3H, C*H*$_3$-C4), 2.38 (br s, 3H, C*H*$_3$Ar), 3.69 (s, 2H, C*H*$_2$Ar), 5.81 (br, 1H, OH), 6.80–6.83 (m, 2H, H-3"), 7.11–7.14 (m, 2H, H-2"), 7.16–7.19 (m, 2H, H-2'), 7.24–7.26 (m, 2H, H-3'). ^{13}C NMR (150 MHz, $CDCl_3$): δ 8.8 (*C*H$_3$-C4), 21.1 (*C*H$_3$Ar), 30.1 (*C*H$_2$Ar), 115.6 (C-3"), 118.6 (C-4), 126.8 (C-2'), 128.4 (C-1"), 129.6 (C-2"), 130.1 (C-3'), 130.9 (C-1'), 135.1 (C-5), 138.6 (C-4'), 154.9 (C-2 or C-4"), 155.0 (C-4" or C-2). HRMS (EI, [M^+]): *m/z* calcd for $C_{18}H_{17}NO_3$: 295.1208; found: 295.1218.

5-(4-Hydroxybenzyl)-3-(4-methoxyphenyl)-4-methyloxazol-2(3*H*)-one (25c). Following the method for preparing **25a**, a mixture of **1c** (0.065 g, 0.3 mmol), **21d** (0.056 g, 0.6 mmol), and H_3PO_4 (85 %) (0.058 g, 0.5 mmol) in CH_2Cl_2 (5 mL) provided **25c** (0.079 g, 85 %) as a yellow solid. R*f* 0.12 (hexane/EtOAc, 7:3); mp 194–195 °C. IR (KBr): $\bar{\upsilon}$ = 3359, 1751, 1702, 1611, 1596, 1515, 1444, 1401, 1300, 1247, 1227, 1168, 1028, 989, 833, 757, 683 cm^{-1}. ^1H NMR (500 MHz, $CDCl_3$): δ 1.84 (br s, 3H, C*H*$_3$-C4), 3.69 (br s, 2H, C*H*$_2$Ar), 3.83 (s, 3H, C*H*$_3$O), 6.81–6.84 (m, 2H, H-3"), 6.94–6.98 (m, 2H, H-3'), 7.09–7.13 (m, 2H, H-2"), 7.18–7.22 (m, 2H, H-2'), 7.36 (br, 1H, OH). ^{13}C NMR (125 MHz, $CDCl_3$): δ 8.5 (*C*H$_3$-C4), 30.0 (*C*H$_2$Ar), 55.4 (*C*H$_3$O), 114.6 (C-3'), 115.5 (C-3"), 118.5 (C-4), 126.2 (C-1'), 127.8 (C-1"), 128.3 (C-2'), 129.4 (C-2"), 134.8 (C-5), 154.8 (C-2), 155.5 (C-4"), 159.3 (C-4'). HRMS (EI, [M^+]): *m/z* calcd for $C_{18}H_{17}NO_4$: 311.1158; found: 311.1154.

5-(1-Methoxyethyl)-4-methyl-3-phenyloxazol-2(3*H*)-one (26a). In a round-bottom flask (100 mL) equipped with a magnetic stirring bar, **2a** (0.060 g, 0.30 mmol), **21a** (2.37 g, 74.0 mmol), and HCl (38 %) (0.062 g, 0.65 mmol) were mixed and stirred under N_2 atmosphere at -10 ºC for 24 h. The mixture was dissolved in CH_2Cl_2 (5 mL) and washed in an aqueous saturated solution of $NaHCO_3$ (2 x 5 mL) and EtOAc (2 x 5 mL). The organic layer was dried with Na_2SO_4 and the solvent was removed under vacuum. The residue was purified by column chromatography over silica gel (30 g/g crude, hexane/EtOAc, 75:25), leading to **26a** (0.046 g, 67%) as a yellow solid. R*f* 0.31 (hexane/EtOAc, 7:3); mp 100–102 °C. IR (KBr): $\bar{\upsilon}$ = 3054, 2987, 2936, 1746, 1693, 1598, 1504, 1396, 1259, 1116, 1090, 991, 767, 752, 712 cm^{-1}. ^1H NMR (500 MHz, $CDCl_3$): δ 1.51 (d, *J* = 6.5 Hz, 3H, H-2"), 1.96 (s, 3H, C*H*$_3$-C4), 3.31 (s, 3H, C*H*$_3$O), 4.25 (q, *J* = 6.5 Hz, 1H, H-1"), 7.30–7.33 (m, 2H, H-2'), 7.39–7.43 (m, 1H, H-4'), 7.46–7.51 (m, 2H, H-3'). ^{13}C NMR (125 MHz, $CDCl_3$): δ 8.8 (*C*H$_3$-C4), 18.7 (C-2"), 55.9 (*C*H$_3$O), 69.4 (C-1"), 121.1 (C-4), 127.0 (C-2'), 128.5 (C-4'), 129.5 (C-3'), 133.3 (C-1'), 134.5 (C-5), 154.3 (C-2). HRMS (EI, [M^+]): *m/z* calcd for $C_{13}H_{15}NO_3$: 233.1052; found: 233.1046.

5-(1-Methoxyethyl)-4-methyl-3-(*p*-tolyl)oxazol-2(3*H*)-one (26b). Following the method for preparing **26a**, a mixture of **2b** (0.060 g, 0.28 mmol), **21a** (2.38 g, 74.4 mmol), and HCl (38 %) (0.068 g, 0.71 mmol) produced **26b** (0.047 g, 69 %) as a yellow solid. R*f* 0.26 (hexane/EtOAc, 7:3); mp 84–86 °C. IR (film): $\bar{\upsilon}$ = 2986, 2931, 1760, 1698, 1519, 1450, 1398, 1387, 1351, 1258, 1117, 1088, 994, 981, 821, 757, 723 cm^{-1}. ^1H NMR (500 MHz, $CDCl_3$): δ 1.50 (d, *J* = 6.5 Hz, 3H, H-2"), 1.94 (s, 3H, C*H*$_3$-C4), 2.39 (br s, 3H, C*H*$_3$Ar), 3.31 (s, 3H, C*H*$_3$O), 4.24 (q, *J* = 6.5 Hz, 1H, H-1"), 7.17–7.21 (m, 2H, H-2'), 7.25–7.30 (m, 2H, H-3'). ^{13}C NMR (125 MHz, $CDCl_3$): δ 8.7 (*C*H$_3$-C4), 18.7 (C-2"), 21.1 (*C*H$_3$Ar), 55.9 (*C*H$_3$O), 69.5 (C-1"), 121.3 (C-4), 126.9 (C-2'), 130.1 (C-3'), 130.7 (C-1'), 134.3 (C-5) 138.6 (C-4'), 154.4 (C-2). HRMS (EI, [M^+]): *m/z* calcd for $C_{14}H_{17}NO_3$: 247.1208; found: 247.1215.

5-(1-Methoxyethyl)-3-(4-methoxyphenyl)-4-methyloxazol-2(3*H*)-one (26c). (*Z*)-5-Ethylidene-4-methoxy-3-(4-methoxyphenyl)-4-methyloxazolidin-2-one (26c'). Following the method for preparing **26a**, a mixture of **2c** (0.060 g, 0.26 mmol), **21a** (2.38 g, 74.4 mmol), and HCl (38 %) (0.063 g, 0.66 mmol) afforded **26c** (0.05 g, 73 %) and **26c'** (0.01 g, 15%) as yellow solids. Data for **26c**: R*f* 0.21 (hexane/EtOAc, 7:3); mp 88–90 °C. IR (film): $\bar{\upsilon}$ = 2985, 2936, 1759, 1698, 1610, 1517, 1444, 1399, 1351, 1301, 1252, 1168, 1117, 1088, 1033, 981, 836, 758 cm^{-1}. ^1H NMR (500 MHz, $CDCl_3$): δ 1.50 (d, *J* = 6.5 Hz, 3H, H-2"), 1.93 (s, 3H, C*H*$_3$-C4), 3.31 (s, 3H, C*H*$_3$O), 3.84 (s, 3H, C*H*$_3$OAr), 4.24 (q, *J* = 6.5 Hz, 1H, H-1"), 6.96–7.00 (m, 2H, H-3'), 7.20–7.24 (m, 2H, H-2'). ^{13}C NMR (125 MHz, $CDCl_3$): δ 8.7 (*C*H$_3$-C4), 18.8 (C-2"), 55.5 (*C*H$_3$OAr), 55.9 (*C*H$_3$O), 69.5 (C-1"), 114.8 (C-3'), 121.4 (C-4), 125.9 (C-1'), 128.5 (C-2'), 134.2 (C-5), 154.6 (C-2), 159.6 (C-4'). HRMS (EI, [M^+]): *m/z* calcd for $C_{14}H_{17}NO_4$: 263.1158; found 263.1158. Data for **26c'**: R*f* 0.57 (hexane/EtOAc, 7:3); mp 58–60 °C. IR (film): $\bar{\upsilon}$ = 2938, 1785, 1713, 1515, 1376, 1298, 1250, 1169, 1120, 1065, 1035, 833 cm^{-1}. ^1H NMR (600 MHz, $CDCl_3$): δ 1.47 (s, 3H, C*H*$_3$-C4), 1.82 (d, *J* = 6.9 Hz, 3H, C*H*$_3$CH=), 3.29 (s, 3H, C*H*$_3$O), 3.82 (s, 3H, C*H*$_3$OAr), 5.03 (q, *J* = 6.9 Hz, 1H, CH$_3$C*H*=), 6.92–6.96 (m, 2H, H-3'), 7.27–7.31 (m, 2H, H-2'). ^{13}C NMR (150 MHz, $CDCl_3$)**:** δ 10.0 (*C*H$_3$CH=), 24.8 (*C*H$_3$-C4),

J. Mex. Chem. Soc. **2025**, *69*(4)
Regular Issue

ISSN-e 2594-0317

50.1 (*C*H_3O), 55.5 (*C*H_3OAr), 92.2 (C-4), 100.6 (CH_3*C*H=), 114.5 (C-3'), 126.6 (C-1'), 127.1 (C-2'), 146.7 (C-5), 153.2 (C-2), 158.7 (C-4'). HRMS (EI, [M^+]): *m/z* calcd for $C_{14}H_{17}NO_4$: 263.1158; found: 263.1159.

5-(1-((4-Chlorophenyl)thio)ethyl)-4-methyl-3-phenyloxazol-2(3*H*)-one (27a). In a round-bottom flask (100 mL) equipped with a magnetic stirring bar, **2a** (0.050 g, 0.25 mmol), **21c** (0.069 g, 0.48 mmol), and H_3PO_4 (85 %) (0.034 g, 0.30 mmol) in CH_2Cl_2 (5 mL) were mixed under N_2 atmosphere at rt and stirred for 24 h. The mixture was dissolved in CH_2Cl_2 (10 mL) and washed in an aqueous saturated solution of $NaHCO_3$ (2 x 5 mL). The organic layer was dried with Na_2SO_4 and the solvent was removed under vacuum. The residue was purified by column chromatography over silica gel (30 g/g crude, hexane/EtOAc, 9:1) to furnish **27a** (0.051 g, 60%) as a yellow solid. R*f* 0.50 (hexane/EtOAc, 7:3); mp 128–129 °C. IR (film): $\bar{\upsilon}$ = 2979, 2930, 1760, 1694, 1598, 1504, 1475, 1395, 1384, 1261, 1167, 1094, 1013, 981, 824, 768, 709, 696 cm^{-1}. ^{1}H NMR (500 MHz, $CDCl_3$): δ 1.41 (s, 3H, C*H*$_3$-C4), 1.63 (d, *J* = 7.1 Hz, 3H, H-2"), 4.14 (q, *J* = 7.1 Hz, 1H, H-1"), 7.14–7.17 (m, 2H, H-2'), 7.28–7.31 (m, 2H, H-3'"), 7.37–7.41 (m, 3H, H-4', H-2'"), 7.43–7.48 (m, 2H, H-3'). ^{13}C NMR (125 MHz, $CDCl_3$): δ 8.4 (*C*H_3-C4), 18.1 (C-2"), 40.0 (C-1"), 120.2 (C-4), 126.9 (C-2'), 128.6 (C-4'), 129.0 (C-3'"), 129.5 (C-3'), 132.4 (C-1'"), 133.3 (C-1'), 134.3 (C-5), 135.0 (C-4'"), 136.6 (C-2'"), 154.0 (C-2). HRMS (EI, [M^+]): *m/z* calcd for $C_{18}H_{16}ClNO_2S$: 345.0590; found: 345.0580.

5-(1-((4-Chlorophenyl)thio)ethyl)-4-methyl-3-(*p*-tolyl)oxazol-2(3*H*)-one (27b). Following the method for preparing **27a**, a mixture of **2b** (0.050 g, 0.23 mmol), **21c** (0.067 g, 0.46 mmol), and H_3PO_4 (85 %) (0.032 g, 0.28 mmol) in CH_2Cl_2 (5 mL) yielded **27b** (0.053 g, 64 %) as a yellow solid. R*f* 0.51 (hexane/EtOAc, 7:3); mp 109–111 °C. IR (film): $\bar{\upsilon}$ = 2979, 2928, 1756, 1694, 1572, 1518, 1475, 1396, 1386, 1262, 1168, 1095, 1013, 984, 820, 754 cm^{-1}. ^{1}H NMR (500 MHz, $CDCl_3$): δ 1.38 (s, 3H, C*H*$_3$-C4), 1.62 (d, *J* = 7.0 Hz, 3H, H-2"), 2.37 (s, 3H, C*H*$_3$Ar), 4.13 (q, *J* = 7.0 Hz, 1H, H-1"), 7.00–7.05 (m, 2H, H-2'), 7.23–7.27 (m, 2H, H-3'), 7.28–7.31 (m, 2H, H-3'"), 7.35–7.40 (m, 2H, H-2'"). ^{13}C NMR (125 MHz, $CDCl_3$): δ 8.4 (*C*H_3-C4), 18.1 (C-2"), 21.1 (*C*H_3Ar), 40.0 (C-1"), 120.3 (C-4), 126.8 (C-2'), 129.0 (C-3'"), 130.1 (C-3'), 130.6 (C-1'), 132.4 (C-1'"), 134.1 (C-5), 135.0 (C-4'"), 136.6 (C-2'"), 138.7 (C-4'), 154.2 (C-2). HRMS (EI, [M^+]): *m/z* calcd for $C_{19}H_{18}NO_2SCl$: 359.0747; found: 359.0741.

5-(1-((4-Chlorophenyl)thio)ethyl)-3-(4-methoxyphenyl)-4-methyloxazol-2(3*H*)-one (27c). Following the method for preparing **27a**, a mixture **2c** (0.060 g, 0.26 mmol), **21c** (0.075 g, 0.52 mmol), and H_3PO_4 (85 %) (0.036 g, 0.31 mmol) in CH_2Cl_2 (5 mL) provided **27c** (0.06 g, 62 %) as a yellow solid. R*f* 0.37 (hexane/EtOAc, 7:3); mp 117–119 °C. IR (film): $\bar{\upsilon}$ = 2931, 1754, 1694, 1516, 1475, 1397, 1388, 1301, 1251, 1165, 1095, 1032, 1013, 983, 832 cm^{-1}. ^{1}H NMR (500 MHz, $CDCl_3$): δ 1.37 (s, 3H, C*H*$_3$-C4), 1.63 (d, *J* = 7.0 Hz, 3H, H-2"), 3.82 (s, 3H, C*H*$_3$O), 4.13 (q, *J* = 7.0 Hz, 1H, H-1"), 6.93–6.98 (m, 2H, H-3'), 7.04–7.08 (m, 2H, H-2'), 7.27–7.32 (m, 2H, H-3'"), 7.36–7.40 (m, 2H, H-2'"). ^{13}C NMR (125 MHz, $CDCl_3$): δ 8.3 (*C*H_3-C4), 18.1 (C-2"), 40.0 (C-1"), 55.5 (*C*H_3O), 114.8 (C-3'), 120.5 (C-4), 125.8 (C-1'), 128.3 (C-2'), 129.0 (C-3'"), 132.5 (C-1'"), 134.0 (C-5), 135.0 (C-4'"), 136.6 (C-2'"), 154.3 (C-2), 159.6 (C-4'). HRMS (EI, [M^+]): *m/z* calcd for $C_{19}H_{18}NO_3ClS$: 375.0696; found: 375.0690.

5-(1-(4-Hydroxyphenyl)ethyl)-4-methyl-3-phenyloxazol-2(3*H*)-one (28a). In a round-bottom flask (100 mL) equipped with a magnetic stirring bar, **2a** (0.06 g, 0.30 mmol), **21d** (0.052 g, 0.55 mmol), and H_3PO_4 (85 %) (0.086 g, 0.75 mmol) in CH_2Cl_2 (3 mL) were mixed under N_2 atmosphere at rt and stirred for 24 h. The mixture was dissolved in CH_2Cl_2 (5 mL) and washed in an aqueous saturated solution of $NaHCO_3$ (2 x 5 mL) and EtOAc (2 x 5 mL). The organic layer was dried with Na_2SO_4 and the solvent was removed under vacuum. The residue was purified by column chromatography over silica gel (30 g/g crude, hexane/EtOAc, 7:3), resulting in **28a** (0.053 g, 60%) as a yellow solid. R*f* 0.33 (hexane/EtOAc, 7:3); mp 168–170 °C. IR (KBr): $\bar{\upsilon}$ = 3398, 2979, 2930, 1732, 1689, 1610, 1594, 1515, 1504, 1389, 1263, 1224, 1174, 1057, 987, 839, 773, 761, 710, 694 cm^{-1}. ^{1}H NMR (500 MHz, $CDCl_3$): δ 1.58 (d, *J* = 7.5 Hz, 3H, H-2"), 1.83 (br s, 3H, C*H*$_3$-C4), 3.91 (q, *J* = 7.5 Hz, 1H, H-1"), 6.81–6.84 (m, 2H, H-3'"), 7.17–7.22 (m, 2H, H-2'"), 7.26–7.30 (m, 2H, H-2'), 7.36–7.40 (m, 1H, H-4'), 7.42–7.47 (m, 2H, H-3'). ^{13}C NMR (125 MHz, $CDCl_3$): δ 8.8 (*C*H_3-C4), 19.9 (C-2"), 35.4 (C-1"), 115.6 (C-3'"), 117.1 (C-4), 127.1 (C-2'), 128.3 (C-2'"), 128.4 (C-4'), 129.5 (C-3'), 133.5 (C-1'), 134.2 (C-1'"), 138.9 (C-5), 154.8 (C-2), 155.0 (C-4'"). HRMS (EI, [M^+]): *m/z* calcd for $C_{18}H_{17}NO_3$: 295.1208; found: 295.1199.

5-(1-(4-Hydroxyphenyl)ethyl)-4-methyl-3-(*p*-tolyl)oxazol-2(3*H*)-one (28b). Following the method for preparing **28a**, a mixture of **2b** (0.060 g, 0.28 mmol), **21d** (0.047 g, 0.50 mmol), and H_3PO_4 (85 %) (0.081 g, 0.7 mmol) in CH_2Cl_2 (5 mL) gave **28b** (0.058 g, 67 %) as a yellow solid. R*f* 0.31 (hexane/EtOAc, 7:3); mp 197–199 °C.

J. Mex. Chem. Soc. **2025**, *69*(4)
Regular Issue

ISSN-e 2594-0317

IR (KBr): $\tilde{\upsilon}$ = 3282, 2980, 1731, 1692, 1614, 1516, 1448, 1393, 1259, 1231, 1173, 835, 756 cm^{-1}. ^1H NMR (600 MHz, $CDCl_3$): δ 1.57 (d, *J* = 7.2 Hz, 3H, H-2”), 1.81 (br s, 3H, C*H*$_3$-C4), 2.37 (s, 3H, C*H*$_3$Ar), 3.90 (q, *J* = 7.2 Hz, 1H, H-1”), 6.55 (br, 1H, OH), 6.81–6.84 (m, 2H, H-3’”), 7.13–7.16 (m, 2H, H-2’), 7.17–7.20 (m, 2H, H-2’”), 7.23–7.26 (m, 2H, H-3’). ^{13}C NMR (150 MHz, $CDCl_3$): δ 8.7 (*C*H$_3$-C4), 19.9 (C-2”), 21.1 (*C*H$_3$Ar), 35.3 (C-1”), 115.6 (C-3’”), 117.3 (C-4), 126.9 (C-2’), 128.2 (C-2’”), 130.1 (C-3’), 130.8 (C-1’), 134.0 (C-1’”), 138.6 (C-4’), 138.9 (C-5), 155.1 (C-2), 155.3 (C-4’”). HRMS (EI, [M^+]): *m/z* calcd for $C_{19}H_{19}NO_3$: 309.1365; found: 309.1366.

5-(1-(4-Hydroxyphenyl)ethyl)-3-(4-methoxyphenyl)-4-methyloxazol-2(3*H*)-one (28c). Following the method for preparing **28a**, a mixture of **2c** (0.07 g, 0.3 mmol), **21d** (0.048 g, 0.51 mmol), and H_3PO_4 (85 %) (0.086 g, 0.75 mmol) in CH_2Cl_2 (3 mL) led to **28c** (0.063 g, 64 %) as a yellow solid. R*f* 0.15 (hexane/EtOAc, 7:3); mp 179–180 °C. IR (KBr): $\tilde{\upsilon}$ = 3318, 2972, 1732, 1690, 1611, 1516, 1442, 1393, 1305, 1255, 1228, 1169, 1035, 992, 834 cm^{-1}. ^1H NMR (500 MHz, $CDCl_3$): δ 1.58 (d, *J* = 7.3 Hz, 3H, H-2”), 1.79 (s, 3H, C*H*$_3$-C4), 3.82 (s, 3H, C*H*$_3$O), 3.90 (q, *J* = 7.3 Hz, 1H, H-1”), 6.22 (br, 1H, OH), 6.80–6.84 (m, 2H, H-3’”), 6.93–6.97 (m, 2H, H-3’), 7.16–7.21 (m, 4H, H-2’, H-2’”). ^{13}C NMR (125 MHz, $CDCl_3$): δ 8.7 (*C*H$_3$-C4), 19.9 (C-2”), 35.4 (C-1”), 55.5 (C*H*$_3$O), 114.7 (C-3’), 115.6 (C-3’”), 117.4 (C-4), 126.1 (C-1’), 128.2 (C-2’”), 128.5 (C-2’), 134.2 (C-1’”), 138.7 (C-5), 155.1 (C-4’”), 155.2 (C-2), 159.5 (C-4’) HRMS (EI, [M^+]): *m/z* calcd for $C_{19}H_{19}NO_4$: 325.1314; found: 325.1308.

5-(Hydroxymethyl)-4-methyl-3-phenyloxazol-2(3*H*)-one (29a). In a round-bottom flask (100 mL) equipped with a magnetic stirring bar, **23a** (0.150 g, 0.60 mmol) and NaOH (0.036 g, 0.90 mmol) in MeOH/H_2O (8:2) (12 mL) were mixed at rt and stirred for 30 min. The mixture was neutralized with AcOH (1.0 M) and extracted with EtOAc (2 x 5 mL). The organic layer was dried with Na_2SO_4 and the solvent was removed under vacuum. The residue was purified by column chromatography over silica gel (30 g/g crude, hexane/EtOAc, 6:4) to produce **29a** (0.11 g, 90 %) as a yellow solid. R*f* 0.05 (hexane/EtOAc, 7:3); mp 126–128 °C. IR (film): $\tilde{\upsilon}$ = 3404, 1756, 1698, 1597, 1504, 1398, 1385, 1277, 1215, 1185, 1047, 1003, 767, 712, 696 cm^{-1}. ^1H NMR (600 MHz, $CDCl_3$): δ 1.94 (br s, 3H, C*H*$_3$-C4), 2.77 (br, 1H, OH), 4.45 (br d, *J* = 4.8 Hz, 2H, C*H*$_2$OH), 7.29–7.32 (m, 2H, H-2’), 7.40–7.43 (m, 1H, H-4’), 7.46–7.50 (m, 2H, H-3’). ^{13}C NMR (150 MHz, $CDCl_3$): δ 8.8 (*C*H$_3$-C4), 54.0 (*C*H$_2$OH), 121.6 (C-4), 127.1 (C-2’), 128.7 (C-4’), 129.6 (C-3’), 133.4 (C-1’), 134.9 (C-5), 154.5 (C-2). HRMS (ESI, [M + H]$^+$): *m/z* calcd for $C_{11}H_{12}NO_3$: 206.0817; found: 206.0769.

5-(Hydroxymethyl)-4-methyl-3-(*p*-tolyl)oxazol-2(3*H*)-one (29b). Following the method for preparing **29a**, a mixture of **23b** (0.25 g, 0.96 mmol) and NaOH (0.057 g, 1.43 mmol) in MeOH/H_2O (8:2) (18 mL) furnished **29b** (0.19 g, 91 %) as a yellow solid. R*f* 0.058 (hexane/EtOAc, 7:3); mp 128–131 °C. IR (film): $\tilde{\upsilon}$ = 3411, 2926, 1760, 1740, 1702, 1518, 1398, 1386, 1277, 1213, 1048, 991, 820, 757 cm^{-1}. ^1H NMR (500 MHz, $CDCl_3$): δ 1.92 (br s, 3H, C*H*$_3$-C4), 2.39 (br s, 3H, C*H*$_3$Ar), 2.64 (br, 1H, OH), 4.45 (br s, 2H, C*H*$_2$OH), 7.15–7.19 (m, 2H, H-2’), 7.26–7.29 (m, 2H, H-3’). ^{13}C NMR (125 MHz, $CDCl_3$): δ 8.8 (*C*H$_3$-C4), 21.1 (*C*H$_3$Ar), 54.0 (*C*H$_2$OH), 121.7 (C-4), 126.9 (C-2’), 130.2 (C-3’), 130.7 (C-1’), 134.6 (C-5), 138.8 (C-4’), 154.6 (C-2). HRMS (EI, [M^+]): *m/z* calcd for $C_{12}H_{13}NO_3$: 219.0895; found: 219.0897.

5-(Hydroxymethyl)-3-(4-methoxyphenyl)-4-methyloxazol-2(3*H*)-one (29c). Following the method for preparing **29a**, a mixture of **23c** (0.04 g, 0.14 mmol) and NaOH (0.009 g, 0.22 mmol) in MeOH/H_2O (8:2) (6 mL) afforded **29c** (0.03 g, 87 %) as a yellow solid. R*f* 0.034 (hexane/EtOAc, 7:3); mp 162–164 °C. IR (film): $\tilde{\upsilon}$ = 3413, 2929, 1738, 1698, 1516, 1398, 1249, 1170, 1030, 990, 841, 757 cm^{-1}. ^1H NMR (500 MHz, $CDCl_3$): δ 1.92 (br s, 3H, C*H*$_3$-C4), 2.00 (br, 1H, OH), 3.84 (s, 3H, C*H*$_3$O), 4.47 (br s, 2H, C*H*$_2$OH), 6.97–7.00 (m, 2H, H-3’), 7.19–7.22 (m, 2H, H-2’). ^{13}C NMR (125 MHz, $CDCl_3$): δ 8.8 (*C*H$_3$-C4), 54.3 (*C*H$_2$OH), 55.6 (*C*H$_3$O), 114.9 (C-3’), 122.0 (C-4), 126.0 (C-1’), 128.5 (C-2’), 134.2 (C-5), 154.6 (C-2), 159.7 (C-4’). HRMS (EI, [M^+]) *m/z* calcd for $C_{12}H_{13}NO_4$: 235.0845; found: 235.0850.

4-Methyl-2-oxo-3-phenyl-2,3-dihydrooxazole-5-carbaldehyde (30a). Method A: In a round-bottom flask (100 mL) equipped with a magnetic stirring bar, **29a** (0.110 g, 0.54 mmol) and IBX (0.760 g, 2.70 mmol) in DMSO (20 mL) were mixed at rt and stirred for 24 h. The mixture was washed with water (2 x 5 mL) and extracted with EtOAc (2 x 5 mL). The organic layer was dried with Na_2SO_4 and the solvent was removed under vacuum. The residue was purified by column chromatography over silica gel (30 g/g crude, hexane/EtOAc, 8:2) to provide **30a** (0.07 g, 64 %) as a brown solid. **Method B:** In a round-bottom flask (50 mL) equipped with a magnetic stirring bar, a mixture of DMF (0.042 g, 0.57 mmol) and $POCl_3$ (0.097 g, 0.63 mmol) under N_2 atmosphere at 0 ºC was

J. Mex. Chem. Soc. **2025**, *69*(4)
Regular Issue

ISSN-e 2594-0317

stirred for 30 min. Subsequently, **32a** (0.100 g, 0.46 mmol) dissolved in CH_2Cl_2 (3 mL) was added dropwise and the mixture was stirred at rt for 24 h. The mixture was neutralized with a 5% aqueous solution of NaOH at 0 ºC and extracted with CH_2Cl_2 (4 x 10 mL). The organic layer was dried with Na_2SO_4 and the solvent was removed under vacuum. The residue was purified by column chromatography over silica gel (40 g/g crude, hexane/EtOAc, 8:2) to yield **30a** (0.03 g, 51%) as a brown solid. R*f* 0.18 (hexane/EtOAc, 7:3); mp 154–155 °C. IR (film): $\bar{\upsilon}$ = 1776, 1723, 1667, 1499, 1401, 1332, 1270, 1056, 729 cm^{-1}. ^1H NMR (600 MHz, DMSO-d_6): δ 2.26 (s, 3H, CH_3-C4), 7.52–7.56 (m, 3H, H-2', H-4'), 7.57–7.60 (m, 2H, H-3'), 9.58 (s, 1H, C*H*O). ^{13}C NMR (150 MHz, DMSO-d_6): δ 8.9 (*C*H_3-C4), 127.6 (C-2'), 129.5 (C-4'), 129.6 (C-3'), 132.0 (C-1'), 134.3 (C-5), 141.4 (C-4), 152.0 (C-2), 175.1 (*C*HO). HRMS (ESI, $[M + H]^+$): *m/z* calcd for $C_{11}H_{10}NO_3$: 204.0661; found: 204.0626.

4-Methyl-2-oxo-3-(*p*-tolyl)-2,3-dihydrooxazole-5-carbaldehyde (30b). Method A: Following method A for preparing **30a**, a mixture of **29b** (0.100 g, 0.46 mmol) and IBX (0.638 g, 2.28 mmol) in DMSO (10 mL) resulted in **30b** (0.074 g, 75 %) as a brown solid. **Method B:** Following method B for preparing **30a**, a mixture of DMF (0.039 g, 0.53 mmol), $POCl_3$ (0.088 g, 0.57 mmol), and **32b** (0.050 g, 0.26 mmol) led to **30b** (0.028 g, 48 %) as a brown solid. R*f* 0.21 (hexane/EtOAc, 7:3); mp 141–142 °C. IR (film): $\bar{\upsilon}$ = 2925, 1773, 1668, 1516, 1408, 1337, 1271, 1062, 990, 741 cm^{-1}. ^1H NMR (500 MHz, DMSO-d_6): δ 2.24 (s, 3H, CH_3-C4), 2.38 (s, 3H, CH_3Ar), 7.35–7.38 (m, 2H, H-3'), 7.39–7.42 (m, 2H, H-2'), 9.57 (s, 1H, C*H*O). ^{13}C NMR (125 MHz, DMSO-d_6): δ 8.9 (*C*H_3-C4), 20.7 (*C*H_3Ar), 127.4 (C-2'), 129.4 (C-1'), 130.0 (C-3'), 134.2 (C-5), 139.3 (C-4'), 141.6 (C-4), 152.1 (C-2), 175.0 (*C*HO). HRMS (EI, $[M^+]$) *m/z* calcd for $C_{12}H_{11}NO_3$: 217.0739; found: 217.0736.

3-(4-methoxyphenyl)-4-methyl-2-oxo-2,3-dihydrooxazole-5-carbaldehyde (30c). Method A: Following method A for preparing **30a**, a mixture of **29c** (0.30 g, 1.3 mmol) and IBX (1.76 g, 6.3 mmol) in DMSO (20 mL) gave **30c** (0.205 g, 69 %) as a brown solid. **Method B:** Following method B for preparing **30a**, a mixture of DMF (0.035 g, 0.48 mmol), $POCl_3$ (0.082 g, 0.54 mmol), and **32c** (0.050 g, 0.24 mmol) generated **30c** (0.032 g, 56 %) as a brown solid. R*f* 0.16 (hexane/EtOAc, 7:3); mp 162–163 °C. IR (film): $\bar{\upsilon}$ = 2931, 1771, 1667, 1516, 1404, 1337, 1301, 1252, 1143, 1029, 837, 746 cm^{-1}. ^1H NMR (600 MHz, DMSO-d_6): δ 2.23 (s, 3H, CH_3-C4), 3.82 (s, 3H, CH_3O), 7.08–7.12 (m, 2H, H-3'), 7.43–7.47 (m, 2H, H-2'), 9.56 (s, 1H, C*H*O). ^{13}C NMR (150 MHz, DMSO-d_6): δ 8.9 (*C*H_3-C4), 55.5 (*C*H_3O), 114.8 (C-3'), 124.4 (C-1'), 129.0 (C-2'), 134.2 (C-5), 141.9 (C-4), 152.3 (C-2), 159.8 (C-4'), 175.0 (*C*HO). HRMS (EI, $[M^+]$): *m/z* calcd for $C_{12}H_{11}NO_4$: 233.0688; found: 233.0691.

6-Acetyl-3-(*p*-tolyl)-4,5-dihydrobenzo[*d*]oxazol-2(3*H*)-one (31b). In a round-bottom flask (50 mL) equipped with a magnetic stirring bar, KO*t*-Bu (0.048 g, 0.43 mmol) was added to a solution of **30b** (0.050 g, 0.23 mmol) in anhydride THF (10 mL) under N_2 atmosphere at -78 ºC and stirred for 40 min. Then, MVK (0.031 g, 0.44 mmol) was added dropwise and the mixture was stirred for 1 h, then at 0 ºC for 30 min before removing the solvent under vacuum. The residue was purified by column chromatography over silica gel (30 g/g crude, hexane/EtOAc, 8:2) to produce **31b** (0.013 g, 21 %) as a yellow solid. R*f* 0.31 (hexane/EtOAc, 7:3); mp 113–116 °C. IR (film): $\bar{\upsilon}$ = 2924, 1770, 1668, 1644, 1570, 1516, 1422, 1371, 1322, 1288, 1218, 1004, 819, 748 cm^{-1}. ^1H NMR (600 MHz, $CDCl_3$): δ 2.37 (s, 3H, CH_3CO), 2.40 (s, 3H, CH_3Ar), 2.66 (br t, *J* = 9.9 Hz, 2H, H-4), 2.79 (br t, *J* = 9.9 Hz, 2H, H-5), 7.12 (br s, 1H, H-7), 7.22–7.24 (m, 2H, H-2'), 7.27–7.30 (m, 2H, H-3'). ^{13}C NMR (150 MHz, $CDCl_3$): δ 19.9 (C-4), 20.9 (C-5), 21.1 (*C*H_3Ar), 24.9 (*C*H_3CO), 124.2 (C-7), 124.9 (C-2'), 128.6 (C-3a), 130.2 (C-3'), 130.5 (C-1'), 131.4 (C-6), 134.1 (C-7a), 138.6 (C-4'), 154.1 (C-2), 196.2 (CH_3*C*O). HRMS (ESI, $[M + H]^+$): *m/z* calcd for $C_{16}H_{16}NO_3$: 270.1130; found: 270.1080.

6-Acetyl-3-(4-methoxyphenyl)-4,5-dihydrobenzo[*d*]oxazol-2(3*H*)-one (31c). Following the method for preparing **31b**, a mixture of **30c** (0.050 g, 0.21 mmol), KO*t*-Bu (0.043 g, 0.38 mmol), and MVK (0.028 g, 0.40 mmol) afforded **31c** (0.014 g, 22 %) as a yellow solid. R*f* 0.35 (hexane/EtOAc, 7:3); mp 168–170 °C. IR (film): $\bar{\upsilon}$ = 2933, 1770, 1669, 1644, 1570, 1515, 1372, 1288, 1252, 1218, 1029, 1002, 834 cm^{-1}. ^1H NMR (600 MHz, $CDCl_3$): δ 2.37 (s, 3H, CH_3CO), 2.64 (br t, *J* = 9.9 Hz, 2H, H-4), 2.79 (br t, *J* = 9.9 Hz, 2H, H-5), 3.84 (s, 3H, CH_3O), 6.98–7.01 (m, 2H, H-3'), 7.12 (br s, 1H, H-7), 7.25–7.28 (m, 2H, H-2'). ^{13}C NMR (150 MHz, $CDCl_3$): δ 19.8 (C-4), 20.9 (C-5), 24.9 (*C*H_3CO), 55.6 (*C*H_3O), 114.9 (C-3'), 124.3 (C-7), 125.7 (C-1'), 126.6 (C-2'), 128.9 (C-3a), 131.3 (C-6), 134.0 (C-7a), 154.3 (C-2), 159.5 (C-4'), 196.3 (CH_3*C*O). HRMS (EI, $[M^+]$): *m/z* calcd for $C_{16}H_{15}NO_4$: 285.1001; found: 285.1011.

J. Mex. Chem. Soc. **2025**, *69*(4)
Regular Issue

ISSN-e 2594-0317

(*E*)-3-((3-Methoxyphenyl)imino)butan-2-one (11c). In a round-bottom flask (250 mL) equipped with a magnetic stirring bar, a mixture of **4a** (0.98 g, 11.4 mmol) and *m*-anisidine (1.40 g, 11.4 mmol) in MeOH (150 mL) was stirred under N_2 atmosphere at rt for 24 h. The solvent was removed under vacuum and the residue was purified by column chromatography over silica gel (10 g/g crude, hexane/EtOAc, 98:2) to furnish **11c** (1.63 g, 75 %) as a yellow oil. R*f* 0.75 (hexane/EtOAc, 80:20). IR (film): $\bar{\upsilon}$ = 2938, 1698, 1504, 1243, 1033, 841 cm^{-1}. ^1H NMR (300 MHz, $CDCl_3$): δ 1.97 (s, 3H, H-4), 2.51 (s, 3H, H-1), 3.81 (s, 3H, C*H*$_3$O), 6.30–6.37 (m, 2H, H-2', H-4'), 6.66–6.72 (m, 1H, H-6'), 7.23–7.31 (m, 1H, H-5'). ^{13}C NMR (75.4 MHz, $CDCl_3$): δ 14.0 (C-4), 24.5 (C-1), 55.2 (*C*H$_3$O), 104.3 (C-2'), 110.0 (C-4'), 110.6 (C-6'), 129.9 (C-5'), 150.8 (C-1'), 160.2 (C-3'), 166.1 (C-3), 200.3 (C-2). MS (70 eV): *m/z* 191 (M^+, 6), 162 (10), 148 (100), 108 (13), 92 (24), 77 (9), 63 (20). HRMS (EI, $[M]^+$): *m/z* calcd for $C_{11}H_{13}NO_2$: 191.0946; found: 191.0956.

1-(3-Methoxyphenyl)-4,5-dimethylene-3-(*p*-tolyl)imidazolidin-2-one (16c). In a round-bottom flask (100 mL) equipped with a magnetic stirring bar, a mixture of **11c** (0.499 g, 2.61 mmol), dried Li_2CO_3 (1.93 g, 26.1 mmol), and dried Et_3N (0.659 g, 6.53 mmol) in anhydrous PhMe (30 mL) was stirred at rt under N_2 atmosphere in the dark for 90 min. Subsequently, a solution of **5b** (1.04 g, 7.83 mmol) in PhMe (10 mL) was added dropwise, and the mixture was stirred at rt for 24 h. The mixture was filtered over Celite and washed with CH_2Cl_2 (3 x 20 mL), and the solvent was removed under vacuum. The residue was purified by column chromatography over silica gel (10 g/g crude, hexane/EtOAc, 95:5) to provide **16c** (0.610 g, 76%) as a white solid. R*f* 0.65 (hexane/EtOAc, 80:20); mp 112–113 °C. IR (film): $\bar{\upsilon}$ = 1737, 1604, 1517, 1494, 1399, 1267, 1044, 818, 756 cm^{-1}. ^1H NMR (300 MHz, $CDCl_3$): δ 2.39 (s, 3H, C*H*$_3$Ar), 3.82 (s, 3H, C*H*$_3$O), 4.32 (d, *J* = 2.4 Hz, 1H, =C*H*), 4.39 (d, *J* = 2.4 Hz, 1H, =C*H*), 4.79 (d, *J* = 2.4 Hz, 1H, =C*H*), 4.82 (d, *J* = 2.4 Hz, 1H, =C*H*), 6.91 (dm, *J* = 8.1 Hz, 1H, H-4'), 6.95 (dd, *J* = 2.4, 2.1 Hz, 1H, H-2'), 6.99 (dm, *J*= 8.1 Hz, 1H, H-6'), 7.28 (s, 4H, H-2", H-3"), 7.37 (t, *J* = 8.1 Hz, 1H, H-5'). ^{13}C NMR (75.4 MHz, $CDCl_3$): δ 21.2 (*C*H$_3$Ar), 55.4 (*C*H$_3$O), 82.7 (*C*H$_2$=), 82.9 (*C*H$_2$=), 112.9 (C-2'), 114.0 (C-4'), 119.7 (C-6'), 127.3 (C-2"), 130.0 (C-5'), 130.1 (C-3"), 131.5 (C-1"), 135.3 (C-1'), 137.9 (C-4"), 140.0 (C-4 or C-5), 140.2 (C-5 or C-4), 153.5 (C-2), 160.3 (C-3'). HRMS (EI, $[M]^+$): *m/z* calcd for $C_{19}H_{18}N_2O_2$: 306.1368; found: 306.1376.

1,3,6-Triphenyl-4,4a,7a,8-tetrahydroimidazo[4,5-*f*]isoindole-2,5,7(1*H*,3*H*,6*H*)-trione (**33a**) [21]. In a round-bottom flask (100 mL) equipped with a magnetic stirring bar, a mixture of **15a** (0.05 g, 0.19 mmol) and **19** (0.036 g, 0.21 mmol) in anhydrous CH_2Cl_2 (20 mL) was stirred at 0 ºC under N_2 atmosphere for 1 h. The solvent was removed under vacuum, and the residue was purified by column chromatography over silica gel (20 g/g crude, hexane/EtOAc, 8:2), leading to **33a** (0.075 g, 90%) as a pale green solid. R*f* 0.20 (hexane/EtOAc, 7:3); mp 128–129 °C [Lit. [21] 128–129 °C].

1-(4-Methoxyphenyl)-3,6-diphenyl-4,4a,7a,8-tetrahydroimidazo[4,5-*f*]isoindole-2,5,7(1*H*,3*H*,6*H*)-trione (**33b**). Following the procedure for **33a**, a mixture of **16a** (0.10 g, 0.34 mmol) and **19** (0.065 g, 0.38 mmol) yielded **33b** (0.151 g, 95 %) as a pale green solid. R*f* 0.40 (hexane/EtOAc, 1:1); mp 107–108 °C. IR (KBr): $\bar{\upsilon}$ = 2917, 1710, 1514, 1501, 1383, 1250, 1170, 1028, 838, 735, 693 cm^{-1}. ^1H NMR (500 MHz, $CDCl_3$): δ 2.74–2.86 (m, 2H, H-4, H-8), 3.05 (d, *J* = 16.0 Hz, 1H, H-4 or H-8), 3.10 (d, *J* = 15.0 Hz, 1H, H-8 or H-4), 3.42–3.52 (m, 2H, H-4a, H-7a), 3.82 (s, 3H, C*H*$_3$O), 6.97 (d, *J* = 8.5 Hz, 2H, H-3'), 7.23–7.30 (m, 4H, H-2', 2ArH), 7.30–7.50 (m, 8H, PhH). ^{13}C NMR (125 MHz, $CDCl_3$): δ 19.9 (C-4 or C-8), 20.0 (C-8 or C-4), 38.7 (C-4a or C-7a), 38.8 (C-7a or C-4a), 55.5 (*C*H$_3$O), 114.5 (C-3'), 114.6 (C-3a or C-8a), 115.6 (C-8a or C-3a), 126.1 (2ArH), 126.2 (2ArH), 126.9 (C-1'), 127.4 (ArH), 127.6 (2ArH), 128.7 (ArH), 129.2 (2ArH), 129.3 (2ArH), 131.7 (C-1" or C-1'"), 134.5 (C-1'" or C-1"), 152.4 (C-2), 158.9 (C-4'), 177.8 (C-5, C-7). MS (70 eV): *m/z* 465 (M^+, 58), 444 (77), 415 (43), 339 (26), 321 (36), 291 (59), 217 (54), 122 (91), 53 (100). HRMS (EI, $[M^+]$): *m/z* calcd for $C_{28}H_{23}N_3O_4$: 465.1689; found: 465.1692.

1-(4-Chlorophenyl)-3,6-diphenyl-4,4a,7a,8-tetrahydroimidazo[4,5-*f*]isoindole-2,5,7(1*H*,3*H*,6*H*)-trione (**33c**). Following the procedure for **33a**, a mixture of **16b** (0.100 g, 0.34 mmol) and **19** (0.059 g, 0.34 mmol) gave **33c** (0.146 g, 92 %) as a pale green solid. R*f* 0.40 (hexane/EtOAc, 1:1); mp 112–113 °C. IR (film): $\bar{\upsilon}$ = 2970, 2932, 1735, 1708, 1596, 1505, 1388, 1279, 1059 cm^{-1}. ^1H NMR (300 MHz, $CDCl_3$): δ 2.74–2.90 (m, 2H, H-4, H-8), 3.06–3.18 (m, 2H, H-4, H-8), 3.43–3.58 (m, 2H, H-4a, H-7a), 7.25–7.53 (m, 14H, ArH). ^{13}C NMR (75.4 MHz, $CDCl_3$): δ 19.9 (C-4 or C-8), 20.0 (C-8 or C-4), 38.6 (C-4a or C-7a), 38.7 (C-7a or C-4a), 114.9 (C-3a or C-8a). 115.6 (C-8a or C-3a), 126.1 (4ArH), 127.2 (2ArH), 127.6 (ArH), 128.8 (C-4"), 129.2 (2ArH),

J. Mex. Chem. Soc. **2025**, *69*(4)
Regular Issue

ISSN-e 2594-0317

129.4 (2ArH), 129.5 (2ArH), 131.5 (Ar), 132.8 (Ar), 133.1 (Ar), 134.0 (Ar), 151.9 (C-2), 177.7 (C-5, C-7). HRMS (EI, [M^+]): *m/z* calcd for $C_{27}H_{20}N_3O_3Cl$: 469.1193; found: 469.1184.

1-(3-Methoxyphenyl)-6-phenyl-3-(*p*-tolyl)-4,4a,7a,8-tetrahydroimidazo[4,5-*f*]isoindole-2,5,7(1*H*,3*H*,6*H*)-trione (**33d**). Following the procedure for **33a**, a mixture of **16c** (0.150 g, 0.49 mmol) and **19** (0.093 g, 0.54 mmol) generated **33d** (0.174 g, 74 %) as a white solid. R*f* 0.21 (hexane/EtOAc, 70:30); mp 175–176 °C. IR (film): $\bar{\upsilon}$ = 1717, 1632, 1517, 1411, 1397, 1255, 1131, 853, 820, 785 cm^{-1}. ^1H NMR (500 MHz, $CDCl_3$): δ 2.38 (s, 3H, C*H*$_3$), 2.75–2.88 (m, 2H, H-4, H-8), 3.06 (br d, *J* = 15.0 Hz, 1H, H-4 or H-8), 3.13 (br d, *J* =16.0 Hz, H-8 or H-4), 3.41–3.43 (m, 2H, H-4a, H-7a), 3.80 (s, 3H, C*H*$_3$O), 6.87–6.92 (m, 1H, H-4'), 6.89–6.96 (m, 2H, H-2', H-6'), 7.20–7.52 (m, 10H, Ar-H). ^{13}C NMR (125 MHz, $CDCl_3$): δ 19.9 (C-4 or C-8), 20.0 (C-8 or C-4). 21.1 (*C*H$_3$), 38.7 (C-4a or C-7a), 38.8 (C-7a or C-4a), 55.4 (*C*H$_3$O), 111.7 (C-2'), 113.7 (C-4'), 115.0 (C-3a or C-8a), 115.4 (C-8a or C-3a), 118.3 (C-6'), 126.1 (2ArH), 126.2 (2ArH), 128.8 (C-4"), 129.2 (2ArH), 130.0 (2ArH), 130.1 (Ar-H), 131.5 (Ar), 131.6 (Ar), 135.3 (Ar), 137.6 (Ar), 152.2 (C-2), 160.3 (C-3'), 177.7 (C-5 or C-7), 177.8 (C-7 or C-5). HRMS (EI, [M^+]): *m/z* calcd for $C_{28}H_{23}N_3O_4$: 465.1689; found: 465.1652.

1,3-Diphenyl-4,9-dihydro-1*H*-naphtho[2,3-*d*]imidazol-2(3*H*)-one (35a). In a round-bottom flask (50 mL) equipped with a magnetic stirring bar, TBAF in furane (1.0 M) (0.120 g, 0.46 mmol) was added dropwise at 0 ºC under N_2 atmosphere to a mixture of **15a** (0.080 g, 0.31 mmol) and **34** (0.091 g, 0.31 mmol) in anhydrous CH_2Cl_2 (2 mL), stirring it in the dark for 24 h while it rose from 0 ºC to rt. The solvent was removed under vacuum, and the residue was purified by column chromatography over silica gel (10 g/g crude, hexane/EtOAc, 85:15) to obtain **35a** (0.058 g, 56%) as a white solid. R*f* 0.61 (hexane/EtOAc, 80:20); mp 211–212 ºC. IR (film): $\bar{\upsilon}$ = 1727, 1681, 1596, 1497, 1470, 1394, 1242, 1182, 1024, 857, 740, 692 cm^{-1}. ^1H NMR (300 MHz, $CDCl_3$): δ 3.76 (s, 4H, H-4, H-9), 7.18 (br s, 6H, H-6, H-7, H-2', H-2"), 7.34–7.40 (m, 2H, H-4', H-4"), 7.40–7.54 (m, 8H, H-5, H-8, H-3', H-3", H-1', H-1"). ^{13}C NMR (75.4 MHz, $CDCl_3$): δ 26.6 (C-4, C-9), 115.2 (C-3a, C-9a), 126.4 (C-2', C-2", C-6, C-7), 127.3 (C-4', C-4"), 129.2 (C-3', C-3"), 129.3 (C-5, C-8), 131.8 (C-4a, C-8a), 135.1 (C-1', C-1"), 152.4 (C-2). HRMS (EI, [M^+]): *m/z* calcd for $C_{23}H_{18}N_2O$: 338.1419; found: 338.1422.

1-Phenyl-3-(*p*-tolyl)-4,9-dihydro-1*H*-naphtho[2,3-*d*]imidazol-2(3*H*)-one (35b). Following the procedure for **35a**, a mixture of **16d** (0.100 g, 0.36 mmol), **34** (0.108 g, 0.36 mmol), and TBAF in furane (1.0 M) (0.141 g, 0.54 mmol) produced **35b** (0.076 g, 60 %) as a white solid. R*f* 0.50 (hexane/EtOAc, 1:1); 189–190 °C. IR (film): $\bar{\upsilon}$ = 1726, 1680, 1603, 1518, 1501, 1473, 1398, 1246, 1175, 859, 738 cm^{-1}. ^1H NMR (300 MHz, $CDCl_3$): δ 2.42 (s, 3H, C*H*$_3$), 3.76 (s, 4H, H-4, H-9), 7.20 (br s, 4H, ArH), 7.26–7.44 (m, 5H, ArH), 7.46–7.54 (m, 4H, ArH). ^{13}C NMR (75.4 MHz, $CDCl_3$): δ 21.1 (*C*H$_3$), 26.5 (C-4 or C-9), 26.6 (C-9 or C-4), 115.0 (C-9a or C-3a), 115.4 (C-3a or C-9a), 126.4 (4ArH), 126.5 (2ArH), 127.3 (ArH), 129.2 (2ArH), 129.3 (2ArH), 129.9 (2ArH), 131.8 (Ar), 131.9 (Ar), 132.3 (Ar), 135.1 (Ar), 137.3 (C-4"), 152.5 (C-2). HRMS (EI, [M^+]): *m/z* calcd for $C_{24}H_{20}N_2O$: 352.1576; found: 352.1568.

1,3,6-Triphenylimidazo[4,5-*f*]isoindole-2,5,7(1*H*,3*H*,6*H*)-trione (36a). A mixture of **33a** (0.070 g, 0.16 mmoles) and DDQ (0.073 g, 0.32 mmol) in anhydrous CH_2Cl_2 (15 mL) was stirred at 20 ºC under N_2 atmosphere for 24 h. The mixture was filtered over a mixture of Celite/silica gel (3:5 g) with CH_2Cl_2. The solvent was removed under vacuum, and the residue was purified by column chromatography over silica gel (20 g/g crude, hexane/EtOAc, 95:5) to provide **36a** (0.058 g, 90%) as a white solid. R*f* 0.52 (hexane/EtOAc, 1:1); mp 190–191 °C. IR (KBr): $\bar{\upsilon}$ = 1727, 1593, 1498, 1383, 1272, 1105, 756, 692 cm^{-1}. ^1H NMR (500 MHz, $CDCl_3$): δ 7.37–7.41 (m, 1H, ArH), 7.42–7.45 (m, 2H, ArH), 7.47–7.54 (m, 4H, ArH), 7.58–7.64 (m, 8H, ArH), 7.62 (s, 2H, H-4, H-8). ^{13}C NMR (125 MHz, $CDCl_3$): δ 104.4 (C-4, C-8), 126.3 (C-2', C-2"), 126.4 (C-4a, C-7a), 126.4 (C-2'"), 127.9 (C-4'"), 128.9 (2ArH), 129.1 (2ArH), 130.0 (C-3', C-3"), 131.8 (C-1'"), 133.2 (C-1', C-1"), 134.3 (C-3a, C-8a), 152.3 (C-2), 167.1 (C-5, C-7). HRMS (EI, [M^+]): *m/z* calcd for $C_{27}H_{17}N_3O_3$: 431.1270; found: 431.1261.

1-(4-Methoxyphenyl)-3,6-diphenylimidazo[4,5-*f*]isoindole-2,5,7(1*H*,3*H*,6*H*)-trione (36b). Following the procedure for **36a**, a mixture of **33b** (0.100 g, 0.21 mmol) and DDQ (0.098 g, 0.43 mmol) yielded **36b** (0.074 g, 75 %) as a yellow solid. R*f* 0.53 (hexane/EtOAc, 1:1); mp 135–136 °C. IR (film): $\bar{\upsilon}$ = 1738, 1592, 1483, 1395, 1264, 1236, 824, 780 cm^{-1}. ^1H NMR (300 MHz, $CDCl_3$): δ 3.90 (s, 3H, C*H*$_3$O), 7.08–7.14 (m, 2H, H-3'), 7.35–7.54 (m, 8H, ArH), 7.56 (s, 1H, H-4 or H-8), 7.58–7.66 (m, 5H, H-4 or H-8, ArH). ^{13}C NMR (75.4 MHz, $CDCl_3$): δ 55.6 (*C*H$_3$O), 104.2 (C-4 or C-8), 104.3 (C-8 or C-4), 115.2 (C-3'), 125.6 (Ar), 126.2 (2ArH), 126.40

J. Mex. Chem. Soc. **2025**, *69*(4)
Regular Issue

ISSN-e 2594-0317

(Ar), 126.42 (ArH), 127.7 (2ArH), 127.9 (2ArH), 128.9 (2ArH), 129.1 (2ArH), 130.0 (2ArH), 131.7 (Ar), 133.3 (Ar), 134.1 (Ar), 134.8 (Ar), 152.5 (C-2), 159.8 (C-4'), 167. 2 (C-5, C-7). HRMS (EI, [M^+]): *m/z* calcd for $C_{28}H_{19}N_3O_4$: 461.1376; found: 461.1381.

1-(4-Chlorophenyl)-3,6-diphenylimidazo[4,5-*f*]isoindole-2,5,7(1*H*,3*H*,6*H*)-trione (36c). Following the procedure for **36a**, a mixture of **33c** (0.071 g, 0.15 mmol) and DDQ (0.069 g, 0.30 mmol) gave **36c** (0.071 g, 72 %) as a yellow solid. R*f* 0.61 (hexane/EtOAc, 1:1); p.f. 117–118 °C. IR (film): $\bar{\upsilon}$ = 1734, 1708, 1596, 1519, 1505, 1387, 1277, 1059, 874, 751 cm^{-1}. ^1H NMR (300 MHz, $CDCl_3$): δ 7.39–7.47 (m, 3H, Ar-H), 7.48–7.67 (m, 13H, Ar-H). ^{13}C NMR (75.4 MHz, $CDCl_3$): δ 104.2 (C-4 or C-8), 104.5 (C-8 or C-4), 126.2 (2Ar-H), 126.4 (2ArH), 126.5 (Ar), 126.6 (Ar), 127.5 (2ArH), 128.0 (ArH), 129.0 (ArH), 129.1 (2ArH), 130.1 (2ArH), 130.2 (2ArH), 131.6 (Ar), 131.7 (Ar), 133.0 (Ar), 133.8 (Ar), 134.3 (C-3a or C-8a), 134.7 (C-8a or C-3a), 152.1 (C-2), 167.0 (C-5, C-7). HRMS (EI, [M^+]): *m/z* calcd for $C_{27}H_{16}N_3O_3Cl$: 465.0880; found: 465.0875.

1-(3-Methoxyphenyl)-6-phenyl-3-(*p*-tolyl)imidazo[4,5-*f*]isoindole-2,5,7(1*H*,3*H*,6*H*)-trione (36d). Following the procedure for **36a**, a mixture of **33d** (0.100 g, 0.21 mmol) and DDQ (0.098 g, 0.43 mmol) furnished **36d** (0.074 g, 75 %) as a yellow solid. R*f* 0.50 (hexane/EtOAc, 1:1); mp 113–114 °C. IR (film): $\bar{\upsilon}$ = 1730, 1710, 1600, 1499, 1385, 1281, 1111, 762, 688 cm^{-1}. ^1H NMR (500 MHz, $CDCl_3$): δ 2.47 (s, 3H, C*H*$_3$), 3.87 (s, 3H, C*H*$_3$O), 7.05 (ddd, *J* = 8.4, 2.7, 0.9 Hz, 1H, H-4'), 7.11–7.18 (m, 2H, H-2', H-6'), 7.37–7.54 (m, 10H, H-5', H-2", H-3", PhH), 7.57 (d, *J* = 0.5 Hz, 1H, H-4 or H-8), 7.64 (d, *J* = 0.5 Hz, 1H, H-8 or H-4). ^{13}C NMR (125 MHz, $CDCl_3$): δ 21.2 (*C*H$_3$), 55.5 (*C*H$_3$O), 104.3 (C-4 or C-8), 104.4 (C-8 or C-4), 112.1 (C-6'), 114.7 (C-4'), 118.2 (C-2'), 126.1 (2ArH), 126.2 (Ar), 126.3 (Ar), 126.4 (2ArH), 127.9 (ArH), 129.1 (2ArH), 130.4 (Ar), 130.5 (2ArH), 130.5 (ArH), 131.7 (Ar), 134.1 (Ar), 134.2 (Ar), 134.4 (Ar), 139.1 (Ar), 152.3 (C-2), 160.7 (C-3'), 167.2 (C-5, C-7). HRMS (EI, [M^+]): *m/z* calcd for $C_{29}H_{21}N_3O_4$: 475.1532; found: 475.1537.

1,3-Diphenyl-1*H*-naphtho[2,3-*d*]imidazol-2(3*H*)-one (37a). A mixture of **35a** (0.086 g, 0.25 mmol) and DDQ (0.114 g, 0.50 mmol) in anhydrous CH_2Cl_2 (5 mL) was stirred under N_2 atmosphere at rt for 24 h. The mixture was filtered over Celite and washed with CH_2Cl_2 (15 mL). The filtered solution was concentrated under vacuum, and the residue purified by column chromatography over silica gel (10 g/g of crude, hexane/EtOAc, 8:2) to deliver **37a** (0.084 g, 99 %) as a white solid. R$_f$ 0.52 (hexane/EtOAc, 8:2); mp 211–212 °C. IR (film): $\bar{\upsilon}$ = 1728, 1497, 1471, 1394, 1245, 743, 692 cm^{-1}. ^1H NMR (300 MHz, $CDCl_3$): δ 7.32–7.39 (m, 2H, H-6, H-7), 7.42–7.49 (m, 4H, H-4, H-9, H-4', H-4"), 7.55–7.63 (m, 4H, H-3', H-3"), 7.64–7.70 (m, 4H, H-2', H-2"), 7.70–7.78 (m, 2H, H-5, H-8). ^{13}C NMR (75.4 MHz, $CDCl_3$): δ 104.7 (C-4, C-9), 124.5 (C-6, C-7), 126.3 (C-2', C-2"), 127.2 (C-5, C-8), 127.9 (C-4', C-4"), 129.6 (C-3', C-3"), 130.0 (C-3a, C-9a), 130.3 (C-4a, C-8a), 134.5 (C-1'), 134.7 (C-1"), 153.1 (C-2). HRMS (EI, [M^+]): *m/z* calcd for $C_{23}H_{16}N_2O$: 336.1263; found: 336.1267.

1-Phenyl-3-(*p*-tolyl)-1*H*-naphtho[2,3-*d*]imidazol-2(3*H*)-one (37b). Following the procedure for **37a**, a mixture of **35b** (0.080 g, 0.23 mmol) and DDQ (0.104 g, 0.46 mmol) in CH_2Cl_2 (15 mL) resulted in **37b** (0.077 g, 97 %) as a white solid. R$_f$ 0.55 (hexane/EtOAc, 1:1); mp 178–179 °C. IR (film): $\bar{\upsilon}$ = 1727, 1603, 1518, 1502, 1472, 1397, 1246, 1176, 856, 744 cm^{-1}. ^1H NMR (300 MHz, $CDCl_3$): δ 2.46 (s, 3H, ArC*H*$_3$), 7.33–7.38 (m, 2H, H-6, H-7), 7.38–7.42 (m, 3H, H-4 or H-9, H-3"), 7.45 (s, 1H, H-9 or H-4), 7.42–7.49 (m, 1H, H-4'), 7.51–7.56 (m, 2H, H-2"), 7.56–7.63 (m, 2H, H-3'), 7.65–7.70 (m, 2H, H-2'), 7.71–7.78 (m, 2H. H-5, H-8). ^{13}C NMR (75.4 MHz, $CDCl_3$): δ 21.2 (Ar*C*H$_3$), 104.7 (C-4, C-9), 124.4 (C-6 or C-7), 124.5 (C-7 or C-6), 126.2 (C-2"), 126.3 (C-2'), 127.1 (C-5 or C-8), 127.2 (C-8 or C-5), 127.9 (C-4'), 129.6 (C-3'), 129.9 (Ar), 130.0 (Ar), 130.26 (C-3"), 130.29 (Ar), 130.6 (Ar), 131.7 (Ar), 134.5 (Ar), 138.0 (C-4"), 153.2 (C-2). HRMS (EI, [M^+]): *m/z* calcd for $C_{24}H_{18}N_2O$: 350.1419; found: 350.1418.

Results and discussion

Regioselective functionalization of exo-oxazolidin-2-one dienes 1 and 2

The previously reported method [7,10] was applied for the preparation of dienes **1a**–**c**, which were submitted to the Brønsted acid-catalyzed addition of a series of nucleophiles (Table 1). Thus, the addition of MeOH/HCl at room temperature (rt) for 1 h provided the series of 4-oxazolin-2-ones **22a**–**c** in good yields

J. Mex. Chem. Soc. **2025**, *69*(4)
Regular Issue

ISSN-e 2594-0317

(entries 1–3), while the addition of acetic acid furnished the series **23a**–**c** in moderate to good yields (entries 4–6). Regarding the addition of 4-chlorothiophenol (**21c**) to afford the series of 4-oxazolin-2-ones **24a**–**c**, the optimal catalyst (phosphoric acid) rendered satisfactory yields (entries 7–9).

Table 1. Acid-catalyzed addition of nucleophiles **21a**–**c** to dienes **1a**–**c** to prepare the series of 4-oxazolin-2-ones **22a**–**c**, **23a**–**c**, and **24a**–**c**.[a]

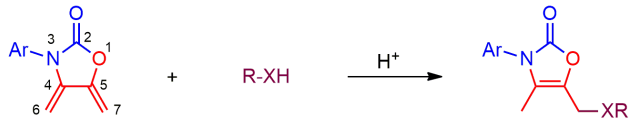

1a, Ar = Ph
1b, Ar = C_6H_4-4-Me
1c, Ar = C_6H_4-4-OMe

21a, X = O, R = Me
21b, X = O, R = Ac
21c, X = S, R = C_6H_4-4-Cl

22a–**c**, RX = OMe
23a–**c**, RX = OAc
24a–**c**, RX = SC_6H_4-4-Cl

Entry	**1**	**21**	H^+	Ar	**22**–**24**	Yield (%)[b]
1	**1a**	**21a**	HCl	Ph	**22a**	92
2	**1b**	**21a**	HCl	C_6H_4-4-Me	**22b**	83
3	**1c**	**21a**	HCl	C_6H_4-4-OMe	**22c**	84
4	**1a**	**21b**	AcOH	Ph	**23a**	95
5	**1b**	**21b**	AcOH	C_6H_4-4-Me	**23b**	81
6	**1c**	**21b**	AcOH	C_6H_4-4-OMe	**23c**	59
7	**1a**	**21c**	H_3PO_4	Ph	**24a**	60
8	**1b**	**21c**	H_3PO_4	C_6H_4-4-Me	**24b**	75
9	**1c**	**21c**	H_3PO_4	C_6H_4-4-OMe	**24c**	74

[a] Standard conditions: **1a**–**c** (1.0 mol equiv), **21a**–**c** (2.0–75.0 mol equiv), and H^+ (1.0–11.0 mol equiv), at rt, 1–24 h. For **21b** and **21c**, the reaction was performed in CH_2Cl_2. [b] Isolated yields.

Interestingly, the dienic moiety underwent a regioselective addition of the nucleophiles to the terminal C-7 carbon atom of the double bond, possibly because of the capture of the proton, liberated by the catalyst, from the terminal C-6 carbon atom of the double bond to give species **I** (Scheme 4). The latter C-4/C-6 vinyl bond is more likely to be activated by the heterocyclic nitrogen electron lone pair than is the C-5/C-7 double bond by the oxygen lone pair, which is more electronegative. This difference in reactivity was supported experimentally and by theoretical calculations in relation to the regioselective Diels-Alder additions of dienes **1a**–**c** with unsymmetrical dienophiles [7a], and to the electrophilic addition to the double bond of 4-oxazolin-2-ones **9** [28].

Due to the formation of the conjugated vinylogous iminium ion in **I**, the nucleophiles (**21a**–**c**) attack the terminal C-7 carbon atom of the C-5/C-7 vinylic moiety, which is softer [29] and less hindered than the C-4 iminium carbon atom, leading to the observed products **22**–**24**.

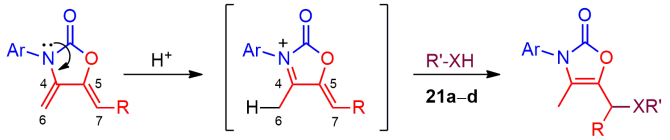

1a–**c**, R = H
2a–**c**, R = Me

I
II

22–**24**, R = H
26–**28**, R = Me

Scheme 4. Mechanism of reaction of dienes **1a**–**c** with nucleophiles **21a**–**d** to furnish 4-oxazolin-2-ones **22**–**28**.

J. Mex. Chem. Soc. **2025**, *69*(4)
Regular Issue

ISSN-e 2594-0317

Given that thiophenol **21c** was an efficient nucleophile in the addition to dienes **1a**–**c**, the reaction of phenol (**21d**) with the same dienic substrates was explored, using phosphoric acid as the catalyst and CH_2Cl_2 as the solvent (Scheme 5). In contrast to the series of **22**–**24**, where the oxygen and sulfur atoms were the nucleophilic center, the addition of **21d** took place at the *para* position of the aryl ring to provide the series of 4-oxazolin-2-ones **25a**–**c**. This is probably because of the effect of the greater softness of the aryl ring than the oxygen atom of **21d** when reacting with the soft conjugated iminium species **I**.

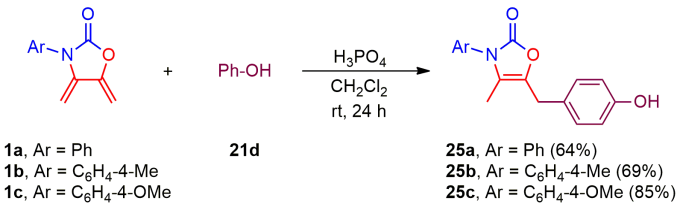

Scheme 5. Preparation of 4-oxazolin-2-ones **25a**–**c** by addition of **21d** to **1a**–**c**.

Dienes **2a**–**c** were also synthesized by the reported procedure [7,10], and their reaction with nucleophiles **21a** and **21c**–**d** was catalyzed by a Brønsted acid (Table 2). With these dienes, the addition of MeOH/HCl was carried out at –10 ºC for 24 h to avoid a larger amount of polymerization, resulting in the series of 4-oxazolin-2-ones **26a**–**c** in modest yields (entries 1–3). With diene **2c**, the mixture of adducts **26c**/**26c'** (83:17) found by ^{1}H NMR was separated and characterized. With dienes **2a** and **2b**, the ^{1}H NMR analysis of the crude reaction mixtures detected trace signals attributed to the corresponding regioisomers **26a'** and **26b'**. However, the isolation of these compounds was not viable.

Table 2. Acid-catalyzed addition of nucleophiles **21a**, **21c**, and **21d** to dienes **2a**–**c** for the preparation of the series 4-oxazolin-2-ones **26a**–**c**, **27a**–**c**, and **28a**–**c**.[a]

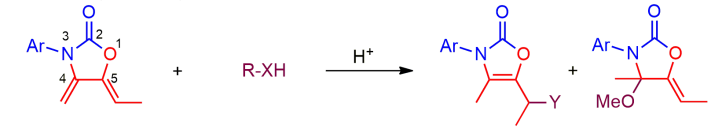

Entry	**2**	**21**	H^+	Ar	**26**–**28**	Yield (%)[b]
1	**2a**	**21a**	HCl	Ph	**26a**	67
2	**2b**	**21a**	HCl	C_6H_4-4-Me	**26b**	69
3	**2c**	**21a**	HCl	C_6H_4-4-OMe	**26c**/**26c'** (83:17)	73/15
4	**2a**	**21c**	H_3PO_4	Ph	**27a**	60
5	**2b**	**21c**	H_3PO_4	C_6H_4-4-Me	**27b**	64
6	**2c**	**21c**	H_3PO_4	C_6H_4-4-OMe	**27c**	62
7	**2a**	**21d**	H_3PO_4	Ph	**28a**	60
8	**2b**	**21d**	H_3PO_4	C_6H_4-4-Me	**28b**	67
9	**2c**	**21d**	H_3PO_4	C_6H_4-4-OMe	**28c**	64

[a] Standard conditions: **2a**–**c** (1.0 mol equiv), **21a**, **21c**, or **21d** (1.6–240.0 mol equiv), and H^+ (1.2–2.5 mol equiv), at -10–25 ºC, 1–24 h. For **21c** and **21d**, the reactions were carried out in CH_2Cl_2. [b] Isolated yields.

J. Mex. Chem. Soc. **2025**, *69*(4)
Regular Issue

ISSN-e 2594-0317

The presence of **26c'** could be explained by the plausible addition of the hard nucleophile (MeOH) to the hard C-4 iminium carbon atom of species **II** (Scheme 4). Another factor is the greater stability of the intermediate species **II** in relation to species **I**, caused by the supplementary methyl group [30].

Of course, the addition of soft nucleophiles **21c** and **21d** did not result in the C-4 addition regioisomers, but rather exclusively to the expected series of 4-oxazolin-2-ones **27a**–**c** and **28a**–**c**, respectively, in modest yields (entries 4–9). On the other hand, the addition of acetic acid (**21b**) promoted the formation of complex mixtures of products.

Conversion of 4-oxazolin-2-ones 23a–c into 4,5-dihydrobenzo[*d*]oxazol-2(3*H*)-ones 31

The satisfactory preparation of 4-oxazolin-2-ones **23a**–**c** allowed for an exploration of a further transformation in route to the construction of a fused six-membered ring, as with 4,5-dihydrobenzo[*d*]oxazol-2(3*H*)-ones **31a**–**c** (Scheme 6). The synthetic route comprised the consecutive saponification and oxidation of 4-oxazolin-2-ones **23a**–**c** to provide alcohols **29a**–**c** and aldehydes **30a**–**c**, respectively. The first step consisted of the common and efficient hydrolysis with NaOH in a mixture of MeOH/H_2O (8:2) to give the desired alcohols **29a**–**c** in high yields. Analogous alcohols prepared with reported procedures have shown great value as synthons in the construction of molecules with potential synthetic and pharmacological activity [31].

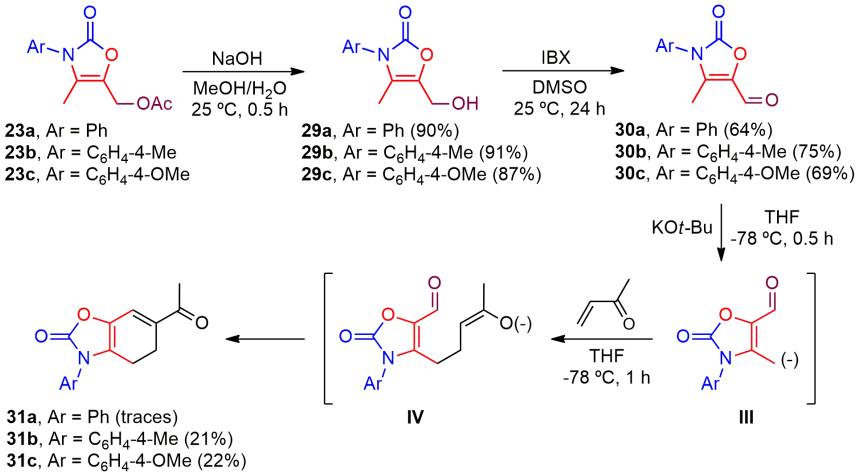

Scheme 6. Preparation of 5-formyl-4-oxazolin-2-ones **30a**–**c** and their conversion into compounds **31b**–**c**.

Although diverse reagents were employed, including PCC, PDC, MnO_2, and IBX [32], it was very difficult to establish the optimal oxidation conditions for the conversion of alcohols **29a**–**c** into aldehydes **30a**–**c**. The reaction of IBX in DMSO at rt for 24 h turned out to be the best procedure, furnishing the desired products in good yields (Scheme 6). On the other hand, the starting material was recovered with the use of PCC, and the decomposition of the substrate was observed with PDC or MnO_2.

The Staunton–Weinreb annulation is a valuable strategy for the synthesis of a six-membered ring based on the condensation of an *ortho*-toluate (as the nucleophile) with a conjugated carbonyl compound (as the electrophile), involving a Michael addition followed by a Dieckmann condensation and, if possible, a subsequent aromatization [33]. Hence, the exocyclic crotonaldehyde–like moiety of the 4-oxazolin-2-one scaffold (**30a**–**c**) was examined as a potential synthon in the construction of 4,5-dihydrobenzo[*d*]oxazol-2(3*H*)-ones **31a**–**c** through a Staunton–Weinreb–like reaction (Scheme 6).

The classical procedure of the Staunton–Weinreb cascade annulation involves a strong base, such as LDA or LiHMDS. With either of these two bases, the reaction of **30b**–**c** with MVK as the electrophile led a complex mixture of products. With the base KO*t*-Bu, the reaction provided the desired products **31b**–**c**, but in low yields. It is likely that the presence of the heteroatoms in the 4-oxazolin-2-one ring decreased the acidity of the C-4 methyl protons and consequently diminished the stability of the conjugated anion species **III**. The conjugated addition of the latter species to MVK afforded species **IV**, which underwent the Dieckmann

J. Mex. Chem. Soc. **2025**, *69*(4)
Regular Issue

ISSN-e 2594-0317

condensation to generate the isolated adducts **31b**–**c**. When the process was carried out with **30a**, the starting material was recovered and only a trace amount of the expected adduct **31a** was obtained.

Owing to the interest in insuring a readily supply of aldehydes **30a**–**c**, a shorter synthetic route was designed. Thus, the straightforward construction of the 4-oxazolin-2-ones **32a**–**c** was achieved in accordance with the previously reported methodology [15], involving a solvent-free addition/cyclization/dehydration cascade reaction between ketol **8a** and isocyanates **5a**–**c** under MW irradiation (Scheme 7). With slight modifications in the reaction conditions, such as a reduction in the MW potency (from 200 to 150 W) and an increase in the temperature (from 120 to 150 ºC) and reaction time (from 1.5 to 5.0 h), the yields of 5-formyl-4-oxazolin-2-ones **32a**–**c** were improved. The application of the usual Vilsmeier–Haack reaction conditions to **32a**–**c** gave the desired products **30a**–**c** in modest yields.

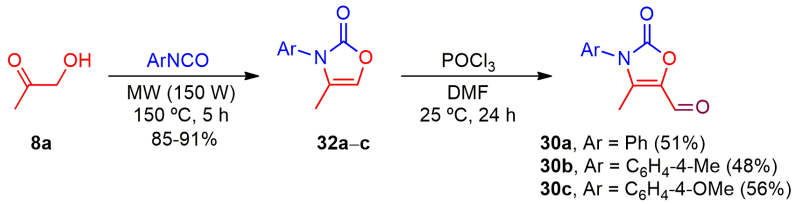

Scheme 7. Preparation of 4-oxazolin-2-ones **32a**–**c** and their conversion into aldehydes **30a**–**c**.

Synthesis of tricyclic benzimidazol-2-ones via Diels–Alder cycloadditions of exo-imidazolidin-2-one dienes 15a and 16a–f

The symmetrical diene **15a** and unsymmetrical dienes **16a**–**d** (R = H) were elaborated based on previously described methods [21,22]. The reaction of α-iminoketones **11a-c** with the corresponding isocyanates **5a-d** furnished the desired dienes **15a** and **16a**–**d** in good yields. The new diene **16c** was obtained starting from α-iminoketone **11c** with isocyanate **5b** (Scheme 8).

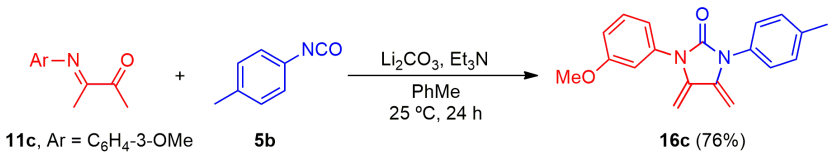

Scheme 8. Synthesis of diene **16c**.

Preliminary results shown that diene **15a** undergoes Diels–Alder cycloaddition with *N*-phenylmaleimide (**19**) under mild conditions (CH_2Cl_2, 0 ºC, 1 h) to furnish adduct **33a** in high yield [21]. In order to gain more insight into the reactivity of unsymmetrical dienes, analogues **16a**–**c** were submitted to cycloaddition with **19** under the same reaction conditions, leading to adducts **33b**–**d** in high yields (Table 3, entries 2–4). As can be appreciated, the cycloaddition takes place regardless of the substituents located at the aryl ring of the dienes. Hence, reactivity is not dependent on the perturbation of the electron density of *N,N'*-aryl rings on the conjugated dienic moiety, a phenomenon that can be attributed to the almost orthogonal orientation of the aryl ring with respect to the heterocycle. This conformational preference of the substituted aryl rings, shown by quantic calculations and X-ray crystallography [22], impedes their conjugation with the nitrogen lone pairs of the imidazolidin-2-one ring. Thus, the aryl rings do not have any significant electronic effect, which agrees with previous results [21,22].

J. Mex. Chem. Soc. **2025**, *69*(4)
Regular Issue

ISSN-e 2594-0317

Table 3. Diels–Alder cycloaddition of dienes **15a** and **16a**–**d** to dienophiles **19** and **20** to afford adducts **33a**–**d** and **35a**–**b**.[a]

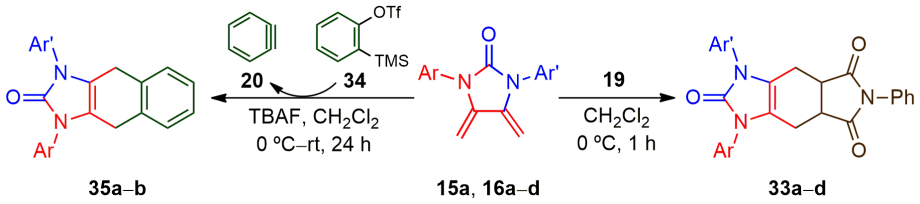

35a–b **15a, 16a–d** **33a–d**

Entry	Diene	Dienophile	Ar	Ar'	**33** or **35**	Yield (%)[b]
1	**15a**	**19**	Ph	Ph	**33a**	90
2	**16a**	**19**	Ph	C_6H_4-4-OMe	**33b**	95
3	**16b**	**19**	Ph	C_6H_4-4-Cl	**33c**	92
4	**16c**	**19**	C_6H_4-3-OMe	C_6H_4-4-Me	**33d**	74
5	**15a**	**20**	Ph	Ph	**35a**	56
6	**16d**	**20**	C_6H_4-4-Me	Ph	**35b**	60

[a] Standard conditions: Method A: **15a** and **16a**–**c** (1.0 mol equiv) with **19** (1.1 mol equiv), in CH_2Cl_2, 0 °C, 1 h. Method B: **15a** and **16d** (1.0 mol equiv) with **34** (1.0 mol equiv) and TBAF (1.5 mol equiv) in CH_2Cl_2 0 °C–rt, 24 h. [b] Isolated yields.

Benzyne (**20**), an *in situ*-formed highly reactive molecule [34], is one of the most important dienophiles in Diels–Alder cycloadditions, generating linear and non-linear homologation of aromatic multicyclic six-membered rings [4,35], and be involved in natural product synthesis [36]. 2-(Trimethylsilyl)phenyl triflate (**34**) reacts under mild conditions with TBAF to generate **20** (Table 3) [35,36].

Dienes **15a** and **16d** were evaluated in Diels–Alder cycloadditions with benzyne (**20**) (Table 3, entries 5–6). The latter was generated *in situ* by reacting **34** with TBAF in the presence of the corresponding diene at 0 °C. The mixture was stirred until reaching rt (for about 24 h), to obtain adducts **35a**–**b** in moderate yields. Despite the high reactivity of **20**, the conversion rate is not always complete, due to the well-known behavior of **20**. Once formed, this molecule undergoes dimerization, thus decreasing its concentration in the reaction medium [34].

In the Diels–Alder additions with dienophiles **19** and **20**, derivatives **15a** and **16a**–**d** proved to be potent dienes capable of providing a series of tricyclic tetrahydrobenzo[*d*]imidazol-2-ones **33a**–**d** and **35a**–**b**, which in turn can serve as precursors of aromatic analogues with potential synthetic and pharmacological value [23–27].

With the aim of exploring a preliminary synthetic application of adducts **33a**–**d** and **35a**–**b**, they were aromatized with 2,3-dichloro-5,6-dicyano-*p*-benzoquinone (DDQ) under mild conditions, converting them into aromatic tricyclic benzo[*d*]imidazol-2-ones **36a**–**d** (Scheme 9, Eq. 1) and naphtho[2,3-*d*]imidazol-2-ones **37a**–**b** (Eq. 2), respectively, in high to excellent yields. The yields for the second series of aromatic products were higher, because of the greater stability gained by the formation of a naphthalene ring.

J. Mex. Chem. Soc. **2025**, *69*(4)
Regular Issue

ISSN-e 2594-0317

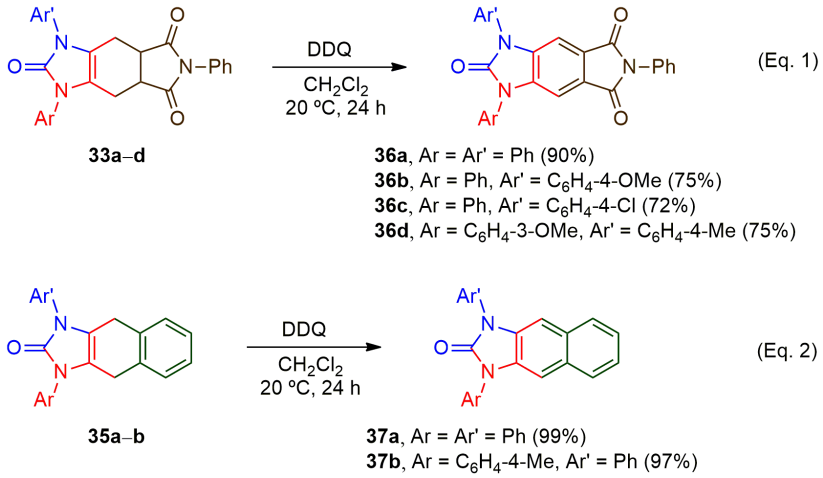

Scheme 9. Synthesis of tricyclic benzo[*d*]imidazol-2-ones **36a**–**d** (Eq. 1) and naphtho[2,3-*d*]imidazol-2-ones **37a**–**b** (Eq. 2).

All the structures of the intermediates and products of these synthetic pathways were characterized by IR, ^{1}H and ^{13}C NMR spectroscopy, assisted by 2D (HMQC, HSQC, and HMBC) experiments and high-resolution mass spectrometry (HRMS).

Conclusions

Dienes **1**–**2** proved to be versatile compounds not only as reactive and regioselective dienes in Diels–Alder additions, as previously demonstrated, but also as substrates for the regioselective synthesis of functionalized 4-oxazolin-2-ones **22**–**28**. The latter compounds were uncommon substrates in a Staunton–Weinreb-like annulation, converting aldehydes **30b**–**c** into 4,5-dihydrobenzo[*d*]oxazol-2(3*H*)-ones **31b**–**c**, although in low yields. A shorter synthetic approach for an alternative preparation of aldehydes **30a**–**c** was carried out through a two-step route starting from ketol **8a**.

Symmetrical *exo*-2-imidazolidinone diene **15a** and unsymmetrical dienes **16a-d** were reactive substrates in the Diels–Alder cycloadditions with dienophiles *N*-phenylmaleimide (**19**) and benzyne (**20**). The corresponding adducts were efficiently aromatized to furnish a series of benzo- and naphtho[*d*]imidazol-2-ones, which potentially have pharmacological activity.

Acknowledgments

We thank Dr. Carlos Espinoza-Hicks for his help in spectrometric measurements and Bruce A. Larsen for proofreading. J.T. acknowledges SIP/IPN (Grants 20195228, 20200227, 20200950, 202110700, 2022900, and 20221003) and CONAHCYT (178319 and A1-S-17131) for financial support. G.A.M.-F., P.M., A.N.G.-G., C.H.E, R.U.G., R.I.H., and E.B. thank CONAHCYT for awarding them graduate scholarships, and thank SIP/IPN (PIFI) and Ludwig K. Hellweg Foundation for scholarship complements. O.G.-G., F.D. and J.T. are fellows of the EDI-IPN and/or COFAA-IPN programs.

J. Mex. Chem. Soc. **2025**, *69*(4)
Regular Issue

ISSN-e 2594-0317

References

1. (a) Sauer, J.; Sustmann, R. *Angew. Chem., Int. Ed. Engl.* **1980**, *19*, 779–807. DOI: https://doi.org/10.1002/anie.198997791; (b) Pindur, U.; Lutz, G.; Otto, C. *Chem. Rev.* **1993**, *93*, 741–761. DOI: https://doi.org/10.1021/cr00018a006; (c) Herges, R.; Jiao, H.; von Ragué Schleyer, P. *Angew. Chem., Int. Ed. Engl.* **1994**, *33*, 1376–1378. DOI: https://doi.org/10.1002/anie.199413761; (d) Diedrich, M. K.; Klärner, F.-G. *J. Am. Chem. Soc.* **1998**, *120*, 6212–6218. DOI: https://doi.org/10.1021/ja973936p; (e) Suárez, D.; Sordo, J. A. *Chem. Commun.* **1998**, 385–386. DOI: https://doi.org/10.1039/A707086A; (f) Brocksom, T. J.; Nakamura, J.; Ferreira, M. L.; Brocksom, U. *J. Braz. Chem. Soc.* **2001**, *12*, 597–622. DOI: https://doi.org/10.1590/S0103-50532001000500004; (g) Kumar, A. *Chem. Rev.* **2001**, *101*, 1–19. DOI: https://doi.org/10.1021/cr990410; (h) Tantillo, D. J.; Houk, K. N.; Jung, M. E. *J. Org. Chem.* **2001**, *66*, 1938–1940. DOI: https://doi.org/10.1021/jo001172h; (i) Ayers, P. W.; Morell, C.; De Proft, F.; Geerlings, P. *Chem. Eur. J.* **2007**, *13*, 8240–8247. DOI: https://doi.org/10.1002/chem.200700365; (j) Domingo, L. R.; Sáez, J. A. *Org. Biomol. Chem.* **2009**, *7*, 3576–3583. DOI: https://doi.org/10.1039/B909611F; (k) Wang, Z.; Hirschi, J. S.; Singleton, D. A. *Angew. Chem. Int. Ed.* **2009**, *48*, 9156–9159. DOI: https://doi.org/10.1002/anie.200903293; (l) Ishihara, K.; Sakakura, A. Intermolecular Diels-Alder Reactions, in *Comprehensive Organic Synthesis*; Knochel, P., Molander, G.A., Eds.; Elsevier: Amsterdam, 2014; Vol. 5, Chap. 5.09, 351–408.
2. (a) Patman, R. L.; Bower, J. F.; Kim, I. S.; Krische, M. J. *Aldrichim. Acta* **2008**, *41*, 95–104; (b) Longo, P.; Pragliola, S.; Milano, G.; Guerra, G. *J. Am. Chem. Soc.* **2003**, *125*, 4799–4803. DOI: https://doi.org/10.1021/ja028462; (c) Li, Y.; Chen, J.; Ng, J. J. W.; Chiba, S. *Angew. Chem. Int. Ed.*. **2023**, *62*, e202217735. DOI: https://doi.org/10.1002/anie.202217735.
3. (a) Gleiter, R.; Böhm, M. C. *Pure Appl. Chem.* **1983**, *55*, 237–244. DOI: https://doi.org/10.1351/pac198855020237; (b) Kahn, S. D.; Pau, C. F.; Overman, L. E.; Hehre, W. J. *J. Am. Chem. Soc.* **1986**, *108*, 7381–7396. DOI: https://doi.org/10.1021/ja00283a038; (c) Houk, K. N.; Li, Y.; Evanseck, J. D. *Angew. Chem., Int. Ed. Engl.* **1992**, *31*, 682–708. DOI: https://doi.org/10.1002/anie.199206821; (d) Damoun, S.; Van de Woude, G.; Méndez, F.; Geerlings, P. *J. Phys. Chem. A* **1997**, *101*, 886–893. DOI: https://doi.org/10.1021/jp9611840; (e) Xidos, J. D.; Poirier, R. A.; Pye, C. C.; Burnell, D. J. *J. Org. Chem.* **1998**, *63*, 105–112. DOI: https://doi.org/10.1021/jo9712815; (f) García, J. I.; Martínez-Merino, V.; Mayoral, J. A.; Salvatella, L. *J. Am. Chem. Soc.* **1998**, *120*, 2415–2420. DOI: https://doi.org/10.1021/ja97282279; (g) Kong, S.; Evanseck, J. D. *J. Am. Chem. Soc.* **2000**, *122*, 10418–10427. DOI: https://10.1021/ja0010249; (h) Quadrelli, P.; Romano, S.; Toma, L.; Caramella, P. *J. Org. Chem.* **2003**, *68*, 6035–6038. DOI: https://10.1021/jo034401j; (i) Çelebi-Ölçüm, N.; Ess, D. H.; Aviyente, V.; Houk, K. N. *J. Org. Chem.* **2008**, *73*, 7472–7480. DOI: https://10.1021/jo801076t; (j) Domingo, L. R.; Chamorro, E.; Pérez, P. *Org. Biomol. Chem.* **2010**, *8*, 5495–5504. DOI: https://10.1039/c0ob00563k; (k) Ramírez-Gualito, K.; López-Mora, N.; Jiménez-Vázquez, H. A.; Tamariz, J.; Cuevas, G. *J. Mex. Chem. Soc.* **2013**, *57*, 267–275. DOI: https://10.29356/jmcs.v57i4.189; (l) Jasiński, R.; Kubik, M.; Łapczuk-Krygier, A.; Kącka, A.; Dresler, E.; Boguszewska-Czubara, A. *Reac. Kinet. Mech. Cat.* **2014**, *113*, 333–345. DOI: https://10.1007/s11144-014-0753-8; (m) Mlostoń, G.; Urbaniak, K.; Sobiecka, M.; Heimgartner, H.; Würthwein, E.-U.; Zimmer, R.; Lentz, D.; Reissig, H.-U. *Molecules* **2021**, *26*, 2544. DOI: https://10.3390/molecules26092544.
4. (a) Carruthers, W., in: *Cycloaddition Reactions in Organic Synthesis*; Pergamon Press: Oxford, 1990; (b) Oppolzer, W., in: *Comprehensive Organic Synthesis*; Trost, B. M.; Fleming, I.; Paquette, L. A., Eds.; Pergamon Press: Oxford, 1991; Vol. 5, Chapter 4.1; (c) Fringuelli, F.; Taticchi, A. *The Diels-Alder Reaction: Selected Practical Methods*; J. Wiley & Sons: Chichester, 2002; (d) Corey, E. J. *Angew. Chem. Int. Ed.* **2002**, *41*, 1650–1667. DOI: https://doi.org/10.1002/1521-3773(20020517)41:10<1650::AID-ANIE1650>3.0.CO;2-B; (e) Nicolaou, K. C.; Snyder, S. A.; Montagnon, T.; Vassilikogiannakis, G. *Angew. Chem. Int. Ed.* **2002**, *41*, 1668–1698, and references

J. Mex. Chem. Soc. **2025**, *69*(4)
Regular Issue

ISSN-e 2594-0317

cited therein. DOI: https://doi.org/10.1002/1521-3773(20020517)41:10<1668::AID-ANIE1668>3.0.CO;2-Z; (f) Reymond, S.; Cossy, J. *Chem Rev.* **2008**, *108*, 5359–5406. DOI: https://doi.org/10.1021/cr078346g; (g) Wang, J.; Ma, D. *Angew. Chem. Int. Ed.* **2019**, *58*, 15731–15735. DOI: https://doi.org/10.1002/anie.201909349; (h) Schwinger, D. P.; Peschel, M. T.; Jaschke, C.; Jandl, C.; de Vivie-Riedle, R.; Bach, T. *J. Org. Chem.* **2022**, *87*, 4838–4851. DOI: https://doi.org/10.1021/acs.joc.2c00186; (i) Ghosh, S.; Erchinger, J. E.; Maji, R.; List, B. *J. Am. Chem. Soc.* **2022**, *144*, 6703–6708. DOI: http://doi.org/10.1021/jacs.2c01971; (j) Li, L.-X.; Min, L.; Yao, T.-B.; Ji, S.-X.; Qiao, C.; Tian, P.-L.; Sun, J.; Li, C.-C. *J. Am. Chem. Soc.* **2022**, *144*, 18823–18828. DOI: https://doi.org/10.1021/jacs.2c09548.

5. (a) Wiersum, U. E. *Aldrichimica Acta* **1981**, *14*, 53–58; (b) Fringuelli, F.; Taticchi, A., in: *Dienes in the Diels-Alder Reaction*; J. Wiley & Sons: New York, 1990; (c) Martin, N.; Seoane, C.; Hanack, M. *Org. Prep. Proc. Int.* **1991**, *23*, 237–272. DOI: https://doi.org/10.1080/00304949109458320; (d) Manoharan, M.; De Proft, F.; Geerlings, P. *J. Org. Chem.* **2000**, *65*, 7971–7976. DOI: https://doi.org/10.1021/jo001156k; (e) Alcaide, B.; Almendros, P.; Aragoncillo, C. *Chem. Soc. Rev.* **2014**, *43*, 3106–3135 DOI: https://doi.org/10.1039/c3cs60462d.
6. (a) Haber, M.; Pindur, U. *Tetrahedron* **1991**, *47*, 1925–1936. DOI: https://doi.org/S0040-4020(01)96104-6; (b) Ruiz, N.; Pujol, M. D.; Guillaumet, G.; Coudert, G. *Tetrahedron Lett.* **1992**, *33*, 2965–2968. DOI: https://doi.org/S0040-4039(00)79573-6; (c) Chaloner, L. M.; Crew, A. P. A.; O'Neill, P. M.; Storr, R. C.; Yelland, M. *Tetrahedron* **1992**, *37*, 8101–8116. DOI: https://doi.org/S0040-4020(01)80480-4; (d) Chou, T. S.; Chang, R. C. *J. Org. Chem.* **1993**, *58*, 493–496. DOI: https://doi.org/jo00054a037; (e) Hercouet, A.; Berrée, F.; Lin, C. H.; Toupet, L.; Carboni, B. *Org. Lett.* **2007**, *9*, 1717–1720. DOI: https://doi.org/10.1021/ol070400s; (f) Samanta, S.; Mohapatra, H.; Jana, R.; Ray, J. K. *Tetrahedron Lett.* **2008**, *49*, 7153–7156. DOI: https://doi.org/10.1016/j.tetlet.2008.09.162; (g) Inagaki, F.; Mizutani, M.; Kuroda, N.; Mukai, C. *J. Org. Chem.* **2009**, *74*, 6402–6405. DOI: https://doi.org/10.1021/jo901325d; (h) Zhou, L.; Zhang, M.; Li, W.; Zhang, J. *Angew. Chem. Int. Ed.* **2014**, *53*, 6542–6545. DOI: https://doi.org/10.1002/anie.201403709; (i) Li, G.-N.; Chen, G.-Y.; Niu, Z.-G.; Lei, B.-X.; Feng, H.-J. *J. Heterocycl. Chem.* **2014**, *51*, E367–E371. DOI: https://doi.org/10.1002/jhet.1945; (j) Hirata, G.; Yamada, N.; Sanada, S.; Onodera, G.; Kimura, M. *Org. Lett.* **2015**, *17*, 600–603. DOI: https://doi.org/10.1021/ol503614d.
7. (a) Mandal, A. B.; Gómez, A.; Trujillo, G.; Méndez, F.; Jiménez, H. A.; Rosales, M. J.; Martínez, R.; Delgado, F.; Tamariz, J. *J. Org. Chem.* **1997**, *62*, 4105–4115. DOI: https://doi.org/10.1021/jo962403g; (b) Fuentes, A.; Martínez-Palou, R.; Jiménez-Vázquez, H. A.; Delgado, F.; Reyes, A.; Tamariz, J. *Monatsh. Chem.* **2005**, *136*, 177–192. DOI: https://doi.org/10.1007/s00706-004-0244-0.
8. Martínez, R.; Jiménez-Vázquez, H. A.; Reyes, A.; Tamariz, J. *Helv. Chim. Acta* **2002**, *85*, 464–482. DOI: https://doi.org/10.1002/1522-2675(200202)85:2<464::AID-HLCA464>3.0.CO;2-U.
9. Martínez, R.; Jiménez-Vázquez, H. A.; Delgado, F.; Tamariz, J. *Tetrahedron* **2003**, *59*, 481–492. DOI: https://doi.org/10.1016/S0040-4020(02)01536-3.
10. González-Romero, C.; Bernal, P.; Jiménez, F.; Cruz, M. C.; Fuentes-Benites, A.; Benavides, A.; Bautista, R.; Tamariz, J. *Pure Appl. Chem.* **2007**, *79*, 181–191. DOI: https://doi.org/10.1351/pac200779020181.
11. Mandal, A. B.; Delgado, F.; Tamariz, J. *Synlett* **1998**, 87–89. DOI: https://doi.org/10.1055/s-1998-1571.
12. (a) Bautista, R.; Benavides, A.; Jiménez-Vázquez, H. A.; Tamariz, J. *Nat. Prod. Res.* **2013**, *27*, 1749–1756, and references cited therein. DOI: https://doi.org/10.1080/14786419.2012.751599; (b) Ávila-Melo, J. L.; Benavides, A.; Fuentes-Gutiérrez, A.; Tamariz, J.; Jiménez-Vázquez, H. A. *Synthesis* **2021**, *53*, 2201–2211. DOI: https://doi.org/10.1055/a-1385-9052.
13. Ortega-Jiménez, F.; Benavides, A.; Delgado, F.; Jiménez-Vázquez, H. A.; Tamariz, J. *Organometallics* **2010**, *29*, 149–159. DOI: https://doi.org/10.1021/om900772z.

J. Mex. Chem. Soc. **2025**, *69*(4)
Regular Issue

ISSN-e 2594-0317

14. Reyes, L.; Mendoza, H.; Vázquez, M. A.; Ortega-Jiménez, F.; Fuentes-Benítes, A.; Flores-Conde, M. I.; Jiménez-Vázquez, H.; Miranda, R.; Tamariz, J.; Delgado, F. *Organometallics* **2008**, *27*, 4334–4345. DOI: https://doi.org/10.1021/om8002416.
15. Santoyo, B. M.; González-Romero, C.; Merino, O.; Martínez-Palou, R.; Fuentes-Benites, A.; Jiménez-Vázquez, H. A.; Delgado, F.; Tamariz, J. *Eur. J. Org. Chem.* **2009**, 2505–2518. DOI: https://doi.org/10.1002/ejoc.200900114.
16. Merino, O.; Santoyo, B. M.; Montiel, L. E.; Jiménez-Vázquez, H. A.; Zepeda, L. G.; Tamariz, J. *Tetrahedron Lett.* **2010**, *51*, 3738–3742. DOI: https://doi.org/10.1016/j.tetlet.2010.05.034.
17. Zárate-Zárate, D.; Aguilar, R.; Hernández-Benitez, R. I.; Labarrios, E. M.; Delgado, F.; Tamariz, J. *Tetrahedron.* **2015**, *71*, 6961–6978. DOI: https://doi.org/10.1016/j.tet.2015.07.010.
18. Santoyo, B. M.; González-Romero, C.; Zárate-Zárate, D.; Hernández-Benitez, R. I.; Pelayo, V.; Barrera, E.; Escalante, C. H.; Fuentes-Benites, A.; Martínez-Morales, G.; López, J.; Vázquez, M. A.; Delgado, F.; Jiménez-Vázquez, H. A.; Tamariz, J. *Chirality* **2019**, *31*, 719–749. DOI: https://doi.org/10.1002/chir.23109.
19. Barrera, E.; Hernández-Benitez, R. I.; González-González, C. A.; Escalante, C. H.; Fuentes-Benites, A.; González-Romero, C.; Becerra-Martínez, E.; Delgado, F.; Tamariz, J. *Eur. J. Org. Chem.* **2022**, *2022*, e202200364. DOI: https://doi.org/10.1002/ejoc.202200364.
20. Yescas-Galicia, D.; Restrepo-Osorio, R. A.; García-González, A. N.; Hernández-Benítez, R. I.; Espinoza-Hicks, J. C.; Escalante, C. H.; Barrera, E.; Santoyo, B. M.; Delgado, F.; Tamariz, J. *J. Org. Chem.* **2022**, *87*, 13034–13052. DOI: https://doi.org/10.1021/acs.joc.2c01563.
21. Bautista, R.; Bernal, P.; Herrera, R.; Santoyo, B. M.; Lazcano-Seres, J. M.; Delgado, F.; Tamariz, J. *J. Org. Chem.* **2011**, *79*, 7901–7911. DOI: https://doi.org/10.1021/jo201335y.
22. Espinoza-Hicks, C.; Montoya, P.; Bautista, R.; Jiménez-Vázquez, H. A.; Rodríguez-Valdez, L. M.; Camacho-Dávila, A. A.; Cossío, F. P.; Delgado, F.; Tamariz, J. *J. Org. Chem.* **2018**, *83*, 5347–5364. DOI: https://doi.org/10.1021/acs.joc.7b02344.
23. Rémond, G.; Portevin, B.; Bonnet, J.; Canet, E.; Regoli, D.; De Nanteuil, G. *Eur. J. Med. Chem.* **1997**, *32*, 843–868. DOI: https://doi.org/10.1016/S0223-5234(97)82771-7.
24. Edvinsson, L.; Sams, A.; Jansen-Olesen, I.; Tajti, J.; Kane, S. A.; Rutledge, R. Z.; Koblan, K. S.; Hill, R. G.; Longmore, J. *Eur. J. Pharmacol.* **2001**, *415*, 39–44. DOI: https://doi.org/10.1016/S0014-2999(00)00934-1.
25. Tapia, I.; Alonso-Cires, L.; López-Tudanca, P. L.; Mosquera, R.; Labeaga, L.; Innerárity, A.; Orjales, A. *J. Med. Chem.* **1999**, *42*, 2870–2880. DOI: https://doi.org/10.1021/jm981098j.
26. (a) Zhang, P.; Terefenko, E. A.; Wrobel, J.; Zhang, Z.; Zhu, Y.; Cohen, J.; Marschke, K. B.; Mais, D. *Bioorg. Med. Chem. Lett.* **2001**, *11*, 2747–2750. DOI: https://doi.org/10.1016/S0960-894X(01)00554-6; (b) Terefenko, E. A.; Kern, J.; Fensome, A.; Wrobel, J.; Zhu, Y.; Cohen, J.; Winneker, R.; Zhang, Z.; Zhang, P. *Bioorg. Med. Chem. Lett.* **2005**, *15*, 3600–3603. DOI: https://doi.org/10.1016/j.bmcl.2005.05.082.
27. Li, Q.; Li, T.; Woods, K. W.; Gu. W.-Z.; Cohen, J.; Stoll, V. S.; Galicia, T.; Hutchins, C.; Frost, D.; Rosenberg, S. H.; Sham, H. L. *Bioorg. Med. Chem. Lett.* **2005**, *15*, 2918–2922. DOI: https://doi.org/10.1016/j.bmcl.2005.03.049.
28. Martínez, R.; Jiménez-Vázquez, H. A.; Tamariz, J. *Tetrahedron.* **2000**, *56*, 3857–3866. DOI: https://doi.org/10.1016/S0040-4020(00)00311-2.
29. Fleming, I., in: *Molecular orbitals and organic chemical reactions. Reference Edition*. John Wiley & Sons: Chichester, UK, 2010.
30. Carrol, F. A., in: *Perspectives on structure and mechanism in organic chemistry*. John Wiley & Sons: New Jersey, 2010.
31. Toda, Y.; Gomyou, S.; Tanaka, S.; Komiyama, Y.; S.; Kikuchi, A.; Suga, H, *Org. Lett.* **2017**, *19*, 5786–5789. DOI: https://doi.org/10.1021/acs.orglett.7b02722; (b) Toda, Y.; Tanaka, S.; Gomyou, S.; Kikuchi, A.; Suga, H. *Chem. Commun*. **2019**, *55*, 5761–5764. DOI: https://doi.org/10.1039/C9CC01983A.

J. Mex. Chem. Soc. **2025**, *69*(4)
Regular Issue

ISSN-e 2594-0317

32. Tojo, G.; Fernández, M. *Oxidation of alcohols to aldehydes and ketones. A guide to current common practice*. Springer Science & Business Media: USA, 2006.
33. Donner, C. D. *Tetrahedron.* **2013**, *69*, 3747–3773. DOI: https:// doi.org/10.1016/j.tet.2013.03.034.
34. (a) Gilchrist, T. L. Supplement C: *The chemistry of triple bonded functional groups, Part 1.* Patai, S; Rappoport, Z. (Eds.). John Wiley and Sons: New York, 1983; (b) Wentrup, C. *Aust. J. Chem.* **2010**, *63*, 979–986. DOI: https:// doi.org/10.1071/CH10179.
35. Holden, C.; Greaney, M. F. *Angew. Chem. Int. Ed.* **2014**, *53*, 5746–5749. DOI: https://10.1002/anie.201402405.
36. (a) Gampe, C. M.; Carreira, E. M. *Angew. Chem. Int. Ed.* **2012**, *51*, 3766–3778. DOI: https://10.1002/anie.201107485; (b) Tadross, P. M.; Stoltz, B. M. *Chem. Rev.* **2012**, *112*, 3550–3577. DOI: https://10.1021/cr200478h.

Article

J. Mex. Chem. Soc. **2025**, *69*(4)
Regular Issue

ISSN-e 2594-0317

Excellent Catalytic Performance of Co_3O_4/CuO Nanocomposite for Catalytic Reduction of Nitroaromatic Compounds and Dyes Pollutants

Amir Hossein Sepahvand, Zohreh Derikvand*, Saeid Menati

Department of Chemistry, Khor.C., Islamic Azad University, Khorramabad, Iran.

***Corresponding author:** Zohreh Derikvand**,** e-mail: zderik@yahoo.com; zo.derik@iau.ac.ir

Received July 29th, 2024; Accepted January 7th, 2025.

DOI: http://dx.doi.org/10.29356/jmcs.v69i4.2340

Abstract. The paper investigates the catalytic reduction of nitroaromatic compounds (4-nitroaniline (4-NA) and 2-nitroaniline (2-NA)) by Co_3O_4/CuO nanocomposite. Also, the degradative property of nanocomposite was assessed using both anionic (methyl orange (MO)) and cationic (safranin O (SO)) dyes pollutants and simulated by the linear isotherm models and kinetic equations. Nano metal oxides CuO and Co_3O_4, as well as its nanocomposite, were synthesized using a precipitation-calcination method. The crystalline pattern, morphological structure, functionality, surface chemistry, and elemental content were evaluated. The catalytic efficiency in the reduction of nitroanilines and dyes was evaluated by sodium borohydride ($NaBH_4$). 100 % conversion of nitroanilines to their corresponding amines could be achieved in just 2 minutes for 4-nitroaniline and 10 minutes for 2-nitroaniline. The Co_3O_4/CuO nanocomposite shows 100 % and 76.6 % TOC for degradation of MO and SO. Additionally, the nanocomposite demonstrated stable performance over five consecutive reduction cycles for both dyes and NAs. Overall, the synthesized Co_3O_4/CuO nanocatalyst proves to be a cost-effective and high-performing candidate for remediation of pollutants in wastewater. Its easy recovery nature and efficient catalytic performance make it an excellent choice for environmental cleanup efforts.
Keywords: 4-Nitroaniline; Co_3O_4/CuO; safranin O; methyl orange; catalytic reduction.

Resumen. El artículo investiga la reducción catalítica de compuestos nitroaromáticos (4-nitroanilina (4-NA) y 2-nitroanilina (2-NA)) mediante un nanocompuesto de Co_3O_3/CuO. Además, se evaluó la propiedad degradativa del nanocompuesto utilizando colorantes contaminantes aniónicos (naranja de metilo (MO)) y catiónicos (safranina O (SO_3)) y se simuló mediante modelos de isotermas lineales y ecuaciones cinéticas. Los nanoóxidos metálicos CuO y Co_3O_3, así como su nanocompósito, se sintetizaron mediante un método de precipitación-calcinación. Se evaluaron el patrón cristalino, la estructura morfológica, la funcionalidad, la química superficial y el contenido elemental. La eficiencia catalítica en la reducción de nitroanilinas y colorantes se evaluó mediante borohidruro de sodio ($NaBH_3$). La conversión del 100 % de nitroanilinas a sus aminas correspondientes se logró en tan solo 2 minutos para la 4-nitroanilina y 10 minutos para la 2-nitroanilina. El nanocompuesto de Co_3O_3/CuO muestra un 100 % y un 76,6 % de COT para la degradación de MO y SO. Además, el nanocompuesto demostró un rendimiento estable durante cinco ciclos de reducción consecutivos tanto para colorantes como para NA. En general, el nanocatalizador de Co_3O_3/CuO sintetizado demuestra ser un candidato rentable y de alto rendimiento para la remediación de contaminantes en aguas residuales. Su fácil recuperación y su eficiente rendimiento catalítico lo convierten en una excelente opción para las iniciativas de limpieza ambiental.
Palabras clave: 4-Nitroanilina; Co_3O_3/CuO; safranina O; naranja de metilo; reducción catalítica.

J. Mex. Chem. Soc. **2025**, *69*(4)
Regular Issue

ISSN-e 2594-0317

Introduction

N Nitroanilines (NAs) are commonly utilized in the fabrication of fuel additives, insecticides, pharmaceuticals, dyestuffs and plastics [1-4]. Among them, 4-nitroaniline (4-NA) is an especially hazardous chemical that poses serious environmental risks, including mutagenic and teratogenic effects [5,6]. This dangerous compound is often found in wastewater from industries involved in pesticide manufacturing, dyeing, petrochemicals, oil refining, and chemical paints [7-9]. Due to its high solubility, 4-NA can easily infiltrate water and soil, leading to environmental contamination [9]. In some regions, sewage sludge is commonly recycled and used as fertilizer in agricultural fields [10]. However, the presence of toxic compounds such as chloroaniline and nitroaniline in sewage sludge can be detrimental to the environment [11]. The Environmental Protection Agency (EPA) has categorized 4-NA as a priority pollutant, with levels recorded in the environment reaching up to 100 mg L^{-1} [8]. The presence of 4-nitroaniline (4-NA) in water is a serious concern for both developed and developing countries due to its harmful effects on human and aquatic life [8]. As a high-priority water contaminant, there are strict regulations on the manufacturing, use, and disposal of 4-NA [12]. It is imperative to find sustainable and environmentally friendly methods for removing 4-NA pollution. Numerous methods have been employed to detect and remove 4-NA using various materials. The use of nanomaterials in developing new catalyst platforms has emerged as a promising alternative to traditional methods. Recent research has highlighted the unique characteristics and applications of nanomaterials in addressing 4-NA contamination in water [13]. Bimetallic oxides have garnered considerable attention due to their unique properties that differ from those of monometallic components [14,15]. It is widely recognized that incorporating a second metallic component can improve the selectivity, activity and stability of pure metal catalysts [16,17]. The urgent need to remove 4-nitroaniline (4-NA) from the environment is undeniable, prompting the exploration of various technologies to address this challenge. Despite the use of technologies such as thermal degradation, electrocoagulation, adsorption, ozonation, photodegradation, electrochemical degradation, electro-Fenton method, and biodegradation [18-24], these methods often face drawbacks such as generation of secondary pollutants, prolonged treatment times, low efficiency, adverse environmental impacts and high costs [25-28]. This has led to the search for alternative methods [29], among which catalytic reduction via $NaBH_4$ has emerged as a promising and environmentally friendly approach to converting nitroaniline to aminoaniline [30-31]. The reduction reaction is of significant interest due to the production of 4-aminoaniline, an intermediate with various industrial applications in engineering polymer, hair dyes, rubber antioxidant and hena. Catalytic reduction reactions rely heavily on the choice of catalyst, emphasizing the importance of developing efficient catalysts with robust adsorption capacity for $NaBH_4$, stability, affordability, and excellent electron transfer capabilities. This not only benefits industrial and economic aspects but also plays a crucial role in achieving environmental goals.

The presence of toxic dyes, which pose serious risks to both aquatic ecosystems and human health, is a significant environmental concern that leads to the depletion of aquatic life [32]. Some of the detrimental effects include respiratory issues, skin cancer, pneumonia, genetic disorders, and cardiovascular diseases. [33]. To address the challenges posed by toxic dyes in water, various technologies and processes have been developed to effectively remove these contaminants from wastewater. These methods encompass physical, chemical, and biological approaches [34]. Catalytic reactions are particularly important in this context, as they can function under mild conditions, thereby lowering the costs and energy requirements of the treatment process while maintaining high selectivity [35].

This study focused on the synthesis and application of Co_3O_4/CuO nanocomposite for the reduction of dye pollutants and nitroanilines with $NaBH_4$ as a reductant. The results clearly show the effectiveness of the nanocomposite in reducing all mentioned contaminants. A key benefit of this nanocatalyst is its easy recyclability and reusability, making it cost-effective for practical use. Additionally, the nanocomposite is easy to synthesize, highly stable, exhibits strong catalytic activity, aligns with green chemistry principles, and can operate under mild reaction conditions. It is worth mentioning that all experiments were conducted using water as a solvent, known for being the most environmentally friendly option due to its low impact, safety, affordability, and eco-friendliness.

J. Mex. Chem. Soc. **2025**, *69*(4)
Regular Issue

ISSN-e 2594-0317

Experimental

Preparation of Co_3O_4/CuO nanocatalyst

To synthesize the Co_3O_4/CuO nanocomposite, a well-defined procedure was followed. Initially, an aqueous solution containing cobalt (III) nitrate hexahydrate and copper (II) nitrate trihydrate in a 3:4 molar ratio in 20 mL of distilled water was prepared. The reaction mixture was stirred until a clear solution was obtained. Subsequently, the pH of reaction mixture was carefully adjusted to 9 using ammonium solution (3M). The obtained solid product was sonicated for 1 hour. The resulting product was filtered, washed with deionized water and ethanol several times, and dried at 80 °C for 24 hours. The Co_3O_4/CuO nanocomposite was obtained by calcined precursor at 700 °C in air for 5 hours. Similar experiments have been done for preparation of CuO and Co_3O_4 nanoparticles.

Characterization of catalyst

The Fourier transform infrared (FT-IR) spectra were taken by means of a Perkin-Elmer Spectrum RXI FT-IR spectrophotometer in the range of 4000-400 cm^{-1}. Powder X-ray diffraction (XRD) analyses were performed with a Ni-filtered Cu Kα radiation X-ray diffractometer (PANalytical/X'Pert Pro MPD) with a wavelength (λ) of 1.5406 Å. UV-vis spectra were obtained through a Perkin-Elmer Lambda 25 UV-vis spectrophotometer, covering the wavelength range of 200–600 nm. An in-depth investigation into the size and morphology of the Co_3O_4/CuO nanocomposite was conducted using a MIRA3 TESCAN field emission scanning electron microscope (FESEM) equipped with an energy dispersive X-ray (EDX) analyzer. The surface area of the nanocomposite was determined using the Brunauer Emmett Teller (BET) model. This involved N_2 gas adsorption–desorption isotherm measurements conducted on a BELSORP Mini II instrument. Furthermore, the Barrett-Joyner-Halenda (BJH) method was utilized to study the pore size and volume pore distribution of the nanocomposite.

Catalytic activities test for the reduction of nitroanilines and dyes

The catalytic activity of the CuO, Co_3O_4 and Co_3O_4/CuO nanocomposite in the reduction of nitroanilines and dyes (MO and SO) with an excess of $NaBH_4$ was methodically evaluated in a quartz cell at indoor temperature. The catalytic reduction of 2-nitroaniline (2-NA) by $NaBH_4$ served as the model reaction, and the reaction progress was monitored via UV-vis spectroscopy. For the catalytic assessment, a quartz cell containing 2 mL of 2-NA (0.2 mM) was utilized. To this, 0.5 mL of $NaBH_4$ (20 mM) was added, followed by the introduction of a proper amount of the catalyst. Subsequently, at 2-minute intervals, the conversion of 2-NA was scrutinized within the scanning range of 200-500 nm. Upon completion of the reaction, the catalyst was separated from the solution, subjected to multiple washes with deionized water (DI-H_2O), and then dried for subsequent cycles. The dosage of catalyst for the reduction reaction was investigated from 1 to 5 mg of catalyst, and the best amount of catalyst was 3 mg and the other experiment was done with 3 mg of catalyst. The degradation of methyl orange and safranin O (0.2 mM) was assessed in a quartz cell consisting of 2 mL of dye and 0.5 mL fresh $NaBH_4$ (20 mM). The progress of dyes reduction by Co_3O_4/CuO nanocomposite in the present and absence of $NaBH_4$ and desired amount of catalyst was monitored via UV-vis in the range of 200-700 nm.

Equations (1) and (2) were employed to calculate the rate constant and conversion efficiency. Also, the total conversion of dyes (TOC) was calculated by equations (2). C_0 and C_t represent the initial and time-dependent concentrations of nitroanilines or dyes, as determined by the absorption spectrum.

$$K_t = - \ln\frac{C_t}{C_0} \quad (1)$$

$$R(\%) = \frac{C_0 - C_t}{C_0} \times 100 \quad (2)$$

It's important to highlight that the pH of the solution created by mixing the dyes with $NaBH_4$ was initially measured at about 6.5 before the nanocomposite was added. A pH level below 7.0 is generally more conducive to the degradation process and has been shown to enhance catalytic activity. Therefore, no modifications to the pH were necessary, eliminating the need for any adjustments during the experiment.

J. Mex. Chem. Soc. **2025**, *69*(4)
Regular Issue

ISSN-e 2594-0317

Optimization of the synthesis conditions

In this study the impact of various factors such as amount of catalyst, concentration of dyes and nitroanilines were investigated for catalytic reduction reaction. Also, we evaluated the effect of molar ratio, temperature, pH and aging time on the production of Co_3O_4/CuO nanocomposite to determine the most positive synthesis conditions. Moreover, the concentration of $NaBH_4$ in the catalytic experiments underwent assessment. The results show that the best condition for preparation a pure nanocomposite obtain at pH=9 and calcinations at 700 °C. Consequently, it was observed that lower temperatures are insufficient for the production of Co_3O_4/CuO nanocomposite, leading in a multi-phase structure.

Results and discussion

Characterization of pure samples and Co_3O_4/CuO nanocomposite

The FT-IR spectrum of the pure samples and Co_3O_4/CuO nanocomposite was recorded at the 400-4000 cm^{-1} range to distinguish the functional groups and chemical bonds present in the samples (Fig. 1). The absorption bands at 536 cm^{-1} and 584 cm^{-1} are related to the Cu–O stretching vibrations of CuO nanoparticles in the monoclinic system. The bands appear at 700-500 cm^{-1} are assigned to metal oxides in nanocomposite. The stretching band for T_d system in Co_3O_4 are discernible at 725 cm^{-1} and 532 cm^{-1}, respectively [36]. A strong band at 1630 cm^{-1} corresponds to the OH vibration of water molecules that physically adsorbed on the surface of nanocomposite [37].The stretching vibrations in the range of 3000–3500 cm^{-1} are associated with the –OH groups of water molecules [37]. These FT-IR spectral features provide important insights into the chemical composition and functional groups present in the synthesized samples.

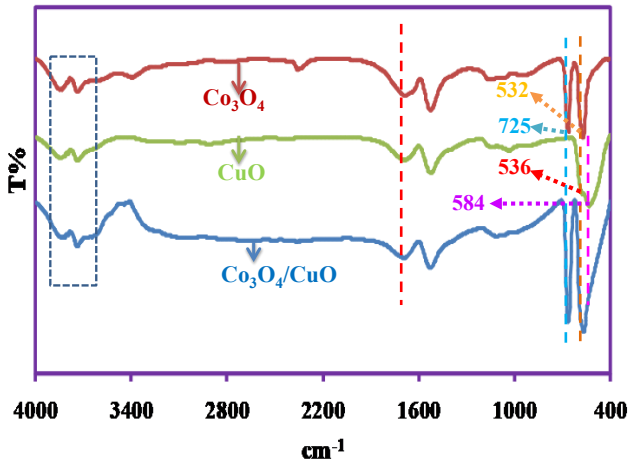

Fig.1. FT-IR spectra of Co_3O_4, CuO and Co_3O_4/CuO nanocomposite.

The XRD diffraction patterns of Co_3O_4/CuO nanocomposite, CuO and Co_3O_4 nanoparticles are illustrated in Fig. 2. Strong diffraction peaks located at 2θ =19.07 °, 31.33 °, 36.91 °, 44.88 °, 59.41 ° and 65.29 °, corresponding to (220), (311), (511), and (440) correspond to the (111), (220), (311), (400), (511) and (440) crystal planes of Co_3O_4 phases in accordance with the JCPDS card number 71–0816 [33]. Additionally, the peaks at 2θ =32.65 °, 35.68 °, 38.85 °, 48.91 °, 53.59 °, 61.67 °, 66.37 ° and 68.18 ° corresponding to various crystallographic planes, including (110), (002), (111), (202), (020), (113), (311), and (220), which are indicative of copper oxide, in accordance with the JCPDS card number 45-1548. The peaks of CuO were determined to be pure copper oxide, and the diffraction peaks of the samples were sharp, which indicates that the CuO is monoclinic. As depicted in Fig. 2, the Co_3O_4/CuO nanocomposite exhibits the coexistence of CuO and Co_3O_4 phases without any impurity phase.

J. Mex. Chem. Soc. **2025**, *69*(4)
Regular Issue

ISSN-e 2594-0317

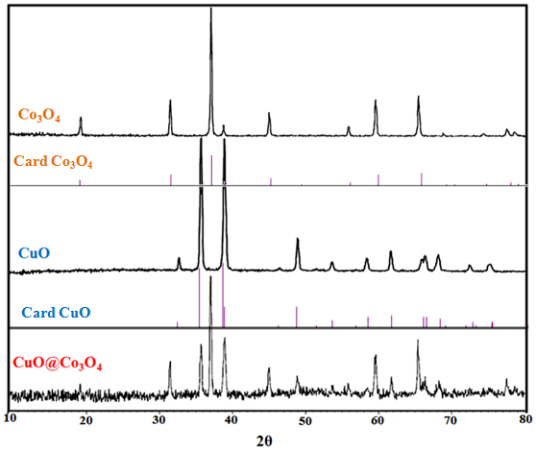

Fig. 2. XRD pattern of CuO, Co_3O_4 and Co_3O_4/ CuO nanocomposite.

The results of SEM analysis are shown in Fig. 3, revealing the shape, size and surface morphology, of the prepared structures. The SEM images in Fig. 3 demonstrate that the nanocomposite comprises nanohexagonal persmatic. The particle sizes are uniform with average diameter of about 57-59 nm. The particle sizes for CuO and Co_3O_4 are about 38-40 nm and 55-57 nm respectively. To further investigate the elemental distribution and composition of the Co_3O_4/CuO nanocomposite, EDX mapping measurements were conducted (Fig. 4). The EDX analysis shows the existence of Cu, Co, and O elements with atomic percentages of 18.76, 29.56, and 51.68 respectively. Indeed, these obtained atomic percentages are in well agreement with the prepared Co_3O_4/CuO nanocomposite. It can been seen from the maps in Fig.4 all elements are uniformly distributed over the samples, validating the homogeneity of the nanocomposites. Fig. 5 presents the N_2 adsorption-desorption isotherm curves for the synthesized Co_3O_4/CuO nanocomposite, which exhibits a type IV isotherm along with an H_3 hysteresis loop in the relative pressure range of P/P_0 = 0.4-1. This behavior indicates the presence of a porous structure. The effective BET specific surface areas of the synthesized nanoparticles were measured to be 4.59 m^2/g for the Co_3O_4/CuO nanocomposite, 4.19 m^2/g for Co_3O_4, and 4.10 m^2/g for CuO. Notably, the adsorption capacity of the Co_3O_4/CuO nanocomposite significantly increased at a relative pressure of P/P_0<0.4. This enhancement can be attributed to the nanocomposite's specific surface area, which promotes monolayer adsorption of N_2 onto the walls of its mesoporous structure. Additionally, using the BJH method applied to the adsorption branch of the N_2 isotherm, the average pore diameter was calculated to be 2 nm, with a total pore volume of 0.014 cm^3/g for the Co_3O_4/CuO nanocomposite.

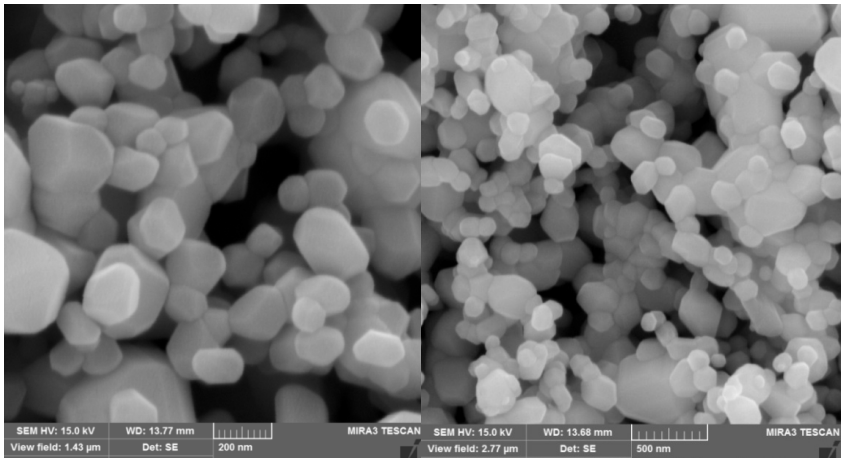

Fig. 3. SEM images of Co_3O_4/CuO nanocomposite.

J. Mex. Chem. Soc. **2025**, *69*(4)
Regular Issue

ISSN-e 2594-0317

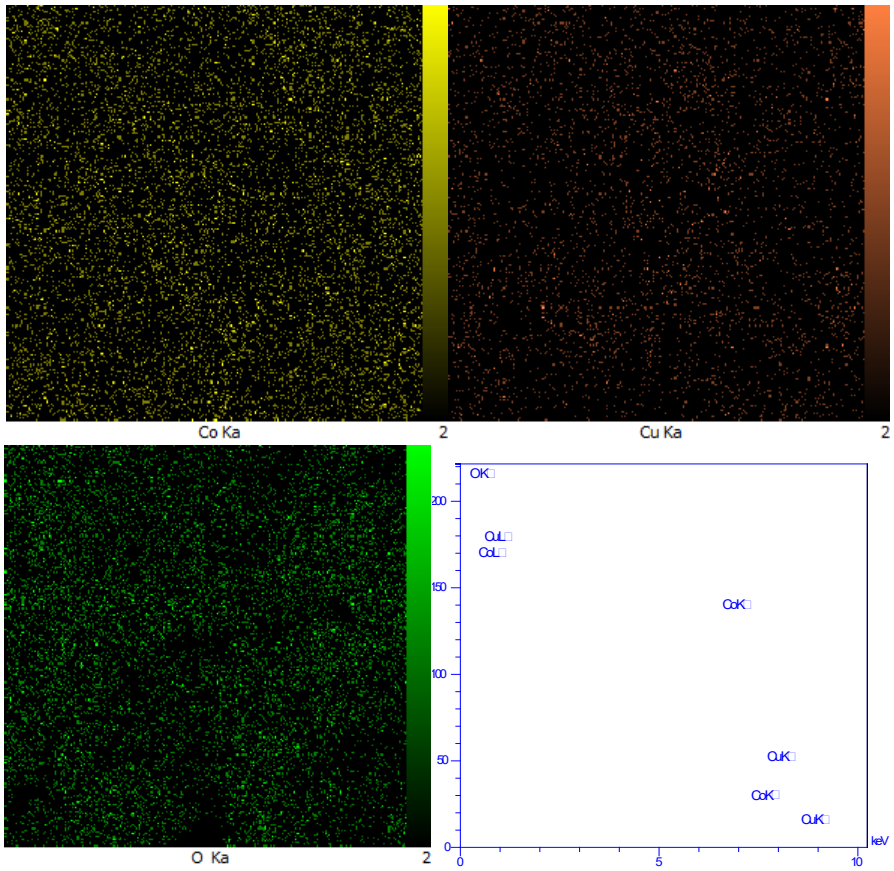

Fig.4. EDX diagrams and the corresponding elemental mapping images of Co_3O_4/CuO nanocomposite.

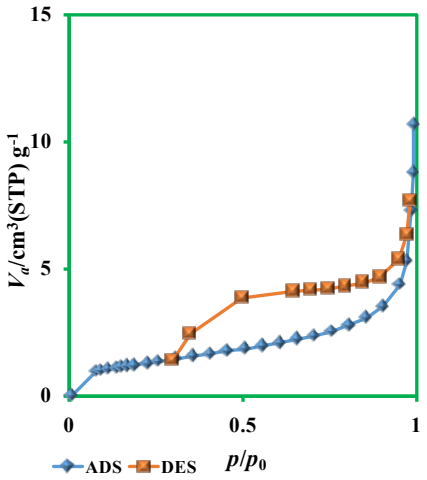

Fig.5. N_2 desorption-desorption isotherm of Co_3O_4/CuO nanocomposite.

J. Mex. Chem. Soc. **2025**, *69*(4)
Regular Issue

ISSN-e 2594-0317

Catalytic reduction of nitroanilines

The as prepared Co_3O_4, CuO and Co_3O_4/CuO samples used as catalyst for the reduction of nitroanilines, in the presence of $NaBH_4$ as a reducing agent. Initially, we used 2-nitroaniline to optimum the reaction condition and the progress of reduction reaction was monitored by UV–vis spectroscopy. Normally, 2-nitroaniline solution shows a broad peak around 412 nm [31]. Upon adding $NaBH_4$ to the reaction mixture, the intensity of this peak remains unchanged after 30 minutes validating that the reduction reaction has not occurred without a catalyst due to a high kinetic barrier between the donor and acceptor molecules (BH_4^- and 2-NA, respectively). As a result, the addition of a catalyst to the reaction mixture is essential to conquer this kinetic barrier, providing the monitoring of the reduction reaction by UV–vis spectroscopy. To explore this, parallel experiments were carried out by the 2-NA-$NaBH_4$-catalyst solution. With adding catalyst into the reaction mixture, the intensity peak at 412 nm starts to reduce. The reduction reaction of 2-NA was completed within 18 minutes and 30 minutes in the presence of CuO and Co_3O_4**,** respectively (Fig. 6**(a)** and **(b)**). However the reduction reaction was completed after 10 minutes with Co_3O_4/CuO nanocomposite (Fig. 6**(c)**). Outstandingly, with the reduction reaction completion a clear, colorless solution was obtained. Based on the obtained results the Co_3O_4/CuO nanocomposite illustrates excellent activity toward 2-nitroaniline reduction into its corresponding 2-aminaniline (2-AA). For finding the best amount of catalyst some experiments were performed with 1mg to 5 mg catalyst and the best performance was observed for 3 mg of catalyst in the presence of 2−NA−$NaBH_4$−H_2O solution. The results show a distinguished acceleration in the rate of reduction reaction with increasing dosage of Co_3O_4/CuO nanocatalyst, carrying out the reaction below 1 minute and it was hard to monitor the progress of reaction in appropriate time. Therefore, we chose 3mg of catalyst as the optimal quantity for subsequent experiments with Co_3O_4/CuO nanocatalyst. The increase of Co_3O_4/CuO nanocatalyst dosage facilitates better accessibility to active sites for 2-NA adsorption, thus enhancing the reduction reaction rate. The better catalytic efficiency of the Co_3O_4/CuO nanocomposite can be attributed to the close contact between Co_3O_4 and CuO, which facilitates electron transfer from BH_4^- to 2-NA. The synergistic effect of Co_3O_4 and CuO into the nanocomposite raises the accessibility of active sites for the production of H_2 and e^- (from $NaBH_4$) on the Co_3O_4/CuO surface, accordingly accelerating the reduction reaction speed. At first, H_2 molecules are generated by the reaction of water and BH_4^- ions. Then, these molecules and 2-nitroaniline are adsorbed simultaneously onto the surface of the Co_3O_4/CuO nanocomposite. The nanoparticles in the Co_3O_4/CuO nanocomposite facilitate electron transfer to 2-NA, effectively overcoming the reaction kinetic barrier. After that adsorbed BH_4^- ions, released hydrogen as hydride, the hydride anion transfers to the metal in the Co_3O_4/CuO nanocomposite and producing a complex. Eventually, the nitro group of the 2-nitroaniline is reduced by taking the hydride from the complex. Subsequent to three hydro-deoxygenation reactions, 2-AA is formed. In the final step, 2-AA is desorbed from the nanocomposite's surface. The Langmuir-Hinshelwood model was applied to estimate the performance of the Co_3O_4/CuO nanocomposite for kinetic analysis. Since the concentration of $NaBH_4$ solution was high relative to 2-NA concentration, the pseudo-first-order kinetics model was considered to determine the reaction rate constants (k). The kinetics were investigated using the equation $\ln(C_t/C_0) = -kt$, where C_0 and C_t correspond to the first and time 't' concentrations of 2-nitroaniline, respectively [29-31]. Fig. 6**(d)** illustrates a linear relationship between $\ln(C_t/C_0)$ and time during the reduction reaction catalyzed by Co_3O_4/CuO nanocomposite, validating the pseudo-first-order kinetics. The rate constant (k) was determined from the slope of the straight line, yielding a value about 0.408 min^{-1} for the Co_3O_4/CuO nanocatalyst, indicating excellent performance in converting 2-NA to 2-AA. This excellent catalytic efficiency is related to the close contact and interaction between Co_3O_4 and CuO nanoparticles. The results of this study on reducing 2-nitroaniline using the 2-NA-$NaBH_4$-H_2O system was compared with other studies, as illustrated in Table 1 [31,36-40]. Here we compared different parameters with other reported previously for reducing 2-nitroaniline to 2-aminoaniline (Table 1). The Co_3O_4/CuO nanocomposite exhibited exceptional catalytic activity in reducing 2-nitroaniline (Table 1). The dosage of the catalyst in our study was lower compared to those given in Table 1. Additionally, the concentration of 2-nitroaniline in our study was higher than in previous reports. The Co_3O_4/CuO nanocatalyst used in this study was constructed without toxic or expensive materials, making it suitable for practical applications. Furthermore, the prepared Co_3O_4/CuO nanocomposite displayed astonishing efficacy in reducing 4-nitroaniline (4-NA) with $NaBH_4$, as shown in Fig. 6**(e)**. The data clearly indicate a significant decrease in the characteristic absorption peak of 4-nitroaniline (4-NA) at 374 nm, which is accompanied by the emergence of two new peaks at 239 nm and 305 nm. These new peaks correspond to the characteristic absorption of 4-aminoaniline (4-AA). As shown in Fig. 6**(e)**, the addition of the Co_3O_4/CuO nanocomposite resulted in a notable reduction in UV-vis absorption at 374 nm, while the absorption at 305 nm

J. Mex. Chem. Soc. **2025**, *69*(4)
Regular Issue

ISSN-e 2594-0317

increased. This change reflects a decrease in the concentration of 4-NA and a corresponding increase in the concentration of 4-AA at 305 nm. The reduction reaction was completed within just 2 minutes. To study the stability and reusability of Co_3O_4/CuO nanocomposite, the used catalyst was collected, washed with H_2O/EtOH several times and dried to use for new runs. Based on the results, the catalytic activity remained unchanged after four runs. These findings confirm the stability and excellent catalytic efeciency of the Co_3O_4/CuO nanocomposite compared to the fresh catalyst. As a result, the Co_3O_4/CuO nanocomposite appears as an excellent, efficient, stable, and reusable catalyst for the reduction of nitroanilines and other nitroaromatic compounds.

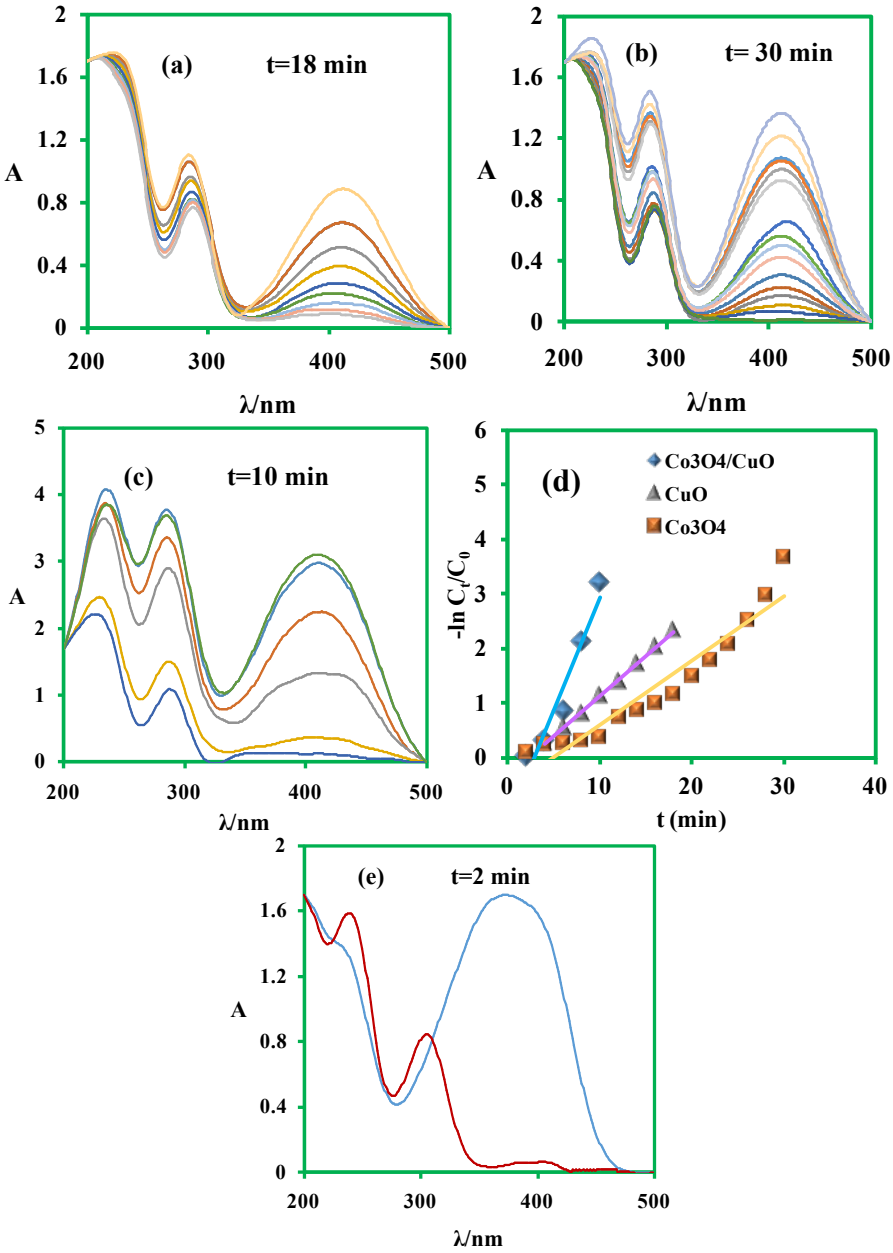

Fig. 6. The reduction of 2-nitroaniline (2-NA) in the presence of **(a)** CuO, **(b)** Co_3O_4, **(c)** Co_3O_4/CuO with $NaBH_4$ and 3 mg of catalysts **(d)** plot illustrating pseudo-first order kinitic, $\ln(C_t/C_0)$ verses reaction time (k = 0.147 min^{-1} (CuO), k = 0.117 min^{-1} (Co_3O_4), k = 0.408 min^{-1} (Co_3O_4/ CuO), **(e)** The reduction of 4-nitroaniline (4-NA) in the presence of Co_3O_4/CuO nanocomposite.

J. Mex. Chem. Soc. **2025**, *69*(4)
Regular Issue

ISSN-e 2594-0317

Table 1. Comparative characteristics of catalysts for reducing 2-nitroaniline.

Entry	Catalyst	$NaBH_4$ conc.	Catalytic activity (%)	Catalyst amount	2-NA conc.	Time (min)	Ref.
1	$CoFe_2O_4$/ZrMCM4125%	20 mM	100%	5mg	0.2 mM ($k=0.15\ min^{-1}$)	12	[31]
2	Ag_3PO_4/PPy/PANI	10 mM	100%	1 mg	1 mM ($k=0.022 min^{-1}$)	120	[34]
3	$Cu_2O/TiO_2/Ti_3C_2$	10 mM	100%	10 mg	5mM ($K=0.163 min^{-1}$)	15	[35]
4	NiO NPs	14 mM	62%	5 mg	0.15 mM ($k=0.007\ min^{-1}$)	120	[36]
5	Co_3O_4/CuO	20 mM	100%	3 mg	0.2 mM ($0.408\ min^{-1}$)	10	This work

Reduction of safranin O and methyl orange by Co_3O_4/CuO

The degradation of carcinogenic anionic and cationic dyes, such as safranin O (SO) and methyl orange (MO) were investigated using $NaBH_4$ as a green reductant. The main aim was to evaluate the catalytic performance of Co_3O_4/CuO in the degradation of these dyes pollutants. Some experiments were carried out with SO and MO, and their results are exhibited in Figs. 7**(a)** and **(b)**. The results show that the peak intensity of SO and MO start to decrease when Co_3O_4/CuO nanocomposite and $NaBH_4$ solution added to the reaction mixture. In UV-vis spectrum MO show absorption peak at 482 nm assigned to the azo bond [41] and this absorption peak was monitored to follow the reduction reaction. As shown in Fig. 7**(a)** the peak at 482 nm disappeared after 4 minutes with 100 % TOC (total conversion). The first-order kinetic model depicting the reduction of MO is illustrated in Fig. 7**(c)**, showing the efficient catalytic behavior. In the absence of nanocatalyst the reduction reaction was not progressed. The calculated rate constant for MO is about 1.57 min^{-1} as shown in Fig. 7**(c)**. Table 2 compares the prepared Co_3O_4/CuO nanocomposite and others reported in the literature [42-44]. The spectrum of SO demonstrated a absorption peak at 507 nm [45] and it was selected to monitor the influence of the Co_3O_4/CuO nanocatalyst. The results show that, the absorption spectra of SO remain constant after one-hour reaction period, suggesting that decolorization did not happen in the absence of the catalyst. Furthermore, comparable outcomes were found in the case where only $NaBH_4$ was used. Upon adding Co_3O_4/CuO and $NaBH_4$ into the reaction mixture, the degradation profile of SO undergoes a gradual change, with approximately 76.6% degradation observed within 12 minutes, the degradation reaction was stopped after 12 minutes (Fig. 7**(b)**). These results emphasize the excellent catalytic ability of Co_3O_4/CuO nanocatalyst in the reduction of SO and MO with $NaBH_4$, confirming the vital role played by the nanocomposite due to its excellent catalytic activity. The first-order kinetic model of SO reduction in the presence of Co_3O_4/CuO is shown in Fig.7**(c)**. The Langmuir-Hinshelwood mechanism [46] accurately elucidates the degradation process of MO and SO dyes. In this mechanism, the dyes and BH_4^- ions undergo adsorption onto the surface of the Co_3O_4/CuO catalyst. The Co_3O_4/CuO catalyst facilitates transmit of electrons from BH_4^- ions to dyes. The Co_3O_4/CuO reduces the energy obstacle between the product and reactant, resulted in the achievement of the degradation reaction within 12 and 4 minutes for SO and MO, respectively [47]. The percentage of degradation was calculated by equation (3):

$$\% \text{ Degradation} = (C_0 - C_t)/C_0 \times 100 \quad (3)$$

J. Mex. Chem. Soc. **2025**, *69*(4)
Regular Issue

ISSN-e 2594-0317

The used Co_3O_4/CuO catalyst was collected, thoroughly washed with a mixture of H_2O and EtOH multiple times, and then dried for reuse in subsequent experiments. The results indicate that the catalytic activity remained consistent after four cycles for MO catalytic reduction. These findings demonstrate the stability and exceptional catalytic efficiency of the Co_3O_4/CuO nanocomposite in comparison to the fresh catalyst (Figures 7**(d)** and 8).

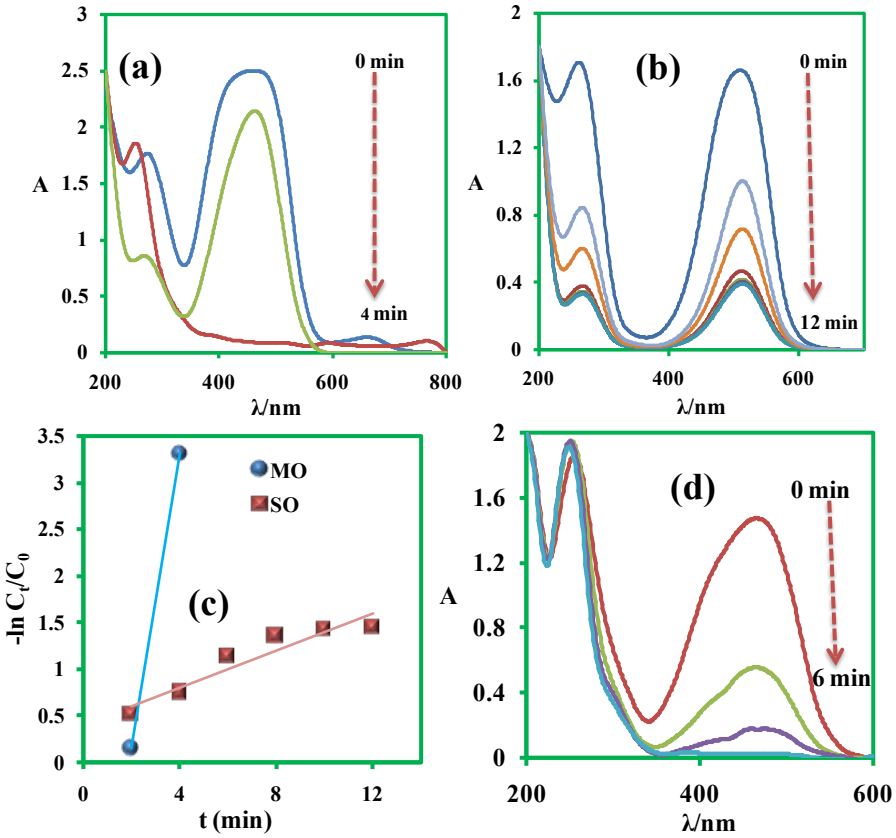

Fig.7. Degradation absorption spectra of MO **(a)** and SO **(b)** with $NaBH_4$ and Co_3O_4/CuO nanocomposite, **(c)** plot of $\ln(C_t/C_0)$ verses t (min) for Co_3O_4/CuO nanocomposite (3mg) (k=1.5 min^{-1} for MO and 0.1 min^{-1} for SO), **(d)** MO degradation with recycled catalyst.

Table 2. Comparative characteristics of catalysts for reducing methyl orange.

Entry	Catalyst	Amount	$NaBH_4$ conc.	Catalytic activity (%)	MO conc.	Time (min)	Ref.
1	$TiO_2/CoFe_2O_4/SiO_2$	5mg	20 mM	100 %	0.2 mM (k=0.59 min^{-1})	8	[38]
2	Ag@MIL-100(Fe)	1 mg	100mM	100 %	0.1 mM (k=0.236min^{-1})	5	[39]
3	BiTiOS	5 mg	13 mM	100 %	0.06 mM (k=0.809 min^{-1})	4	[40]
4	Co_3O_4/CuO	3 mg	20 mM	100 %	0.2 mM (k=1.5 min^{-1})	4	This work

J. Mex. Chem. Soc. **2025**, *69*(4)
Regular Issue

ISSN-e 2594-0317

Conclusions

The Co_3O_4/CuO nanocomposite was successfully synthesized using the calcination method, resulting in a hexagonal structure with an average particle size of approximately 25 nm. The combination of Co_3O_4 and CuO significantly enhanced the catalytic activity of the nanocomposite towards the reduction of 4-nitroaniline, 2-nitroaniline, and toxic dye pollutants (MO, SO). The synthesized Co_3O_4/CuO nanocomposite exhibits numerous merits, including excellent performance, ease of fabrication, cost-effectiveness, and recyclability, distinguishing it from other nanocatalysts. The results indicated that the reduction of 2-nitroaniline in the presence of Co_3O_4/CuO was superior to use CuO or Co_3O_4 alone, highlighting the synergistic effect between these metal oxides. Furthermore, the nanocatalyst maintained its activity after being recycled for four runs. This study provides a new strategy for developing an efficient reusable nanocatalyst for pollutant degradation via an environmentally safe process in which the nanocatalyst is easily collected from water thus mitigating its environmental impact.

Acknowledgments

We thank Biocomputational Laboratory, Department of Biology, Brawijaya University for provided the research facility for this study.

References

1. Lai, C.; Li, B.; Chen, M.; Zeng, G.; Huang, D.; Qin, L.; Liu, X.; Cheng, M.; Wan, J.; Du, C.; Huang, F.; Liu, S.; Yi, H. *Int. J. Hydrogen Energy.* **2018**, *43*, 1749-1757.
2. Bakhsh, E.M.; Ali, F.; Khan, S.B.; Marwani, H.M.; Danish, E.Y.; Asiri, A.M. *Int. J. Biol. Macromol*. **2019**, *131*, 666-675.
3. Ameen, F.; Dawoud, T.M.; Alshehrei, F.; Alsamhary, K.; Almansob, A. *Chemosphere.* **2021**, *271*, 129532.
4. de Barros, M.R.; Winiarski, J.P.; Elias, W.C.; de Campos, C.E.M.; Jost, C.L. *J. Environ. Chem. Eng*. **2021**, *9*, 105821.
5. Josephy, P.D.; Dhanoa, J.; Elzawy, G.; Heney, K.; Petrie, L.; Senis, C. *Environ. Mol. Mutagen.***2018**, *59*, 114-122.
6. Melinte, V.; Stroea, L.; Buruiana, T.; Chibac, A.L. *Eur. Polym. J.* **2019**, *121*, 109289.
7. Mei, X.; Ding, Y.; Wang, Y.; Yang, Y.; Xu, L.; Wang, Y.; Shen, W.; Zhang, Z.; Ma, M.; Guo, Z.; Xiao, Y.; Yang, X.; Zhou, B.; Xu, K.; Guo, W.; Wang, C. *Bioresour. Techno*l. **2020**, *307*, 123241.
8. Malakootian, M.; Gharaghani, M.A.; Dehdarirad, A.; Khatami, M.; Ahmadian, M.; Heidari, M.R.; Mahdizadeh, H. *J. Mol. Struct.* **2019**, *1176*, 766-776.
9. Amani, A.; Derikvand, Z.; Ghadermazi, M. *Inorg. Nano-Metal Chem.* **2025**, *55*, 864–879.
10. Pereira, I.D.S.; Bamberg, A.L.; Oliveira de Sousa, R.; Monteiro, A.B.; Martinazzo, R.; Posser Silveira, C.A.; de Oliveira Silveira, A. *J. Environ. Manag*. **2020**, *275*, 111203.
11. Smith, S.R. *Philos. Trans. A Math. Phys. Eng. Sci*. **2009**, *367*, 4005-4041.
12. Gu, Y.; Wang, Y.;; Zhang, H. *Spectrochim. Acta, Part A*. **2018**, *202*, 260-268.
13. Mazari, S.A.; Ali E.; Abro, R.; Khan, F.S.A.; Ahmed, I.; Ahmed, M.; Nizamuddin, S.; Siddiqui, T.H.; Hossain, N.; Mubarak, N.M.; Shah, A. *J. Environ. Chem. Eng,* **2021**, *9*, 105028.
14. (a) Gerent, G.G.; Santana, E.R.; Martins, E.C.; Spinelli, A. *Food Chem*. **2021**, *343*, 128419; (b) Azadbakht, A.; Abbasi, A.R.; Derikvand, Z.; Amraei S. *Mater. Sci. Engin.: C.* **2015**, *48*, 270-278; (c) Rahimi Fard, M.; Pourghobadi, Z. *Anal. Bioanal. Chem. Res*. **2018**, *5*, 249-259; (d) Saki, A.: Pourghobadi, Z.; Derikvand Z. *J. Electrochem Soc.* **2022**, *169*, 116507; (e) Alvandi, H.; Dorosti, N.; Afshar; F. *Mater. Tech*. **2022**, 37, 1691-1702.

J. Mex. Chem. Soc. **2025**, *69*(4)
Regular Issue

ISSN-e 2594-0317

15. (a) Santana, E.R.; de Lima, C.A.; Piovesan, J.V.; Spinelli, A. *Sens. Actuators B Chem.* **2017**, *240*, 487-496; (b) Beiranvand, S.; Abbasi, A.R.; Roushani, M.; Derikvand, Z.; Azadbakht, A. *J. Electroanal. Chem.* **2016**, *776*, 170-179; (c) Azadbakht, A.; Abbasi, A.R.; Derikvand, Z.; Karimi Z. Nano-Micro Lett. **2015**, *l.7*, 152-164; (d) Dorosti, N.; Delfan, B.; Khodadadi, M. *Appl. Organomet. Chem*. **2017**, *31*, e3875.
16. Maiyalagan,T.; Wang, X.; Manthiram, A. *RSC Ad*v. **2014**, *4*, 4028-4033.
17. Hosseinkhani, B.; Søbjer, L.S. g.; Rotaru, A.E.; Emtiazi, G., krydstrup, T. S.; Meyer, R.L. *Biotechnol. Bioeng.,* **2012**, *109*, 45-52.
18. Ai, L.; Li, L. *Chem. Eng. J.*, **2013**, *223*, 688-695.
19. Zhang, H.; Jiang, M.; Zhang, D.; Xia, Q. *Chem. Eng. Commun*. **2009**, *197*, 377-386.
20. Jiang, P.; Zhou, J.; Zhang, A.; Zhong, Y. *J. Environ. Sci.* **2010**, *22*, 500-506.
21. Kumar Dutta, R.; Verma S. *J. Environ. Chem.Eng.* **2017**, *5*, 4776-4787.
22. Liu, Z.; Yang, C.; Qiao, C. *FEMS Microbiol. Lett.*, **2007**, *277*, 150-156.
23. Modirshahla, N.; Behnajady, M.; Mohammadi-Aghdam S. *J. Hazard. Mater*. **2008**, *154*, 778-786.
24. Elfiad, A.; Galli, F.; Boukhobza, L.M.; Djadoun, A.; Boffito D.C. *J. Environ. Chem. Eng.* **2020**, *8*, 104214.
25. Ghosh, B.K.; Ghosh, N.N. *J. Nanosci. Nanotechnol.* **2018**, *18*, 3735-3758.
26. Wang, C.; Zhang, H.; Feng, Gao.; Shang, C. S.; Wang N. Z. *Catal. Commun.* **2015**, *72*, 29-32.
27. Tokazhanov, G.; Ramazanova, E.; Hamid, S.; Bae, S.; Lee W. *Chem. Eng. J.*, **2020**, *384*, 123252.
28. Wunder, S.; Polzer, F.; Lu, Y.; Mei, Y. *J. Phys. Chem. C*. **2010**, *114*, 8814-8820.
29. Derikvand, Z.; Rahmati, F.; Azadbakht, A. *Appl. Organomet. Chem.* **2019**, *33*, e4864.
30. Derikvand, Z.; Azadbakht, A.; Amiri Rudbari H. *J. Inorg. Organomet. Poly. Mater.* **2019**, *29*, 502-516.
31. Bahrami, M.; Derikvand, Z. *J. Mol. Struct.*, **2022**, *1254*, 132367.
32. Lellis, B.; F´avaro-Polonio, C.Z.; Pamphile, J.A.; Polonio, J.C. *Biotechnol. Res. Innov.,* **2019**, *3*, 275–290.
33. Burakov, A.E.; Galunin, E.V.; Burakova, I.V.; Kucherova, A.E.; Agarwal, S.; Tkachev, A. G.; Gupta, V.K. *Ecotoxicol. Environ. Saf*. **2018**, *148*, 702–712.
34. Alsukaibi, A.K.D. *Processes* **2022**, *10*, 1968.
35. Javaid, R.; Qazi, U.Y. *Int. J. Environ. Res. Public Health.* **2019**, *16*, 2066.
36. Hosseini, S. A. *Iran. J. Chem. Engin*. **2017**, *14*, 83-90.
37. Kumar, R.; Kumar, K.; Thakur, N. *Hybrid Advances*, **2024**, *5*, 100129.
38. Ma, J.; Deng , H.; Zhang , Z.; Zhang , L.; Qin, Z.; Zhang, Y.; Gao, L.; Jiao, T. *Colloids Surf. A: Physicochem. Eng. Asp*, **2022**, *632*, 127774.
39. Yin, J. J.; Ge, B. C.; Jiao, T. F.; Qin, Z. H.; Yu, M. Q.; Zhang, L. X.; Zhang, Q. R.; Peng Q. M. *Langmuir*, **2021**, *37*, 1267-1278.
40. Jeon, S.; Ko, J.W.; Bae, K.W. *Elastom. Compos*., **2020**, *55*, 191-198.
41. Lin, X.; Huang, T.; Huang, F.; Wang, W.; Shi, J. *J. Mater. Chem*. **2007**, *17*, 2145-2150.
42. Zarbakhsh, E.; Derikvand, Z. *Appl. Organomet. Chem.* **2024**, *38*, e7674.
43. Rattanakit, P.; Chutimasakul, T.; Darakai, V.; Nurerk, P.; Putnin, T. *S. Afr. J. Chem. Eng.* **2024**, *47*, 270–278.
44. Su, Z.; Wu, B.; Chen, L.; Tadesse Mosisa, M.; Zhang, P.; Wu, Q.; Kuo, D.-H.; Lu, D.; Ahmed Zelekew, O.; Lin, J.; Chen, X. *J. Sci.: Adv. Mater. Devices* **2023**, *8*, 100645.
45. Derikvand, Z.; Akbari, S.; Kouchakzadeh, G.; Azadbakht, A.; Nemati, A. *Russ. J. Phys. Chem. A.* **2019**, *93*, 2604-2612.
46. Arul, V.; M.G. Sethuraman, *Opt. Mater*. **2018**, *78*, 181-190.
47. Mallick, K.; Witcomb, M. Scurrell, M. *Mate. Chem. Phys*. **2006**, *97*, 283-287.

Article

J. Mex. Chem. Soc. **2025**, *69*(4)
Regular Issue

ISSN-e 2594-0317

Effects of Eco-Agricultural Production of Phenolic Active Principles Synthesis in sect. Nepetoideae (Lamiaceae) Species

Katarina Radovanović[1*], Biljana Božin[†1], Nebojša Kladar[1], Milica Aćimović[2], Maja Hitl[1], Neda Gavarić[1]

[1]University of Novi Sad, Faculty of Medicine, Department of Pharmacy, Hajduk Veljkova 3, Novi Sad, Serbia.
[2]Institute of Field and Vegetable Crops Novi Sad, National Institute of the Republic of Serbia, Maksima Gorkog 30, Novi Sad, Serbia.

***Corresponding author:** Katarina Radovanović, email: katarina.radovanovic@mf.uns.ac.rs

Received February 22nd, 2024; Accepted January 28th, 2025.

DOI: http://dx.doi.org/10.29356/jmcs.v69i4.2224

[†]This paper is dedicated to our beloved deceased Professor Biljana Božin, PhD

Abstract. One way of cultivating different aromatic Lamiaceae species, especially those classified in the Nepetoideae section, is eco-agricultural production. This modern trend makes new products with less environmental pollution and a high value for human health and nutrition. Winter savory (Satureja montana), peppermint (Mentha piperita), thyme (Thymus vulgaris), and sage (Salvia officinalis) are highly important medicinal plants that were introduced and are being successfully cultivated in agricultural fields in Vojvodina. This study aimed to determine 10 phenolic compounds in ethanolic extracts of peppermint, sage, thyme, and winter savory cultivated according to eco-agricultural principles. The amount of examined phenolic compounds was measured using liquid chromatography method (HPLC-DAD). In all four extracts, rosmarinic acid (RA) was the most abundant compound, with the highest amount recorded in peppermint (12863.6 µg/g), followed by thyme (7083.76 µg/g). Other detected compounds ranged from 29.29 to 484.37 µg/g for chlorogenic acid, 22.67 to 979.77 µg/g for caffeic acid, 11.8 to 339.59 µg/g for ferulic acid, not detected (ND) to 45.93 µg/g for p-coumaric acid, 14.9 to 63.72 µg/g for cinnamic acid, ND to 68.13 µg/g for gallic acid, LOD to 125.03 µg/g for rutin, 38.98 to 82.75 µg/g for quercetin. Quercitrin was detected only in sage (50.78 µg/g). The results suggest that peppermint especially accumulates higher amounts of RA when cultivated under ecological conditions. Therefore, it represents a valuable resource of biologically active compounds, and the whole process could contribute to sustainable development if post-distillation waste material is used.
Keywords: Lamiaceae; ecological cultivation; phenolics; rosmarinic acid; HPLC.

Resumen. Una forma de cultivar diferentes especies aromáticas de Lamiaceae, especialmente aquellas clasificadas en la sección Nepetoideae, es la producción ecoagrícola. Esta nueva tendencia genera nuevos productos con menor contaminación ambiental y un alto valor para la salud y nutrición humana. La ajedrea (Satureja montana), la menta (Mentha piperita), el tomillo (Thymus vulgaris) y la salvia (Salvia officinalis) son plantas medicinales muy importantes que se introdujeron y se cultivan con éxito en los campos agrícolas de Vojvodina. Este estudio tuvo como objetivo determinar 10 compuestos fenólicos en extractos etanólicos de menta, salvia, tomillo y ajedrea cultivadas según principios ecoagrícolas. La cantidad de compuestos fenólicos examinados se midió utilizando el método de cromatografía líquida (HPLC-DAD). En los cuatro extractos, el ácido rosmarínico (AR) fue el compuesto más abundante, registrándose la mayor cantidad en la menta (12,863.6 µg/g), seguida del tomillo (7,083.76 µg/g). Otros compuestos detectados variaron de 29.29 a 484.37 µg/g para el ácido clorogénico, de 22.67 a 979.77 µg/g para el ácido cafeico, de 11.8 a 339.59 µg/g para el ácido ferúlico, de

J. Mex. Chem. Soc. **2025**, *69*(4)
Regular Issue

ISSN-e 2594-0317

no detectado (ND) a 45.93 μg/g para el ácido p-cumárico, de 14.9 a 63.72 μg/g para el ácido cinámico, de ND a 68.13 μg/g para el ácido gálico, de LOD a 125.03 μg/g para la rutina, de 38.98 a 82.75 μg/g para la quercetina. La quercetina se detectó solo en salvia (50.78 μg/g). Los resultados sugieren que la menta, especialmente, acumula mayores cantidades de RA cuando se cultiva en condiciones ecológicas. Por lo tanto, representa una valiosa fuente de compuestos biológicamente activos y todo el proceso podría contribuir al desarrollo sostenible si se utilizan los residuos de la post-destilación.
Palabras clave: Lamiaceae; cultivo ecológico; compuestos fenólicos; ácido rosmarínico; HPLC.

Introduction

The Lamiaceae plant family, one of the most prominent plant families, is divided into two subfamilies: Nepetoideae and Lamioideae [1]. Plants from the Neptoideae subfamily are characterized by rosmarinic acid and a higher amount of essential oil [2]. On the other hand, plants from the Lamioideae subfamily contain iridoids and smaller amounts of essential oil [3]. However, plants from the Nepetoideae section possess the most significant pharmaceutical potential due to their expansive range of uses, including medicinal and aromatic properties [4]. They are also often used as culinary herbs, mainly for flavoring and food preservation. They are also used in condiments, beverages, aromatics, and cosmetics [5].

Species from this family show cosmopolitan distribution as they grow wild and are cultivated worldwide. Modern trends in agriculture, such as eco-agriculture, especially in medicinal and aromatic plant production, make new products less polluting and damaging to the environment and ecology, with a high value for human health and nutrition [6]. Eco-agriculture production preserves biological diversity and soil fertility, protects the environment, and, at the same time, improves the health and safety of produced herbs [7]. This production method involves pesticide-free cultivation but is not organic [8]. It was developed using organic fertilizer to support the farm's environmental sustainability [6]. It is characterized by diverse products with high quality, pests and weeds controlled without harmful ecological input, and improvement in soil quality [9]. These facts are of massive importance because medicinal plants are mainly consumed as tea or spices, row, without any chemical engineering processes. Consequently, herbal material produced in this way reaches a higher price on the processing market of medicinal plants and also in the production of preparations based on them (both drugs and dietary supplements).

In recent decades, the production of medicinal and aromatic plants has been an essential part of agriculture. However, nowadays, a relatively small part of arable land is covered with these plants when compared to areas used for producing cereals, fruits, vegetables, and industrial and fodder plants [10]. Due to the increased demand on the global market, the production of medicinal and aromatic plants also shows a growth tendency. Yet, despite favorable natural conditions, producers still fail to provide sufficient amounts of these plants. Floristic analysis of the Vojvodina region (Republic of Serbia) reveals the presence of around 650 plant species known for their medicinal potential. Although the demand, especially for some aromatic herbs, is constantly growing, numerous factors affect the quality of herbal material regarding pharmacologically active compound content. The concentration of phenolic compounds, which were the focus of this study, is influenced by climate conditions. Some plants, such as sage and winter savory, are more prone to reducing phenolic compounds' production. In contrast, peppermint and thyme produce considerable amounts of rosmarinic acid on Vojvodinian fields. However, only a few species are being cultivated regularly, and efforts are being made to promote and introduce important medicinal and aromatic herbs to the fields [11]. Winter savory (Satureja montana L.), peppermint (Mentha piperita L.), thyme (Thymus vulgaris L.), and sage (Salvia officinalis L.), though some native to the Mediterranean region are promising examples of highly important medicinal plants that were introduced and are being successfully cultivated on fields in Vojvodina. Food- and pharmaceutical products derived from these plants are available worldwide in the form of teas, tea mixtures, various types of dietary supplements, and herbal remedies and are widely used by the general population [12]. Active principles of these plants exhibit, among others, vigorous antibacterial, antifungal, and antioxidant activities [1]. Furthermore, these species are used to extract and isolate a significant number of biologically active compounds, such as rosmarinic acid, chlorogenic acid, and rutin [13]. Although numerous representatives of the Lamiaceae family, especially those belonging to the Nepetoideae subfamily, are characterized by the essential oil, the high content of various phenolic compounds, which contribute to overall medicinal potential, must not be neglected. Namely, rosmarinic acid, one of the most important phenolic

J. Mex. Chem. Soc. **2025**, *69*(4)
Regular Issue

ISSN-e 2594-0317

compounds, is a promising agent for various ailments [14]. However, the percentage of produced rosmarinic acid and other active principles vary due to numerous environmental (photoperiod, cold stress, and soil type) as well as biotic factors (phenophase of collected plant material), which could be reduced using controlled eco-cultivation. Consequently, plant material of uniform quality would lead to better quality control of produced extracts in the pharmaceutical industry [15]. Therefore, the aim of this study was detailed chemical profiling of water-alcoholic liquid extracts of winter savory, mint, thyme, and sage cultivated according to eco-agricultural principles as well as evaluation of positioning of these extracts in comparison to literature data of extracts obtained from wild-growing plants or cultivated regularly.

Experimental

Plant material and preparation of extracts

Four medicinal crops from the Lamiaceae family (sect. Nepetoideae) – winter savory cv. Domaći (S. montana), peppermint cv. Danica (M. piperita), thyme cv. N-19 (T. vulgaris), and sage cv. Primorska (S. officinalis) – were cultivated at the Institute of Field and Vegetable Crops in Novi Sad, Alternative Crops Department, located in Bački Petrovac (45°21'N, 19°35'E). Voucher specimens were confirmed and deposited at the BUNS Herbarium under the numbers 2-1561, 2-1530, 2-1557, and 2-1548, respectively [16].

The selected plants were planted in spring 2017 using seedlings for winter savory, thyme, sage, and stolons for mint. The experiment was conducted on carbonate chernozem soil, and planting was done with a 70 cm row spacing for all plants to enable mechanical weed control. The application of nutrients is harmonized with soil fertility, and irrigation is performed as needed. Neither foliar fertilization nor plant protection agents were used. The experimental plot size was approximately 10m2 (5 rows, 3m long). The harvest was conducted in the second year of cultivation (2018), at the optimal development stage for each species, which occurs during July under the agroecological conditions of Serbia. The plant material was cut approximately 5 cm above the ground (one row per repetition, with the two marginal rows excluded from the test). The harvested plant material was then transferred to a solar dryer, where the temperature did not exceed 40 °C until constant weight was achieved (within 3 days). Dry plant materials were ground to a size of 200 mesh and placed into percolation devices. Extracts were obtained by triple percolation with 40 % ethanol at a drug/solvent ratio 1:4 for 72 hours.

Chemicals and reagents

Methanol and formic acid (HPLC grade) were purchased from Merck KGaA (Darmstadt, Germany). Standard substances including gallic acid (GA), caffeic acid (CA), chlorogenic acid (CHA), ferulic acid (FA), rutin (R), rosmarinic acid (RA), p-coumaric acid (pQA), trans-cinnamic acid (CNA), quercetin-dihydrate (Qe) and quercitrin (Qt) were purchased from Sigma-Aldrich GmbH (Sternheim, Germany).

Preparation of standard solutions

A stock standard solution containing a mixture of GA, CA, CHA, FA, RA, pQA, CAN, R, Qe, and Qt at a concentration of 1 mg/mL was prepared in methanol. A series of working solutions ranging from 0.18 – 36 μg/mL were prepared by dilution of stock standard solutions with methanol.

Sample preparation

Each liquid extract in 2.5 g was evaporated and redissolved in 5 mL of methanol. Before injection, the sample solutions were filtered through a 0.45 μm membrane PTFE filter (Rotilabo-Spritzenfilter 13 mm, Roth, Karlsruhe, Germany). The amounts of quantified phenolics and flavonoids were expressed as μg/g of liquid ethanolic extract and μg/g of dry extract (after quantification of dry extract yield).

Instrumentation and analytical conditions

HPLC was performed on Nucleosil C18 4.6 μm, 250 mm column by Agilent 1100 series instrument equipped with a diode array detector (DAD). The solvent gradient was performed by varying the proportion of solvent A (1 % formic acid in water (v/v)) to solvent B (methanol) as follows: initial 10 % B (flow 1 mL/min); 10 min, 25 % B (flow 0.8 mL/min); 20 min, 45 % B (flow 0.7 mL/min); 35 min, 70 % B (flow 0.7 mL/min); 40 min, 100 % B (flow 1mL/min). The total running time, including post-run time, was 48 min. The column temperature

J. Mex. Chem. Soc. **2025**, *69*(4)
Regular Issue

ISSN-e 2594-0317

was maintained at 30 ºC, while the injection volume was 10 µL. The elution of compounds of interest was monitored at 280, 330, and 350 nm. The UV λmax for gallic, caffeic, and trans-cinnamic acids was 280 nm for p-coumaric, chlorogenic, rosmarinic, ferulic, and quercetin at 330 nm. In comparison, rutin and quercitrin were monitored at 350 nm.

Method validation

The developed method was validated in terms of linearity, repeatability, reproducibility, recovery, limit of detection (LOD), and limit of quantification (LOQ). Linearity was established by least-squares regression analysis of the results obtained after injection of six calibration standards mixture of increasing concentration in duplicate. The goodness-of-fit of the data was established by the determination of the linear regression coefficient (R2). Recoveries were assessed by spiking each extract at two concentration levels with a mixture of standards. The precision of the method was estimated through repeatability and reproducibility expressed as relative standard deviations (RSDs) of six replicates performed on the same day (intra-day) and three different days (inter-day) at three concentration levels for each compound. Limits of detection and quantification were determined as three and 10 standard deviations (SD) obtained after injection of natural samples spiked with low concentrations of analytes. These values were considered acceptable when the signal-to-noise ratio was ≥3 for LOD and ≥10 for LOQ.

Data processing

The results were processed using Microsoft Office Excel v2016 and Statsoft Statistica v12.5 software packages. The differences between analyzed extracts regarding the quantity of secondary metabolites were tested by the Kruskal-Wallis test, followed by the posthoc Dunn test. In contrast, the level of significance was kept at p= 0.05.

Results and discussion

Validation results

The applied chromatographic elution protocol separated peaks of interest well in the examined samples (Figures 1 and 2), enabling simultaneous quantification of ten phenolic compounds with suitable sensitivity, accuracy, and precision. Validation data are summarized in Table 1.

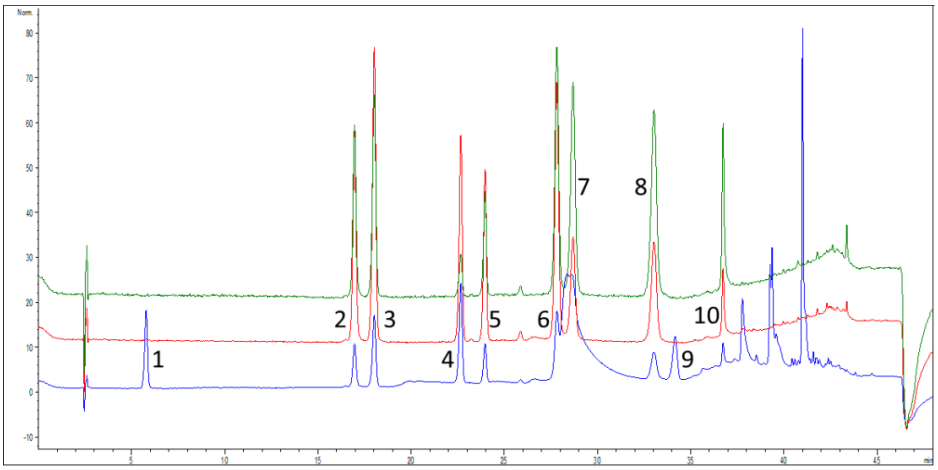

Fig. 1. HPLC-DAD chromatogram of calibration standards mixture (c = 8 µg/mL) with detection at 280 nm (blue), 330 nm (red) and 350 nm (green): 1 – gallic acid, 2 - p-coumaric acid, 3-quercetin, 4 -caffeic acid, 5 - chlorogenic acid, 6 - rosmarinic acid, 7 – rutin, 8 – quercetin, 9 - *trans*-cinnamic acid, 10 – ferulic acid.

J. Mex. Chem. Soc. **2025**, *69*(4)
Regular Issue

ISSN-e 2594-0317

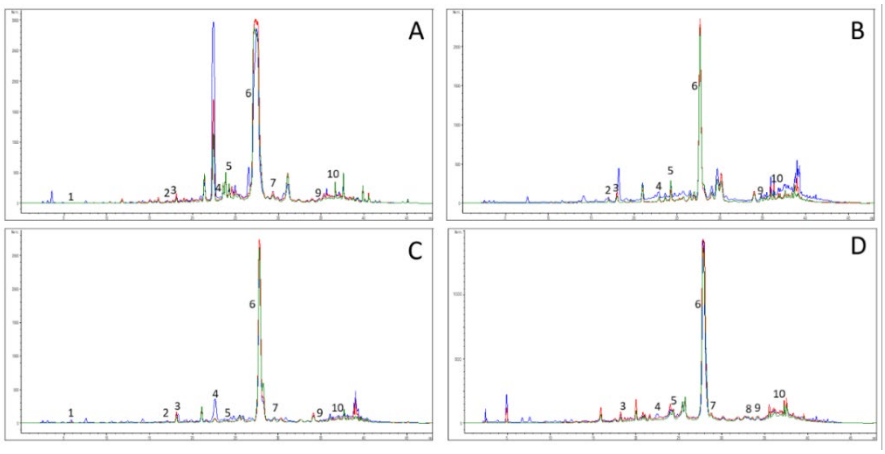

Fig. 2. HPLC-DAD chromatograms of analyzed liquid extracts of *M. piperita* **(A)**, *S. montana* **(B)**, *T. vulgaris* **(C)**, and *S. officinalis* **(D)** with detection at 280 nm (blue), 330 nm (red), and 350 nm (green). Detected compounds: 1 – gallic acid, 2 - p-coumaric acid, 3-quercetin, 4 -caffeic acid, 5 - chlorogenic acid, 6 - rosmarinic acid, 7 – rutin, 8 – quercetin, 9 - *trans*-cinnamic acid, 10 – ferulic acid.

Table 1. Analytical method validation data.

Analyte	Equation	R^2	Accuracy (recovery, %)	Precision RSD (%)		LOD (µg/g)	LOQ (µg/g)	Linearity range (µg/mL)	U* (%)
				Intra-day	Inter-day				
RA	y=3.5125x+0.3322	0.9983	91.20-101.47	1.33	1.27	0.15	0.50	0.5-30.0	6
CHA	y=2.9003x+4.6876	0.9995	100.71-101.32	4.50	1.40	0.15	0.30	0.3-30.0	5
CA	y=6.4807x+1.4903	0.9999	100.17-100.46	1.70	1.19	0.05	0.20	0.2-12.0	5
FA	y=1.6072x-5.5118	0.9979	96.96-101.38	0.95	0.64	0.10	0.20	0.2-36.0	6
pQA	y=5.5894x+12.473	0.9901	94.65-102.41	1.70	2.01	0.05	0.20	0.2-12.0	10
CNA	y=7.9398x+6.5653	0.9997	101.82-106.44	1.34	1.77	0.05	0.10	0.1-6.0	11
GA	y=3.0497+5.4495	0.9986	90.07-101.44	1.19	2.33	0.10	0.30	0.3-18.0	15
R	y=2.1225x+5.4787	0.9959	99.56-104.91	1.46	1.38	0.20	0.50	0.15-30.0	8
Qe	y=9.4489x+8.399	0.9981	97.61-102.78	1.42	1.24	0.05	0.20	0.18-10.71	7
Qt	y=2.4017x+2.8372	0.9996	98.39-99.87	1.80	0.94	0.15	0.50	0.5-30.0	5

*Expanded measuring uncertainty calculated with factor k=2

Analysis of samples

According to ethnobotanical studies performed throughout Serbia, Lamiaceae species and preparations based on them are the most frequent plant agents of traditional usage, including medicinal and culinary applications [17]. Their widespread use is supported by general recognition throughout history as safe and health-promoting. Still, nowadays, many scientific studies confirm the effectiveness and safety of these plants and their bioactive constituents [18]. The biological and medicinal potential of Lamiaceae species mostly correlates to the content of phenolic substances and

J. Mex. Chem. Soc. **2025**, *69*(4)
Regular Issue

ISSN-e 2594-0317

essential oils, which are being extracted under various conditions, including different types of solvents and techniques such as maceration, ultrasonic extraction, extraction at elevated pressures, etc. [19-21] Beside essential oil characterization, the phenolic profile is of unquestionable interest for evaluating the pharmacological activity of medicinal plant raw materials. The chemical profiles of examined winter savory, mint, thyme, and sage ethanol extracts are presented in Table 2. In all four extracts, rosmarinic acid was the most abundant compound. The highest amount of rosmarinic acid was recorded in peppermint extract (12.86 mg/g), followed by thyme extract (7.1 mg/g). The lowest amount was characteristic of winter savory extract (4 mg/g). These results correspond to one of the previous chemical screening studies of 29 species belonging to the Lamiaceae family. However, the same investigation showed a higher amount of RA in Salvia officinalis extract when compared to *Mentha piperita* extract, which is not the case in this study [22]. The mint extract examined was also characterized by the highest amounts of phenolic acids (caffeic, chlorogenic, and ferulic acid) and rutin. However, the quantity quantified of rutin was significantly lower than previously reported [23].

The application of principal components analysis to a dataset containing results of detailed chemical characterization from the current study and results from previously conducted studies about investigated species shows that the first two Principal components (PCAs) describe around 60 % of samples' variability (Fig. 3). Results from previous studies, which were the basis for statistical analysis, are presented in Table 3 [21,23-41]. In terms of the first principal component (PCA1), the explained variability mostly correlates with the detected amounts of rosmarinic, gallic, and ferulic acids, while the amounts of chlorogenic acid and rutin dictate the shape of variability (PCA2). The position of the examined samples in the space defined by the first and second-factor axis indicates the separative grouping of processed samples. Namely, it can be concluded that most *S. officinalis* extracts usually contain lower amounts of chlorogenic acid and higher amounts of rutin, opposite to mint. However, the sage extract examined in this study (So1), obtained from ecologically grown *S. officinalis*, contained a lower amount of rutin. The explanation for this difference may be the impact of climate change on sage cultivation. In the studies above, plants were collected from their natural habitat, unlike plants in this research that were cultivated in Vojvodina, which is characterized by specific ecological abiotic factors. The same pattern can also be noticed in the case of *S. Montana* extract (Sm1), whose position is in the positive part of PCA2. On the other hand, thyme (Tv1) and peppermint (Mp1) extracts show separative grouping about other samples, mainly as a result of caffeic and rosmarinic acids amount, which allows us to hypothesize that the ecological cultivation of mint favorizes accumulation of RA. Rosmarinic acid, the most abundant in all extracts, has exciting properties. These properties have led to various applications, from food preservatives to cosmetics [42]. Different studies have shown that RA possesses more antioxidant activity than vitamin E, enabling its use as a stabilizer in natural cosmetics products [42,43]. Also, RA has been reported to have some important biological activities such as antiviral, antibacterial, and anticancerogenic [44,45]. In *in vivo* studies, it has been noticed that RA exhibits anti-allergic, anti-thrombotic, anti-inflammatory, and anticarcinogenic properties as well [46,47]. The inhibition of cyclooxygenase, especially inducible COX-2 isoform, whose expression and activity can be stimulated by various carcinogens, growth factors, inflammatory cytokines, and tumor promoters, is significant in terms of antiinflammatory action but also in cancer prevention [48]. Interestingly, RA and rosmarinic acid-rich extracts protect the skin from the oxidative stress induced by UVA radiation and thus may find their usage in photoprotective dermo-cosmetic preparations [49].

Because of the high content of RA, ethanolic extracts obtained from examined plants can present a good way to consume rosmarinic acid and achieve its benefits for the body. Consuming mint supplements containing phenolic compounds can lead to various benefits because of the highest content of RA and other phenolic acids, such as chlorogenic and ferulic acids. Chlorogenic acid (CHA) is an essential dietary polyphenol that possesses several important therapeutic activities such as antioxidant activity, antibacterial, hepatoprotective, cardioprotective, anti-inflammatory, antipyretic, neuroprotective, anti-obesity, antiviral, anti-microbial, anti-hypertension, and a central nervous system stimulator. Furthermore, it has been found that CHA could modulate lipid and glucose metabolism. The hypocholesterolemic influence of CHA may result from the altered metabolism of nutrients, including amino acids, glucose, and fatty acids [50]. Ferulic acid (FA) is another phenolic acid with high medical potential. Based on preclinical research, FA has been suggested as a potential treatment for many health problems, including Alzheimer's disease, cancer, cardiovascular disorders, diabetes mellitus, and skin disease [51]. Also, flavonol rutin has demonstrated several pharmacological activities, including antioxidant, cytoprotective, vasoprotective, anticarcinogenic, neuroprotective, and cardioprotective activities, and is also present in a notable concentration in the mint extract [43]. This increases the potential benefits of this extract. Furthermore, it must not be neglected that the examined aromatic plants are widely used to isolate essential oil, where valuable phenolic compounds remain unused. It has been suggested that the plant waste material remaining after the isolation of essential oil could be used to isolate various phenolic compounds, especially rosmarinic acid [28]. In conclusion, it can be stated that medicinal and aromatic plants, especially peppermint and thyme, are highly suitable for ecological cultivation in Vojvodina. This may represent an adequate response to worldwide

J. Mex. Chem. Soc. **2025**, *69*(4)
Regular Issue

ISSN-e 2594-0317

increased demand for such species. Furthermore, the results suggest that mint mainly accumulates higher amounts of rosmarinic acid when cultivated under ecological conditions. Although these plant species are extensively studied and well-documented, it is recognized that their secondary metabolite content can vary significantly based on factors such as environmental conditions, geographical origin, and cultivation methods. This variation in chemical composition ultimately influences the medicinal potential of the plant. The innovation of this study lies in comparing the chemical profiles of plants grown using a novel cultivation approach—one that excludes pesticide use while promoting sustainability and environmental stewardship—against those from wild sources or alternative cultivation practices. Considering that evaluated species are mainly being used for essential oil extraction, in this case, the post-distillation waste material would represent a valuable resource of biologically active compounds, and the whole process would contribute to sustainable development.

Table 2. Chemical profiles of examined winter savory, mint, thyme and sage liquid ethanolic extracts (different small Latin letters indicate statistically significant differences at p=0.05 level).

Analyte	***Satureja montana* - Sm1**	***Mentha piperita* - Mp1**	***Thymus vulgaris* - Tv1**	***Salvia officinalis* - So1**
	(µg/g extract)			
RA	4011.4±240.68^{a}	12863.6±771.82^{b}	7083.76±425.02^{c}	5432.4±325.94^{d}
CHA	239.85±11.99^{a}	484.37±24.22^{b}	29.29±1.46^{c}	98.87±4.94^{d}
CA	31.17±1.56^{a}	979.77±48.99^{a}	334.07±16.70^{a}	22.67±1.13^{a}
FA	90.54±5.43^{a}	331.59±19.89^{b}	11.8±0.71^{c}	45.82±2.75^{d}
pQA	45.93±4.59^{a}	29.53±2.95^{b}	16.99±1.70^{c}	<LOD^{d}
CNA	63.72±7.01^{a}	23.13±2.54^{b}	62.74±6.90^{a}	14.9±1.64^{c}
GA	<LOD^{a}	0.42±0.07^{b}	68.13±10.22^{c}	<LOD^{a}
R	<LOD^{a}	125.03±10.00^{b}	40.35±3.23^{c}	114.76±9.18^{b,d}
Qe	70.64±4.94^{a}	71.85±5.03^{a}	82.75±5.79^{a}	38.98±2.74^{b}
Qt	<LOD^{a}	<LOD^{a}	<LOD^{a}	50.78±2.54^{b}
Dry extracts yield (%)	6.82	15.33	7.21	14.1

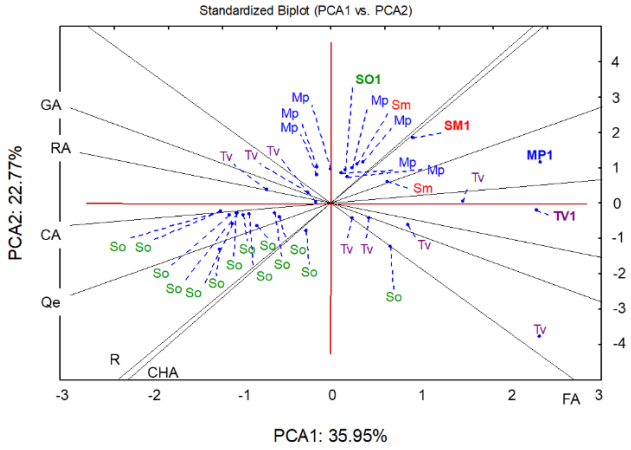

Fig. 3. Principal component analysis biplot.

J. Mex. Chem. Soc. **2025**, *69*(4)
Regular Issue

ISSN-e 2594-0317

Table 3. Input data for principal component analysis.

µg/g d.e.	RA	CHA	CA	FA	pQA	pCA	tCNA	GA	R	Qe	Qt	Ref.	Origin of plant material
S. montana	1826.2	NDt	2079.6	726.9	NDt	NDt	25.8	772.05	5681.2	1200.5	NDt	[24]	Cultivated in an experimental farm
	17000	NDt	ND	NDt	100	NDt	100	NDt	500	1500	NDt	[25]	Wild growing plants
	NDt	NDt	65.95	25.2	24.1	NDt	NDt	NDt	NDt	NDt	NDt	[26]	Wild growing plants
	NDt	NDt	NDt	NDt	NDt	NDt	NDt	NDt	12160	NDt	NDt	[27]	Wild growing plants
	58818.18	3516.86	457.04	362.16	183.72	183.72	254.88	ND	ND	282.56	ND	TS	Eco-agricultural production
M. pipreita	10190	560	2530	180	NDt	NDt	NDt	130	1250	ND	NDt	[28]	Cultivated
	12400	730	1860	ND	NDt	ND	NDt	ND	2180	840	NDt	[23]	Cultivated
	35330	NDt	1460	NDt	NDt	NDt	NDt	NDt	NDt	NDt	NDt	[29]	Cultivated
	NDt	NDt	NDt	NDt	NDt	NDt	NDt	NDt	6080	NDt	NDt	[27]	Wild growing plants
	NDt	1074.5	483.5	215.5	NDt	NDt	NDt	ND	560	ND	NDt	[30]	Wild growing plants
	NDt	NDt	NDt	17.5	NDt	31	NDt	NDt	621.5	NDt	ND	[31]	Cultivated in an experimental farm
	19085	NDt	271	NDt	NDt	ND	NDt	ND	NDt	NDt	NDt	[32]	Comercially available
	83911.29	3159.62	6391.19	2163.01	192.63	192.63	150.9	2.74	815.59	468.69	ND	TS	Eco-agricultural production
T. vulgaris	94200	560	900	8640	180	NDt	NDt	1004.18	14160	830	NDt	[28]	Cultivated
	534.36	ND	102.2	267.18	70.08	NDt	2083.42	ND	NDt	NDt	NDt	[21]	Cultivated
	56620	NDt	1460	NDt	NDt	NDt	NDt	NDt	NDt	NDt	NDt	[29]	Cultivated
	NDt	NDt	NDt	NDt	NDt	NDt	NDt	NDt	14400	NDt	NDt	[27]	Wild growing plants
	14720	NDt	590	NDt	NDt	NDt	NDt	NDt	NDt	NDt	NDt	[33]	Cultivated

J. Mex. Chem. Soc. **2025**, *69*(4)
Regular Issue

ISSN-e 2594-0317

	ND	NDt	58	ND	NDt	12.00	NDt	ND	NDt	NDt	NDt	[34]	Comercially available or wild growing plants
	21861	NDt	1215	NDt	NDt	400	NDt	375	NDt	NDt	NDt	[32]	Comercially available
	NDt	NDt	5170	905	NDt	ND	NDt	NDt	NDt	NF	NDt	[35]	Comercially available
	5700	ND	550	ND	NDt	180	NDt	NDt	NDt	NDt	NDt	[36]	Comercially available
	98249.10	406.24	4633.43	163.66	235.64	235.64	870.18	944.94	559.64	539.79	ND	TS	Eco-agricultural production
S. officinalis	1035.3	70.76	114.84	1089.82	69.6	NDt	149.06	ND	NDt	NDt	NDt	[21]	Cultivated
	34520	NDt	1460	NDt	NDt	NDt	NDt	NDt	NDt	NDt	NDt	[29]	Cultivated
	6500	NDt	520	NDt	NDt	NDt	NDt	NDt	NDt	NDt	NDt	[37]	Comercially available
	NDt	NDt	NDt	NDt	NDt	NDt	NDt	NDt	26880	NDt	NDt	[27]	Wild growing plants
	16330	NDt	680	NDt	NDt	NDt	NDt	NDt	NDt	NDt	NDt	[33]	Cultivated
	48656	NDt	1298.05	1220.5	NDt	NDt	NDt	18.7	NDt	NDt	NDt	[38]	Wild growing plants
	91890	ND	3475.2	1562.15	NDt	ND	NDt	94.1	NDt	NDt	NDt	[39]	Cultivated
	36434	783.5	594	NDt	NDt	562.5	NDt	NDt	NDt	NDt	NDt	[40]	Wild growing plants
	504.58	NDt	ND	ND	NDt	NDt	NDt	NDt	NDt	NDt	NDt	[41]	Cultivated in an experimental farm
	201.55	NDt	1.94	3.1	NDt	NDt	NDt	NDt	NDt	NDt	NDt	[41]	Cultivated in an experimental farm
	NDt	NDt	ND	49	NDt	ND	NDt	ND	NDt	NDt	NDt	[34]	Comercially available or wild growing plants
	6811	NDt	548	NDt	NDt	559	NDt	ND	NDt	NDt	NDt	[32]	Comercially available
	NDt	NDt	2960	135	NDt	103	NDt	NDt	NDt	1780	NDt	[35]	Comercially available
	5500	ND	510	50	NDt	ND	NDt	NDt	NDt	NDt	NDt	[36]	Comercially available
	38527.66	701.21	160.78	324.96	ND	ND	105.67	ND	813.9	283.5	360.14	TS	Eco-agricultural production

NDt − not determined; ND − not detected; TS – this study

J. Mex. Chem. Soc. **2025**, *69*(4)
Regular Issue

ISSN-e 2594-0317

Acknowledgments

The authors are grateful to The Ministry of Education, Science and Technological Development, Republic of Serbia (451-03-68/2020-14/200114 and 451–03–66/2024–03/200032).

References

1. Bekut, M.; Brkić, S.; Kladar, N.; Dragović, G.; Gavarić, N.; Božin, B. *Pharmacol. Res.* **2018,** *133*. DOI: http://dx.doi.org/10.1016/j.phrs.2017.12.016
2. Zhao, F.; Chen, Y.P.; Salmaki, Y.; Drew, B.T.; Wilson, T.C.; Scheen, A.C.; Celep, F.; Bräuchler, C.; Bendiksby, M.; Wang, Q.; Min, D.Z.; Peng, H.; Olmstead, R.G.; Li, B.; Xiang, C.L. *BMC Biol*. **2021**, *19*, 2. DOI: http://dx.doi.org/10.1186/s12915-020-00931-z
3. Takhtadzhian, A. L.; Takhtajan, L. A.; Takhtajan, A., in: *Diversity and classification of flowering plants*. Columbia University Press: 1997.
4. Mimica-Dukic, N.; Bozin, B. *Curr. Pharm. Des.* **2008,** *14*, 3141-3150. DOI: https://doi.org/10.2174/138161208786404245
5. Astutik, S.; Pretzsch, J.; Ndzifon Kimengsi, J. *Sustainability.* **2019,** *11*, 5483. DOI: https://doi.org/10.3390/su11195483
6. Marcelino, S.; Hamdane, S.; Gaspar, P.D.; Paço, A. *Sustainability.* **2023**, *15*, 14095. DOI: https://doi.org/10.3390/su151914095
7. Shang, Y.; Hasan, M.; Ahammed, G. J.; Li, M.; Yin, H.; Zhou, J. *Molecules.* **2019,** *24*, 2558. DOI: https://doi.org/10.3390/molecules24142558
8. Möhring, N.; Finger, R. *Food Policy.* **2022**, *106*, 102188. DOI: http://dx.doi.org/10.1016/j.foodpol.2021.102188
9. Shao, Y.; Chen, Z.; Xiao, H.; Zhu, Z.; Li, B. *Environ. Sci. Eur.* **2019,** *31*, 22. DOI: https://doi.org/10.1186/s12302-019-0204-2
10. Golijan, J. *Lekovite sirovine.* **2016**, 74-83. DOI: https://doi.org/10.5937/leksir1636074G
11. Sikora, V.; Stojanović, A.; Popović, V.; Brdar-Jokanović, M.; Aćimović, M.; Kiprovski, B. *Selekcija i semenarstvo.* **2017**, *23*, 49-55. DOI: https://doi.org/10.5937/SelSem1701049S
12. Jeremić, K.; Todorović, N.; Goločorbin-Kon, S.; Pavlović, N.; Milošević, N.; Gavarić, N.; Lalić-Popović, M. *Timočki medicinski glasnik.* **2019,** *44*, 56-62.
13. Raja, R. R. *Res. J. Med. Plant* **2012**, *6*, 203-213. DOI: https://doi.org/10.3923/rjmp.2012.203.213
14. Hase, T.; Shishido, S.; Yamamoto, S.; Yamashita, R.; Nukima, H.; Taira, S.; Toyoda, T.; Abe, K.; Hamaguchi, T.; Ono, K. *Sci. Rep.* **2019**, *9*, 8711.
15. Fletcher, R. S.; Slimmon, T.; Kott, L. S. *Open Agric. J.* **2010**, *4*.
16. https://sweetgum.nybg.org/science/ih/herbarium-details/?irn=126775 accessed in January 2025.
17. Zlatković, B. K.; Bogosavljević, S. S.; Radivojević, A. R.; Pavlović, M. A. *J. Ethnopharmacol.* **2014,** *151*, 704-713. DOI: https://doi.org/10.1016/j.jep.2013.11.037
18. World Health Organisation (WHO). WHO Traditional Medicinal Strategy: 2014-2023, 2013, https://iris.who.int/bitstream/handle/10665/92455/9789241506090_eng.pdf;jsessionid=90AB2063DEA42EADA317D933706EEFCD?sequence=1, accessed in August 2020.
19. Zhang, X.-L.; Guo, Y.-S.; Wang, C.-H.; Li, G.-Q.; Xu, J.-J.; Chung, H. Y.; Ye, W.-C.; Li, Y.-L.; Wang, G.-C. *Food Chem.* **2014,** *152*, 300-306. DOI: https://doi.org/10.1016/j.foodchem.2013.11.153
20. Grygierczyk, G.; Sajewicz, M.; Staszek, D.; Wojtal, Ł.; Waksmundzka-Hajnos, M.; Kowalska, T. *J. Liq. Chromatogr. Relat. Techn.* **2009,** *32*, 1223-1240.
21. Roby, M. H. H.; Sarhan, M. A.; Selim, K. A.-H.; Khalel, K. I. *Ind Crops Prod.* **2013,** *43*, 827-831. DOI: https://doi.org/10.1016/j.indcrop.2012.08.029
22. Shekarchi, M.; Hajimehdipoor, H.; Saeidnia, S.; Gohari, A. R.; Hamedani, M. P. *Pharmacogn. Mag.* **2012,** *8*, 37. DOI: https://doi.org/10.4103/0973-1296.93316

J. Mex. Chem. Soc. **2025**, *69*(4)
Regular Issue

ISSN-e 2594-0317

23. Mišan, A.; Mimica-Dukić, N.; Mandić, A.; Sakač, M.; Milovanović, I.; Sedej, I. *Open Chem.* **2011,** *9*, 133-142. DOI: https://doi.org/10.2478/s11532-010-0126-8
24. El Tawab, A. M. A.; Shahin, N. N.; AbdelMohsen, M. M. *Chem. Biol. Interact.* **2014**, *224*, 196-205. DOI: https://doi.org/10.1016/j.cbi.2014.11.001
25. Kremer, D.; Kosir, I. J.; Koncic, M. Z.; Cerenak, A.; Potocnik, T.; Srecec, S.; Kosalec, I. *Curr. Drug Targets* **2015**, *16*, 1623-1633. DOI: https://doi.org/10.2174/1389450116666150202161926
26. Ćetković, G. S.; Mandić, A. I.; Čanadanović-Brunet, J. M.; Djilas, S. M.; Tumbas, V. T. *J. Liq. Chromatogr. Rel. Technol.* **2007,** *30*, 293-306.
27. Sofic, E.; Copra-Janicijevic, A.; Salihovic, M.; Tahirovic, I.; Kroyer, G. Med. *Plants - Int. J. Phytomed. Relat. Ind.* **2010**, *2*, 97-102. DOI: https://doi.org/10.5958/j.0975-4261.2.2.015
28. Gavarić, N.; Kladar, N.; Mišan, A.; Nikolić, A.; Samojlik, I.; Mimica-Dukić, N.; Božin, B. *Ind. Crops Prod.* **2015**, *74*, 457-464. DOI: https://doi.org/10.1016/j.indcrop.2015.05.070
29. Kozlowska, M.; Laudy, A. E.; Przybyl, J.; Ziarno, M.; Majewska, E. *Acta Pol. Pharm.* **2015**, *72*, 757-767.
30. Farnad, N.; Heidari, R.; Aslanipour, B. *J. Food Meas. Charact.* **2014**, *8*, 113-121. DOI: https://doi.org/10.1007/s11694-014-9171-x
31. Moldovan, R.; Oprean, R.; Benedec, D.; Hanganu, D.; Duma, M.; Oniga, I.; Vlase, L. *Dig. J. Nanomater. Biostruct*. **2014**, *9*, 559-566.
32. Shan, B.; Cai, Y. Z.; Sun, M.; Corke, H. *J. Agric. Food Chem.* **2005**, *53*, 7749-7759. DOI: https://doi.org/10.1021/jf051513y
33. Kozics, K.; Klusová, V.; Srančíková, A.; Mučaji, P.; Slameňová, D.; Hunáková, Ľ.; Kusznierewicz, B.; Horváthová, E. *Food Chem.* **2013,** *141*, 2198-2206. DOI: https://doi.org/10.1016/j.foodchem.2013.04.089
34. Proestos, C.; Chorianopoulos, N.; Nychas, G.-J.; Komaitis, M. *J. Agric. Food Chem.* **2005,** *53*, 1190-1195. DOI: https://doi.org/10.1021/jf040083t
35. Wojdyło, A.; Oszmiański, J.; Czemerys, R. *Food Chem.* **2007,** *105*, 940-949. DOI: https://doi.org/10.1016/j.foodchem.2007.04.038
36. Zgórka, G.; Głowniak, K. *J. Pharm. Biomed. Anal.* **2001,** *26*, 79-87. DOI: https://doi.org/10.1016/S0731-7085(01)00354-5
37. Milevskaya, V.; Temerdashev, Z.; Butyl'skaya, T.; Kiseleva, N. *J. Anal. Chem.* **2017**, *72*, 342-348. DOI: https://doi.org/10.1134/S1061934817030091
38. Ben Farhat, M.; Jordán, M. a. J.; Chaouech-Hamada, R.; Landoulsi, A.; Sotomayor, J. A. *J. Agric. Food Chem.* **2009**, *57*, 10349-10356. DOI: https://doi.org/10.1021/jf901877x
39. Farhat, M. B.; Landoulsi, A.; Chaouch-Hamada, R.; Sotomayor, J. A.; Jordán, M. J. *Ind. Crops Prod.* **2013**, *49*, 904-914. DOI: https://doi.org/10.1016/j.indcrop.2013.06.047
40. Coisin, M.; Necula, R.; Grigoras, V.; Gille, E.; Rosenhech, E.; Zamfirache, M. M. *Analele Stiintifice ale Universitatii" Al. I. Cuza" din Iasi.* **2012,** *58*, 35.
41. Lima, C. F.; Valentao, P. C.; Andrade, P. B.; Seabra, R. M.; Fernandes-Ferreira, M.; Pereira-Wilson, C. *Chem. Biol. Interact.* **2007,** *167*, 107-115. DOI: https://doi.org/10.1016/j.cbi.2007.01.020
42. Petersen, M.; Simmonds, M. S. *Phytochemistry.* **2003,** *62*, 121-125.
43. Lin, Y.-L.; Chang, Y.-Y.; Kuo, Y.-H.; Shiao, M.-S. *J. Nat. Prod.* **2002**, *65*, 745-747. DOI: https://doi.org/10.1021/np010538y
44. Huang, S.-s.; Zheng, R.-l. *Cancer Lett.* **2006,** *239*, 271-280. DOI: https://doi.org/10.1016/j.canlet.2005.08.025
45. Sanbongi, C.; Takano, H.; Osakabe, N.; Sasa, N.; Natsume, M.; Yanagisawa, R.; Inoue, K. i.; Sadakane, K.; Ichinose, T.; Yoshikawa, T. *Clin. Exp. Allergy* **2004**, *34*, 971-977. DOI: https://doi.org/10.1111/j.1365-2222.2004.01979.x
46. Lee, J.; Kim, Y. S.; Park, D. *Biochem. Pharmacol.* **2007**, *74*, 960-968. DOI: https://doi.org/10.1016/j.bcp.2007.06.007
47. Osakabe, N.; Yasuda, A.; Natsume, M.; Yoshikawa, T. *Carcinogenesis* **2004**, *25*, 549-557. DOI: https://doi.org/10.1093/carcin/bgh034

J. Mex. Chem. Soc. **2025**, *69*(4)
Regular Issue

ISSN-e 2594-0317

48. Lin, Y.; Shi, R.; Wang, X.; Shen, H.-M. *Curr. Cancer Drug Targets* **2008**, *8*, 634-646. DOI: https://doi.org/10.2174/156800908786241050
49. Psotova, J.; Svobodova, A.; Kolarova, H.; Walterova, D. *J. Photochem. Photobiol. B: Biol.* **2006**, *84*, 167-174. DOI: https://doi.org/10.1016/j.jphotobiol.2006.02.012
50. Naveed, M.; Hejazi, V.; Abbas, M.; Kamboh, A. A.; Khan, G. J.; Shumzaid, M.; Ahmad, F.; Babazadeh, D.; FangFang, X.; Modarresi-Ghazani, F. *Biomed. Pharmacother.* **2018**, *97*, 67-74. DOI: https://doi.org/10.1016/j.biopha.2017.10.064
51. Mancuso, C.; Santangelo, R. *Food Chem. Toxicol.* **2014**, *65*, 185-195. DOI: https://doi.org/10.1016/j.fct.2013.12.024

Article

J. Mex. Chem. Soc. **2025**, *69*(4)
Regular Issue

ISSN-e 2594-0317

Computational Study of New Isatin Molecules as Potential Thymidine Phosphorylase (TP) Inhibitors Against Cancer Activity. 3D-QSAR, Molecular Docking, ADME-Tox, And Molecular Dynamics Simulation Analysis

Reda EL-Mernissi[1], Marwa Alaqarbeh[2*], Ayoub Khaldan[1], Abdelouahid Sbai[1], Mohammed Aziz Ajana[1], Tahar Lakhlifi[1], Mohammed Bouachrine[1]

[1]Molecular Chemistry and Natural Substances Laboratory, Faculty of Science, University of Moulay Ismail. Meknes. Morocco.
[2]Applied Science Research Center, Applied Science Private University, Jordan.

***Corresponding author:** Marwa Alaqarbeh, email: marwaqarbh@hotmail.com; m_alaqarbeh@asu.edu.jo

Received December 5th, 2024; Accepted January 29th, 2025.

DOI: http://dx.doi.org/10.29356/jmcs.v69i4.2150

Abstract. The quenching of TP enzyme activity helps treat and control diseases. In this research, computational methods investigated a series of thirty isatin-based oxadiazoles as potential TP inhibitors. 3D-QSAR was used to design four isatins (A, B, C, and D) derivatives with high anticancer activity. Molecular Docking was used to investigate interaction types between designed isatin derivatives (A, B, C, and D) and the TP enzyme (PDB: 4EAD); the results show that all compounds have several types of exciting interactions with no unfavorable interactions, but only compounds A and B have conventional hydrogen bond interactions as promising inhibition activity. The Binding Energy between (A, B, C, and D) compounds with TP enzyme were obtained by molecular dynamic simulation at 100 ns. A and B compounds had a more substantial binding free energy than C and D compounds, with binding energies of-20.1374 +/- 0.1189 kJ/mol, -20.1897 +/- 0.1333 kJ/mol, -18.1344 +/-0.1604 kJ/mol, and 19.077 +/-0.1549 kJ/mol, respectively. The pharmacokinetics of (A, B, C, and D) molecules were obtained by using ADMET predictions. Based on the above findings, the current work recommends four compounds as potential TP enzyme inhibitors that activate colorectal and breast cancers.
Keywords: Cancer; isatin; molecular modeling; thymidine phosphorylase (TP).

Resumen. La inhibición de la actividad de la enzima TP ayuda a tratar y controlar las enfermedades. En esta investigación, se utilizaron métodos computacionales para investigar una serie de treinta oxadiazoles basados en isatina como posibles inhibidores de TP. Se utilizó 3D-QSAR para diseñar cuatro derivados de isatinas (A, B, C y D) con alta actividad anticancerígena. Se utilizó el acoplamiento molecular para investigar los tipos de interacción entre los derivados de isatina diseñados (A, B, C y D) y la enzima TP (PDB: 4EAD); los resultados muestran que todos los compuestos tienen varios tipos de interacciones excitantes sin interacciones desfavorables, pero solo los compuestos A y B tienen interacciones de enlace de hidrógeno convencionales como actividad de inhibición prometedora. La energía de enlace entre los compuestos (A, B, C y D) y la enzima TP se obtuvo mediante simulación dinámica molecular a 100 ns. Los compuestos A y B tenían una energía libre de enlace más sustancial que los compuestos C y D, con energías de enlace de -20,1374 +/- 0,1189 kJ/mol, -20,1897 +/- 0,1333 kJ/mol, -18,1344 +/- 0,1604 kJ/mol y 19,077 +/- 0,1549 kJ/mol, respectivamente. La farmacocinética de las moléculas (A, B, C y D) se obtuvo mediante predicciones ADMET. Con base en los hallazgos anteriores, recomendamos considerar cuatro compuestos como posibles inhibidores de la enzima TP que activan los cánceres colorrectales y de mama.

J. Mex. Chem. Soc. **2025**, *69*(4)
Regular Issue

ISSN-e 2594-0317

Palabras clave: Cáncer; isatina; docking molecular; timidina fosforilasa (TP).

Introduction

Cancer is a dangerous, deadly disease and is considered the second leading cause of premature death in the world after cardiovascular diseases [1–2]. The growth of cancer cells contributes to the spread of tumor cells to other organs by moving cancer cells through the blood vessels, a process called malignant disease [3–4]. The spread of cancer and its infecting various parts of the human body prompted researchers worldwide to find practical solutions to treat this disease, which exhausted the health sector and drained a lot of money [5]. TP is a nucleoside enzyme that plays an essential role in pyrimidine metabolism. It catalyzes thymidine conversion to thymine and 2-deoxy-α-D-ribose-1-phosphate (dRib-1-P) by a catabolic pathway. TP has been shown to promote tumor angiogenesis and is overexpressed in several human cancers, metastasis, invasion, immune response evasion, and resistance to apoptosis. Indeed, TP is used clinically against several cancer diseases, such as colon and metastatic breast cancer [6], because it is vital in activating capecitabine drugs against lung cancer and colorectal cancer [7–8]. Thymidine phosphorylase results in various pathological diseases such as rheumatoid arthritis, atherosclerosis, psoriasis, and inflammatory bowel disease [9]. Previous research investigations have revealed that isatin compounds have a wide range of biological activities, including anti-inflammatory [10], anti-HIV [11], antidepressant [12], anticonvulsant [13], antimalarial [14], antimicrobial [15], antiviral [16], antibacterial [17], and potential anticancer drugs [18-20]. In addition, isatin is widely distributed in the central nervous system and has been detected as a metabolite of epinephrine or tryptophan [21]. Isatin molecule was discovered by two chemists, Auguste Laurent and Otto Linné Erdmann [22]; it has a molecular formula of C_8H_5NO, a naturally occurring substance found in *Couroupita guianensis* plants of isatis [23-24].

In this work, computational studies based on 3D-QSAR, Comparative Molecular Similarity Indices Analysis, and Field Analysis (CoMSIA and CoMFA) [25–26] were used to understand the relationship between the structure of isatin-based oxadiazole and activity as TP inhibitors. Furthermore, four novel isatins were designed as effective inhibitors of TP inhibitors as potential anticancer drugs by utilizing the structural information obtained from the two models that exhibit excellent predictive potencies.

The pharmaceutical properties for designed (A, B, C, and D) molecules were explored by ADMET studies [27]. Furthermore, molecular dynamics simulations were performed for designs (A, B, C, and D) to investigate the stability of interactions with TP inhibitor enzyme.

Materials and methods

In the computational investigation of anticancer isatin-based oxadiazoles activity, the 30 compounds were divided into 2 groups: a training set of twenty-four molecules and six a test set of the remaining compounds. For the calculations, all experimental IC_{50} (μM) activity values were transformed to the negative logarithm of pIC_{50}, the pIC_{50} calculated to use the formula (pIC_{50} = -logIC_{50}) and (1μM=$\mathbf{1.0\times10^{-6}}$M). Table 1 and Fig. 1 show the isatin-based oxadiazoles' structures and their pIC_{50} biological activity [9].

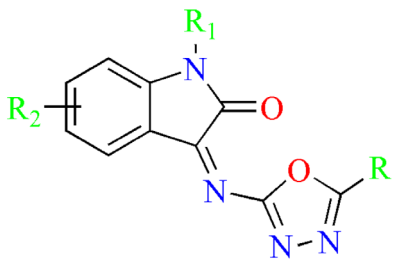

Fig. 1. Structures of isatin-based oxadiazole in the current study.

J. Mex. Chem. Soc. **2025**, *69*(4)
Regular Issue

ISSN-e 2594-0317

Table 1. Structures of isatin-based oxadiazole with TP inhibition activities.

N	R	R_1	R_2	pIC_{50} (M)
1*	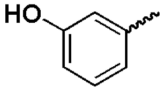	N-Isopropyl	H	5.11
2	-	N-Butyl	H	5.03
3	-	H	5-isopropyl	5.28
4	-	N-Pentyl	H	4.78
5	-	H	-	4.71
6	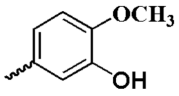	-	5-isopropyl	5.21
7	-	N-Isopropyl	H	5.33
8	-	N-Butyl	-	5.28
9*	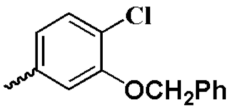	H	5-isopropyl	4.84
10*	-	N-Isopropyl	H	4.95
11	-	N-Butyl	-	4.75
12	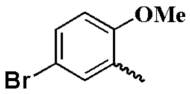	H	5-isopropyl	4.31
13	-	N-Isopropyl	H	4.54
14	-	N-Butyl	-	4.41
15	-	N-Pentyl	-	4.34
16	-	H	-	4.31
17	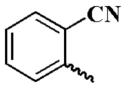	N-Isopropyl	-	4.60
18	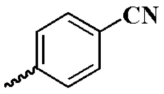	N-Butyl	-	4.71
19*	-	N-Pentyl	-	4.46
20	-	H	5-isopropyl	4.57
21	-	N-Isopropyl	H	4.74

J. Mex. Chem. Soc. **2025**, *69*(4)
Regular Issue

ISSN-e 2594-0317

N	R	R_1	R_2	pIC_{50} (M)
22	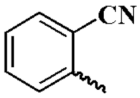	N-Butyl	-	4.43
23	-	N-Pentyl	-	4.58
24	-	H	5-isopropyl	4.66
25	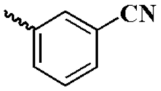	H	-	4.47
26*	-	N-Pentyl	H	4.46
27	-	N-Butyl	-	4.52
28	-	H	-	4.73
29*	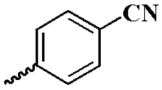	-	-	4.75
30	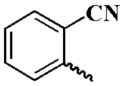	-	-	4.79

Minimization and alignment

The essential characteristic in 3D-QSAR investigations is molecular alignment [28]. Sybyl was used to study molecular structures, then reduced using the Tripos Force Field [29] with 0.01 kcal/mol gradient convergence criteria and Gasteiger–Huckel charges, as well as the conjugate gradient approach. The Sybyl software was utilized to align the isatin compounds by using the most active molecule **C7** template.

QSAR Studies

CoMFA and CoMSIA contours

To determine CoMFA and CoMSIA contour as QSAR keys, the electrostatic (E) and steric (S) fields are observed on the first contour. Whereas in the second contour, the hydrogen bond acceptor (A), hydrogen bond donor (D), and hydrophobic (H) fields are observed. The calculations are made at 2.0 Å for each lattice, and Gasteiger–Hückel method is loaded for each structure [30].

PLS validations

Partial Least Squares (PLS) is an application used to predict a linear correlation between anticancer activity values and the two contours by obtaining the Leave-One-Out (LOO) approach was used to obtain the optimal number of components (N) and the coefficient of cross-validation correlation (Q^2) [31]. The non-cross-validation approach yielded the correlation coefficient (R^2), F-test value (F), and standard error of the estimate (SEE). At the same time, external validation was also used to evaluate the testing sets by ($r^2_{ext} > 0.6$), the needed criterion.

External validation

The criteria of Golbraikh, Tropsha, and Roy [32] are relationships to create reliable models and can be used to predict molecular activities for the test set. Table 4 below shows all the criteria results $r^2 ext = 1 - \frac{PRESS}{SD}$

J. Mex. Chem. Soc. **2025**, *69*(4)
Regular Issue

ISSN-e 2594-0317

PRESS: Indicates squared deviations between predicted and measured values.
SD: The total of the squared deviations between the average activity of the test set and training set.

$$k' = \frac{\sum\left(Y_{\frac{pred}{test}} \times Y_{test}\right)^2}{\sum(Y_{test})^2},\ k = \frac{\sum\left(Y_{test} \times Y_{\frac{pred}{test}}\right)^2}{\sum(Y_{\frac{pred}{test}})^2},\ r_0'^2 = 1 - \frac{\sum\left(\bar{Y}_{\frac{pred}{test}} - k \times \bar{Y}_{\frac{pred}{test}}\right)^2}{\sum\left(Y_{\frac{pred}{test}} - k \times Y_{\frac{pred}{test}}\right)^2},\ r_0^2 = 1 - \frac{\sum(Y_{pred/test} - k \times Y_{pred/test})^2}{\sum(Y_{pred/test} - k \times \bar{Y}_{pred/test})^2}$$

Y test and Y pred: Indicates the experimental and calculated values successively.

At zero intercepts, we start the calculation with K, K' then we can calculate $r_0'^2$ and r_0^2. In addition to these external validation criteria, and in order to obtain a predictable and reliable model, the researchers have used another criterion called Roy [33], Roy's criteria are determined using the parameters, r_m^2, Δr_0^2, Δr_m^2 and $r_m'^2$, both require the expressions below:

$$r_m^2 = r^2\left(1 - \sqrt{(r^2 - r_0^2)}\right);\quad r_m'^2 = r^2\left(1 - \sqrt{(r^2 - r_0'^2)}\right);\ \Delta r_0^2 = r_0^2 - r_0'^2;\ \Delta r_m^2 = r_m'^2 - r_m^2.$$

Molecular docking

Molecular Docking was used to determine the interactions with ligands (A, B, C, and D) and the TP enzyme (4EAD) [34-35]. The preparation of Protein is the first step after downloading this Protein from a PDB (Protein Data Bank) database (www.rcsb.org), then eliminating the water molecules of this receptor and adding polar hydrogens and Kohlman charges. In addition, the Surflex-dock technique available in Sybyl-x.2.0 was used for the docking protocol's protein and ligand preparation steps. Each complex of ((A, B, C, and D) and the TP enzyme (4EAD)) was investigated by the pymol program to be exported in a single file in pdb form [36]. The complex structures were studied by Discovery Studio in 2016 to know and see the types of interaction [37].

ADMET properties

The term ADMET uses in silico techniques to better forecast and understand how medications affect the body. It can optimize clinical usage, reduce unwanted side effects, direct research toward development, and improve therapeutic options. The developed drugs' physicochemical characteristics were assessed using the SwissADME and pKCSM online programs [38]. The absorption, distribution, metabolism, excretion, and toxicities are examples of traditional pharmacokinetic parameters (ADMET) [39].

Molecular dynamics simulation (MD)

The four complexes (A, B, C, and D) were chosen for MD simulation, and the Gromacs simulation package [40] was used, using a truncated octahedral box containing TIP3P Water molecules with Charmm36 force field [41-44]. To ensure a fully converged system, the NPT and NVT are fixed at 1000ps (1,000,000 steps) and 100ps (50,000 steps), using 0.1 and 0.2 fs, respectively. To eliminate any steric problems, the convergence was attained within the maximum force limit of 1000(KJ mol-1 nm-1), the steepest descent method was used to do a depreciation for 5000 cycles, and the neutral solution was obtained with the addition of chlorine and potassium ions. The simulation was also carried out with a pressure (1 atm) and a temperature (300K) as a reference. They were controlled using Parrinello–Rahman barostat and Berendsen thermostat, respectively. In the following part and to obtain a time step (2 fs), the hydrogen atom lengths were held rigid at ideal bond lengths using the Linear Constraint Solver (lincs) algorithm. The systems were subjected to free 100 ns production simulations, with the Particle Mesh Ewald (PME) to calculate the electrostatic interactions, the verlet scheme for calculating non-bonded interactions, and Periodic Boundary Conditions (PBC) for all x, y, and z directions.

Binding energy calculations

The energies of complexes play a critical part in many biological functions. Thus, it is crucial to figure out what they are. The binding energies of interactions were determined using the molecular mechanics

J. Mex. Chem. Soc. **2025**, *69*(4)
Regular Issue

ISSN-e 2594-0317

generalized Born surface area (MM-GBSA) technique and the total energy was obtained using the equation below:

$$\Delta G_{bind} = \Delta G_{RL} - \Delta G_R - \Delta G_L \qquad and \qquad \Delta G_{bind} = \Delta H - T\Delta S = \Delta E_{MM} + \Delta G_{Sol} - T\Delta S$$

Experimental

Materials and methods

The alignment of molecules

The alignment of molecules is the most precise method to explore molecules databases belonging to the same families is the alignment of the molecules, where the alignment cores are illustrated in Fig. 2.

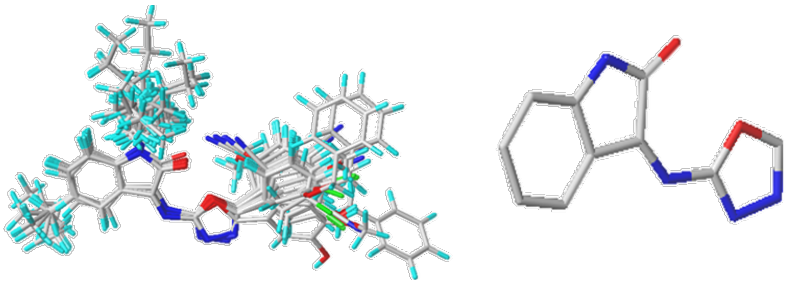

Fig. 2. Alignment compounds left, a core right.

3D-QSAR results

The compounds are separated into two groups: a training set of 24 and a test set of six compounds. The appropriate values for the COMFA model are R^2 (0.93), F (91.51), Q^2 (0.56), and S_{cv} (0.09). With three being the ideal number of indicators, the external validation gave the value of r^2_{ext} (0.98), the steric (S) contribution was 65%, but the electrostatic (E) did not exceed 35%.

CoMSIA's results suggest that non-cross-validated R^2 (0.85), Q^2 (0.60), a three-component optimum number, F (39.55), S_{cv} (0.13), as well as solid regard for external validation r^2_{ext} (0.98), all values are acceptable. The contributions of the steric (S), hydrophobic (H), electrostatic (E), H-donor (D), and acceptor (A) fields were 24 %, 20 %, 13 %,10 %, and 33 %, respectively, indicating that the H-bond acceptor, steric, and hydrophobic fields are essential in this contour. Table 2 shows the statistical findings of the models, whereas Table 3 and Fig. 3 shows the expected and actual values of pIC_{50}. The difference between these values is not higher (at most 1). It indicates that these calculations are reliable.

Table 2. The study results.

Contours	R^2	Q^2	S_{CV}	F	N	r^2_{ext}	S	E	H	D	A
CoMFA	0.93	0.56	0.09	91.51	3	0.98	0.65	0.35	-	-	-
CoMSIA	0.85	0.60	0.13	39.55	3	0.98	0.24	0.13	0.20	0.10	0.33

J. Mex. Chem. Soc. **2025**, *69*(4)
Regular Issue

ISSN-e 2594-0317

Table 3. The pIC_{50} is the actual and predicted value.

		CoMFA		**CoMSIA**	
N°	pIC_{50} (M)	**Predicted**	**Residuals**	**Predicted**	**Residuals**
1*	5.11	5.11	0.00	5.06	0.05
2	5.03	5.03	0.00	5.04	-0.01
3	5.28	5.13	0.14	5.30	-0.02
4	4.78	4.84	-0.06	4.83	-0.05
5	4.71	4.67	0.04	4.86	-0.29
6	5.21	5.23	-0.02	5.21	-0.01
7	5.33	5.36	-0.04	5.37	-0.04
8	5.28	5.32	-0.04	5.29	-0.01
9*	4.84	4.88	-0.04	4.88	-0.04
10*	4.95	4.96	-0.01	4.93	0.02
11	4.75	4.75	0.01	4.75	0.01
12	4.31	4.33	-0.02	4.34	-0.02
13	4.54	4.52	0.02	4.48	0.06
14	4.41	4.39	0.03	4.37	0.04
15	4.34	4.38	-0.05	4.36	-0.03
16	4.31	4.32	-0.01	4.31	0.00
17	4.60	4.62	-0.02	4.63	-0.03
18	4.71	4.70	0.00	4.71	-0.01
19*	4.46	4.42	0.04	4.44	0.02
20	4.57	4.68	-0.11	4.71	-0.14
21	4.74	4.76	-0.02	4.77	-0.03
22	4.43	4.43	0.00	4.45	-0.02
23	4.58	4.52	0.06	4.52	0.06
24	4.66	4.63	0.03	4.64	0.02
25	4.47	4.45	0.02	4.44	0.02
26*	4.46	4.54	-0.08	4.53	-0.07
27	4.52	4.64	-0.12	4.65	-0.13

J. Mex. Chem. Soc. **2025**, *69*(4)
Regular Issue

ISSN-e 2594-0317

		CoMFA		CoMSIA	
N°	pIC_{50} (M)	**Predicted**	**Residuals**	**Predicted**	**Residuals**
28	4.73	4.63	0.10	4.75	-0.02
29*	4.75	4.67	0.07	4.68	0.06
30	4.79	4.77	0.02	4.79	0.00

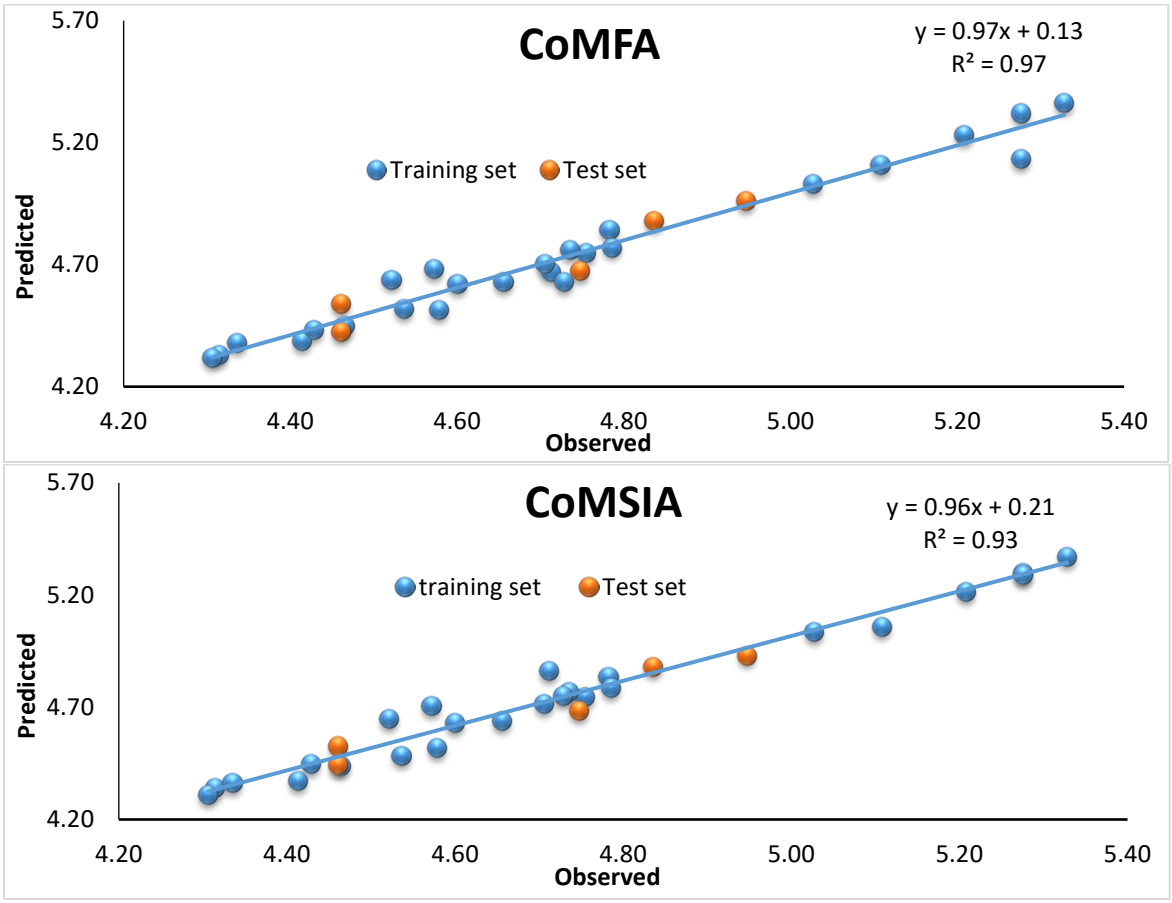

Fig. 3 Observed and predicted pIC_{50} of all compounds employed in constructing CoMSIA and CoMFA contours.

Graphical interpretation

The contours were generated to determine the types of substituents that can decrease or increase activity. The Steric and electrostatic contours of COMFA are given in (Fig. 4**(a)** and **(b)**). In contrast, Hydrophobic, hydrogen bond donor and acceptor contours of COMSIA are displayed in (Fig. 5**(a)**, **(b)**, and **(c)**). In this study, all contours indicated the default 80 percent and 20 percent level contributions of the select and unfavored areas, respectively, utilizing the structure of compound 7 as a model.

J. Mex. Chem. Soc. **2025**, *69*(4)
Regular Issue

ISSN-e 2594-0317

CoMFA contour

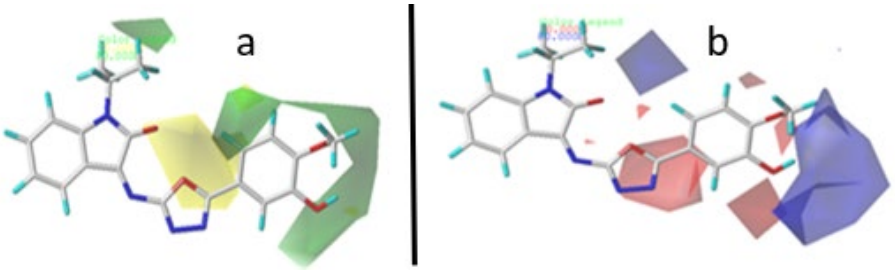

Fig. 4 CoMFA analysis. **(a)** Steric, **(b)** Electrostatic.

In the steric field (Fig. 4**(a)**), the green color is seen near the phenyl ring of 1,3,4 oxadiazole parts and N-methyl. This indicates that the inhibitors with bulky molecules at these positions could increase the activity. So, compounds 2, 7, and 3 have higher activity than 5, 1, and 6.

In (Fig. 3**(b)**), the blue contour indicates that the electron donor groups near the 3-hydroxyl and methoxy groups of the phenyl part and N-alkylated methane group might have high activity, so compounds 3 and 8 are higher than 12 and 14.

CoMSIA contour maps

CoMSIA contour explains H bond donor-acceptor (D-A) and hydrophobic (H), Fig. 5**(a)**, **(b)**, and **(c)** present the graphs of these fields, and the other fields (S, E) are the same in both contours.

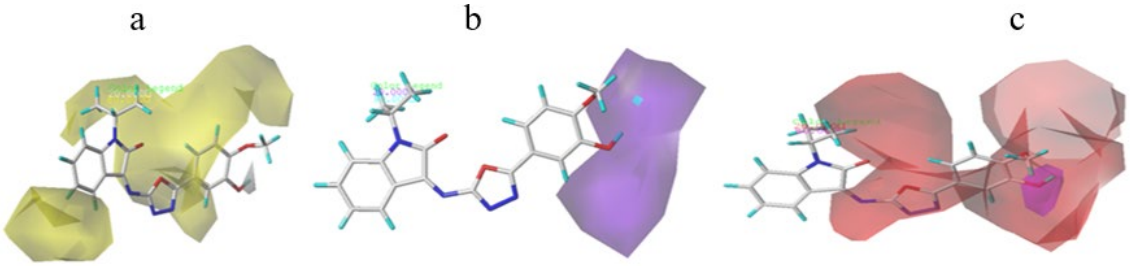

Fig. 5. CoMSIA analysis. **(a)** Hydrophobic, **(b)** H bond donor, **(c)** H bond acceptor fields.

The hydrophobic field was presented in (Fig. 5**(a)**) a large yellow color map that covers all the compounds except the 3-hydroxyl and methoxy on phenyl positions, which indicates that groups with hydrophobic character are favored more in these positions and might have enhanced activity. Compounds 2 and 4 are higher than 14 and 12. The purple color (Fig. 4**(b)**) appears near the OH, OCH3, and C2 substituents of the phenyl ring, revealing that the hydrogen bond donor is not preferred in this region, and the substituents of this type might decrease the activity. The Magenta contour (Fig. 4**(c)**) seen near the hydroxyl (OH) of the phenyl ring explains that substituents with hydrogen bond acceptor type can enhance the activity. In contrast, the red color around **C1, C2, C3, C4,** and **C6** of the phenyl ring part and N-isopropyl reveals that hydrogen acceptor is not preferred in this region. This fraction is less than the others, so it will not be considered**.**

External validation results

The Golbraikh, Roy, and Tropsha criteria are essential expressions for creating accurate models and applying them to the prediction of compound activities, as shown in Table 5, which lists the criteria results. In this table, the values of $r_0'^2$ and r_0^2 are more significant than 0.5; CoMFA has 0.962 and 0.965; CoMSIA has 0.971 and 0.999, respectively. That explains the ratio of the two values ($\frac{r^2 - r_0^2}{r^2}$, $\frac{r^2 - r_0'^2}{r^2} < 0.1$) remains

J. Mex. Chem. Soc. **2025**, *69*(4)
Regular Issue

ISSN-e 2594-0317

less than 0.1, (r_m^2, $r_m'^2 > 0.5$), $\Delta r_0^2 < 0.3$ and $\Delta r_m^2 < 0.2$ for both fields. In addition, the slopes k' and K have 1.012 and 1.013 in CoMFA. Moreover, CoMSIA has 0.991 and 0.995, respectively. The values are less than 1.15 and more significant than 0.85 in both contours. All parameters respect their margins of variation, which gives credibility to the present studied model to design new molecules, such as thymidine Phosphorylase (TP) inhibitors against cancer activity.

Table 4. The results of the Golbraikh Roy and Tropsha.

Criteria	**Acceptance criteria**		**CoMFA**	**CoMSIA**
Golbraikh and Tropsha	r^2 ext	$r^2 > 0.6$	0.981	0.984
	k	$0.85 \leq k \leq 1.15$	1.013	0.995
	$r_0'^2$	$r_0'^2 > 0.5$	0.962	0.971
	r_0^2	$r_0^2 > 0.5$	0.965	0.999
	k'	$0.85 \leq k \leq 1.15$	1.012	0.991
	$\frac{r^2 - r_0^2}{r^2}$	< 0.1	0.016	-0.015
	$\frac{r^2 - r_0'^2}{r^2}$	< 0.1	0.019	0.013
Roy	$r_m'^2$	$r_m'^2 > 0.5$	0.845	0.871
	r_m^2	$r_m^2 > 0.5$	0.856	0.863
	Δr_0^2	$\Delta r_0^2 < 0.3$	0.003	0.028
	Δr_m^2	$\Delta r_m^2 < 0.2$	-0.011	0.008

Newly designed compounds

The discovery of new drugs is one of the most complicated steps because this process involves several very complex steps. In this context, and according to the 3D QSAR study based on steric and H-bond acceptor fields, four more active compounds were designed with higher thymidine phosphorylase inhibitors against cancer activity. The pIC50 values and structures of designed compounds are shown in Table 5.

Table 5. Newly designed compounds.

N°	**Compounds**	**The expected pIC_{50} (M)**	
		CoMFA	**CoMSIA**
A	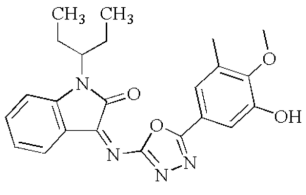	5.545	5.540

J. Mex. Chem. Soc. **2025**, *69*(4)
Regular Issue

ISSN-e 2594-0317

N°	Compounds	The expected pIC_{50} (M)	
		CoMFA	CoMSIA
B	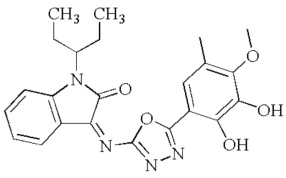	5.422	5.420
C	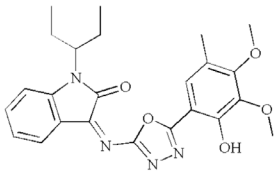	5.346	5.341
D	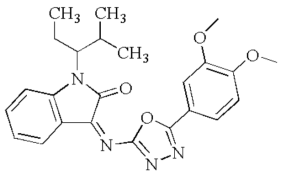	5.323	5.319

Docking results

To verify its reliability, it is essential to study the redocking of co-crystal ligands before studying molecular docking. Fig. 6 shows the highly superimposable and consistent between the two conformations, and the RMSD was 0.861 Å. This indicates that the docking protocol that was performed was reliable and could be used for subsequent studies.

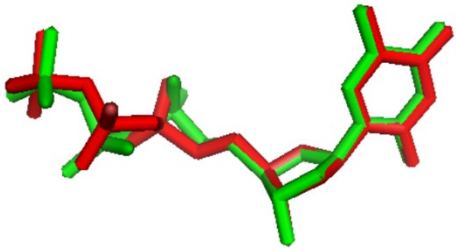

Fig. 6. Superimposition of the redocking pose (red) and the ligand pose in the co-crystal structure (green).

In an efficient state form (designed compounds-receptor), the Molecular Docking method was subjected to explore the interactions between the currently designed compounds and the TP inhibitor. The structure of thymidine phosphorylase (4EAD) was used as the receptor, and the compounds designed are the ligands; Table 6 summarizes the results of docking molecular.

J. Mex. Chem. Soc. **2025**, *69*(4)
Regular Issue

ISSN-e 2594-0317

Table 6. Results of docking molecules: show the interaction of designed compounds (A, B, C, and D) as ligands with the thymidine phosphorylase (receptor).

N°	2D View	N°	2D View
A	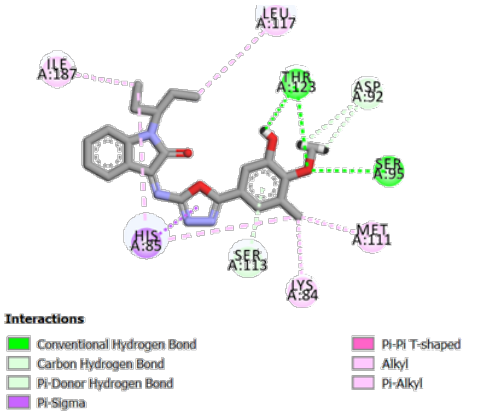	C	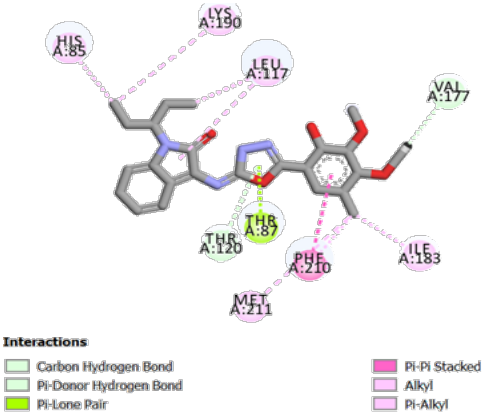
B	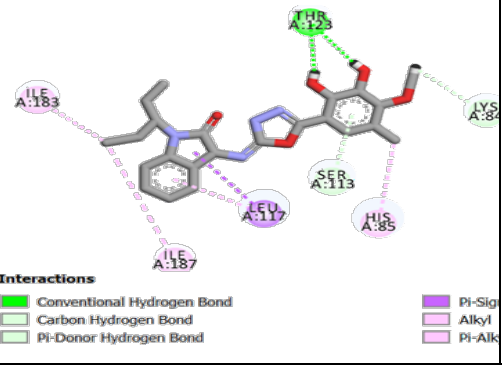	D	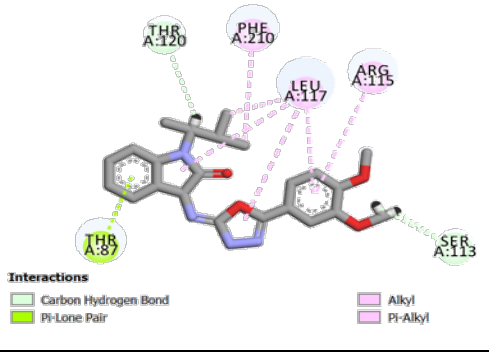

The first component, A, demonstrates two conventional hydrogen bond interactions with THR123 and SER95, two mixed interactions between carbon H-bond and Pi-donor are ASP92 and SER113, one of pi-sigma with HIS85 residues, and four mixed interactions between Alkyl and Pi-Alkyl (LYS84, MET111, LEU117, ILE187). The second compound, B, has different types of interactions: one of conventional hydrogen bond interaction with THR123, two mixed interactions between carbon H-bond and Pi-donor (SER113, LYS84), one of pi-sigma is LEU117, and three mixed interactions between Alkyl and Pi-alkyl are HIS85, ILE187-183.

The third component, C, has diverse interactions: two mixed interactions between the carbon-hydrogen bond and pi-donor hydrogen bond (VAL177, THR120), one of pi-lone is THR87, and one of Pi-Pi stacked interactions is PHE 210. Five mixed interactions between Alkyl and pi-alkyl are HIS85, LYS190, LEU117, ILE183, and MET211. The fourth compound, D, has two interactions in the carbon-hydrogen bond (THR120 and SER113), one of pi-Lone is THR87, and three mixed interactions between Alkyl and pi-alkyl are PHE210, LEU117, and ARG115. The interaction types are summarized in Table 7. Compounds A and B have two groups (OH, OCH3) and (OH, OH) in the substituent R), respectively. These groups are close to each other; because of these groups, compound A has two interactions of type conventional hydrogen bond interactions with THR 123 and SER95. Moreover, compound B has a single bond of conventional hydrogen bond interaction with THR 123. The types of interaction increase the stability of compounds A and B compared to the rest of the compounds (C and D), but compound A is more stable compared to B. Compound C has bulky groups occupying most of the R substituent positions. At the same time, Compound D has only two OCH_3 groups, and one (CH_3-CH-CH_2 (CH_3)-CH_3) group at the R1 substituent; these types of groups decrease the stability of compounds.

J. Mex. Chem. Soc. **2025**, *69*(4)
Regular Issue

ISSN-e 2594-0317

Table 7. The summary of the interaction types with the designed compounds and thymidine phosphorylase.

Interactions	Compounds			
	A	**B**	**C**	**D**
Conventional H-Bond	THR123, SER95	THR123		
Pi-Donor, H-bond/Carbon H-Bond	ASP92, SER113	SER113, LYS84	VAL177, THR120	HR120, SER113
Pi-Sigma, Pi-lone, Pi-Pi stacked	HIS85	LEU117	THR87, PHE210	THR87
Pi-Alkyl/ Alkyl	LYS84, MET111, LEU117, ILE187	HIS85, ILE187-183		

All the designed compounds do not have unfavorable interactions. The designed compound A has nine interactions, characterized by two essential interactions of the conventional hydrogen bond type. Moreover, compound B contains seven interactions in all, including one interaction of the conventional hydrogen bond. These interactions play an essential role in increasing the stability of their compounds. However, compounds C and D do not have any conventional hydrogen bond types. Therefore, it is crucial to determine the pharmaceutical properties of these compounds.

ADMET prediction

ADMET method is used to understand the pharmacokinetics and determine the toxicity and safety of active molecules as potential drugs in the human body. Table 8 summarizes ADMET results of (A, B, C, and D) compounds.

Table 8. ADMET prediction results of (A, B, C, and D) compounds.

Model		Compounds			
		A	**B**	**C**	**D**
Absorption (A)					
Intestinal absorption (human)		100	90.61	94.84	96.97
Distribution (D)					
Blood-brain barrier (logBB)		-1.932	-0.752	-1.073	-1.994
Volume of distribution Vdss(log L/kg)		0.194	0.249	0.344	0.246
Metabolism (M)					
Substrate (CYP)	3A4	+	+	+	+
	2D6	-	-	-	-
Inhibition (CYP)	1A2	-	-	-	-
	2C19	+	-	-	+
	2C9	+	+	+	+
	2D6	-	-	-	-
	3A4	+	+	+	+

J. Mex. Chem. Soc. **2025**, *69*(4)
Regular Issue

ISSN-e 2594-0317

Model	Compounds			
	A	**B**	**C**	**D**
Excretion (E)				
Clearance (log ml/min/kg)	0.66	0.59	0.53	0.65
AMES toxicity	-	-	-	-

The absorption of active molecules by the human intestinal system is indicated by the letter A, computed by unit (% Absorbed). All molecules have a value closer to 100 %, indicating that this behavior is highly favorable to the human gastrointestinal intestine [45]. The second letter, D, indicates distribution; it is generally based on the (logBB) and VDss (log L/kg) that show the pathway of introducing drugs into the central nervous system is dangerous for the brain. Therefore, it is essential to eliminate the passage of drugs to the brain to protect the cerebral environment. The compounds A, D, and C have a value < -1, which indicates that they will not cross the blood-brain barrier.

Moreover, compound C has a -1 <-0.752< 0.3, indicating an intermediate value. The second parameter studied in the distribution is the volume of distribution VDss (log L/kg); the higher the volume, the more the molecule will leave the vascular flow to diffuse in the body, but the brain has a protective barrier called the blood-brain barrier, the values of VDss vary between -0.15 and 0.45, if this value is lower than -0.15, it is considered a low. In contrast, if higher than 0.45, it is considered a high distribution. If -0.15 <VDss< 0.45, these are intermediate values. The third letter in the ADMET is M, which indicates metabolism; this shows the body's enzymatic system transforms the drug at the level of the liver; studies have shown that there are 57 CYP genes from 17 families in humans. Still, only CYPs (1A2, 2C9, 2C19, 2D6, and 3A4) are responsible for the biotransformation of 90 % of drugs. In our case, all compounds are not substrates or inhibitors of the cytochrome 2D6. Still, they are substrates and inhibitors of CYP3A4; for the rest, all compounds do not inhibit 1A2, but for cytochrome 2C19, only the B and C compounds are inhibitors. For the last cytochrome, all molecules are inhibitors of 2C9. The fourth letter, E, indicates excretion or clearance; it is a value that calculates the relationship between the rate of drug elimination and its concentration in the body. The results show a somewhat high value and are acceptable, and all predicted compounds are not toxic; this indicates that these compounds can be potent inhibitors of thymidine phosphorylase.

MD simulation analysis

Calculations of RMSD, RMSF, Radius of Gyration Rg, Hydrogen Bonding, Average Center-of-Mass Distance, Contact Frequency (CF) Analysis, Potential energy, Pressure and Temperature, and MMGBSA Binding Energy were carried out to evaluate the study of each structure about time.

Root mean square deviations (RMSD)

RMSD was used for the protein and ligand by using GROMACS program. RMSD graph (Fig. 7, Row 1), for the protein, the deviations of the proteins vary between 0.15 nm and 0.3 nm within 100ns of the simulation. These minimal deviations indicate that the proteins are stable throughout the simulation, which is the expected behavior of globular proteins. The RMSD of the ligand is shown in (Fig. 7, row 1); ligands A and B show fewer deviations in the last 80 ns of the simulations. These deviations are less compared to the deviations of ligands C and D. It indicates that ligands A and B showed higher stability than C and D. However, the minimum deviation for all ligands (less than 0.3 nm) for 100 ns indicates that the ligand can attack the active site of the protein.

Root mean square fluctuations (RMSF)

RMSF was calculated for protein based on 'C-alpha' atoms using GROMACS program. (Fig. 7, Row 2) shows that the maximum fluctuation of all four complexes did not exceed 0.5 nm with residue 390 for complex C. Moreover, all four complexes showed similar dynamic fluctuations, indicating that these inhibitors have a similar binding mode with the enzyme Thymidine Phosphorylase.

J. Mex. Chem. Soc. **2025**, *69*(4)
Regular Issue

ISSN-e 2594-0317

Radius of gyration (Rg)

The radius of gyration (Rg) was calculated for (A, B, C, and D) TP enzyme (4EAD)) complex based on 'C-alpha' atoms using GROMACS program, where the values were measured in nm. As (Fig. 7, Row 3) shows, ROG values for complex A stay between 2.26 nm and 2.34 nm or 22.6 Å and 23.4 Å. ROG for complex B increased values from the beginning of the simulation until 40ns, then stabilized after that, where its values stay between 22.9 Å and 23.2 Å with some slight fluctuations. After 10ns, ROG values after 10ns values 22.6 Å and 23.4 Å. ROG values complex D have an increasing pattern from the beginning of the simulation up to 40ns, stabilizing to values between 22.7 Å and 23.2 Å with some slight fluctuations. All four complexes show a very stable radius of gyration with a fluctuation of around 1-1.2 Å after 10ns, indicating the stability and compactness of the structure. The slight fluctuation around 1.0 Å Rog value during the MD simulation time indicates a slight opening and closing of the N and C terminal domains.

Hydrogen bonds (HB)

The total number of HB formed between ligands (A, B, C, and D) and Protein (TP enzyme (4EAD) during 100 ns of the simulation time is shown in (Fig. 9, Row 1), the maximum number of Hydrogen Bonds formed by TP and ligands A, B, C, and D are found to be 3, 4, 5, and 5 respectively.

Average Center-of-Mass Distance

The average Center-of-Mass Distance between ligands (A, B, C, and D) and Protein (TP enzyme (4EAD)) during 100 ns of the simulation time is shown in (Fig. 9, Row 2). All compounds have unstable variations before 80 ns, but these graphs remain constant after this instant.

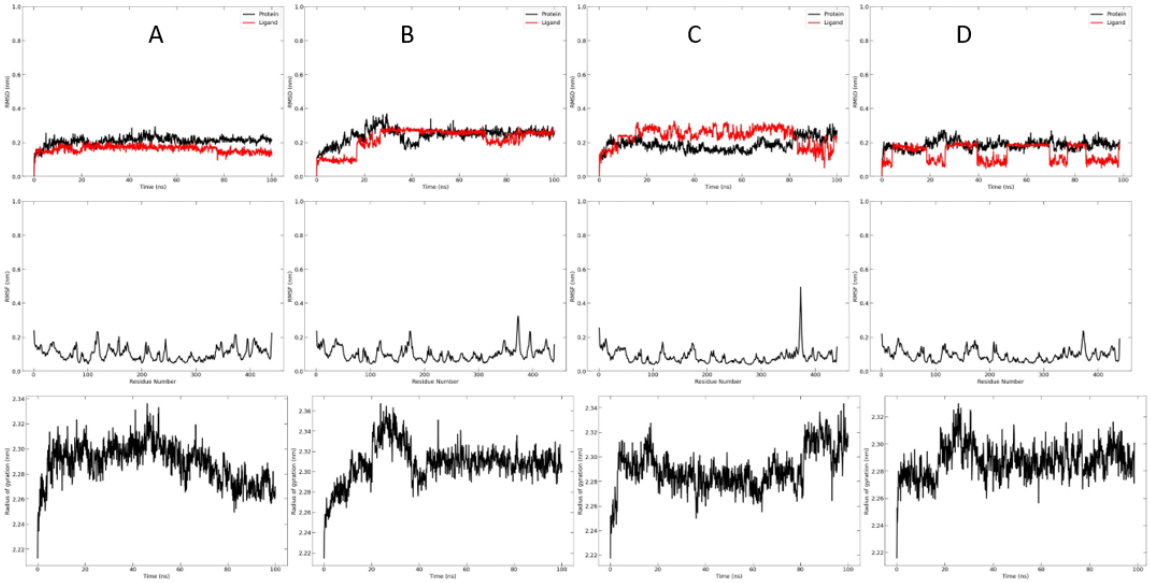

Fig. 7. From top to bottom: (1) RMSD, (2) RMSF, and (3) Rg of the complexes during 100ns MD simulation. Compounds A (Column A), B (Column B), C (Column C) and D (Column D).

After completing the proposed compounds' RMSD, RMSF, and Rg, Fig. 9 of the most ligands were added to compare (below). The average value of RMSD of both the ligand and protein studied was similar at all times of MD simulation analysis. We noticed they don't have any intersection (C7-protein), indicating that most compounds (C7) are unstable. Several fluctuations, e.g. characterize the mean RMSF values for the ligand (C7). The figure shows four fluctuations over 0.4 nm. In all systems, the RMSF for this compound is unstable.

Rg assessment. Rg analysis determines whether the protein under study is compact and folded during MD simulation. The overall results of Rg analysis show that the total Rg of compound 7 (C7) is comparatively

J. Mex. Chem. Soc. **2025**, *69*(4)
Regular Issue

ISSN-e 2594-0317

higher than the proposed compounds in each complex (Fig. 7). The Rg of C7 was initially lower but increased to 2.5Å at 10 ns and then remained unstable up to 50 ns, after which the Rg of C7 reached a value between 2.6 Å and 2.65 Å, after 60 ns of simulation. We noticed that the Rg value in the C7 COMPOUND remained unstable throughout the MD simulation compared to the proposed compounds.

Generally, the RMSD, RMSF, and Rg results indicate that the four predicted complexes (A, B, C, and D) are stable and may serve as potential drug candidates as potential Thymidine Phosphorylase (TP) inhibitors against cancer activity.

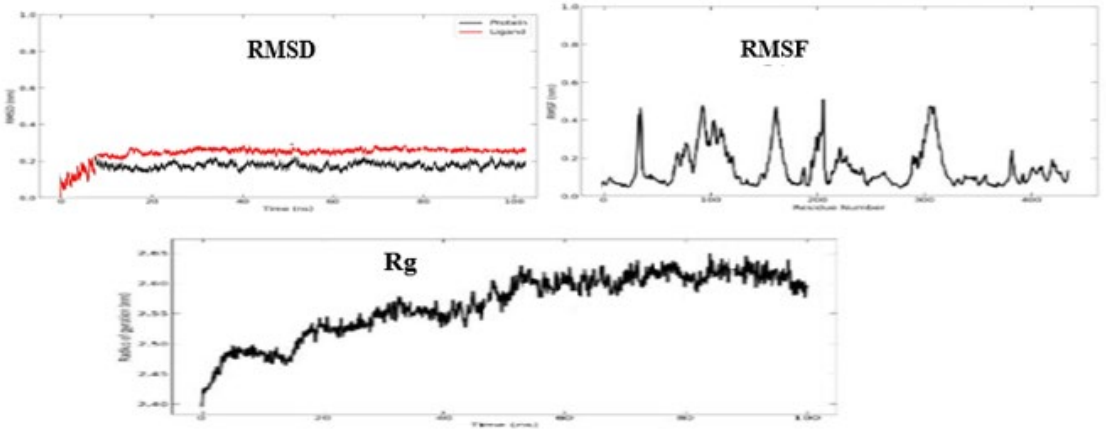

Fig. 8. RMSD, RMSF, and Rg of the complex (Compound7 (C7) - TP enzyme (4EAD)) during 100ns MD simulation.

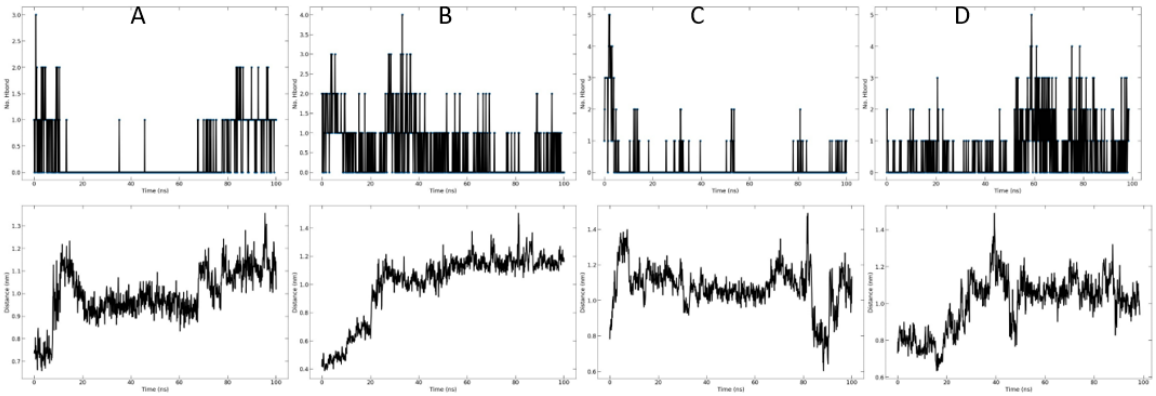

Fig. 9. From top to bottom: (1) Hydrogen Bonds (Protein-ligand) and (2) Average distance between Ligand and the Protein form of the complexes during 100ns MD simulation. Compounds A (Column A), B (Column B), C (Column C) and D (Column D).

Percentage of Contact Frequency (CF)

The contact frequency (CF) analysis for (ligand (A, B, C, and D) and Protein (TP enzyme (4EAD)) complexes was done with 4 Å as a cutoff threshold. The names of residues in function to the CF percentage are presented in Fig. 10, where ligand D shows the highest contact frequency percentage.

J. Mex. Chem. Soc. **2025**, *69*(4)
Regular Issue

ISSN-e 2594-0317

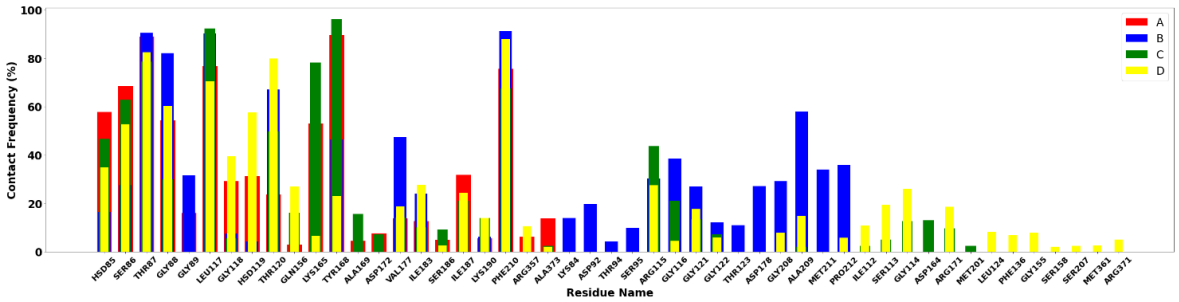

Fig. 10. Contact frequency (CF) analysis.

The supplementary section

Variation of pressure, temperature, and potential energy

The system's potential energy, pressure, and temperature during 100 ns of MD simulation, as obtained from the GROMACS file (Fig. 11), shows the evolution of the pressure, potential energy, and temperature through the MD simulations. In MD simulation, fluctuation of thermodynamic parameters is expected due to statistical fluctuation and sampling of different microstates. The running average of these data is the critical value to be stable during the simulation because it represents the system's ensemble property or the actual thermodynamic macroscopic property. As shown in (Fig. 11), the average temperature, pressure, and potential energy are constant throughout the simulation. The graph shows the converged potential energy, pressure, and temperature throughout the 100ns simulations.

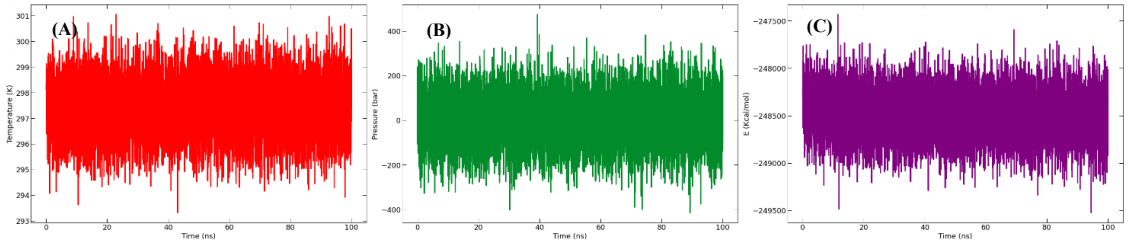

Fig. 11. From left to right: **(A)** Temperature, **(B)** pressure, and **(C)** potential energy during the 100ns MD simulations.

MMGBSA Binding Energy

To calculate the free energy between the ligands (A, B, C, and D) and the thymidine phosphorylase enzyme, the most popular methods were the Molecular Mechanics/Generalized Born or Poisson Boltzmann Surface Area (MM (GBSA, PBSA)). MM/GBSA calculation was performed because it is more precise and faster. The results are shown in Table 9.

Table 9. The binding free energies [kcal/mol].

Complex	**ΔG**	**$\Delta E_{(internal)}$**	**$\Delta E_{(electrostat)} + \Delta G_{(sol)}$**	**$\Delta E_{(VDW)}$**
A	-20.1374 ± 0.1189	0	10.6882	-30.8256
B	-20.1897 ± 0.1333	0	15.0771	-35.2668
C	-18.1344 ± 0.1604	0	14.2583	-32.3926
D	-19.077 ± 0.1549	0	13.5052	-32.5822

J. Mex. Chem. Soc. **2025**, *69*(4)
Regular Issue

ISSN-e 2594-0317

The results showed that the A and the B complex had a solid binding free energy with the thymidine phosphorylase enzyme (TP), and their binding energies were -20.1374 +/- 0.1189 kJ/mol and -20.1897 +/- 0.1333 kJ/mol, respectively. In addition, the other compounds, C and D, had less binding energy with the thymidine phosphorylase enzyme (TP), and their binding energies were -18.1344 +/-0.1604 kJ/mol and -19.077 +/-0.1549 kJ/mol, respectively. The energy types are divided into *internal* energy, solvation energy, e*lectrostat* energy, and van der Waals energy. Among them, the solvation and electrostatic energy between the B and the TP enzyme was 15.0771 kJ/mol; this was the most critical factor in the binding energy. In addition, the energies of the compounds C, D, A, and TP enzymes have been classified as 14.2583, 13.5052, and 10.6882 kJ/mol, respectively. The final energy remains zero for all compounds. The van der Waals energy of compounds A, B, C, and D are -30.8256, -35.2668, -32.3926, and -32.5822 successively.

Comparative study

The selective inhibition potential of Thymidine phosphorylase (TP) is the mainstay intervention in treating cancer activity in the absence of effective therapy for this severe disease. The design of new specific and selective inhibitors based on an isatin scaffold by applying computational methods to investigate the binding properties of isatin scaffold compounds as cancer inhibitors with target enzymes. In a previous study by *Jian-Bo et al.,* the quantitative structure-activity relationship of isatin-based oxadiazole derivatives as Thymidine Phosphorylase Inhibitors was investigated by 3D-QSAR and molecular docking study [46]. The present work investigated the cancer inhibitors' activity of Thymidine Phosphorylase by 3D-QSAR, molecular docking, and molecular dynamic simulation. Also, the pharmacokinetics and toxicity of designed compounds were visually screened by ADMETox study. In this work, we used a 3D-QSAR, Molecular Docking, ADME-Tox, and Molecular Dynamics Simulation analysis investigation of 30 compounds of anticancer isatin-based oxadiazoles activity, and each method has a vital role in this study.

3D QSAR

Used after the reliability check and the robustness for determining the nature of the substituents, which can decrease or increase the biological activities of the target compounds. Two contours determine the types of substituents, Comparative Molecular Similarity Indices Analysis and CoMSIA and Comparative Molecular Field Analysis CoMFA, which are essential to building QSAR.

Molecular docking

It is an important method for exploring the interaction between ligands (A, B, C, and D) and the TP enzyme (4EAD).

ADME-Tox

Drug research and development speed is accelerating, and the number of candidate compounds is increasing. It would waste a lot of resources to put them into experiments directly. Therefore, it is necessary to use computational modeling methods to evaluate their bioavailability and pharmacokinetics. The absorption, distribution, metabolism, excretion, and toxicities are examples of traditional pharmacokinetic parameters (ADMET) evaluation including Intestinal absorption (human), Blood-brain barrier (logBB), Volume of distribution Vdss(log L/kg), cytochrome(CYP) enzyme inhibition and substrate, Clearance (log ml/min/kg), and AMES toxicity.

Molecular dynamics (MD) simulation

MD simulation is essential for analyzing protein-ligand complexes. In this case, the ligands are the proposed compounds (A, B, C, and D), and the enzyme is Thymidine Phosphorylase TP (4EAD).

We found that just one work used 3D-QSAR, but in this work, they proposed other compounds that were different from our proposed compounds. The comparison between the results of both studies is summarized in Table 10. The docking result of the current study shows different types of interactions: conventional H-bond, Pi-Donor, H-bond/Carbon H-Bond, Pi-Sigma, Pi-lone, Pi-Pi stacked, and Pi-Alkyl/

J. Mex. Chem. Soc. **2025**, *69*(4)
Regular Issue

ISSN-e 2594-0317

Alkyl. In addition, the present work contains other complementary studies, ADMET prediction, and MD simulation analysis to study the properties and stability of the proposed compounds. The ADMET method is used to understand the pharmacokinetics and determine the toxicity and safety of active molecules as potential drugs in the human body. Section 3.6 (Table 8) summarizes the ADMET results (A, B, C, and D). The molecular dynamics simulation used binding stability between ligand- thymidine phosphorylase enzyme (TP) (compounds A, B, C, and D)- thymidine phosphorylase enzyme (TP) complexes. RMSD, RMSF, Radius of Gyration Rg, Hydrogen Bonding, Average Center-of-Mass Distance, Contact Frequency (CF) Analysis, and MMGBSA Binding Energy were carried out to assess the stability of each complex structure as shown in section3.7 MD simulation analysis, figures 7, 8, 9, 10 and table 9.

Table 10. The comparison between the results of both studies.

<table>
<tr><th>N°</th><th>Present work</th><th>N°</th><th>Present work</th></tr>
<tr><td>A</td><td> 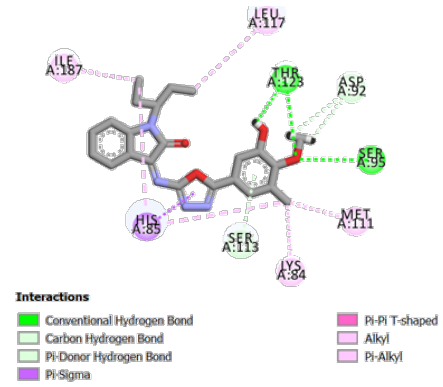
</td><td>C</td><td> 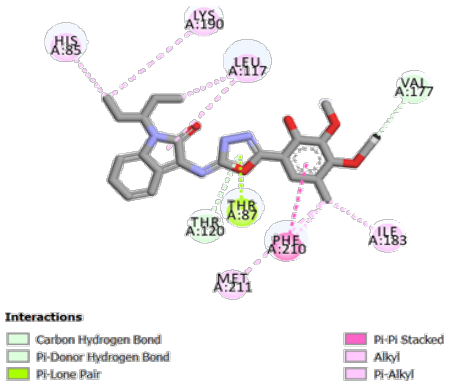
</td></tr>
<tr><td>B</td><td> 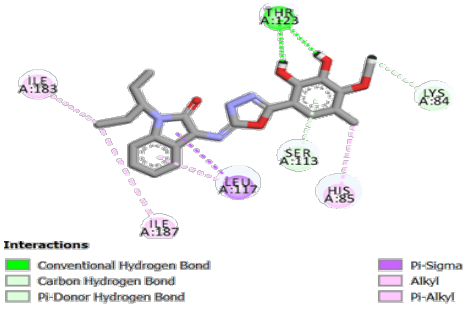
</td><td>D</td><td> 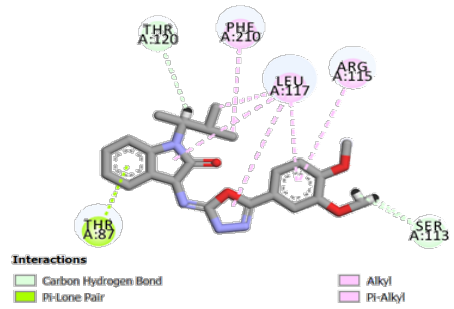
</td></tr>
<tr><td colspan="4">Other study</td></tr>
<tr><td colspan="2">(B) Hydrogen bond interaction between the newly designed molecule 1 and 5.</td><td colspan="2"> 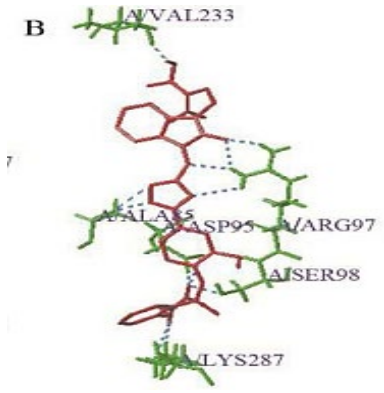
</td></tr>
</table>

J. Mex. Chem. Soc. **2025**, *69*(4)
Regular Issue

ISSN-e 2594-0317

In literature, we can find work using these computational chemistry methods on other derivates and other activities. Generally, each molecule has a specific activity (anti-cancer, anti-diabetic, anti-inflammatory....). We used computational chemistry methods in several works, for example. In the work titled"3D-QSAR, molecular docking, ADMET, simulation dynamic, and retrosynthesis studies on new styrylquinolines derivatives against breast cancer [27]". We used other derivatives of styrylquinolines derivatives and their activity against breast cancer. In the second work titled"2-Oxoquinoline Arylaminothiazole Derivatives in Identifying Novel Potential Anticancer Agents by Applying 3D-QSAR, Docking, and Molecular Dynamics Simulation Studies [42]". We used other derivatives of 2-Oxoquinoline Arylaminothiazole. Generally, we have applied these methods to the design of new compounds against several diseases, and we have also applied them to the validation of compounds proposed.

Conclusions

The 3D-QSAR study was used to determine the connection between molecules' structure and activity to determine the types of substituents that can increase the activity of the compounds. Both CoMFA and CoMSIA contours are the critical basis for designing new compounds. In this study, the two contours were used to design four molecules (A, B, C, and D), and the proposed compounds' binding mechanism and interaction with the active site of Thymidine Phosphorylase (TP) were studied using molecular Docking. Docking results showed that compound A is ranked first in terms of stability with two types of classical hydrogen bonding interactions, followed by compound B, which has only one kind of interaction. Two (A and B) compounds remain more stable than (C and D) because they do not have any classic hydrogen bond with TP inhibitor enzyme. The pharmacokinetic properties (ADMET) for (A, B, C, and D) compounds, including cell Blood-brain barrier, intestinal absorption, the volume of distribution, and metabolism, where the results were found to be non-Ames toxicity. Molecular dynamic (MD) results at 100 ns showed that all the compounds remained stable during the simulation. Current results encourage in vitro and in vivo studies of the designed isatin compounds as potent TP inhibitors.

References

1. Ferlay, J.; Soerjomataram, I.; Dikshit, R.; Eser, S.; Mathers, C.; Rebelo, M.; Parkin, D. M.; Forman, D.; Bray, F. *Int. J. Cancer.* **2015**, *136*, E359–E386.DOI: https://doi.org/10.1002/ijc.29210.
2. Nagai, H.; Kim, Y. H. *J. Thorac. Dis.* **2017**, *9*, 448–451. DOI: https://doi.org/10.21037/jtd.2017.02.75.
3. Bronckaers, A.; Gago, F.; Balzarini, J.; Liekens, S. *Med. Res. Rev.* **2009**, *29*, 903–953. DOI: https://doi.org/10.1002/med.20159.
4. Akiyama, S.; Furukawa, T.; Sumizawa, T.; Takebayashi, Y.; Nakajima, Y.; Shimaoka, S.; Haraguchi, M. *Cancer Sci.* **2004**, *95*, 851–857.DOI: https://doi.org/10.1111/j.1349-7006.2004.tb02193.x.
5. Elamin, Y. Y.; Rafee, S.; Osman, N.; O'Byrne, K. J.; Gately, K. *Cancer Microenviron.* **2016**, *9*, 33–43. DOI: https://doi.org/10.1007/s12307-015-0173-y.
6. Walko, C. M.; Lindley, C. *Ther.* **2005**, *27*, 23–44. DOI: https://doi.org/10.1016/j.clinthera.2005.01.005.
7. Meropol, N. J.; Gold, P. J.; Diasio, R. B.; Andria, M.; Dhami, M.; Godfrey, T.; Kovatich, A. J.; Lund, K. A.; Mitchell, E.; Schwarting, R. *J. Clin. Oncol. Off. J. Am. Soc. Clin. Oncol.* **2006**, *24*, 4069–4077. DOI: https://doi.org/10.1200/JCO.2005.05.2084.
8. Han, J.-Y.; Hong, E. K.; Lee, S. Y.; Yoon, S. M.; Lee, D. H.; Lee, J. S. *J. Clin. Pathol.* **2005**, *58*, 650–654. DOI: https://doi.org/10.1136/jcp.2004.022764.
9. Javid, M. T.; Rahim, F.; Taha, M.; Nawaz, M.; Wadood, A.; Ali, M.; Mosaddik, A.; Shah, S. A. A.; Farooq, R. K. *Bioorganic Chem.* **2018**, *79*, 323–333. DOI: https://doi.org/10.1016/j.bioorg.2018.05.011.

J. Mex. Chem. Soc. **2025**, *69*(4)
Regular Issue

ISSN-e 2594-0317

10. Sridhar, S. K.; Ramesh, A. *Biol. Pharm. Bull.* **2001**, *24*, 1149–1152. DOI: https://doi.org/10.1248/bpb.24.1149.
11. Selvam, P.; Murugesh, N.; Chandramohan, M.; Debyser, Z.; Witvrouw, M. *Indian J. Pharm. Sci.* **2008**, *70*, 779–782. DOI: https://doi.org/10.4103/0250-474X.49121.
12. Rohini, R.; Reddy, P. M.; Shanker, K.; Kanthaiah, K.; Ravinder, V.; Hu, A. *Arch. Pharm. Res.* **2011**, *34*, 1077–1084. DOI: https://doi.org/10.1007/s12272-011-0705-z.
13. Verma, M.; Pandeya, S. N.; Singh, K. N.; Stables, J. P. *Acta Pharm. Zagreb Croat.* **2004**, *54*, 49–56.
14. Raj, R.; Gut, J.; Rosenthal, P. J.; Kumar, V. *Bioorg. Med. Chem. Lett.* **2014**, *24*, 756–759. DOI: https://doi.org/10.1016/j.bmcl.2013.12.109.
15. Bharathi Dileepan, A. G.; Daniel Prakash, T.; Ganesh Kumar, A.; Shameela Rajam, P.; Violet Dhayabaran, V.; Rajaram, R. *J. Photochem. Photobiol. B.* **2018**, *183*, 191–200.DOI: https://doi.org/10.1016/j.jphotobiol.2018.04.029.
16. Zhang, M.-Z.; Chen, Q.; Yang, G.-F. *Eur. J. Med. Chem.* **2015**, *89*, 421–441.DOI: https://doi.org/10.1016/j.ejmech.2014.10.065.
17. Guo, H. *Eur. J. Med. Chem.* **2019**, *164*, 678–688. DOI: https://doi.org/10.1016/j.ejmech.2018.12.017.
18. Ibrahim, H. S.; Abou-Seri, S. M.; Tanc, M.; Elaasser, M. M.; Abdel-Aziz, H. A.; Supuran, C. T *Eur. J. Med. Chem.* **2015**, *103*, 583–593. DOI: https://doi.org/10.1016/j.ejmech.2015.09.021.
19. Eldehna, W. M.; Altoukhy, A.; Mahrous, H.; Abdel-Aziz, H. A. *Eur. J. Med. Chem.* **2015**, *90*, 684–694.DOI: https://doi.org/10.1016/j.ejmech.2014.12.010.
20. Sharma, P.; Senwar, K. R.; Jeengar, M. K.; Reddy, T. S.; Naidu, V. G. M.; Kamal, A.; Shankaraiah, N. *Eur. J. Med. Chem.* **2015**, *104*, 11–24. DOI: https://doi.org/10.1016/j.ejmech.2015.09.025.
21. Kerzare, D.; Khedekar, P. *J. Pharm. Biosci. Res.* **2016**, *6*, 144–156.
22. Erdmann, O. L. *J. Für Prakt. Chem.* **1840**, *19*, 321–362.DOI: https://doi.org/10.1002/prac.18400190161.
23. Silva, J. F. M. da; Garden, S. J.; Pinto, A. C. *J. Braz. Chem. Soc.* **2001**, *12*, 273–324.DOI: https://doi.org/10.1590/S0103-50532001000300002.
24. Bergman, J.; Lindström, J.-O.; Tilstam, U. *Tetrahedron* **1985**, *41*, 2879–2881.DOI: https://doi.org/10.1016/S0040-4020(01)96609-8.
25. Klebe, G.; Abraham, U.; Mietzner, T. *J. Med. Chem.* **1994**, *37*, 4130–4146.DOI: https://doi.org/10.1021/jm00050a010.
26. Cramer, R. D.; Patterson, D. E.; Bunce, J. D. *J. Am. Chem. Soc.* **1988**, *110*, 5959–5967.DOI: https://doi.org/10.1021/ja00226a005.
27. EL-Mernissi, R.; Alaqarbeh, M.; Khaldan, A.; Kara, M.; Al Kamaly, O.; Alnakhli, A. M.; Lakhlifi, T.; Sbai, A.; Ajana, M. A.; Bouachrine, M. *Open Chemistry*. **2024**, *22*, 1-20. DOI: https://doi.org/10.1515/chem-2024-0041.
28. EL-Mernissi, R.; EL Khatabi, K.; Khaldan, A.; El Mchichi, L.; Ajana, M. A.; Lakhlifi, T.; Bouachrine, M. *Mater. Today Proc.* **2021**, *45*, 7608–7614. DOI: https://doi.org/10.1016/j.matpr.2021.03.080.
29. Clark, M.; Cramer, R. D.; Van Opdenbosch, N. *Comput. Chem.* **1989**, *10*, 982–1012. DOI: https://doi.org/10.1002/jcc.540100804.
30. Purcell, W. P.; Singer, J. A. *J. Chem. Eng. Data* **1967**, *12*, 235–246. DOI: https://doi.org/10.1021/je60033a020.
31. El-Mernissi, R.; El Khatabi, K.; Khaldan, A.; ElMchichi, L.; Ajana, M. A.; Lakhlifi, T.; Bouachrine, M. *Egypt. J. Chemistry*. **2022**, *65*, 9–18.DOI: https://doi.org/10.21608/ejchem.2022.76000.3715.
32. Golbraikh, A.; Tropsha, A. *Mol. Graph. Model.* **2002**, *20*, 269–276. DOI: https://doi.org/10.1016/S1093-3263(01)00123-1.
33. Roy, P. P.; Leonard, J. T.; Roy, K. *Chemom. Intell. Lab. Syst.* **2008**, *90*, 31–42. DOI: https://doi.org/10.1016/j.chemolab.2007.07.004.
34. Edache, E. I.; Uzairu, A.; Mamza, P. A.; Shallangwa, G. A. *J. Mex. Chem. Soc.* **2022**, *66*. DOI: https://doi.org/10.29356/jmcs.v66i4.1726.

J. Mex. Chem. Soc. **2025**, *69*(4)
Regular Issue

ISSN-e 2594-0317

35. Ibrahim, M. T.; Uzairu, A.; Umar, A. B.; Bello, A. S.; Isyaku, Y. *J. Mex. Chem. Soc.* **2019**, *64*. DOI: https://doi.org/10.29356/jmcs.v64i1.1025.
36. DeLano, W. L. DeLano. PyMOL Mol. Graph. Syst. DeLano Sci. San Carlos CA USA 2002
37. Discovery Studio Predictive Science Application | Dassault Systèmes BIOVIA https://www.3dsbiovia.com/products/collaborative-science/biovia-discovery-studio/, accessed in February 2020.
38. Daina, A.; Michielin, O.; Zoete, V. *Sci. Rep.* **2017**, *7*, 42717. DOI: https://doi.org/10.1038/srep42717.
39. El Khatabi, K.; Kumar, S.; El-Mernissi, R.; Singh, A. K.; Ajana, M. A.; Lakhlifi, T.; Bouachrine, M. *J. Biomol. Struct. Dyn.* **2022**, *0* , 1–15. DOI: https://doi.org/10.1080/07391102.2022.2134210.
40. Van Der Spoel, D.; Lindahl, E.; Hess, B.; Groenhof, G.; Mark, A. E.; Berendsen, H. J. C. *J. Comput. Chem.* **2005**, *26*, 1701–1718. DOI: https://doi.org/10.1002/jcc.20291.
41. Boonstra, S.; Onck, P. R.; Giessen, E. van der. *J. Phys. Chem. B* **2016**, *120*, 3692–3698. https://doi.org/10.1021/acs.jpcb.6b01316.
42. El-Mernissi, R.; El Khatabi, K.; Khaldan, A.; Elmchichi, L.; Shahinozzaman, M.; Ajana, M.; Lakhlifi, T.; Bouachrine, M. *J. Mex. Chem. Soc.* **2021**, *66*, 79–94. DOI: https://doi.org/10.29356/jmcs.v66i1.1578.
43. Lee, S.; Tran, A.; Allsopp, M.; Lim, J. B.; Hénin, J.; Klauda, J. B. *J. Phys. Chem. B* **2014**, *118*, 547–556. https://doi.org/10.1021/jp410344g.
44. Hayes, J. M.; Skamnaki, V. T.; Archontis, G.; Lamprakis, C.; Sarrou, J.; Bischler, N.; Skaltsounis, A.-L.; Zographos, S. E.; Oikonomakos, N. G. *Funct. Bioinforma.* **2011**, *79*, 703–719. DOI: https://doi.org/10.1002/prot.22890.
45. El-Mernissi, R.; El khatabi, K.; Khaldan, A.; Bouamrane, S.; ElMchichi, L.; Aziz Ajana, M.; Lakhlifi, T.; Bouachrine, M. *Orbital Electron. J. Chem.* **2022**, *14*, 24–32. DOI: https://doi.org/10.17807/orbital.v14i1.1659.
46. Tong, J.-B.; Feng, Y.; Wang, T.-H.; Luo, D. *Chin. J. Anal. Chem.* **2021**, *49*, e21046–e21054. https://doi.org/10.1016/S1872-2040(21)60095-6.

Article

J. Mex. Chem. Soc. **2025**, *69*(4)
Regular Issue

ISSN-e 2594-0317

Impact of the Chemical Speciation of the Ag^+–Cl^-–e^- System on the Construction of True Reference Electrodes and the Potential Purification of the Ionic Liquid 1-Butyl-3-Methylimidazolium Bis(Trifluoromethylsulfonyl)Imide

Jorge Ruvalcaba-Juárez, Oscar Valenzuela-Bonilla, Norma Rodríguez-Laguna, Arturo García-Mendoza*

Sección de Química Analítica, FES Cuautitlán, Universidad Nacional Autónoma de México, Av. Primero de Mayo S/N, Estado de México, 54740, México.

***Corresponding author:** Arturo García-Mendoza, email: arturogm@unam.mx

Received October 9th, 2024; Accepted February 11th, 2025.

DOI: http://dx.doi.org/10.29356/jmcs.v69i4.2374

Abstract. We present the chemical speciation of $[AgCl_n]^{1-n}/Ag^0$ redox couple in two media: the room temperature ionic liquid (RTIL) 1-butyl-3-methylimidazolium bis(trifluoromethylsulfonyl)imide ($[C_4mim][NTf_2]$) as a model ionic solvent, and aqueous medium. The logarithms of the formation constants ($\log \beta_n$), solubility product constant (pK_{sp}), and formal reduction potential (E°') values of these chemical systems were estimated through open circuit potential measurements using suitable indicator electrodes and representative potentiometric titrations. The estimation of the extraction constant (K_E) of Ag^+ in the interphase water-RTIL was determined through a series of extraction systems at different values of $p(V_{org}/V_{ac})$, finding that the extraction of silver(I) is favorable towards aqueous media at high pCl values. Also, a series of reference electrodes (RE) were constructed under different buffer conditions for use in this ionic liquid to assess the utility of the collected electrochemical data. The potential drift of the half-cells was determined via cyclic voltammetry using the cobaltocene redox couple, $[Co(Cp)_2]^{+/0}$, as an internal redox reference; in addition, information on the Ag(I) extraction constant allowed to explain the effect of water as a contaminant of these devices. Finally, specific configurations were identified for these REs, some exhibiting potential drifts of less than 0.58 $\mu V\ h^{-1}$, rendering them comparable to commonly used REs in aqueous media.
Keywords: Room temperature ionic liquids; reference electrodes; silver; chemical speciation; liquid-liquid extraction.

Resumen. Se presenta la especiación química del par redox $[AgCl_n]^{1-n}/Ag^0$ en dos medios: el líquido iónico a temperatura ambiente (RTIL) bis(trifluorometilsulfonil)imida de 1-butil-3-metilimidazolio ($[C_4mim][NTf_2]$) como solvente iónico modelo, y en medio acuoso. Los logaritmos de las constantes de formación ($\log \beta_n$), la constante del producto de solubilidad (pK_{ps}) y los valores del potencial formal de reducción (E°') de estos sistemas químicos se estimaron mediante mediciones de potencial de circuito abierto utilizando electrodos indicadores adecuados y valoraciones potenciométricas representativas. La estimación de la constante de extracción (K_E) de Ag^+ en la interfase agua-RTIL se determinó a través de una serie de sistemas de extracción a diferentes valores de $p(V_{org}/V_{ac})$, encontrando que la extracción de plata(I) es favorable hacia el medio acuoso a altos valores de pCl. Además, se construyó una serie de electrodos de referencia (RE) bajo diferentes condiciones de amortiguamiento para su uso en este líquido iónico, con el fin de evaluar la utilidad de los datos electroquímicos obtenidos. La deriva potencial de las semiceldas se determinó mediante voltamperometría cíclica usando el par redox de cobaltoceno, $[Co(Cp)_2]^{+/0}$, como referencia redox interna además, la información sobre la constante de extracción de Ag(I) permitió explicar el efecto del agua como contaminante de estos dispositivos. Finalmente, se identificaron configuraciones específicas para estos

J. Mex. Chem. Soc. **2025**, *69*(4)
Regular Issue

ISSN-e 2594-0317

REs, algunos de los cuales exhibieron derivas potenciales de menos de 0.58 μV h^{-1}, haciéndolos comparables con los REs comúnmente utilizados en medios acuosos.
Palabras clave: Líquidos iónicos a temperatura ambiente; electrodos de referencia; plata; especiación química; extracción líquido-líquido.

Introduction

Room-temperature ionic liquids (RTILs) are liquid ionic salts at temperatures below 100 °C [1]. These primarily consist of a bulky organic cation with heteroaromatic atoms and an inorganic anion with low coordinating capacities [2–4]. Given the vast cation-anion combinations and their functionalization capacity, many of these compounds have been documented, each offering versatility and multiple applications in various areas of chemistry. Ionic liquids are used as solvents and supporting electrolytes in routine electrochemical analysis due to their board electroactive window and high specific conductivity, enhancing measurement sensitivity and reproducibility. They are applied in electrochemical sensors for selective detection of redox species, in cyclic voltammetry to study electrochemical stability and electron transfer kinetics, and in controlled electrodeposition systems for characterizing metal film growth processes [5–7].

The reagents used for the synthesis of ionic liquids (ILs) often involve the presence of several metal cations, such as silver, involved in metathesis reactions [8], resulting in solvents that are not entirely pure. Thus, their use as solvents to increase reaction rates and enhance efficiency is a function of their initial purity [9]; furthermore, it must be considered that such processes generate contaminated ionic liquids as waste. Although significant interest in ILs for various applications stems from their properties as solvents, these acquire reference values under certain purity conditions, so achieving successful, sustainable, and economical purification remains a significant challenge.

Reference electrodes (REs) are compartmentalized devices that maintain a known and constant half-cell potential over time due to the presence of a redox couple in a buffered condition. However, the absence or alteration of the relative concentrations of the chemical species defining the specific redox couple will inevitably affect the observed electrode potential [10,11] . In Room Temperature Ionic Liquids (RTILs), several studies have focused on developing reference electrodes, such as Snook *et al*., who proposed a Ag^0/Ag^+ electrode, but interactions with the RTIL's ions can compromise its stability and accuracy [12] . Huber and Roling developed a micro Ag^0/Ag^+ reference electrode, useful for small systems, though its long-term performance in RTILs remains unvalidated [13] . Horwood and Stadermann introduced a $Ag^0/Ag_2S_{(s)}$ electrode with greater stability, but its use is limited to certain RTILs [14]. García-Mendoza and Aguilar-Cordero designed a $Ag^0/[AgCl_n]^{1-n}$ electrode for bis(trifluoromethylsulfonyl)imide-based RTILs. However, its application is not generalizable to other ionic liquids composed of different types of anions [15].

These electrodes must be specifically designed for the solvent in which they are used to ensure stability and accuracy. Properly designed electrodes offer several advantages: (1) reproducible and stable potential over time, (2) reversibility and adherence to the Nernst equation, (3) return to the initial value after a small current is applied and the stopped, and (4) no hysteresis with temperature cycling [16–18] . Thus, it is essential to construct reference electrodes tailored explicitly to the RTIL being studied to ensure reliable and analytically acceptable measurements.

Unfortunately, quasireference electrodes (QREs) are often used when nonaqueous solvents are used. These devices maintain a potential value, albeit not well-defined or reproducible, during a series of measurements [19]. This kind of electrode must be calibrated with respect to an internal reference system to obtain meaningful potential values. Commonly used redox couples for this purpose include ferrocenium/ferrocene ($[Fe(Cp)_2]^{+/0}$) and cobaltocenium/cobaltocene ($[Co(Cp)_2]^{+/0}$) [20]. Furthermore, in QREs, the redox couple responsible for the electrode potential is uncertain, as multiple uncontrolled processes can occur at the metal-solution interface [21,22]. Furthermore, the destruction of QREs in RTILs due to their solubilization effect has been reported [2], making their use not recommended for electrochemical assays conducted over extended periods or for the characterization of processes occurring in the electric double layer (EDL) [23,24].

This work aims to describe the chemical speciation of the Ag^+–Cl^-–e^- system in $[C_4mim][NTf_2]$ and the extraction of Ag(I) from this RITL towards water, using a variety of electrochemical techniques to analyze the chemical species involved in potential drift in different architectures of true reference electrodes of Type 1 and Type 2 based on the concurrent interfaces $Ag^0|Ag^+||$ and $Ag^0|AgCl_{(s)}||$, respectively. The goal is to propose

J. Mex. Chem. Soc. **2025**, *69*(4)
Regular Issue

ISSN-e 2594-0317

these half-cells as constant potential electrodes for use in $[C_4mim][NTf_2]$, thereby minimizing the need for toxic materials, such as mercury, and expensive ones, like platinum or palladium [22,25,26]. Additionally, estimating the silver extraction constant at the water-RTIL interface is intended to provide comments on the exposure of prepared REs in humid environments. This information could be used as a competitive, environmentally friendly, and cost-effective purification technique, as it reduces the use of toxic, volatile, and flammable contaminants required in other methods, such as distillation. Estimating this extraction constant allows us to understand the partitioning behavior of silver(I) between the two phases, considering the effect of their pCl imposed values, pH in the aqueous phase, and the volume ratio of the solvents, $p(V_{org}/V_{ac})$.

Experimental methodology

Reagents

The aprotic ionic liquid used in this work was 1-butyl-3-methylimidazolium bis(trifluoromethylsulfonyl)imide ($[C_4mim][NTf_2]$, Merck, purity ≥ 98 %). For the chemical speciation of the $AgCl_{(s)}/[AgCl_n]^{1-n}$ and $Ag^{+/0}$ systems, silver wire (Ag^0, Sigma–Aldrich, diameter = 1.0 mm, purity ≥ 99.99 %), 1-ethyl-3-methylimidazolium chloride ($[C_2mim]Cl$, Sigma–Aldrich, purity > 98 %), and silver bis(trifluoromethylsulfonyl)imide ($Ag[NTf_2]$, Sigma–Aldrich, purity > 97 %) were used. These materials were common for the construction of the RE in the RTIL. For the identification of the intrinsic solubility of silver in the RTIL, a medium composed of silver nitrate ($AgNO_3$, Sigma–Aldrich, purity ≥ 99.0 %), potassium thiocyanate (KSCN, Sigma–Aldrich, purity > 98.5 %), ammonium nitrate (NH_4NO_3, Sigma–Aldrich, purity ≥ 98 %), sodium sulfite (Na_2SO_3, J.T. Baker, purity ≥ 98.52 %), and sodium thiosulfate pentahydrate ($Na_2S_2O_3 \cdot 5H_2O$, J.T. Baker, purity ≥ 99.5 %) was used. Cobaltocenium hexafluorophosphate ($[Co(Cp)_2][PF_6]$, Sigma–Aldrich, purity ≥ 98 %) was used as an internal reference system in the RTIL, while ferrocenemethanol ($[Fe(Cp)_2CH_2OH]$), Sigma–Aldrich, purity ≥ 97 %) was used as a redox standard in aqueous solution. The reagents were used as received and stored in a desiccator cabinet Bel-Art Amber tinted UV blocking model (relative humidity < 5 %). The $[C_4mim][NTf_2]$ and all solutions prepared in this RTIL as a solvent were dried for 24 h at 90 °C in an oven before use. Deionized water (> 18 MΩ cm^{-1}) obtained from a Milli-Q system was used for washing. Nitrogen 4.8 (N_2, ProSpec, purity ≥ 99.998 %) was used to perform measurements under an inert atmosphere using an appropriate gas−washing glass bottle.

Instruments

For open circuit potential (OCP) measurements and the electrochemical preparation of $AgCl_{(s)}$ coatings, a potentiostat (model 920C, CH Instruments, USA) with a three-electrode setup was used. A silver wire (Ag, Sigma–Aldrich, purity ≥ 99.99 %, 1.0 mm diameter, 30 mm length) was used as the working electrode (WE), a platinum coiled wire (Pt, Sigma–Aldrich, purity ≥ 99.99 %, 0.5 mm diameter, 37 mm length) was used as the counter electrode (CE), and an appropriate RE was utilized. For electrochemical measurements by cyclic voltammetry (CV), a potentiostat (PalmSens4 model, Palm Sens BV, NL) with a three-electrode setup was used. A gold electrode (Au, CH Instruments, 2.0 mm diameter) and a glassy carbon electrode (GC, CH Instruments, 3.0 mm diameter) were employed as working electrodes (WEs); a platinum coiled wire described above was the counter electrode (CE). A Faraday cage (Cypress Systems, USA) was utilized to minimize electrostatic interferences during data acquisition.

Every working electrode was polished with alumina powder (Buehler) with a particle size of 0.05 μm on a microcloth (Buehler) and washed with deionized water (> 18 MΩ cm^{-1}). Immediately, electrodes were sonicated in an appropriate volume of this solvent for 5 min and finally rinsed. Afterward, the electrodes were placed under a flow of dry N_2. All masses were measured using a Mettler balance (XP105DR, ± 0.01 mg, Mettler Toledo, USA). Gravimetric and volumetric errors were typically less than 2 %.

The temperature was ensured at T = 25.0 ± 0.5 °C using a recirculating water bath connected to an optimized thermostated electrochemical cell. The arrangement of the three-electrode cell used is shown schematically in Fig. 1.

J. Mex. Chem. Soc. **2025**, *69*(4)
Regular Issue

ISSN-e 2594-0317

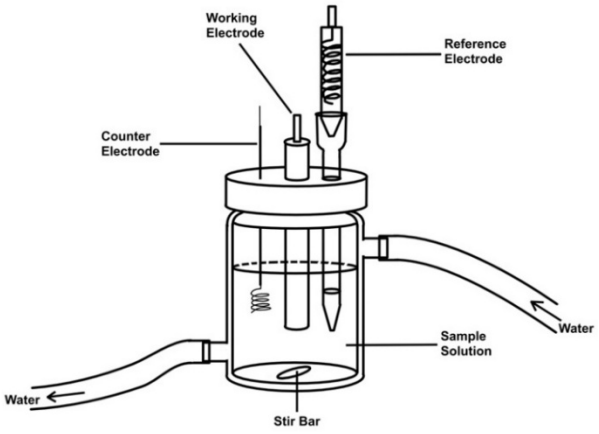

Fig. 1. Schematic of the three-electrode cell setup for electrochemical measurements using a thermostated cell.

Electrochemical measurements

All electrochemical measurements were conducted under a dry N_2 atmosphere by bubbling the gas into a cell with a maximum solution volume of 2.0 mL. The evolution of the RE potential values over time was determined *vs.* the cobaltocene/cobaltocenium redox couple ($[Co(Cp)_2]^{+/0}$) using CV at nine scan rates in V s^{-1}: 0.005, 0.010, 0.025, 0.050, 0.100, 0.250, 0.500, 0.750, and 1.000. The redox standard solution was prepared by weighing the necessary amount of cobaltocenium hexafluorophosphate in $[C_4mim][NTf_2]$ and stirring under a stream of dry N_2 until complete dissolution of the solid. Care was taken to ensure that the concentration was the same in all solutions of the redox standard ($C \approx 25$ mmol L^{-1}), achieving a similar final total mass for all the solutions used by weighing the same amount of ionic liquid and standard. During data acquisition, compensation was made for up to 95% of the electrical resistance of each solution in the form of an ohmic drop, iR.

The OCP of the $[C_2mim]Cl$ and $Ag[NTf_2]$ solutions prepared in the RTIL was monitored in triplicate for 600 s at intervals of 0.2 s using Ag^0 and $AgCl_{(s)}$ wires as convenient indicator electrodes, a Pt wire as the CE, and a freshly calibrated RE with respect to the $[Co(Cp)_2]^{+/0}$ redox couple. In aqueous media, the OCP of the NaCl solutions prepared in water was monitored for 600 s at intervals of 0.2 s using a $AgCl_{(s)}$ wire, a Pt wire as the CE, and a freshly calibrated RE with respect to the $[FcMeOH]^{+/0}$ redox couple.

The determination of Ag(I) in the aqueous phase was carried out through potentiometric titrations because the estimated concentration falls within the technique's linear limit of quantification. Potentiometric monitoring was performed with a three-electrode system using a silver wire as the indicator electrode (IE), a platinum wire as CE, and a $Ag^0/AgCl_{(s)}$ RE. A salt liquid junction containing a saturated KNO_3 solution was used to prevent the migration of Cl^- ions from the internal electrode chamber into the solution. The OCP was measured for 300.0 s with stirring. Aliquots of 10.0 µL of a 0.1 M sodium chloride standard solution were added to the aqueous solution, and the OCP was measured after each addition.

The determination of Ag(I) in the nonaqueous phase, $[C_4mim][NTf_2]$, was carried out using Anodic Stripping Square Wave Voltammetry (ASSWV) because the estimated concentration range falls within the technique's linear limit of quantification. This analysis was performed using a glassy carbon electrode as WE in a coordinating medium prepared in an aqueous solution in which a calibration curve was constructed using standard additions of a previously standardized $AgNO_3$ solution.

Preparation of extraction systems

Two experimental setups were devised to evaluate the silver extraction constant. The pH of the aqueous phase was buffered using a Britton-Robinson buffer solution, which was prepared to achieve the desired pH for the study.

For the first setup, an average volume of 0.4 mL of pure $[C_4mim][NTf_2]$ was weighed into a glass vial, followed by the addition of an average volume of 0.6 mL of a silver nitrate solution (0.095 ± 0.001 M) using a micropipette. The mixture was stirred for 15 min and left to rest for 24 h in the dark before phase separation.

J. Mex. Chem. Soc. **2025**, *69*(4)
Regular Issue

ISSN-e 2594-0317

For the second setup, an average volume of 0.4 mL of a previously prepared solution of silver bis(trifluoromethylsulfonyl)imide in $[C_4mim][NTf_2]$ was measured. Then, an average volume of 0.6 mL of deionized water or Britton-Robinson buffer solution was added to the sample in the glass vial. The mixture was stirred for 15 min and stored in the dark for 24 h before phase separation.

The independent phases were preserved in glass vials for subsequent quantification.

Construction of reference electrodes

Four REs were fabricated. Two were based on the $Ag^0|AgCl_{(s)}|Cl^-||$ half-cell, one based on the $Ag^0|Ag^+||$ half-cell, and another on $Ag^0|Cl^-||$ half-cell. A detailed description of the construction and labeling of the REs is provided in Appendix A, Supporting Information.

Results and discussion

Potentiometric calibration curves

The $Ag^0|AgCl_{(s)}$ interface coating was produced through CV using an acidic medium in an aqueous solution. Due to the imposed pCl value in the solution, there is no predominant presence of $[AgCl_n]^{1-n}$ type complexes, with $1 \leq n \leq 4$ [27]. All coatings were visually inspected and presented a white color without cracks or dark spots. They were dried under N_2 flow and stored in the dark for two days before being used in the RTIL.

A relationship was observed between the OCP values obtained when using Ag^0 and $Ag^0|AgCl_{(s)}$ working electrodes and the logarithm of the concentration of chloride and silver(I) solutions prepared in $[C_4mim][NTf_2]$. This behavior fits linear relationships according to the archetypal model of the Nernst-Peters equation [18], where the slope corresponds to the number of particles exchanged at equilibrium responsible for the potential at the interface in terms of multiples of the quotient 2.3RT/F, as illustrated in Fig. S2 (Appendix B, Supporting Information). Thus, when using a Ag^0 indicator electrode, a reversible and linear response is obtained over the entire range of analyzed concentrations of $Ag[NTf_2]$ in the RTIL, as shown in the first row of Table S2, suggesting a Nernst equation that coincides with the linear fit of E *vs*. log (C/M), where the intercept of the linear fit yields the value of E°'/V for the $Ag^{+/0}$ redox couple. Furthermore, when using a $Ag^0|AgCl_{(s)}$ indicator electrode for these same solutions, a similar OCP response is obtained, expressed in terms of a Nernst equation, as indicated in the second row of Table S2. The intercept obtained from the linear fit is linked to the K_{sp} value of the $AgCl_{(s)}/Ag^+$ couple.

On the other hand, when a $Ag^0|AgCl_{(s)}$ or Ag^0 indicator electrode is used to measure the potential of $[C_2mim]Cl$ solutions of different concentrations prepared in the ionic liquid, the same OCP response is obtained regardless of the WE used. There is experimental evidence of the solubilization of $AgCl_{(s)}$ due to excess Cl^- in molecular solvents and in other RTILs that share structural similarities and physicochemical properties with $[C_4mim][NTf_2]$ [28]. Hence, the formation of $[AgCl_n]^{1-n}$ chemical species in this ionic medium, potentially responsible for the electrode potential at the interface, is probable. Thus, the chemical equilibrium presented in the third and fourth rows of Table 2S is presumed to be responsible for the electrode potential due to the presence of the stabilized $[AgCl_3]^{2-}$ species [15]. These data are accompanied by a Nernst equation, whose intercept the E°'/V of the $[AgCl_3]^{2-}/Ag^0$ redox couple can be estimated.

The potentiometric methodology presented was replicated in an aqueous medium (Fig. S3) to calibrate the $Ag^0/AgCl_{(s)}$ electrode for potentiometric titrations in this medium. Additionally, this methodology allows for determining the number of particles exchanged in the redox pair. According to the experimental results, a slope corresponding to a single particle exchanged in both equilibria was obtained, consistent with what has been reported in the literature (Table S2) [29].

An alternative study to corroborate the number of electrons exchanged in the redox system of the Ag^0/Ag^+ pair in $[C_4mim][NTf_2]$, similar to what occurs in aqueous medium, was performed through chronopotentiometric studies in both aqueous medium and the ionic solvent. The results confirmed the exchange of a single particle (Appendix D, Supporting Information).

Potentiometric titrations

A series of representative potentiometric titrations were carried out in both $[C_4mim][NTf_2]$ and water to obtain information related to the characteristic chemical equilibria of each stage of the analytical process, to elucidate the chemical speciation of the Ag^+–Cl^- system [15]. The general scenarios are established as follows.

J. Mex. Chem. Soc. **2025**, *69*(4)
Regular Issue

ISSN-e 2594-0317

In the first scenario, the potentiometric titration of a $[C_2mim]Cl$ solution was performed, to which aliquots of $Ag[NTf_2]$ as the titrant were added, both solutions prepared in $[C_4mim][NTf_2]$. Potentiometric monitoring was performed using a $Ag^0|AgCl_{(s)}$ as an indicator electrode, previously calibrated with a series of Cl^- solutions of increasing concentration in the RTIL.

For an initial concentration, C_0, higher than the intrinsic solubility of the $AgCl_{(s)}$ species, S_0 ($C_0 > S_0$), the distinctive condition of a heterogeneous system is met, allowing the determination of the solubility product constant, K_{sp}, of the $AgCl_{(s)}/Ag^+$ pair through a Gunnar-Gran type adjustment using the added volume data and the cell potential obtained before the equivalence point (Fig. S4, Appendix C, Supporting Information) [30]. A white precipitate was observed during the titration, whose abundance visually increased from the beginning of the process until the equivalence point, remaining constant thereafter. Potentiometric titration continued up to a 400% excess of titrant relative to the first equivalence volume to form the $[AgCl_2]^-$ and $[AgCl_3]^{2-}$ species, for which there is evidence in these solvents and to estimate the values of the global formation constants, β_2 and β_3, respectively (Fig. S6, Appendix C, Supporting Information). The final titration phase corresponds to a plateau in the cell potential values determined by the $Ag^{+/0}$ redox pair.

The second scenario was examined under one condition: the initial concentration was below the intrinsic solubility, $C_0 < S_0$. Under this premise, a homogeneous system was established, so the titration of $[C_2mim]Cl$ in the RTIL with additions of $Ag[NTf_2]$ resulted in the formation of the soluble [AgCl] species. No solids were observed during the analytical process (Fig. S5, Appendix C, Supporting Information). The cell potential data obtained before the equivalence point were fitted to a Gunnar-Gran function to estimate the global formation constant, β_1, of the soluble [AgCl] species, using the law of mass action for the $[AgCl]/Ag^+$ pair. The final titration stage showed a potential plateau determined by the same process as in the previous scenario.

The values of the constants obtained from the previous Gunnar-Gran type adjustments provided a reference point for applying the ulterior non-linear adjustments, according to Brown's methodology [31]. The Method of Extended Ringbom's Coefficients (MERC) [32], commonly used in aqueous media to describe equilibrium systems, was successfully adapted to this ionic liquid to get a fourth-degree polynomial describing the theoretical titration curve based on electroneutrality balance during the potentiometric titration, incorporating condensed species for a more accurate description of the systems. Once the polynomial was established, the Solver® tool, available as an add-in in Microsoft Excel®, was used to adjust the theoretical values of pAg or pCl (calculated from the recorded cell potential values), minimizing the sum of squared differences with respect to the volume. The goodness of the non-linear fit was verified in terms of $R^{2,}$ showing that theoretical titration curves closely matched the experimental data (Fig. 2**(A)** and 2**(B)**). The logarithm of the formation constants set was reported with a 95.45% confidence interval corresponding to a coverage factor, k = 2 (Table 2), assuming normally distributed data.

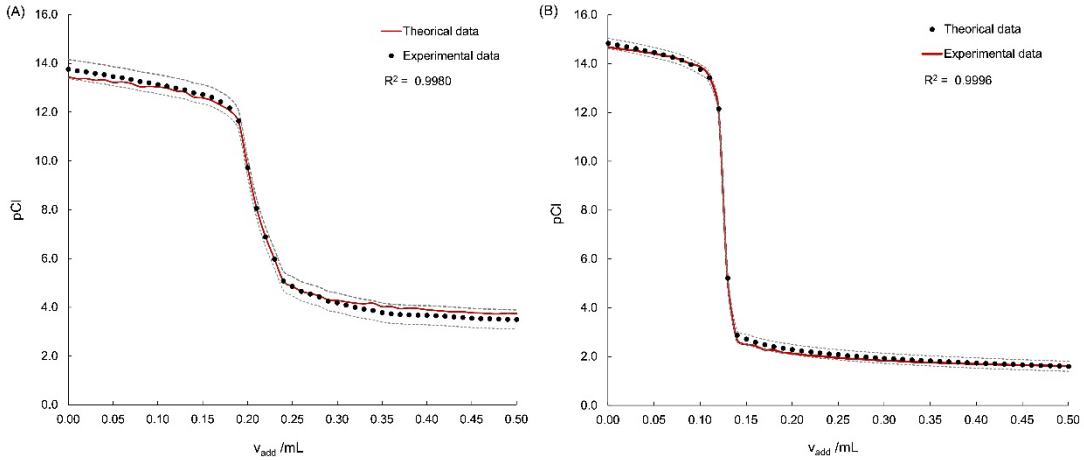

Fig. 2. Experimental curves, represented by a solid red line, and non-linear fits, represented by dots for **(A)** Records of OCP evolution of a Ag^0 indicator electrode during the titration of $[C_2mim]Cl$ ($C_0 = 0.10001$ mol L^{-1}) with additions of $Ag[NTf_2]$ ($C_{Ag^+} = 0.09972$ mol L^{-1}) in $[C_4mim][NTf_2]$; and **(B)** records of OCP evolution of a $Ag^0|AgCl_{(s)}$ indicator electrode during the titration of $Ag[NTf_2]$ ($C_0 = 0.09972$ mol L^{-1}) with additions of $[C_2mim]Cl$ ($C_{Cl^-} = 0.10001$ mol L^{-1}) in $[C_4mim][NTf_2]$. Additionally, the confidence intervals are outlined with a dashed line.

J. Mex. Chem. Soc. **2025**, *69*(4)
Regular Issue

ISSN-e 2594-0317

A similar experiment was conducted in an aqueous solution, where aliquots of NaCl were added to a solution of $AgNO_3$. A typical potential response was obtained (results not shown), with an initial constant potential region given by the $AgCl_{(s)}/Ag^+$ pair and a second plateau determined by the $AgCl_{(s)}/Cl^-$ redox pair (Fig. S7, Appendix C, Supporting Information). The methodology described above was successfully applied to this system, yielding a pK_{sp} value of 9.4 ± 0.5 for the $AgCl_{(s)}/Ag^+$ pair [33,34].

Table S5, Appendix E, Supporting Information, presents the set of polynomials that describe the different theoretical titration curves carried out both in $[C_4mim][NTf_2]$ and in aqueous media, the Gunnar-Gran equations and the explicit expressions of the distributive molar fractions, φ_i, used in such polynomials.

On the other hand, the residual analysis of silver(I) in the aqueous phase of each extraction assay was performed through potentiometric titration using NaCl 0.1 mol L^{-1} as the titrant. The experimental titration curve shows a typical profile of a quantitative reaction. At the beginning of the titration, the solution is colorless; with the first addition of the titrant, turbidity appears due to the formation of a white solid, which corresponds to the formation of $AgCl_{(s)}$. Subsequently, the formation of a violet solid was observed until the equivalence point. Once the endpoint of the titration was exceeded, the precipitate was partially dissolved. The determination of the endpoint for the quantification of silver content in the aqueous phase was carried out using the first derivative, $\Delta pCl/\Delta V$ *vs*. V_{added}. Table S3, Appendix C, Supporting Information presents the amount of substance (in terms of Ag found) in the aqueous phase.

Total determination of soluble silver(I) in $[C_4mim][NTf_2]$

The total solubility of silver(I) in the RTIL, denoted as S_{max}, is given by contributions from molecular and ionic solubility as described by Equation 1.

$$S_{max} = \sum_{n=0}^{i} [[AgCl_n]^{1-n}] = [Ag^+] + [[AgCl]] + [[AgCl_2]^-] + [[AgCl_3]^{2-}] + \cdots \qquad \text{Equation 1}$$

To determine the maximum solubility of Ag(I) in $[C_4mim][NTf_2]$ and its concentration in such phase, several anodic stripping square wave voltammetry (ASSWV) assays were conducted on a glassy carbon electrode using a coordinating medium in aqueous solution [35]. The standard addition method was employed on an aliquot of the sample, followed by the addition of a standardized $AgNO_3$ solution (Fig. S8, Appendix C, Supporting Information). The maximum solubility of Ag(I) in $[C_4mim][NTf_2]$ was determined to be $\log (S_{max}/M) = (2.8 \pm 0.5)$. This solubility value is consistent with reports on other imidazolium-based ionic solvents, where the hydrocarbon chain at position number one of the imidazole ring notably influences the value of S_0. Increasing the number of carbon atoms in the chain leads to a decrease in S_0 [15]. The amount of substance in the nonaqueous phase was determined successfully, and it was observed that its value depends on the volume ratio, $p(V_{org}/V_{ac})$; these results are shown in Table S3, Appendix C, Supporting Information.

Estimation of the conditional extraction constant

The equilibrium associated with the extraction of Ag^+ in the H_2O–$[C_4mim][NTf_2]$ system is represented in Equation 2, where the species in the nonaqueous solvent is denoted with a straight line over the condensed formula as follows $\overline{Ag^+}$; while the species in the aqueous medium simply as Ag^+ [36,37].

$$\overline{Ag^+} \rightleftarrows Ag^+ \qquad \text{Equation 2}$$

However, in the aqueous phase, both soluble and insoluble species may form due to the interaction of silver(I) with the solvent, depending on the pH values in such phase [38]. The reaction scheme considering these reactions is outlined in Equation 3.

$$\overline{Ag^+} \quad \rightleftarrows \quad \begin{array}{c} AgO_{0.5\,(s)} \\ \downarrow\uparrow \\ Ag^+ \\ \downarrow\uparrow \\ [Ag(OH)_n]^{1-n} \end{array} \qquad \text{Equation 3}$$

J. Mex. Chem. Soc. **2025**, *69*(4)
Regular Issue

ISSN-e 2594-0317

A conditional extraction constant is defined since the chemical species Ag^+ in the aqueous medium significantly depends on the system's pH. According to the law of mass action, this constant is defined as the ratio between the total concentration of Ag^+ in the nonaqueous phase and the total concentration of Ag^+ in the aqueous phase [39], as represented in Equation 4.

$$K'_E = \frac{[\overline{Ag^+}]}{[Ag^+]'} = \frac{[\overline{Ag^+}]}{[Ag^+]\bar{\alpha}_{Ag^+(H)}} \qquad \text{Equation 4}$$

By multiplying this conditional extraction constant by the alpha speciation coefficient in the heterogeneous medium, defined according to the Method of Extended Ringbom's Coefficient under the working conditions [32], $\alpha_{Ag^+(H)}$, the apparent extraction constant can be determined, as shown in Equation 5.

$$K_E = K'_E\, \alpha_{Ag^+(H)} = \frac{[\overline{Ag^+}]}{[Ag^+]} \qquad \text{Equation 5}$$

In each system, the amount of Ag^+ in both phases was quantified, and based on the volume ratio, the values of the conditional and apparent extraction constants were calculated under buffered aqueous conditions. The results of this determination are presented in Table 1.

Table 1. Conditional extraction constant values, K_E', apparent extraction constant, K_E, at different pH values and volume ratios, $p(V_{org}/V_{aq})$.

System	$P(V_{org}/V_{aq})$	pH	K_E'	K_E	log K_E
A	-0.01	3.47	362.4	362.5	2.56
B	-0.22	3.47	217.0	217.0	2.34
C	0.17	3.47	186.0	186.0	2.27
D	0.20	3.47	91.8	91.8	1.96
E	0.20	7.86	78.1	128.7	2.11
F	0.19	11.49	72.8	175.7	2.24
G	0.70	8.64	34.9	627.6	2.78

Thus, the apparent extraction constant, expressed in logarithm terms, for silver(I) in the water-1-butyl-3-methylimidazolium bis(trifluorosulfonyl imide) system is log (K_E) = 2.32 ± 0.27.

Compilation of estimated equilibrium constants for Ag^+–Cl^-–e^- redox system in [C_4mim][NTf_2]

Table 2 summarizes the calculated parameters pertaining to the Ag^+–Cl^-–e^- system in [C_4mim][NTf_2]. Fig. 3 presents the solubility diagram for these systems, constructed by deducing a nonsegmented polynomial considering phase transition and incorporating an extended concept of Ringbom's side reaction coefficients (Method of Extended Ringbom's Coefficients) that is usually applied to describe chemical speciation in multicomponent systems (Appendix E, Supporting Information) [15,32]. Although there is evidence of the formation of ion pairs or other associated ionic species in RTILs [40], the effective concentration, being relatively high, often surpasses the concentration of the solutes dissolved in them. Consequently, the ionic strength in these systems is determined mainly by ions originating from the solvent itself. This phenomenon establishes the baseline for estimated equilibrium constants, making them apparent constants. Similarly, the estimated potentials are formal redox potentials, denoted as $E^{\circ\prime}$ [41–43].

J. Mex. Chem. Soc. **2025**, *69*(4)
Regular Issue

ISSN-e 2594-0317

Table 2. Mean formal potential and apparent values of thermodynamic parameters obtained by potentiometry and voltammetry measurements carried out in $[C_4mim][NTf_2]$ (N = 5).

Parameter	Couple (donor/receiver)	Value
$E°'/V^a$	Ag^0/Ag^+	1.604 ± 0.006
$E°'/V^a$	$Ag^0/[AgCl_3]^{2-}$	0.339 ± 0.007
pK_{sp}	$AgCl_{(s)}/Ag^+$	16.6 ± 0.1
pK_{sp}^b	$AgCl_{(s)}/Ag^+$	9.4 ± 0.5
log (β_1)	$[AgCl]/Ag^+$	13.1 ± 0.1
log (β_2)	$[AgCl_2]^-/Ag^+$	16.6 ± 1.5
log (β_3)	$[AgCl_3]^{2-}/Ag^+$	17.9 ± 1.7
log (S_{max})	$AgCl_{(s)}/[AgCl]$	-2.8 ± 0.5
log (K_E)	$(Ag^+)_{RTIL}/(Ag^+)_{H_2O}$	2.3 ± 0.3
C_{H_2O} /ppm	-	121.3 ± 3.4

[a]The potential values are presented relative to the $[Co(Cp)_2]^{+/0}$ redox couple.
[b]Determined in aqueous media.

With the constant values estimated in this work, it was possible to construct the Predominance States Diagram (PSD) of the logarithm of the conditional extraction constant as a function of pCl (Fig. 3) for the $[C_4mim][NTf_2]$-water interface. The diagram was constructed using Equation S6, presented in Appendix E, Supporting Information. It is imperative to highlight that in the present diagram, pCl is evaluated equally in both phases.

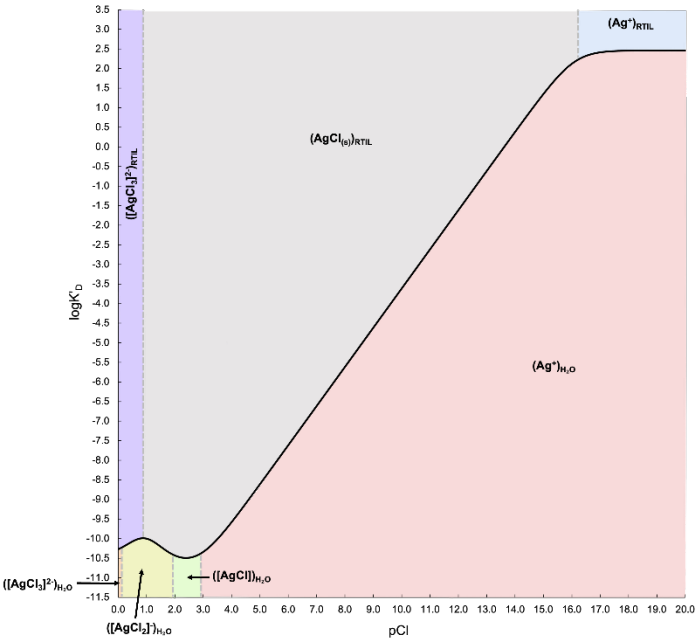

Fig. 3. Predominance Diagram of States of the logarithm of the conditional extraction constant as a function of pCl at $p(V_{org}/V_{aq})$ = -0.01 and an initial concentration of Ag(I)' in $[C_4mim][NTf_2]$ of 0.3 M.

J. Mex. Chem. Soc. **2025**, *69*(4)
Regular Issue

ISSN-e 2594-0317

This diagram can be interpreted as analogous to traditional complex formation diagrams, wherein the reactants are positioned at the apex of the diagram while the products occupy the lower region. Also, it allows us to discern how variations in the pCl value, evaluated at the same concentration in both phases, influence the direction of extraction, thereby facilitating the understanding of why trace water contamination does not affect these systems, provided that pCl values remain low. The subsequent section dedicated to constructing true reference electrodes offers a more detailed explanation.

Evaluation of the reference electrodes constructed in $[C_4mim][NTf_2]$

To evaluate the stability of the electrode potential values over time and determine the pCl and pAg' at which the electrode potential drift of the reference electrodes is minimal, the $E_{½}$ of the $[Co(Cp)_2]^{+/0}$ redox couple was determined by CV using these reference electrodes (Appendix F, Supporting Information) in $[C_4mim][NTf_2]$. The drift was assessed for four electrodes constructed under the conditions described in Appendix A of the Supporting Information over a period of 3500 h, as shown in Fig. 4.

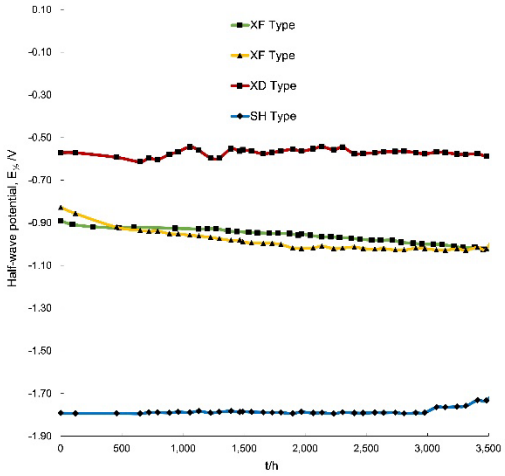

Fig. 4. Variation of the electrode potential for the constructed reference electrodes over time using filling solutions of $[C_2mim]Cl$ and $Ag[NTf_2]$ with concentrations of C = 0.0100 mol L^{-1} (Type XF); C = 1.000 mol L^{-1} (Type XD) and C = 0.3000 mol L^{-1} (Type SH) in $[C_4mim][NTf_2]$. The $E_{1/2}$ value obtained by CV for the $[Co(Cp)_2]^{+/0}$ redox couple is reported.

The electrode potential values obtained were practically constant from the early days of fabrication, with variations not exceeding ±10 mV. The potential drift observed for the reference electrodes over time may be attributed to the gradual degradation of the $AgCl_{(s)}$ coating due to UV radiation, causing the photoreduction of the Ag^0 coating [44]. This phenomenon was not observed in REs that were permanently stored inside the Bel-Art desiccator due to the device's UV protection. Although water absorption was observed by the RTIL that make up the REs when stored without protection from atmospheric humidity, these devices can recover their initial potential value after drying for 24 h in an oven at 90 °C.

It was observed that Type XD and SH electrodes showed the lowest potential drifts, 0.53 μV h^{-1} and 0.58 μV h^{-1}, respectively, compared to Type XF electrodes, which had a drift of approximately 9.5 μV h^{-1}. Thus, according to the solubility diagram in Fig. 5, constructed by deducing a nonsegmented polynomial considering phase transition and incorporating the MERC, the Type D electrode contains buffering conditions to maintain the speciation of Ag(I) predominantly in the form of $[AgCl_3]^{2-}$. On the other hand, the Ag^0/Ag^+ redox couple proves to be a system with a rapid and stable response in this ionic solvent. Although it has been reported that for nonaqueous systems, the most common RE is the Ag^0/Ag^+, and in this work, it has been shown that its potential drift is very low, it should be considered that the extraction of this cation is possible when the $[C_4mim][NTf_2]$ comes into contact with water, causing a perceptible change in its concentration in the nonaqueous phase and consequently, a more significant potential drift. Thus, the REs based on the concomitant

J. Mex. Chem. Soc. **2025**, *69*(4)
Regular Issue

ISSN-e 2594-0317

$Ag^0|AgCl_{(s)}$ interface offer a better response to humidity conditions even to high pCl values in the nonaqueous phase, since the extraction of the $[AgCl_n]^{1-n}$ species from the $[C_4mim][NTf_2]$ towards water is not favored.

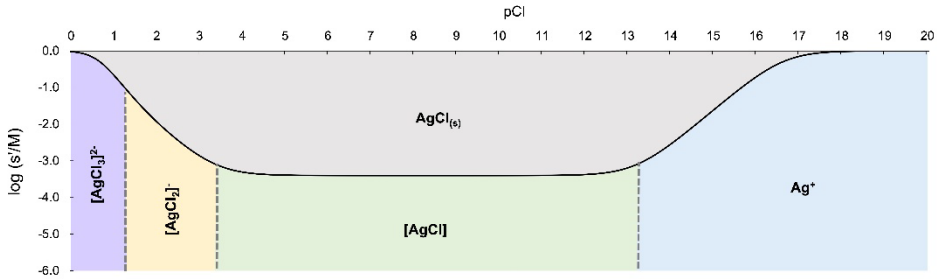

Fig. 5. Solubility diagram of $AgCl_{(s)}$ in $[C_4mim][NTf_2]$. Depicted in blue for Ag^+; green for [AgCl]; yellow for $[AgCl_2]^-$; purple for $[AgCl_3]^{2-}$; and red for $AgCl_{(s)}$.

The liquid junction potential was calculated using the Henderson equation [45] based on the limiting molar conductivity values of the corresponding chemical species [46]. This calculation resulted in potential values below the resolution limit of the instruments used in this study. Additionally, Bülhmann *et al.* have reported that liquid junction potentials in reference electrodes equipped with porous liquid junctions, such as Vycor® type, tend to decrease as ionic strength increases. Since ions are the primary constituents of RTILs, the ionic strength in these solvents is significantly high, resulting in remarkably low liquid junction potential values [47].

Additionally, the water content in this ionic liquid was quantified through electrochemical techniques [48], yielding an approximate water content of 121.3 ppm after a drying process of 48 h in an oven at 90 °C. If, in Equation S6, the concentration of Cl^- in the inner chamber of the Type DB electrode is evaluated under a hypothetical condition of high relative humidity, where a significant amount of water might infiltrate the ionic liquid, a log K_E' value of -15.5 would be obtained. This value indicates that the equilibrium of Ag(I) in the RTIL at elevated pCl values, in $[C_4mim][NTf_2]$ phase, does not favor extraction into the aqueous phase, thus ensuring a homogeneous and unaltered coating on the reference electrode, even in the presence of water contamination.

A similar study was carried out in parallel using commercial reference electrodes for use in aqueous solution, finding that those based on the $Ag^0|AgCl_{(s)}$ interface presented average potential drifts of 7.18 $\mu V\ h^{-1}$ in the same period when using a solution of ferrocenemethanol ($[Fe(Cp)_2CH_2OH)]$), $C \approx 25$ mmol L^{-1} in the presence of $LiClO_4$, C = 0.1 mol L^{-1}, as a redox reference system (Appendix G, Supporting Information).

Conclusions

In this work, we present a methodology to describe the chemical speciation of the system $[AgCl_n]^{1-n}/Ag^0$ in both $[C_4mim][NTf_2]$ and aqueous solution, using various electrochemical techniques to obtain formal potential values and apparent constants associated with the concurrent chemical equilibria in this ionic liquid. Additionally, the logarithm of the extraction constant of Ag^+ in the water–RTIL interface was reported as log $K_E = (2.3 \pm 0.3)$, indicating that the extraction of silver from the 1-butyl-3-methyl imidazolium bis(trifluorosulfonyl imide) ionic liquid with water is favored, particularly at high pCl values imposed in both phases. This phenomenon suggests potential applications for purifying this ionic liquid using water, a ubiquitous and low-cost solvent.

The information collected is useful for describing the processes responsible for the potential observed in the true Type I and Type II reference electrodes, constructed based on the concomitant $Ag^0|[AgCl_n]^{1-n}$ interface, for use in this ionic solvent. For the RTIL $[C_4mim][NTf2]$, it was found that the best electrode configuration was $Ag^0|AgCl_{(s)}||[C_2mim]Cl$, 1.000 mol L^{-1}, $[C_4mim][NTf_2]||$ (0.53 $\mu V\ h^{-1}$), which is competitive with reference electrodes reported in aqueous media. In this way, the reference electrodes presented in this work appear robust and have reproducible potential values. Also, it has been determined that under the pCl values buffered for each phase in the configuration of the RE (low ones in the RTIL and high ones in the aqueous

J. Mex. Chem. Soc. **2025**, *69*(4)
Regular Issue

ISSN-e 2594-0317

medium), the silver(I) does not transfer to the aqueous phase, thereby maintaining a homogeneous coating inside de REs without causing any alteration in their composition.

In summary, the description of chemical reactivity based on the Method of Extended Ringbom's Coefficients was applicable in ionic liquids and offers an opportunity to optimize the design of reference electrodes and specific reaction media, applying what we described in new RTILs.

Acknowledgments

This work was supported by UNAM-PAPIIT IA202122 and UNAM-PAPIIT IA207724. J. Ruvalcaba-Juárez is thankful for the scholarship provided by CONAHCyT (No. 1099976).

References

1. Lei, Z.; Chen, B.; Koo, Y.-M.; MacFarlane, D. R. *Chem. Rev.* **2017**, *117*, 6633–6635. DOI: https://doi.org/10.1021/acs.chemrev.7b00246.
2. Wasserscheid, P.; Welton, T., in: *Ionic Liquids in Synthesis*, 2nd ed.; Wiley, **2008**; Vol. 1. DOI: 10.1002/9783527621194.
3. Barrosse-Antle, L. E.; Bond, A. M.; Compton, R. G.; O'Mahony, A. M.; Rogers, E. I.; Silvester, D. S. *Chem. Asian J.* **2010**, *5*, 202–230. DOI: https://doi.org/10.1002/asia.200900191.
4. Caminiti, R.; Gontrani, L., in: *The Structure of Ionic Liquids*, 1st ed.; Springer, **2013**. DOI: https://doi.org/10.1007/978-3-319-01698-6.
5. Tiago, G. A. O.; Matias, I. A. S.; Ribeiro, A. P. C.; Martins, L. M. D. R. S. *Molecules.* **2020**, *25*, 5812. DOI: https://doi.org/10.3390/molecules25245812.
6. Cruz, C.; Ciach, A. *Molecules.* **2021**, *26*, 3668. DOI: https://doi.org/10.3390/molecules26123668.
7. Piatti, E.; Guglielmero, L.; Tofani, G.; Mezzetta, A.; Guazzelli, L.; D'Andrea, F.; Roddaro, S.; Pomelli, C. S. *J. Mol. Liq.* **2022**, *364*, 120001. DOI: https://doi.org/10.1016/j.molliq.2022.120001.
8. Ratti, R. *Adv. Chem.* **2014**, 1–16. DOI: https://doi.org/10.1155/2014/729842.
9. Riaño, S. Ionic Liquids as Green Solvents: A Critical Analysis, in: *Encyclopedia of Green Chemistry*; Elsevier, **2025**; 43–53. DOI: https://doi.org/10.1016/b978-0-443-15742-4.00019-3.
10. Gong, K.; Fang, Q.; Gu, S.; Li, S. F. Y.; Yan, Y. *Energy Environ. Sci.* **2015**, *8*, 3515–3530. DOI: https://doi.org/10.1039/c5ee02341f.
11. Torriero, A. A. J., in: *Electrochemistry in Ionic Liquids. Volume 1: Fundamentals*; Springer, **2015**; Vol. 1. DOI: https://doi.org/10.1007/978-3-319-13485-7.
12. Snook, G. A.; Best, A. S.; Pandolfo, A. G.; Hollenkamp, A. F. *Electrochem. commun.* **2006**, *8*, 1405–1411. DOI: https://doi.org/10.1016/j.elecom.2006.07.004.
13. Huber, B.; Roling, B. *Electrochim. Acta.* **2011**, *56*, 6569–6572. DOI: https://doi.org/10.1016/j.electacta.2011.02.055.
14. Horwood, C.; Stadermann, M. *Electrochem. Commun.* **2018**, *88*, 105–108. DOI: https://doi.org/10.1016/j.elecom.2018.02.005.
15. García-Mendoza, A.; Aguilar-Cordero, J. C. *Electrochim. Acta.* **2019**, *302*, 344–351. DOI: https://doi.org/10.1016/j.electacta.2019.02.029.
16. Nevell, T. G.; Walsh, F. C. *Trans. IMF* **1992**, *70*, 144–147. DOI: https://doi.org/10.1080/00202967.1992.11870962.
17. Inzelt, G.; Lewenstam, A.; Scholz, F., in: *Handbook of Reference Electrodes*; Springer, **2013**. DOI: https://doi.org/10.1007/978-3-642-36188-3_6.
18. Bard, A. J.; Faulkner, L. R.; White, H. S. *Electrochemical Methods - Fundamentals and Applications*, 3rd ed.; Wiley, **2022**. DOI: https://doi.org/10.1007/s11243-023-00555-6.

J. Mex. Chem. Soc. **2025**, *69*(4)
Regular Issue

ISSN-e 2594-0317

19. Bard, A. J., Inzelt, G., Scholz, F., in: *Electrochemical Dictionary*; Springer, **2008**. DOI: https://doi.org/10.1007/978-3-540-74598-3.
20. Sukardi, S. K.; Zhang, J.; Burgar, I.; Horne, M. D.; Hollenkamp, A. F.; MacFarlane, D. R.; Bond, A. M. *Electrochem. commun.* **2008**, *10*, 250–254. DOI: https://doi.org/10.1016/j.elecom.2007.11.022.
21. Scholz, F., in: *Electroanalytical Methods, Guide to Experiments and Applications*; Springer, **2010**. DOI: https://doi.org/10.1007/978-3-642-02915-8.
22. Inzelt, G.; Lewenstam, A.; Scholz, F., in: *Handbook of Reference Electrodes*; Springer, **2013**. DOI: https://doi.org/10.1007/978-3-642-36188-3_6.
23. Lockett, V.; Horne, M.; Sedev, R.; Rodopoulos, T.; Ralston, J. *Phys. Chem. Chem. Phys.* **2010**, *12* , 12499–12512. DOI: https://doi.org/10.1039/c0cp00170h.
24. Fedorov, M. V.; Kornyshev, A. A.; Georgi, N. *Electrochem. commun.* **2010**, *12*, 296–299. DOI: https://doi.org/10.1016/j.elecom.2009.12.019.
25. Yalcinkaya, F.; Powner, E. T. *Méd. Eng. Phys.* **1997**, *19*, 299–301. DOI: https://doi.org/10.1016/s1350-4533(96)00034-3.
26. Fleischmann, M.; Hiddleston, J. N. *J. Phys. E: Sci. Instrum.* **2002**, *1*, 667. DOI: https://doi.org/10.1088/0022-3735/1/6/424.
27. Martell, A. E.; Smith, R. M., in: *Critical Stability Constants. Volume 4: Inorganic Complexes*; Springer, **1976**; Vol. 4. DOI: https://doi.org/10.1007/978-1-4757-5506-0.
28. Rodil, E.; Aldous, L.; Hardacre, C.; Lagunas, M. C. *Nanotechnology* **2008**, *19*, 105603–105608. DOI: https://doi.org/10.1088/0957-4484/19/10/105603.
29. Martell, A. E.; Smith, R. M., in: *Critical Stability Constants. Volume 6: Second Supplement*; Springer, **1989**; Vol. 6. DOI: https://doi.org/10.1007/978-1-4615-6764-6.
30. Gran, G. *Acta Chem. Scand.* **1950**, *4*, 559–577. DOI: https://doi.org/10.3891/acta.chem.scand.04-0559
31. Brown, A. M. *Comput. Methods Programs Biomed.* **2001**, *65*, 191–200. DOI: https://doi.org/10.1016/S0169-2607(00)00124-3.
32. Briones-Guerash-S. U.; García-Mendoza, A.; Aguilar-Cordero, J. C. *J. Chem. Educ.* **2023**, *100*, 4663–4673. DOI: https://doi.org/10.1021/acs.jchemed.3c00790.
33. Davies, C. W.; Jones, A. L. *Discuss. Faraday Soc.* **1949**, *5*, 103–111. DOI: https://doi.org/10.1039/df9490500103.
34. Kim, J. I.; Duschner, H. *J. Inorg. Nucl. Chem.* **1977**, *39*, 4771–4478.
35. Dilleen, J. W.; Sprules, S. D.; Birch, B. J.; Haggett, B. G. D. *The Analyst* **1998**, *123*, 2905–2907. DOI: https://doi.org/10.1039/a806344c.
36. Johansson, P.-A.; Karlberg, B.; Thelander, S. *Anal. Chim. Acta* **1980**, *114*, 215–226. DOI: https://doi.org/10.1016/s0003-2670(01)84293-8.
37. Gavazov, K. B. *Acta Chim. Slov.* **2012**, *59*, 1–17.
38. Fritz, J. J. *J. Solut. Chem.* **1985**, *14*, 865–879. DOI: https://doi.org/10.1007/bf00646296.
39. Lloyd, P. J. D., in: *Solvent Extraction Principles and Practice, Revised and Expanded*, 2nd ed.; Marcel Dekker, **2004**. DOI: https://doi.org/10.1201/9780203021460-14.
40. Ma, L.; Zhong, Z.; Hu, J.; Qing, L.; Jiang, J. *J. Phys. Chem. B* **2023**, *127*, 5308–5316. DOI: https://doi.org/10.1021/acs.jpcb.3c01559.
41. Tokuda, H.; Tsuzuki, S.; Susan, M. A. B. H.; Hayamizu, K.; Watanabe, M. *J. Phys. Chem. B* **2006**, *110*, 19593–19600. DOI: https://doi.org/10.1021/jp064159v.
42. Gebbie, M. A.; Smith, A. M.; Dobbs, H. A.; Lee, A. A.; Warr, G. G.; Banquy, X.; Valtiner, M.; Rutland, M. W.; Israelachvili, J. N.; Perkin, S.; Atkin, R. *Chem. Commun.* **2016**, *53*, 1214–1224. DOI: https://doi.org/10.1039/c6cc08820a.
43. Nordness, O.; Brennecke, J. F. *Chem. Rev.* **2020**, *120*, 12873–12902. DOI: https://doi.org/10.1021/acs.chemrev.0c00373.
44. Yalcinkaya, F.; Powner, E. T. *Med. Eng. Phys.* **1997**, *19*, 299–301. DOI: https://doi.org/10.1016/s1350-4533(96)00034-3.

J. Mex. Chem. Soc. **2025**, *69*(4)
Regular Issue

ISSN-e 2594-0317

45. Mousavi, M. P. S.; Saba, S. A.; Anderson, E. L.; Hillmyer, M. A.; Bühlmann, P. *Anal. Chem.* **2016**, *88* (17), 8706–8713. DOI: https://doi.org/10.1021/acs.analchem.6b02025.
46. Vranes, M.; Dozic, S.; Djeric, V.; Gadzuric, S. *J. Chem. Eng. Data* **2012**, *57*, 1072–1077. DOI: https://doi.org/10.1021/je2010837.
47. Zoski, C. G., in: *Handbook of Electrochemistry*; Oxford, **2006**.
48. García-Mendoza, A.; Aguilar, J. C. *Electrochim. Acta*. **2015**, *182*, 238–246. DOI: https://doi.org/10.1016/j.electacta.2015.09.045.

Article

J. Mex. Chem. Soc. **2025**, *69*(4)
Regular Issue

ISSN-e 2594-0317

Sesuvioside A from *Gomphrena celosioides* possesses the Dual Anti-gout Actions Via Anti-xanthine Oxidase and Anti-inflammatory Activities

Ngo Van Quang[1]*, Thanh Thi Thu Thuy[1], Dang Vu Luong[1], Trinh Tat Cuong[2], Nguyen Xuan Ha[3], Nguyen Manh Cuong[3], Nguyen Thi Mai Phuong[4,5]*

[1]Institute of Chemistry, Vietnam Academy of Science and Technology, 18 Hoang Quoc Viet Road, Caugiay, Hanoi, Vietnam.
[2]Key Laboratory for Enzyme and Protein Technology, VNU University of Science, 334 Nguyen Trai Road, Thanh Xuan, Hanoi, Vietnam.
[3]Institute of Natural Products Chemistry, Vietnam Academy of Science and Technology, 18 Hoang Quoc Viet Road, Caugiay, Hanoi, Vietnam.
[4]Graduate University of Science and Technology, Vietnam Academy of Science and Technology, 18 Hoang Quoc Viet Road, Caugiay, Hanoi, Vietnam.
[5]Institute of Biology, Vietnam Academy of Science and Technology, 18 Hoang Quoc Viet Road, Caugiay, Hanoi, Vietnam.

***Corresponding author:** Ngo Van Quang, email: nhatquang.ngo@gmail.com; Nguyen Thi Mai Phuong, email: phuongnguyenibt@gmail.com

Received September 6th, 2024; Accepted March 3rd, 2025.

DOI: http://dx.doi.org/10.29356/jmcs.v69i4.2358

Abstract. *Gomphrena celosioides* Mart. has been widely used for the treatment of gout in Vietnam. A bio-guided isolation of xanthine oxidase inhibitors revealed that sesuvioside A, the main constituent in the butanol fraction of the aerial parts of *G. celosioides*, is a potential anti-gout compound. The anti-gout activity of sesuvioside A, a main constituent isolated from the butanol fraction for the first time was further extensively investigated using *in vitro* biological assays, including inhibition of xanthine oxidase (XO) activity, nitric oxide (NO), intracellular reactive oxygen species (iROS), pro-inflammatory cytokines productions. The obtained results indicated that sesuvioside A exhibited inhibitory activity against XO and NO production with the IC_{50} values of 31.6 μM and 18.3 μM, respectively. At concentration of 40.0 μM, the compound significantly reduced iROS level and the production of the pro-inflammatory cytokines TNF-α, IL-6, and IL-8 in the lipopolysaccharide-induced macrophages. A molecular docking study revealed that sesuvioside A strongly binds to the targets XO and p-38 MAPK with the estimated energy of -10.55 kcal/mol and -9.78 kcal/mol, respectively. In conclusion, sesuvioside A from the aerial parts of *G. celosioides* is a new dual anti-gout agent by expressing its inhibitory effects on XO activity and inflammatory targets. The traditional use of *G. celosioides* as a remedy for gout was supported by the findings in this study.
Keywords: *Gomphrena celosioides* Mart; sesuvioside A; xanthine oxidase (XO); anti-inflammatory; anti-gout.

Resumen. La *Gomphrena celosioides* Mart. Es muy usada en Vietnam para el tratamiento de la gota (hiperurisemia). A través de un proceso de aislamiento bio-dirigido de inhibidores de la xantina oxidasa (XO), se identificó que el sesuviósido A, el constituyente principal de la fracción butanólica de las partes aéreas de *G. celosioides*, es un compuesto que mostró actividad farmacológica y es candidato para el desarrollo de medicamentos contra la hiperurisemia. La actividad del sesuviósido A —aislado por primera vez como principal componente de dicha fracción— fue investigada extensamente mediante ensayos biológicos *in vitro*, incluyendo la inhibición de la actividad de la XO, la producción de óxido nítrico (NO), especies reactivas de oxígeno intracelulares (iROS) y citoquinas proinflamatorias. Los resultados obtenidos indicaron que el sesuviósido A

J. Mex. Chem. Soc. **2025**, *69*(4)
Regular Issue

ISSN-e 2594-0317

presentó actividad inhibitoria sobre la XO y la producción de NO, con valores de IC_{50} de 31,6 µM y 18,3 µM, respectivamente. A una concentración de 40,0 µM, el compuesto redujo significativamente los niveles de iROS y la producción de las citoquinas proinflamatorias TNF-α, IL-6 e IL-8 en macrófagos inducidos por lipopolisacáridos. Un estudio de acoplamiento molecular reveló que el sesuviósido A se une fuertemente a los blancos moleculares XO y p38 MAPK, con energías estimadas de -10,55 kcal/mol y -9,78 kcal/mol, respectivamente. En conclusión, el sesuviósido A, aislado de las partes aéreas de *G. celosioides*, representa un nuevo agente anti-gota dual, al ejercer efectos inhibitorios tanto sobre la actividad de la XO como sobre blancos inflamatorios. Los hallazgos de este estudio respaldan el uso tradicional de *G. celosioides* como remedio para la gota.
Palabras clave: *Gomphrena celosioides* Mart.; sesuviósido A; xantina oxidasa (XO); antiinflamatorio; anti-gota (hiperurisemia).

Introduction

Gout is a type of arthritis characterized by sudden and severe pain, redness, and swelling of the joints. This is caused by the accumulation of urate crystals in the joints, ultimately leading to inflammation and severe pain.[1,2] These crystals trigger an immune response, thus inducing the release of inflammatory cytokines such as interferon (IFN)-γ, IL-6, IL-8, IL-10, CCL2, and IL-1β by assembling and activating the pyrin receptor NOD-like containing 3 (NLRP3), which causes inflammation.[3] The negative effects of urate are primarily due to its ability to trigger the production of intracellular reactive oxygen species (iROS). The activation of the enzymes NADPH oxidase, xanthine oxidase (XO), and nitric oxide synthase results in the production of hydrogen peroxide (H_2O_2), superoxide anion (O_2^-), and nitric oxide (NO^-)/proximities ($ONOO^-$), respectively, thereby increasing gout-induced joint damage.[4,5] Current conventional medical treatments for gout focus on chemical drugs, such as nonsteroidal anti-inflammatory drugs (NSAIDs) and urate-lowering drugs; however, long-term treatment also leads to unwanted side effects.

Flavones are a group of naturally occurring compounds that are present in various plants and are known for their diverse biological activities. An important pharmacological property of flavones is their ability to inhibit XO.[6] XO is involved in purine metabolism by catalysing the conversion of hypoxanthine to xanthine and uric acid, which can lead to major complications such as gout and kidney stones.[7] Several flavone compounds, including licoisoflavone A, butein, fisetin, diosmetin, luteolin, chrysin, baicalein, and wogonin were found to be the potent XO inhibitors. These flavones exert their inhibitory effects through a variety of mechanisms, including competitive or non-competitive inhibition of the enzyme active site and regulation of XO expression and activity at the gene level. Studies have reported that flavones possessing XO inhibitory activity can effectively reduce serum uric acid levels, thereby showing their potential as therapeutic agents for treating hyperuricemia in gout patients. Furthermore, these compounds exhibit anti-inflammatory and antioxidant properties that may contribute to their overall beneficial effects in gout treatment.[2,6,8] Moreover, flavones have been demonstrated to modulate the activity of various signalling pathways involved in inflammation, often leading to the generation of iROS, which can cause prolonged inflammation and tissue damage. They can exhibit antioxidant activity by scavenging free radicals and inhibiting oxidative stress.[9] These mechanisms collectively contribute to the suppression of inflammatory processes and make flavones potential candidates for the development of novel anti-inflammatory therapies.

Nitric oxide (NO) is a signaling molecule that plays a key role in the pathogenesis of inflammation the joint, gut and lungs. NO is considered as a pro-inflammatory mediator that induces inflammation due to over production in abnormal situations.[10] Therefore, NO inhibitors represent important therapeutic advance in the management of inflammatory diseases. Selective NO biosynthesis inhibitors and synthetic arginine analogues are proved to be used for the treatment of NO^- induced inflammation. Nitrit (NO_2^-), the one electron oxidation product of NO, is a dietary component and is present basally in red blood cells (RBC; 290 nM) and plasma (120 nM).[11] In tissues, nitrite is reduced along a physiological oxygen and pH gradient by different enzymes to mediate responses, such as the modulation of protein expression, regulation of metabolism,[12, 13] and cytoprotection after ischaemia/reperfusion injury.

J. Mex. Chem. Soc. **2025**, *69*(4)
Regular Issue

ISSN-e 2594-0317

Gomphrena celosioides Mart belonging to the Amaranthaceae family, is distributed throughout South America, Africa, Asia, Australia and Vietnam.[14] The aerial parts of this plant have been used in folk medicine in many countries for the treatment of rheumatism, uninary tract, kidney stones, and several other diseases, including skin, respiratory, gastro-intestine, arthritis, hyperalgesia, and diuretic.[15–17] Phytochemical studies of the aerial parts have yielded isolation of 20-hydroxyecdysone; 20-hydroxyecdysone-20,22-monoacetonide; umbellatoside B; aurantiamide, 3-(4-hydroxyphenyl) methylpropenoate.[18–20] In Vietnam, *G. celosioides* is commonly used as a folk medicinal plant for gout treatment, however its mechanism of actions have not been fully understood.[21]

In this study, to verify the folk uses of *G. celosioides*, sesuvioside A, a major compound, was isolated from the aerial part butanol fraction of *G. celosioides* and the underlying molecular mechanisms of this compound as a dual anti-gout agent were intensively investigated by exploring its inhibitory effects on XO activity and pro-inflammatory cytokines, NO, and iROS formations in LPS-induced RAW 264.7 macrophages. Molecular docking simulations were performed to determine the binding affinity and possible binding mode of the compound to the targets XO and p-38 MAPK enzymes.

Materials and methods

Materials

Gomphrena celosioides Mart. were collected in Nam Dinh Province, Vietnam, in December 2021 and were identified by Dr. Nguyen Quoc Binh, Vietnam National Museum of Nature, Vietnam Academy of Science and Technology (VAST). A voucher (GC04.10/23-24) was deposited at the Institute of Chemistry, Vietnam.

Xanthine, xanthine oxidase (XO), and lipopolysaccharides (LPS) were purchased from Roche Co., Ltd. (Shanghai, China). Other analytical reagents were purchased from Sigma–Aldrich, Singapore. DMEM, and FBS media for cell culture were ordered from Invitrogen (USA). Macrophage RAW 264.7 cells were supplied by Prof. Domenico Delfino, University of Perugia, Italy.

Extraction and isolation

The aerial part dried powder of *G. celosioides* (3.0 kg) was extracted with ethanol at room temperature for 24 hours (3 × 4 L) using ultrasonication, followed by solvent evaporation under reduced pressure to obtain the crude extract (ND, 265 g). This crude extract was suspended in water and then partitioned with *n*-hexane, ethyl acetate (EtOAc), and *n*-butanol (BuOH). After removal of the solvent in *vacuo*, the BuOH layers gave NDB (86.0 g). The fraction was then chromatographed on a silica gel column (Merck Silica gel 60, 70–230 mesh) with an elution system of chloroform-acetone gradient (8: 3 → 8: 7, v/v) to obtain five subfractions: NDB1 (10.5 g), NDB2 (6.5 g), NDB3 (12.0 g), NDB4 (7.5 g), and NDB5 (5.5 g). The NDB4 sub-fraction was separated by column chromatography on silica gel RP-18 (YMC) and eluted with a mobile phase of acetone–water (0.75: 2, v/v) to yield **1** (102 mg). The NDB2 was separated by column chromatography on silica gel, and eluted with chloroform-acetone (6/1, v/v) to yield **2** (35.2 mg). The NDB5 subfraction was further separated by column chromatography on silica gel RP-18 (YMC) and eluted with a mobile phase of acetone–water (2.5: 1, v/v) to yield **3** (14.8 mg), and **4** (16.3 mg). The chemical structure of compounds was identified by 1D- and 2D-NMR and mass spectrometry (MS).

Xanthine oxidase inhibitory activity

XO inhibitory activity of the samples was determined as described by Noro et al. [22] The amount of formed uric acid was measured at 295 nm at 37°C, pH 7.5. Allopurinol was used as a positive control. The reaction mixture contained 100 μL of sesuvioside A solution, 300 μL of 50 mM phosphate buffer with pH 7.5, and 100 μL of XO enzyme solution (0.2 U/mL).

Cell viability

The macrophage cells (RAW264.7) were cultured (3-5 days) in DMEM medium with 2.0 mM L-glutamine, 10.0 mM HEPES, and 1.0 mM sodium pyruvate, and 10 % fetal bovine serum (FBS- GIBCO) at 37 °C in an incubator with a 5 % CO_2. The cell viability was analyzed by an MTT assay. In brief, the cells were

J. Mex. Chem. Soc. **2025**, *69*(4)
Regular Issue

ISSN-e 2594-0317

seeded into 96-well plates ($1x10^4$ cells/mL) and incubated with various concentrations of sesuvioside A (10, 20, 40, 80, and 100 μM) for 12 hours. Then, the MTT solution of 0.5 mg/mL was added and incubated for another 4 hours. The formed formazan crystals were solubilized in dimethyl sulfoxide (DMSO), and the optical density (OD) was measured at 570 nm by a microplate reader (PowerWave XS model, BioTek Instruments, Inc., Winooski, VT, USA). The untreated cells were used as a control. The viability rate was calculated as a percentage compared to the non-treated control.

Effect on nitric oxide production

The macrophage cells RAW264.7 were cultured (3-5 days) in DMEM medium with 1.0 mM sodium pyruvate, 2.0 mM L-glutamine, 10.0 mM HEPES, and 10 % fetal bovine serum (FBS - GIBCO) at 37 ºC in 5 % CO_2. Then, cells were collected and seeded in a 96-well plate at a concentration of 3 x 10^4 cells/well and continued to grow for 24 hours before treatment with sesuvioside A at different concentrations for 2 hours. After treatment, cells were stimulated with LPS (100 ng/mL) for 24 hours to generate NO. N^G-Methyl-L-arginine acetate (L-NMMA) was used as a positive control. Nitrite (NO_2^-), an indicator for NO generation, was determined at 540 nm by a microplate reader (BioTek Elx 800). [23] The NO inhibitory production (IC) was calculated using the formula (1):

$$IC\% = 100\ \% - [OD_{sample}/OD_{LPS}]*100 \quad (1)$$

Effect on cytokine

The macrophage RAW264.7 cells were cultured in DMEM medium supplemented with 10 % FBS in 96-well microplates at 37 °C with 5 % CO_2 for 12 hours. The cells were then seeded into 6-well plates ($3x10^4$ cells/well), followed by treatment with sesuvioside A at concentrations of 5.0, 10.0, 20.0, and 40.0 μM at 37˚C for 1 hour, and stimulated with LPS (100 ng/mL) at 37˚C for 24 hours. The levels of TNF-α, IL- 6, IL8 and IL-10 in the supernatant were measured using the ELISA kits according to the manufacturer's instructions.

Effect on iROS generation

The iROS were assessed as previously described,[24] in which 2′,7′-dichlorofluorescein diacetate (H2DCFDA) is converted to oxidized forms of dichlorofluorescein and 2′,7′-fluorescence (DCF) by iROS. RAW264.7 macrophages in DMEM medium supplemented with 10 % FBS were seeded in a 96-well plate with a density of 3×10^4 cells/well. Cells were incubated for 30 min with different concentrations of sesuvioside A. After that, cells were treated with 20 μM H2DCFDA for 30 min and then incubated with tert-butyl hydroperoxide (tBHP; 200 μM in PBS containing 1 % FBS) at 37^0C for 1 hour. Fluorescence was measured at excitation and emission wavelengths of 535 nm using a fluorescence microscope (ACCU-SCOPE 3012, New York, USA).

Molecular docking

The structures of sesuvioside A and well-known inhibitors were drawn using Marvin JS software, and the geometric optimization of the structures was performed using the MMFF94s force field with OpenBabel software.[25,26] The crystal structures of p38 MAPK involved in inflammation, and XO involved in uric acid formation were downloaded from the RCSB PDB with the PDB ID, 1WBV and 1FIQ, respectively. [27,28] The preparation of protein structures and compounds was carried out similarly to previous studies.[29] Docking simulations between sesuvioside A and anti-gout targets p38 MAPK and XO were conducted using the AutoDock Vina v1.2.3 program.[30] The binding poses with the lowest binding energies for the compound were selected for further in-depth analysis. The docking program was run with an exhaustiveness value of 400 and a grid box size of X: 31.2 Å, Y: 53.0 Å, Z: 99.0 Å for XO and X: 6.2 Å, Y: 14.5 Å, Z: 36.1 for p-38 MAPK. The Discovery Studio Visualizer software was used for visual inspection of the results and graphical representation.[31]

Statistical analysis

The experiments were conducted in triplicate, and the mean values were subsequently calculated. The results are expressed as the means ± standard deviations, calculated using Microsoft Office Excel 2016. Statistical analysis was carried out using the Student's *t-test*, with $p \leq 0.05$ considered to be significant.

J. Mex. Chem. Soc. **2025**, *69*(4)
Regular Issue

ISSN-e 2594-0317

Results and discussion

Isolation of natural compounds from aerial parts of *G. celosioides*

The XO inhibitory activity of three different solvent partition residues (*n*-hexane, EtOAc, and BuOH) of the ethanol extract of the aerial parts of *G. celosioides* was investigated, revealing that the BuOH fraction possessed the highest activity with an IC_{50} of 58.3 μg/mL (Table S1, Supporting Information (SI)). From this fraction, four compounds (**1**-**4**) were isolated (Fig. 1) and their chemical structures were determined, including sesuvioside A (**1**), aurantiamide acetate (**2**), eupalitin (**3**), and myricitrin (**4**) by comparison with their NMR and MS spectral (Figures S1, S2, S3, S4, Supporting Information) data from the literature.[32–35] Among the identified compounds, sesuvioside A (compound 1) showed to be a major compound and was isolated from the aerial parts of *G. celosioides* for the first time.

Sesuvioside A (**1**): ESI-MS *m/z* 637.1 $[M-H]^-$, Calcd for $C_{29}H_{34}O_{16}$, MW: 638; ^{1}H-NMR (DMSO-d_6, 600 MHz) δ_H 6.87 (s, H-8), 8.10 (d, *J* = 8.4 Hz, H-2′/H-6′), 6.88 (d, *J* = 8.4 Hz, H-3′/H-5′), 3.74 (s, 6-OMe), 3.92 (s, 7-OMe), *Galactose:* 5.34 (d, *J* = 7.5 Hz, H-1″), 3.56 (dd, *J* = 9.0, 7.5 Hz, H-2″), 3.40 (dd, *J* = 9.0, 3.0 Hz, H-3″), 3.60 (t, *J* = 3.0 Hz, H-4″), 3.5 7 (m, H-5″), 3.26 (dd, *J* = 11.4, 5.4 Hz, H_a-6″), and 3.57 (dd, *J* = 11.4, 1.8 Hz, H_b-6″), *Rhamnose:* 4.39 (d, *J* = 1.2 Hz, H-1‴), 3.37 (dd, *J* = 3.0, 1.2 Hz, H-2‴), 3.28 (dd, *J* = 9.0, 3.0 Hz, H-3‴), 3.09 (t, *J* = 9.0 Hz, H-4‴), 3.35 (m, H-5‴), 1.05 (d, *J* = 6.6 Hz, H-6‴); ^{13}C-NMR (DMSO-d_6, 150 MHz) δ_C 157 (C-2), 133.3 (C-3), 177.8 (C-4), 151.6 (C-5), 131.7 (C-6), 158.7 (C-7), 91.4 (C-8), 151.8 (C-9), 105.3 (C-10), 120.8 (C-1′), 131.1 (d, C-2′/C-6′), 115.1 (d, C-3′/C-5′), 160.1 (C-4′), 60.1 (6-OMe), 56.5 (7-OMe), *Galactose*: 101.8 (C-1″), 71.1 (C-2″), 73.0 (C-3″), 68.1 (C-4″), 73.7 (C-5″), 65.4 (C-6″), *Rhamnose*: 100.1 (C-1‴), 70.4 (C-2‴), 70.6 (C-3‴), 71.9 (C-4‴), 68.3 (C-5‴), 17.9 (C-6‴).

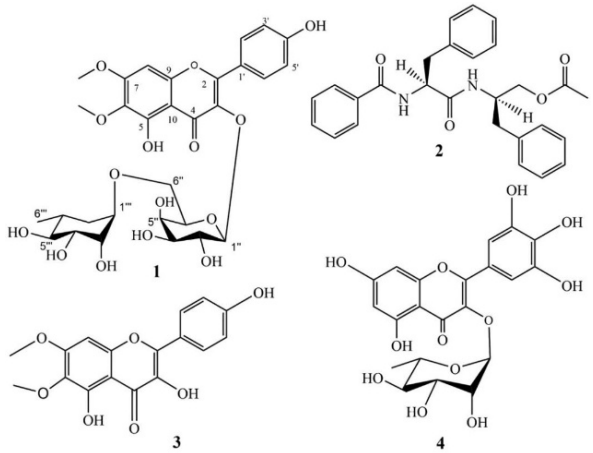

Fig. 1. Chemical structure of sesuvioside A (**1**), aurantiamide acetate (**2**), eupalitin (**3**), and myricitrin (**4**) isolated from the aeriel parts of *G. celosioides*

Besides, the results of screening the XO inhibitory activity of the four compounds also indicated that sesuvioside A and aurantiamide acetate were the strongest XO inhibitors with the IC_{50} values of 31.69 and 28.94 μM, respectively (Table S2, SI). However, cytotoxicity test indicated aurantiamide acetate (compound 2) was significantly cytotoxic toward RAW264.7 cells (Table S3, SI); therefore, sesuvioside A was selected for further study on its anti-inflammatory action mechanism *in vitro*.

Cell cytotoxicity

To select the suitable treatment concentrations for further experiments, sesuvioside A toxicity on RAW 264.7 macrophages was examined. The data in Fig. 2 indicated that sesuvioside A did not affect cell survival at a concentration up to 100.0 μM.

J. Mex. Chem. Soc. **2025**, *69*(4)
Regular Issue

ISSN-e 2594-0317

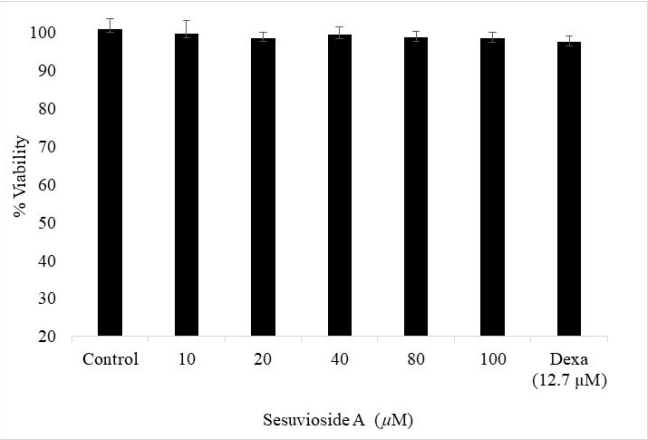

Fig. 2. Cell viability of RAW264.7 cells in the presence of sesuvioside A. Cell viability was determined using the MTT method. The data are expressed as the means ± SD, (n = 3), $p > 0.05$

Xanthine oxidase inhibitory activity

The experimental results (Fig. 3) showed that sesuvioside A exhibited XO inhibitory activity with an IC_{50} value of 31.69 ± 0.49 μM which was higher than that of the positive control allopurinol (IC_{50} value of 8.67 μM) (Table S2, SI). Recently, Xu et al. (2023) reported that rutin, another known flavone compound was an XO inhibitor with IC_{50} value of 167.86 μM. Thus, sesuvioside A showed to be a more potent XO inhibitor with an IC_{50} value of 5 folds lower than that of rutin.[36] Li et al. (2022) showed that, owing to glycosylation at the C3 position and increasing steric hindrance, the ability of rutin to inhibit XO was not strong.[37] The two benzopyranone rings (A-B) of rutin stretch the hydrophobic end of XO, whereas the C-ring was inserted into the XO active site and interacts with Phe-1013 and Phe-649 via π–π hydrophobic bonds with a very low affinity, thereby reducing its XO inhibitory activity.[38] For sesuvioside A, the structure of the two methoxy substituents at positions 6 and 7 of the A ring may affect the binding affinity of amino acids in the XO active site. As a result, its inhibitory activity was improved.

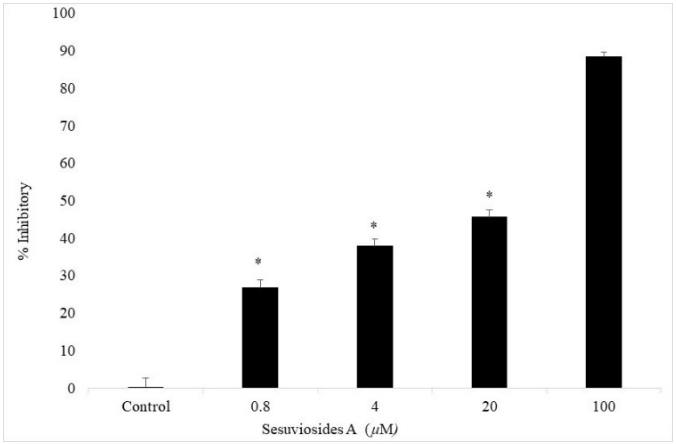

Fig. 3. XO inhibitory effects of sesuvioside A. Data were calculated as a percentage of the untreated sample (control) and are expressed as the means ± SD (n = 3), $p^* < 0.05$.

J. Mex. Chem. Soc. **2025**, *69*(4)
Regular Issue

ISSN-e 2594-0317

Effect on nitric oxide production

Inhibitory activity of sesuvioside A against LPS-induced NO formation in RAW 264.7 cells was evaluated. The data presented in Table 1 indicate that the compound suppressed NO formation with an IC_{50} value of 18.34 ± 0.15 μM. In contrast, allopurinol (a medication for gout) exhibited no effect (Table S3, SI). The positive control, L-NMMA, possessed an IC_{50} value of 31.93 ± 1.13 μM. Thus, the NO inhibitory activity of sesuvioside A was markedly better than that of the L-NMMA positive control and even better than the gout medication allopurinol, in terms of NO inhibition. In a previous study, we have reported three compounds umbellatosides B, 20-hydroxyecdysone, and 20-hydroxyecdysone-20,22-monoacetonide also isolated from the BuOH fraction of *G. celosioides* possessing the moderate XO and NO inhibitory activities. Of which, umbellatosides B was the most potent inhibitor with IC_{50} values of 33.78 μM for XO, and 19.55 μM for NO,[18] nearly the same with sesuvioside A. Thus, our results suggest that there is an anti-gout synergistic effect of multi-compounds rather than a single one. Sesuvioside A and umbellatosides B may be the two significantly contribute to the anti-gout activity of BuOH fraction, as well as of *G. celosioides.*

Table 1. The inhibition of NO production by RAW264.7 macrophages of sesuvioside A.

No	Sesuvioside A			L-NMMA		
	Concentrate (μM)	**% cells inhibition of NO**	**SD**	**Concentrate (μg/mL)**	**% cells inhibition of NO**	**SD**
1	0	0.26	0.05	0	1.65	0.18
2	0.8	16.30	0.02	0.8	9.57	0.29
3	4.0	32.88	0.22	4.0	24.36	0.72
4	20.0	45.20	1.02	20.0	80.73	1.86
5	60.0	61.8	1.06	60.0	92.84	1.08
6	100.0	73.04	1.29	100.0	99.39	1.59
	IC_{50}	18.34 ± 0.15 (μM)		IC_{50}	31.93 ± 1.13 (μM)	

Note: Samples were incubated with RAW264.7 cells with sesuvioside A for 2 hours before LPS (100 ng/mL) was added and incubated for another 24 hours. The NO-levels were measured at 540 nm and quantitated using the $NaNO_2$ standard curve. L-NMMA was used as a positive control. Data were expressed as means ± SD (n = 3), p = 0.017 (for sesuvioside A), p = 0.030 (for L-NNMA).

Effect on cytokine production

The treatment of macrophages with sesuvioside A ≤ 100 μM for 24 hours did not cause any noticeable effect on cell viability (Fig. 2). Therefore, concentrations ranging from 5.0 to 40.0 μM were selected for evaluation of the inhibitory effects on pro-inflammatory cytokines released by the marcrophages. The results presented in Fig. 4 indicate that sesuvioside A 40.0 μM down-regulated TNF-α, IL-6, and IL-8 productions while it had no effect on IL-10 (Fig. 4). It is known that certain inflammatory mediators such as NO, TNF-α, IL-6, and IL-8 are strongly associated with gouty arthritis. [39] The accumulation of these inflammatory mediators in tissues and cells lead to increased damage and consequently promotes severe inflammatory reactions.[40,41] Thus, sesuvioside A suppressed all the pro-inflammatory mediators, thereby reducing inflammation. Our findings agree well with those of quercetin or kaempferol derivatives,[42,43] suggesting the possible applications of sesuvioside A in anti-gouty arthritis.

J. Mex. Chem. Soc. **2025**, *69*(4)
Regular Issue

ISSN-e 2594-0317

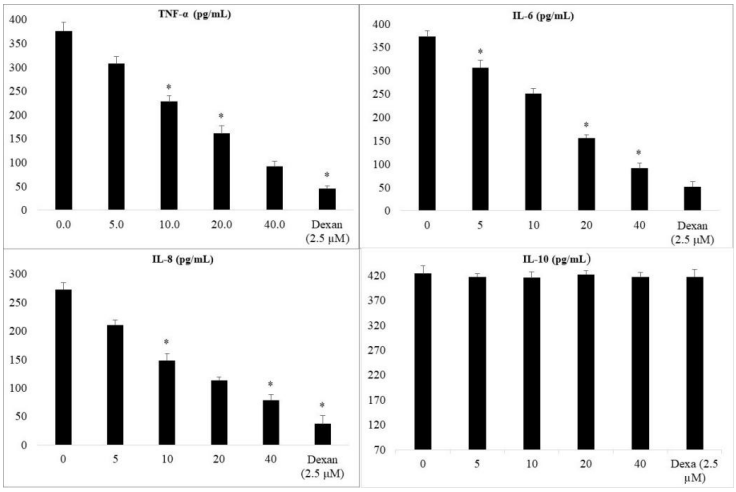

Fig. 4. Effects of sesuvioside A on production of TNF-α, IL-6, IL8, and IL-10 by macrophages. The cells were pretreated with sesuvioside A for 1 hour and then stimulated with LPS (100 ng/mL) for another 24 h. The levels of TNF-α, IL-6, IL-8, and IL-10 were measured using ELISA kits. The data are presented as the means ± SD (n = 3), p* <0.05.

Effect on iROS generation

iROS is an important signaling factor in LPS-stimulated macrophages. iROS formation in LPS-stimulated macrophages can induce oxidative stress and amplifies the inflammatory response factors.[41] The LPS pre-treated RAW264.7 cell lines can induce large amounts of iROS and therefore, activate various signaling pathways involved in inflammation.[42] In this study, iROS levels generated by LPS induced RAW264.7 macrophages were clearly down-regulated after treatment with sesuvioside A (Fig. 5). At a concentration of 20.0 μM, the reduction of iROS was not much different compared to that of the control DMSO. However, at a concentration of 40.0 μM, it was markedly decreased compared to the positive control dexamethasone (Dexa, 2.5 μM).

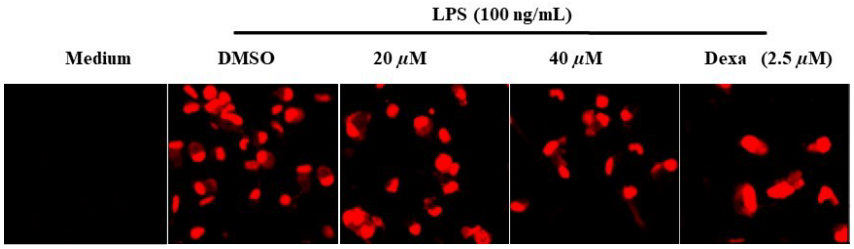

Fig. 5. Effect of sesuvioside A on LPS-induced iROS in RAW264.7 macrophages. The cells were pre-treated with 20.0 μM and 40.0 μM sesuvioside A, DMSO, or dexamethasone (Dexa, 2.5 μM) for 30 min and then treated with LPS (100 ng/ml) for 24 h. The iROS level was detected using a fluorescence microscope (DHE (red) for iROS; scale bar = 200 mm

Molecular docking study

Molecular docking was performed to determine how sesuvioside A binds to possible anti-inflammatory targets such as XO (responsible for uric acid production) and p-38 MAPK (involved in inflammatory signal pathway mitogen activated protein kinase - MAPK). The compound was docked into the active site region of the proteins using a grid box that was determined based on the coordinates of the co-crystallized ligands (Fig. 6).

For XO, it is known that the activation phase of the dehydrogenase to oxidase form by oxidation of sulfhydryl residues or by proteolysis plays an important role in XO activity. [28] The compounds that interfere

J. Mex. Chem. Soc. **2025**, *69*(4)
Regular Issue

ISSN-e 2594-0317

with this process by binding to the flavin adenine dinucleotide (FAD) reaction site, the iron/sulfur domain (Fe/S I-II), and/or the molybdopterin center (Mo-pt), may be potent inhibitors of XO. According to the docking results, we found that sesuvioside A mainly interacts with the FAD domain and partly interacts with the Fe/S II binding site of dehydrogenase. Fig. 6**(A)** clearly shows the function of the di-glycoside moiety to form H-bonding and van der Waals contacts with Glu263, Asp360, and Arg394, which are some of the key residues in the FAD domain. However, the compound could not enter deeply into the domain as the coumarin moiety which exhibited significant hydrophobic interactions at the rim of the pocket (Ile266, Val342) and with residues of the Fe/S II binding site, such as Glu45 and Cys48. This fact could negatively affect the stabilization of sesuvioside A in the complex. In addition, the compound also had some contact with residues of the active loop (pink ribbon from Lys433) that could hinder the dehydrogenase-oxidase transition in XO (Fig. 6). The binding energy of sesuvioside A to XO was estimated to be -10.55 kcal/mol (Table 2).

Table 2. Binding affinity, hydrogen bonding and alkyl interactions of sesuvioside A on proteins XO (PDB ID: 1FIQ) and p38-MAPK (PDB ID: 1WBV).

Compound	***Binding affinity (ΔG, kcal/mol)***		***Hydrogen bonding interactions***		***Alkyl interactions***	
	XO	**p-38 MAPK**	**XO**	**p-38 MAPK**	**XO**	**p-38 MAPK**
Sesuvioside A	-10.55	-9.78	Asp360 Arg394 Glu263	Ile147 Gly170 Ala172 His148 Arg189 Arg149 Glu71	ILe266 Val342	Ile 84, Met 78, Arg 67
Allopurinol	-5.7	-	Thr354, Asn261, Val259, Gly260		Glu263	-
3-fluoro-N-1H-indol-5-yl-5-morpholin-4-ylbenzamide	-	-9.765	-	Asp168 Glu71	-	Ile141, Met78, Leu75, Thr106, Lys53, Ile84, Ala51, His148

For p38-MAPK, it is expected that sesuvioside A could strictly bind to p38, which is a key regulator of pro-inflammatory cytokine biosynthesis. It is widely known that p38 is activated through ATP and UTP.[44] Gill *et al*. explored the binding modes of p38 by designing several indolyl derivatives targeting ATP binding sites.[27] They crystalized a hit compound, 3-fluoro-N-1H-indol-5-yl-5-morpholin-4-ylbenzamide, which shows an IC_{50} of 162 μM. Our compound, while showing better activity than 3-fluoro-N-1H-indol-5-yl-5-morpholin-4-ylbenzamide, exhibited a different interaction network with the target compared to the co-crystal ligand. Having di-glycoside structure, sesuvioside A mostly interacts with the hydrophylic residues (His148, Gly170, Ala172, Arg189) and those of the ATP ribose binding region (Asp168). These structure - activity relationships (SARs) suggest the importance of polar moieties (e.g., glycosides) and flexibility of the inhibitors. Only two methoxy groups could form stacking interactions with hydrophobic regions 1 and 2 (Fig. 6**(B)**). The binding energy of sesuvioside A to p38 was about -9.78 kcal/mol (Table 2). The docking results support a different binding mode of sesuvioside A compared to co-crystal compound, as well as some SARs that may increase the binding ability of p38-MAPK inhibitors toward the ATP binding site. More experimental works are needed to clarify this hypothesis.

J. Mex. Chem. Soc. **2025**, *69*(4)
Regular Issue

ISSN-e 2594-0317

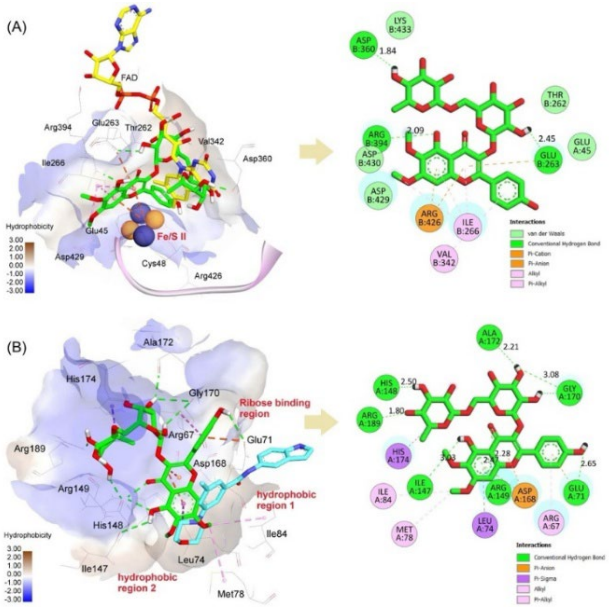

Fig. 6. 3D and 2D interaction diagrams of sesuvioside A (green) against two targets **(A)** XO (PDB ID: 1FIQ) and **(B)** p-38 MAPK (PDB ID: 1WBV). Reference includes two cocrystal-ligands FAD (yellow) and compound 3-fluoro-N-1H-indol-5-yl-5-morpholin-4-ylbenzamide (cyan)

Conclusions

In conclusion, our findings clearly demonstrated that sesuvioside A, a natural compound newly isolated from *G. celosioides*, is a new and promising dual anti-gout agent with multi-target actions, including xanthine oxidase responsible for uric acid synthesis and NO, pro-inflamatory cytokines and iROS formation responsible for inflammation. These results substantiate the potential of *G. celosioides* and sesuvioside A as natural therapeutic agents for the treatment of inflammatory disorders. Nonetheless, further research is essential to fully elucidate their molecular mechanisms of action and to validate their efficacy and safety in animal models. Clinical trials should be followed to examine the optimal dosage, potential drug interactions, and the long-term therapeutic effects in humans.

Acknowledgments

This research was supported by the Vietnam Academy of Science and Technology under grant number VAST04.10/23-24.

References

1. Ragab, G.; Elshahaly, M.; Bardin, T. *J. Adv. Res.* **2017**, *8*, 495–511 DOI: https://doi.org/10.1016/j.jare.2017.04.008
2. Huddleston, E. M.; Gaffo, A. L. *Curr. Opin. Pharmacol.* **2022**, *65*, 102241 DOI: https://doi.org/10.1016/j.coph.2022.102241
3. Martinon, F.; Pétrilli, V.; Mayor, A.; Tardivel, A.; Tschopp, J. *Nature.* **2006**, *440*, 237–241 DOI: https://doi.org/10.1038/nature04516

J. Mex. Chem. Soc. **2025**, *69*(4)
Regular Issue

ISSN-e 2594-0317

4. Pouliot, M.; James, M. J.; McColl, S. R.; Naccache, P. H.; Cleland, L. G. *Blood.* **1998**, *91*, 1769–1776.
5. So, A.; Thorens, B. *J. Clin. Invest.* **2010**, *120*, 1791–1799 DOI: https://doi.org/10.1172/JCI42344
6. Panche, A. N.; Diwan, A. D.; Chandra, S. R. *J. Nutr. Sci.* **2016**, *5*, e47 DOI: https://doi.org/10.1017/jns.2016.41
7. Borges, F.; Fernandes, E.; Roleira, F. *Curr Med Chem.* **2002**, *9*, 195–217 DOI: https://doi.org/10.2174/0929867023371229
8. Mierziak, J.; Kostyn, K.; Kulma, A. *Molecules.* **2014**, *19*, 16240–16265 DOI: https://doi.org/10.3390/molecules191016240
9. Tian, C.; Liu, X.; Chang, Y.; Wang, R.; Lv, T.; Cui, C.; Liu, M. *S. Afr. J. Bot.* **2021**, *137*, 257–264 DOI: https://doi.org/10.1016/j.sajb.2020.10.022
10. Sharma, J. N.; Al-Omran, A.; Parvathy, S. S. *Inflammopharmacol.* **2007**, *15*, 252–259 DOI: https://doi.org/10.1007/s10787-007-0013-x
11. Dejam, A.; Hunter, C. J.; Pelletier, M. M.; Hsu, L. L.; Machado, R. F.; Shiva, S.; Power, G. G.; Kelm, M.; Gladwin, M. T.; Schechter, A. N. *Blood.* **2005**, *106*, 734–739 DOI: https://doi.org/10.1182/blood-2005-02-0567
12. Larsen, F. J.; Weitzberg, E.; Lundberg, J. O.; Ekblom, B. *Free Radical Biol. Med.* **2010**, *48*, 342–347 DOI: https://doi.org/10.1016/j.freeradbiomed.2009.11.006
13. Shiva, S.; Huang, Z.; Grubina, R.; Sun, J.; Ringwood, L. A.; MacArthur, P. H.; Xu, X.; Murphy, E.; Darley-Usmar, V. M.; Gladwin, M. T. *Circ. Res.* **2007**, *100*, 654–661 DOI: https://doi.org/10.1161/01.RES.0000260171.52224.6b
14. Townsend, C. C. *Springer: Berlin, Heidelberg.* **1993**, 70–91 DOI: https://doi.org/10.1007/978-3-662-02899-5_7
15. Macorini, L. F. B.; Radai, J. A. S.; Maris, R. S.; Silva-Filho, S. E.; Leitao, M. M.; de Andrade, S. F.; Gelves, D. I. A.; Salvador, M. J.; Arena, A. C.; Kassuya, C. A. L. *Evid. Based. Complement. Alternat. Med*. **2020**, *2020*, 4170589 DOI: https://doi.org/10.1155/2020/4170589
16. Tarnam, Y. A.; Ilyas, M.; Begum, T. N. *Int. J. Pharma. Res. Rev.* **2014**. *3*, 58-66.
17. de Paula Vasconcelos, P. C.; Spessotto, D. R.; Marinho, J. V.; Salvador, M. J.; Junior, A. G.; Kassuya, C. A. L. *J. Ethnopharmacol.* **2017**, *202*, 85–91 DOI: https://doi.org/10.1016/j.jep.2017.03.007
18. Quang, N.; Phuong, N.; Luong, V.; Huyen, N.; Xuan, D.; Thanh, T. *Vietnam J.Chem.* **2024**, *62* DOI: https://doi.org/10.1002/vjch.202300269
19. Dosumu, O. O.; Idowu, P. A.; Onocha, P. A.; Ekundayo, O. *EXCLI J.* **2010**, *9*, 173–180.
20. Olutola Dosumu, O.; Onocha, P.; Ekundayo, O.; Ali, M. *Iran. J. Pharm. Res.* **2014**, *13*, 143–147.
21. Hoi, H. *Pharmacogn. J.* **2020**, *12*, 1693–1697 DOI: https://doi.org/10.5530/pj.2020.12.228
22. Noro, T.; Oda, Y.; Miyase, T.; Ueno, A.; Fukushima, S. *Chem. Pharm. Bull.* **1983**, *31*, 3984–3987 DOI: https://doi.org/10.1248/cpb.31.3984
23. Cheenpracha, S.; Park, E.-J.; Rostama, B.; Pezzuto, J. M.; Chang, L. C. *Mar. Drugs.* **2010**, *8*, 429–437 DOI: https://doi.org/10.3390/md8030429
24. Han, Y.-H.; Chen, D.-Q.; Jin, M.-H.; Jin, Y.-H.; Li, J.; Shen, G.-N.; Li, W.-L.; Gong, Y.-X.; Mao, Y.-Y.; Xie, D.-P.; et al. *Appl. Biol. Chem.* **2020**, *63*, 21 DOI: https://doi.org/10.1186/s13765-020-00504-2
25. Halgren, T. A. *J. Comput. Chem.* **1999**, *20*, 720–729 DOI: https://doi.org/10.1002/(SICI)1096-987X(199905)20:7<720::AID-JCC7>3.0.CO;2-X
26. O'Boyle, N. M.; Banck, M.; James, C. A.; Morley, C.; Vandermeersch, T.; Hutchison, G. R. *J. Cheminf.* **2011**, *3*, 33 DOI: https://doi.org/10.1186/1758-2946-3-33
27. Gill, A. L.; Frederickson, M.; Cleasby, A.; Woodhead, S. J.; Carr, M. G.; Woodhead, A. J.; Walker, M. T.; Congreve, M. S.; Devine, L. A.; Tisi, D.; et al. *J. Med. Chem.* **2005**, *48*, 414–426 DOI: https://doi.org/10.1021/jm049575n
28. Enroth, C.; Eger, B. T.; Okamoto, K.; Nishino, T.; Nishino, T.; Pai, E. F. *Proceedings of the National Academy of Sciences*, **2000**, *97*, 10723–10728 DOI: https://doi.org/10.1073/pnas.97.20.10723
29. Trott, O.; Olson, A. J. *J. Comput. Chem.* **2010**, *31*, 455–461 DOI: https://doi.org/10.1002/jcc.21334

J. Mex. Chem. Soc. **2025**, *69*(4)
Regular Issue

ISSN-e 2594-0317

30. Eberhardt, J.; Santos-Martins, D.; Tillack, A. F.; Forli, S. *J. Chem. Inf. Model.* **2021**, *61*, 3891–3898 DOI: https://doi.org/10.1021/acs.jcim.1c00203
31. Forli, S.; Huey, R.; Pique, M. E.; Sanner, M. F.; Goodsell, D. S.; Olson, A. J. *Nat. Protoc.* **2016**, *11*, 905–919 DOI: https://doi.org/10.1038/nprot.2016.051
32. Disadee, W.; Mahidol, C.; Sahakitpichan, P.; Sitthimonchai, S.; Ruchirawat, S.; Kanchanapoom, T. *Tetrahedron.* **2011**, *67*, 4221–4226 DOI: https://doi.org/10.1016/j.tet.2011.04.041
33. Zhou, B.; Yang, Z.; Feng, Q.; Liang, X.; Li, J.; Zanin, M.; Jiang, Z.; Zhong, N. *J. Ethnopharmacol.* **2017**, *199*, 60–67 DOI: https://doi.org/10.1016/j.jep.2017.01.038
34. Ghalib, R. M.; Mehdi, S.; Hashim, R.; Sulaiman, O.; Valkonen, A.; Rissanen, K.; Trifunović, S. *J. of Chem. Crystallogr.* **2010**, *40*, 510–513 DOI: https://doi.org/10.1007/s10870-010-9687-9
35. Mahmoud, I. I.; Marzouk, M. S.; Moharram, F. A.; El-Gindi, M. R.; Hassan, A. M. *Phytochemistry.* **2001**, *58*, 1239–1244 DOI: https://doi.org/10.1016/s0031-9422(01)00365-x
36. Xue, H.; Xu, M.; Gong, D.; Zhang, G. *Food. Front*. **2023**, *4* DOI: https://doi.org/10.1002/fft2.287
37. Li, J.; Gong, Y.; Li, J.; Fan, L. *Food. Chem.* **2022**, *379*, 132100 DOI: https://doi.org/10.1016/j.foodchem.2022.132100
38. da Silva, S. L.; da Silva, A.; Honório, K. M.; Marangoni, S.; Toyama, M. H.; da Silva, A. B. F. *J. Mol. Struct. THEOCHEM*. **2004**, *684*, 1–7 DOI: https://doi.org/10.1016/j.theochem.2004.04.003
39. Liang, H.; Deng, P.; Ma, Y.-F.; Wu, Y.; Ma, Z.-H.; Zhang, W.; Wu, J.-D.; Qi, Y.-Z.; Pan, X.-Y.; Huang, F.-S.; et al. *Evid. Based. Complement. Alternat. Med.* **2021**, *2021*, 8698232 DOI: https://doi.org/10.1155/2021/8698232
40. Turner, M. D.; Nedjai, B.; Hurst, T.; Pennington, D. J. *Biochim. Biophys. Acta.* **2014**, *1843*, 2563–2582 DOI: https://doi.org/10.1016/j.bbamcr.2014.05.014
41. Zhang, J.; Li, H.; Wang, W.; Li, H. *Exp. Ther. Med.* **2022**, *23*, 1–8 DOI: https://doi.org/10.3892/etm.2022.11230
42. Ying, J.; Zhang, M.; Qiu, X.; Lu, Y. *Biomed. Pharmacother.* **2018**, *103*, 381–390 DOI: https://doi.org/10.1016/j.biopha.2018.04.088
43. Yang, L.; He, J. *BMC Complement. Med. Ther.* **2022**, *22*, 55 DOI: https://doi.org/10.1186/s12906-022-03540-1
44. Huwiler, A.; Wartmann, M.; van den Bosch, H.; Pfeilschifter, J. *Br. J. Pharmacol.* **2000**, *129*, 612–618 DOI: https://doi.org/10.1038/sj.bjp.0703077

Article

J. Mex. Chem. Soc. **2025**, *69*(4)
Regular Issue

ISSN-e 2594-0317

Fenugreek as a Potential Antiviral Agent against Crimean-Congo Hemorrhagic Fever Virus: an In-depth Theoretical Analysis

Sumit Kumar*, Ravindra Kumar, Nagendra Kumar

PG Department of Chemistry, Magadh University, Bodh Gaya-824234.

***Corresponding author:** Sumit Kumar, email: sumitkrmgr@gmail.com

Received October 27th, 2024; Accepted March 10th, 2025.

DOI: http://dx.doi.org/10.29356/jmcs.v69i4.2384

Abstract. Fenugreek is widely known for its important medicinal, nutritional, and culinary applications, offering antipyretic, anti-inflammatory, and antiviral effects. Its antiviral properties make it particularly interesting for addressing viruses like Crimean-Congo Hemorrhagic Fever Virus (CCHFV). Given the lack of approved treatments for CCHFV and the virus's high fatality rate, it demands urgent attention. The nucleoprotein of CCHFV, a critical factor in the virus's replication process, has been identified as a promising target for the development of antiviral therapies. This study aimed to discover inhibitors of this protein through virtual screening. A combination of docking studies and molecular dynamics simulations was employed to screen active compounds from fenugreek for their ability to inhibit the nucleoprotein. Given that CCHFV is classified as a biosafety level-4 pathogen by the World Health Organization (WHO), making it difficult to study in conventional laboratories, in-silico methods provide a safe and efficient alternative for identifying potential inhibitors. Based on the results of molecular docking and dynamic simulations, Diosgenin, Tigogenone, and Vicenin-2 are proposed as potential inhibitors of the CCHFV nucleoprotein. These findings suggest that fenugreek constituents could be promising leads in the development of antiviral therapies for CCHFV.
Keywords: Fever; diosgenin; tigogenone; vicenin; antiviral.

Resumen. El fenogreco (Trigonella foenum-graecum) es conocido por sus importantes aplicaciones medicinales, nutricionales y culinarias, ofreciendo efectos antipiréticos, antiinflamatorios y antivirales. Estas últimas lo hacen particularmente interesante para enfrentar virus como el de la Fiebre Hemorrágica de Crimea-Congo (CCHFV, por sus siglas en inglés). Dada la ausencia de tratamientos aprobados para el CCHFV y su alta tasa de mortalidad, se requiere una atención urgente. La nucleoproteína del CCHFV, un factor crítico en el proceso de replicación del virus ha sido identificada como un objetivo prometedor para el desarrollo de terapias antivirales. Este estudio tuvo como objetivo descubrir inhibidores de esta proteína mediante cribado virtual. Se empleó una combinación de estudios de acoplamiento molecular y simulaciones de dinámica molecular para evaluar la capacidad de compuestos activos del fenogreco para inhibir la referida nucleoproteína. Dado que el CCHFV está clasificado por la Organización Mundial de la Salud (OMS) como un patógeno de nivel de bioseguridad 4, se dificulta su estudio en laboratorios convencionales, por lo que los métodos in silico ofrecen una alternativa segura y eficiente para la identificación de posibles inhibidores. Con base en los resultados del acoplamiento molecular y las simulaciones dinámicas, se proponen a la diosgenina, la tigogenona y la vicenina-2 como posibles inhibidores de la nucleoproteína del CCHFV. Estos hallazgos sugieren que los componentes del fenogreco podrían constituir candidatos prometedores en el desarrollo de terapias antivirales contra el CCHFV.
Palabras clave: Fiebre; diosgenina; tigogenona; vicenina; antiviral.

Introduction

Fenugreek (also known as Trigonella foenum-graecum) is a plant belonging to the Fabaceae family, widely used for its medicinal properties, nutritional value, and culinary uses.[1] Native to the Mediterranean region, southern

J. Mex. Chem. Soc. **2025**, *69*(4)
Regular Issue

ISSN-e 2594-0317

Europe, and western Asia, fenugreek seeds and leaves have been traditionally used in various forms, such as spices, food supplements, and herbal remedies. Fenugreek seeds and leaves are commonly used in Middle Eastern, Indian, and Mediterranean cuisine. Its seeds have a slightly bitter taste and are used in spice blends like curry powder.

Fenugreek has been traditionally used in many cultures to manage fever, inflammation, and symptoms of viral infections. Although clinical studies on fenugreek's antiviral effects are limited, it is known to possess certain compounds that contribute to its antipyretic, anti-inflammatory, and antiviral properties. [2,3]

Fenugreek has been used in traditional medicine to reduce fevers.[4] The seeds, when boiled into a tea or decoction, are believed to help lower body temperature, soothe inflamed tissues, and boost immune function.[5] This effect is thought to be related to its anti-inflammatory properties, which may help in managing fever as part of the body's inflammatory response to infections. Although specific studies on fenugreek's antiviral activity are not extensive,[6] it has shown promising effects in traditional treatments against viral infections. Its bioactive compounds can enhance the immune system, which helps the body fight viral pathogens. Fenugreek contains flavonoids and polyphenols, which have been known to possess antiviral properties. These compounds may inhibit the replication of viruses, reducing the severity of infections. Fenugreek has also demonstrated benefits in reducing symptoms associated with viral respiratory infections, such as cough, congestion, and sore throat. It is sometimes used as a herbal remedy for managing flu symptoms. Fenugreek's anti-inflammatory compounds, such as saponins and alkaloids, help reduce inflammation in the body. This can be beneficial in managing the symptoms of viral infections, which often involve inflammation of tissues, fever, and other systemic responses. [7,8]

The health benefits of fenugreek are attributed to its diverse chemical composition, which includes Amino Acids, Alkaloid, Saponins, Fibers, Flavonoids and Polyphenols, Vitamins and Minerals.[9, 10] 4-Hydroxyisoleucine, amino acid in fenugreek has been studied for its role in enhancing insulin secretion, which makes fenugreek potentially useful in managing diabetes.[11] However, its impact on viral diseases is not directly established. Trigonelline, a key alkaloid in fenugreek, is known for its potential health benefits, including blood sugar regulation and anti-inflammatory properties.[12] Fenugreek contains various saponins, which are known to possess antioxidant, anti-inflammatory, and immune-modulating properties. Diosgenin, a specific saponin found in fenugreek, is used as a precursor in the synthesis of steroid hormones and has shown potential anticancer and anti-inflammatory effects.[13] Quercetin is a well-known flavonoid with strong antioxidant and antiviral activity.[14] Fenugreek is rich in both soluble and insoluble fibers, which contribute to its use in managing conditions like high cholesterol, blood sugar regulation, and digestive health. Fenugreek seeds contain significant amounts of vitamin C, vitamin A, iron, calcium, and magnesium, all of which support immune function, making it a useful supplement for boosting immunity during illness.

Crimean-Congo Hemorrhagic Fever Virus (CCHFV) is a tick-borne virus that causes Crimean-Congo Hemorrhagic Fever (CCHF), a severe viral disease in humans.[15-17] It belongs to the family Nairoviridae and is primarily transmitted through the bites of infected Hyalomma ticks, or by direct contact with blood or tissues from infected animals or humans.[15, 18-20] Symptoms of Crimean-Congo Hemorrhagic Fever can be severe and may include High fever, headaches, muscle pain, dizziness at initial phase.[17,21-23] After several days, severe bruising, nosebleeds, and uncontrolled bleeding from injection sites or internal organs may occur including Petechiae (small red or purple spots on the skin), bleeding from gums, and bloody vomit or stools. Eventually, organ failure (liver, kidneys) and shock can occur in severe cases. Mortality rates range from 10-40%, depending on timely medical intervention. [15,24]

In this study, the interactions between various active compounds derived from fenugreek and the Crimean-Congo Hemorrhagic Fever Virus (CCHFV) protein were thoroughly investigated to gain a deeper understanding of the molecular mechanisms underlying protein-ligand interactions. Here the CCHFV nucleoprotein is mainly studied. The nucleoprotein is essential for viral genome encapsidation, replication, and transcription, making it a critical component for viral survival. Targeting the nucleoprotein can disrupt these processes, hindering viral propagation. Additionally, inhibitors designed to interact with the nucleoprotein could prevent its interaction with RNA or other viral components, thereby offering a promising antiviral strategy against CCHFV. This aspect will be incorporated into the manuscript to strengthen the discussion on potential therapeutic targets. This was achieved through an integrated approach utilizing both Molecular Docking and Molecular Dynamics (MD) simulations. Molecular Docking helped predict the preferred binding orientations and affinities of the fenugreek constituents within the CCHFV protein's active sites, while MD simulations were employed to monitor the stability and dynamic behavior of these interactions over time. Together, these computational techniques provide valuable insights into how these compounds may inhibit the CCHFV protein, potentially paving the way for future antiviral drug development.

J. Mex. Chem. Soc. **2025**, *69*(4)
Regular Issue

ISSN-e 2594-0317

Computational details

Structural detail

A total of seventeen distinct compounds derived from fenugreek were selected for computational analysis. These molecules are composed of hydrogen (H), carbon (C), oxygen (O), and nitrogen (N) atoms. The chemical structures of these seventeen constituents are depicted in Fig. 1.

Preparation of the target structure for docking

The crystal structure of the Crimean–Congo hemorrhagic fever virus nucleoprotein (CCHFV N) in its monomeric form was obtained from the Protein Data Bank (PDB) under the identifier 4AQG [19]. Upon inspection, the structure was analyzed for any missing side chains or amino acids. It was found that eleven residues between Asn183 and Ser194 were absent from the structure, and these were subsequently modeled using the SWISS-MODEL server.[25,26]

Additionally, sequence alignment was performed using EMBOSS Needle, which compares two input sequences and generates an optimal global sequence alignment, outputting the results to a file (see Fig. S1) .[27] The alignment, visualized in Fig. S1, was computed using the Needleman-Wunsch algorithm, ensuring the best possible match (including gaps) over the full length of the sequences.[28] Preparation of the docked entity: 3D structures of important constituent of fenugreek were downloaded from PubChem Website.

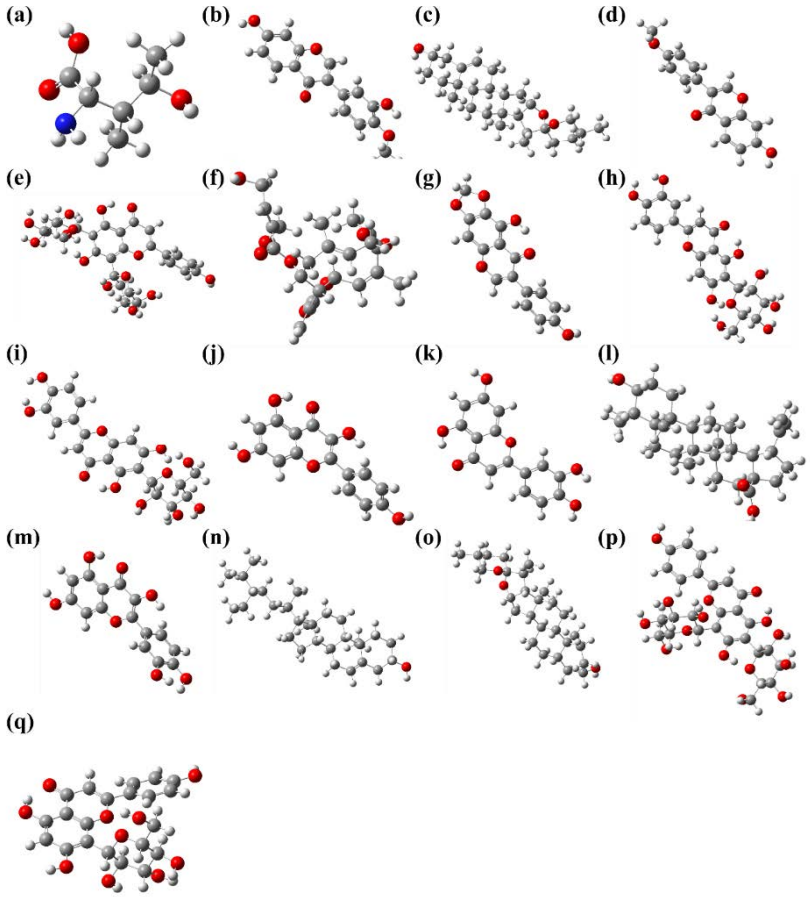

Fig. 1. Molecular structure of **(a)** 4-Hydroxyisoleucine (PubChem ID: 2773624), **(b)** Calycosin (5280448), **(c)** Diosgenin (99474), **(d)** Formononetin (5280378), **(e)** Schaftoside (442658), **(f)** Hiyodorilactone A (5281471), **(g)** Irolone (5281779), **(h)** Isoorientin (114776), **(i)** Isovitexin (162350), **(j)** Kaempferol (5280863), (k) Luteolin (5280445), **(l)** Mairin (64971), (m) Quercetin (5280343), **(n)** Sitosterol (222284), **(o)** Tigogenone (99516), **(p)** Vicenin-2 (442664), and **(q)** Vitexin (5280441).

J. Mex. Chem. Soc. **2025**, *69*(4)
Regular Issue

ISSN-e 2594-0317

Molecular docking

The interaction between a ligand and its receptor has been analyzed using molecular docking, which reveals that ligand-receptor binding occurs via various non-covalent interactions between the protein and the ligand. A single dominant form (at physiological pH) was chosen for the study to ensure consistency in the computational approach. The default pH of 7.0 was used throughout the study. Several software tools are utilized for docking studies. AutoDock Vina Programs and MGL Python-based tools have been employed to investigate the effect of constituent of Fenugreek over **CCHFV**.[29-31]

Molecular dynamics simulation

To examine the influence of Fenugreek constituents on CCHFV, molecular dynamics (MD) simulations were conducted using the Gromacs 2024 software suite.[32] The simulations employed the CHARMM27 force field, which incorporates specialized terms for addressing dihedral potentials. This force field utilizes the TIP3P water model with Lennard-Jones interactions for accurate molecular representation.[33] The simulations used an all-atom force field designed for proteins, with the proteins solvated homogeneously within a cubic box containing water molecules modeled by point charges. Periodic boundary conditions were applied to eliminate boundary artifacts, and an appropriate number of counter ions were introduced to neutralize the system.[34]

To maintain bond lengths, including hydrogen bonds, a constraint-solving algorithm was employed. Simulations were performed under an NVT ensemble (constant number of particles, volume, and temperature) at 300K, using Berendsen temperature coupling. This was followed by an NPT ensemble (constant number of particles, pressure, and temperature) where pressure control was achieved via Parrinello-Rahman pressure coupling with a time constant of 0.1 ps and a pressure of 1 bar. The cutoff radii for short-range electrostatic and van der Waals interactions were set at 1.2 nm. The simulation utilized a time step of 2 fs and a Fourier spacing of 0.16 nm. The MD simulation ran for 4000 ps (4ns), with coordinates saved every 10 ps for post-simulation analysis.

Results and discussion

A docking analysis was conducted for each key constituent of fenugreek with the Crimean-Congo Hemorrhagic Fever Virus (CCHFV). [35, 36] The most energetically stable complexes between fenugreek constituents and CCHFV were examined to identify the amino acids involved in the interactions. The findings, detailing these interactions, are presented in Table 1.

Table 1. Analysis of the interaction of key constituents of fenugreek with the Crimean-Congo Hemorrhagic Fever Virus (CCHFV).

Components	Affinity	Final Intermolecular Energy	Final Total Internal Energy	Torsional Free Energy	Unbound System's Energy
4-Hydroxyisoleucine	-4.7007	-5.830	-0.277	1.237	-0.170
Calycosin	-7.7641	-9.132	-0.377	1.362	-0.383
Diosgenin	**-9.4385**	**-9.714**	**0.000**	**0.276**	**0.000**
Formononetin	-7.5344	-9.031	0.076	1.101	-0.319
Schaftoside	-8.794	-13.420	-1.900	4.627	-1.900
HiyodorilactoneA	-8.1377	-11.260	-2.497	3.806	-1.822
Irolone	-8.1980	-9.139	-0.210	0.959	-0.192
Isoorientin	-8.0093	-11.220	-1.098	3.271	-1.054

J. Mex. Chem. Soc. **2025**, *69*(4)
Regular Issue

ISSN-e 2594-0317

Components	Affinity	Final Intermolecular Energy	Final Total Internal Energy	Torsional Free Energy	Unbound System's Energy
Isovitexin	-8.5264	-11.290	-1.079	3.240	-0.605
Kaempferol	-8.3274	-9.615	-0.279	1.460	-0.106
Luteolin	-8.1310	-9.392	-0.275	1.393	-0.331
Mairin	-9.0790	-10.690	-0.302	1.592	-0.326
Quercetin	-7.7339	-9.308	-0.271	1.582	-0.262
Sitosterol	-8.1720	-11.290	-1.402	3.105	-1.421
Tigogenone	**-9.6047**	**-9.885**	**0.000**	**0.281**	**0.000**
Vicenin2	**-9.3007**	**-13.910**	**-1.828**	**5.709**	**-0.732**
Vitexin	-9.1962	-12.310	-1.154	3.494	-0.778

Table 1 presents molecular docking results, summarizing key interaction energies for key constituents of fenugreek with the CCHFV protein. The data includes values for binding affinity, final intermolecular energy, total internal energy, torsional free energy, and unbound system's energy. The constituents of fenugreek show a range of binding affinities, with Tigogenone (-9.6047 kcal/mol) having the highest affinity, indicating stronger binding with CCHFV protein whereas 4-Hydroxyisoleucine has the weakest affinity (-4.7007 kcal/mol).

Furthermore, Schaftoside shows the lowest final intermolecular energy (-13.420 kcal/mol), indicating strong interactions with the CCHFV protein whereas 4-Hydroxyisoleucine again shows the weakest interaction (-5.830 kcal/mol).

On inspecting the Total Internal Energy values. Most constituents of fenugreek with the CCHFV protein have negative values, but Diosgenin, and Tigogenone show zero internal energy changes, indicating no deformation or strain upon binding.

Interestingly, the Torsional Free Energy gave some relevant information too. Vicenin2 (5.709 kcal/mol) and Schaftoside (4.627 kcal/mol) exhibit the highest torsional free energies, implying more flexibility or conformational changes during binding. In contrast, Diosgenin and Tigogenone have zero torsional free energy, suggesting rigid structures.

Furthermore, Sitosterol and HiyodorilactoneA show significant energy differences when unbound (-1.421 kcal/mol and -1.822 kcal/mol respectively), while Diosgenin, and Tigogenone have zero unbound energy, indicating no energy difference between bound and unbound states.

Eventually, constituents of Fenugreek like Diosgenin, Tigogenone and Vicenin2 exhibit strong binding affinities with minimal conformational changes, whereas Vicenin2 show strong intermolecular interactions but high flexibility.

Interaction of various constituents of Fenugreek with CCHFV

The interactions of seventeen distinct constituents of fenugreek with the CCHFV protein have been investigated and are summarized in Table S1 (see supporting information).[37] Each constituent’s interaction is subsequently detailed individually for a comprehensive analysis.

4-Hydroxyisoleucine against CCHFV

The binding of 4-Hydroxyisoleucine to the active sites of CCHFV was evaluated and documented. It forms interactions with chain A of CCHFV via Gly409 and Leu335 residues. Specifically, a significant hydrogen bond with Gly409 is observed at a distance of 2.71 Å, while a hydrophobic interaction occurs with Leu335 at 3.59 Å.

J. Mex. Chem. Soc. **2025**, *69*(4)
Regular Issue

ISSN-e 2594-0317

Calycosin against CCHFV

The binding of Calycosin to CCHFV's active sites has been studied and presented. It forms interactions with chain A through residues such as Ile305, Ile374, Ile449, Ala451, Ala300, Ser387, and Thr411. Notable hydrogen bond distances include 3.10, 2.13, 2.60, and 2.69 Å with Ala300, Ser387, and Thr411, respectively. Hydrophobic interactions with Ile305, Ile374, Ile449, and Ala451 are found at 3.93, 3.59, 3.77, and 3.81 Å, respectively.

Diosgenin against CCHFV

The interaction of Diosgenin with the binding sites of CCHFV has been analyzed. It forms bonds with chain A via residues Ile305, Arg373, Tyr64, Ile449, and Ala451. Prominent hydrogen bonds are formed with Ile305 and Arg373 at 2.07 and 2.74Å, respectively. Hydrophobic contacts occur with Tyr64, Ile449, and Ala451 at 3.91, 3.21, and 3.51 Å, respectively.

Formononetin against CCHFV

The binding of Formononetin to CCHFV's active sites has been studied and outlined. It interacts with chain A via Arg373, Thr382, Arg385, Ile305, and Ile449. Notable hydrogen bond distances are 2.67, 2.26, and 3.49 Å with Arg373, Thr382, and Arg385, respectively. Hydrophobic contacts with Ile305, Arg373, Arg385, and Ile449 are measured at 3.80, 3.57, 3.84, and 4.49 Å, respectively.

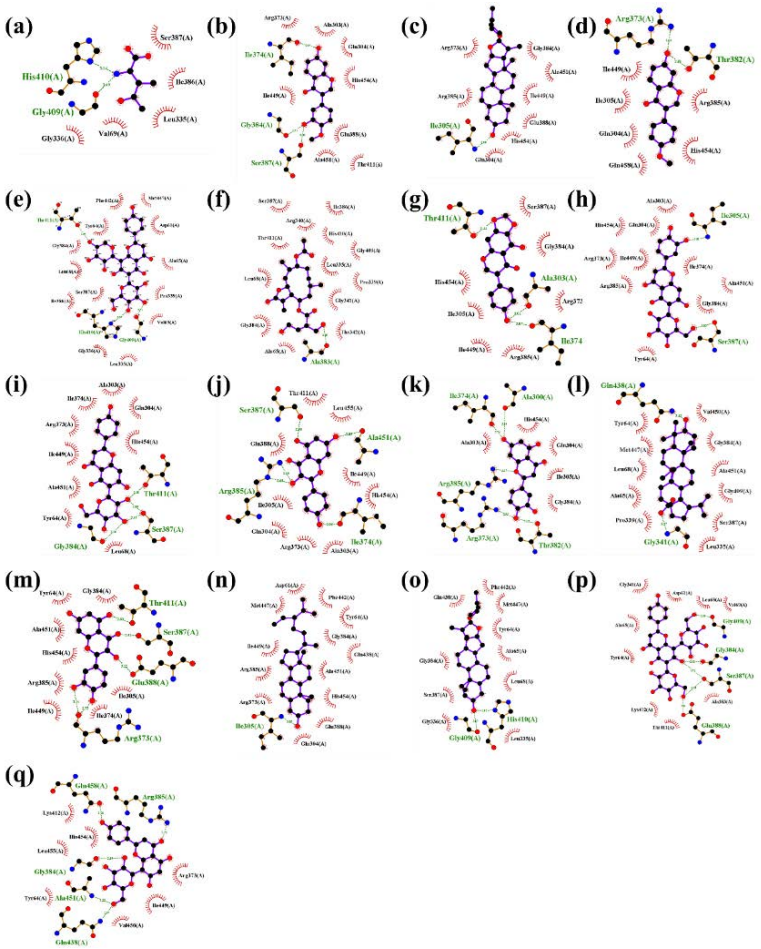

Fig. 2. Ligand-Protein Complex for **(a)** 4-Hydroxyisoleucine, **(b)** Calycosin, **(c)** Diosgenin, **(d)** Formononetin, **(e)** Schaftoside, **(f)** HiyodorilactoneA, **(g)** Irolone, **(h)** Isoorientin, **(i)** Isovitexin, **(j)** Kaempferol, **(k)** Luteolin, **(l)** Mairin, **(m)** Quercetin, **(n)** Sitosterol, **(o)** Tigogenone, **(p)** Vicenin2 and **(q)** Vitexin with CCHFV protein.

J. Mex. Chem. Soc. **2025**, *69*(4)
Regular Issue

ISSN-e 2594-0317

Schaftoside against CCHFV

Schaftoside interacts strongly with the CCHFV protein through a combination of hydrophobic interactions and hydrogen bonding, ensuring stable binding. Hydrophobic contacts with Asp-61, Tyr-64, and Phe-442 (3.44–3.69 Å) enhance ligand retention, with Phe442 likely contributing pi-stacking interactions for additional stability. Hydrogen bonds with Gly341, Ser387, Gly409, His410, and Thr411 further reinforce binding. Ser387 forms multiple bonds, while GLY-409 and THR-411 (both 2.09 Å) provide strong stabilization. His410's imidazole may offer electrostatic support, while Gly residues ensure flexibility for ligand accommodation.

HiyodorilactoneA against CCHFV

The binding of HiyodorilactoneA to CCHFV has been explored. It interacts with chain A via Thr342, Ala65, Leu335, Pro339, and Ile386. A key hydrogen bond with Thr342 is formed at a distance of 3.90 Å, while hydrophobic interactions with Ala65, Leu335, Pro339, Thr342, and Ile386 are noted at 3.63, 3.77, 3.89, 3.70, and 3.76 Å, respectively.

Irolone against CCHFV

The binding of Irolone to the active sites of CCHFV was analyzed and reported. It interacts with chain A via Ser387, Thr411, Ile305, Ile449, and Ala451. Major hydrogen bonds with Ser387 and Thr411 are formed at 3.00 Å and 2.17 Å, respectively. Hydrophobic interactions with Ile305, Ile449, and Ala451 are found at 3.83, 3.45, and 3.91 Å, respectively.

Isoorientin against CCHFV

The binding of Isoorientin to CCHFV's active sites has been studied. It forms interactions with chain A via Ile305, Gly384, Ser387, Thr411, Ile374, and Ile449. Significant hydrogen bond distances are observed at 2.11, 2.15, 2.54, and 3.32 Å with Ile305, Gly384, Ser387, and Thr411, respectively. Hydrophobic contacts with Ile374 and Ile449 are at 3.62 and 3.66 Å, respectively.

Isovitexin against CCHFV

The interaction of Isovitexin with CCHFV's active sites has been studied. It interacts with chain A via Ala233, Gly384, Ser387, Thr411, Ile374, Ile449, and Ala451. Notable hydrogen bond distances include 2.33, 2.99, 1.82, and 2.28 Å with Ala233, Gly384, Ser387, and Thr411. Hydrophobic contacts occur with Ile374, Ile449, and Ala451 at 3.46, 3.66, and 3.77 Å, respectively.

Kaempferol against CCHFV

The binding of Kaempferol to CCHFV has been studied. It interacts with chain A via Ala300, Arg385, Ser387, Ile374, Thr411, Ile449, and His454. Major hydrogen bonds are formed at 3.31, 2.46, and 2.88 Å with Ala300, Arg385, and Ser387, while hydrophobic interactions with Ile374, Thr411, Ile449, and His454 are observed at 3.90, 3.69, 3.66, and 3.53 Å, respectively.

Luteolin against CCHFV

The interaction of Luteolin with CCHFV's binding sites has been explored. It forms bonds with chain A via Ala303, Ile305, Arg373, Thr382, His454, Gln304, and Ile374. Major hydrogen bond distances include 3.63, 4.04, 2.93, and 3.12 Å with Ala303, Ile305, Arg373, and Thr382. Hydrophobic contacts with Gln304, Arg373, and Ile374 are observed at 3.85, 3.60, and 3.92 Å, respectively.

Mairin against CCHFV

The interaction of Mairin with CCHFV's active sites has been analyzed. It binds to chain A via Gly341, Gln438, Ala451, Tyr66, and Val69. Key hydrogen bonds are found at 3.27, 3.13, and 2.69 Å with Gly341, Gln438, and Ala451, while hydrophobic interactions with Tyr66, Val69, and Ala451 are noted at 3.66, 3.95, and 3.24 Å, respectively.

J. Mex. Chem. Soc. **2025**, *69*(4)
Regular Issue

ISSN-e 2594-0317

Quercetin against CCHFV

The interaction of Quercetin with CCHFV has been examined. It binds to chain A via Tyr64, Arg385, Ser387, Glu388, Thr411, and Ile449. Major hydrogen bonds occur at 2.94, 2.73, 2.53, 2.88, and 1.84 Å with respective residues, while hydrophobic interaction with Ile449 is noted at 3.75 Å.

Sitosterol against CCHFV

The binding of Sitosterol to CCHFV's active pockets has been analyzed. It interacts with chain A via Ala303, Ile305, Tyr64, Ile449, and Ala451. Significant hydrogen bonds are formed with Ala303 and Ile305 at 3.21 and 2.15 Å, respectively. Hydrophobic interactions occur with Tyr64, Ile449, and Ala451 at 3.49, 3.29, and 3.36 Å, respectively.

Tigogenone against CCHFV

The interaction of Tigogenone with the binding pockets of CCHFV has been reported. It interacts with chain A through Ala65 and Phe442. Significant hydrogen bonds are noted at 3.87 and 3.47 Å with Ala65 and Phe442, respectively.

Vicenin2 against CCHFV

The binding of Vicenin2 to CCHFV's active sites has been studied. It interacts with chain A via Leu335, Ala383, Gly384, Ser387, Thr411, Asp61, Tyr64, and Ala65. Major hydrogen bond distances are 3.75, 2.48, 3.44, 3.14, and 3.13 Å with respective residues. Hydrophobic interactions occur with Asp61, Tyr64, and Ala65 at 3.88, 4.00, and 3.51 Å, respectively.

Vitexin against CCHFV

The interaction of Vitexin with CCHFV has been evaluated. It binds to chain A via Tyr64, Arg373, Gly384, Arg385, Gln438, Ala451, His454, and Ile449. Major hydrogen bonds occur at 3.12, 2.24, 2.97, 1.84, 2.13, 2.50, and 3.04 Å with respective residues, while hydrophobic interactions with Arg373, Ile449, and His454 are found at 4.00, 3.49, and 3.34 Å, respectively.

Fig. S2 particularly shows the three most stable Ligand-Protein Complexes among all ligands. These complexes are for Diosgenin, Tigogenone and Vicenin2 for CCHFV protein.

Non-Covalent Interaction (NCI) plot

The Non-Covalent Interaction (NCI) plot is a valuable tool for analyzing various non-covalent interactions present in macromolecules.[19,22,30,38] The reduced density gradient is to quantify the parameters associated with non-covalent interactions in the NCI plot.[38] In this study, the NCI plot was employed to investigate the interactions of Diosgenin, Tigogenone, and Vicenin2 within the active site of the CCHFV protein. For this analysis, the docking poses with the lowest binding energies were selected, and Pymol software was used to identify close interactions within a distance of 3.5 Å. Key residues from the CCHFV protein, along with Diosgenin, Tigogenone, and Vicenin2, were chosen to generate the NCI plot.

Fig. 4 illustrates the NCI plots and the associated non-covalent interactions for Diosgenin, Tigogenone, and Vicenin2 in complex with the CCHFV protein. The color scheme used in the isosurfaces is as follows: blue indicates strong attractive interactions, green represents moderately strong interactions such as hydrogen bonding, π-π interactions, and van der Waals (vdW) forces, while red signifies repulsive interactions. The NCI plots predominantly show a mix of green and blue regions, indicating the presence of both electrostatic and dispersion interactions. Fig. 4(a), (b), (c) display RDG plots from the NCI analysis of the docking poses for Diosgenin, Tigogenone, and Vicenin2 with the CCHFV protein. These plots reveal that the binding strength primarily arises from hydrogen bonding and vdW interactions, as reflected by the dominance of blue and green colors in the plots.

Fig. 4(d) illustrates the isosurface extraction from the NCI analysis, highlighting key hydrogen bonds formed between Diosgenin and the CCHFV protein. Notably, these bonds occur with Ile305 and Arg373 at distances of 2.07 Å and 2.74 Å, respectively, corroborating the interactions depicted in Fig. 2. Moving to Fig. 4(e) and 4(f), they show the NCI isosurface extractions for Tigogenone and Vicenin-2, respectively, in complex with the CCHFV protein. In Fig. 4(e), significant hydrogen bonds are observed between Tigogenone and Ala65 (3.87 Å) and Phe442 (3.47 Å). Fig. 5(f), on the other hand, details Vicenin-2's interaction with CCHFV chain A through residues Leu335, Ala383, Gly384, Ser387, Thr411, Asp61, Tyr64, and Ala65. Key hydrogen bond distances here

J. Mex. Chem. Soc. **2025**, *69*(4)
Regular Issue

ISSN-e 2594-0317

include 3.75, 2.48, 3.44, 3.14, and 3.13 Å. These NCI plots offer a comprehensive view of the intermolecular interactions between the ligands and the CCHFV receptor, providing insights into the nature of their binding.

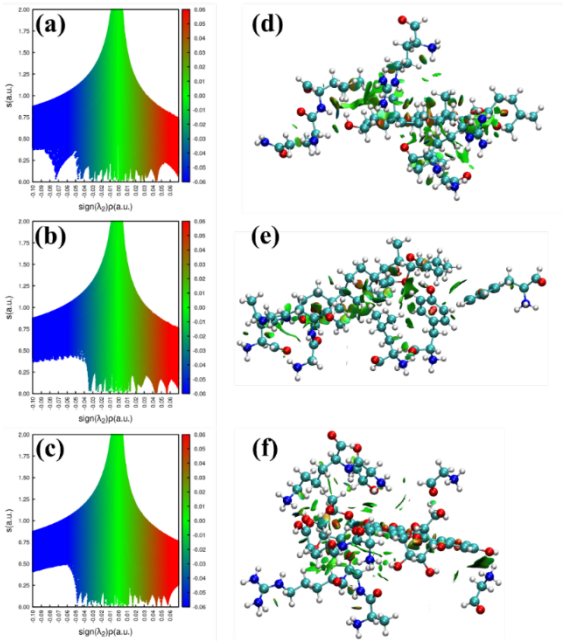

Fig. 4. The RDG plots along with its corresponding isosurface visualizations from the RDG analysis from the NCI analysis for the docking configurations of Diosgenin, Tigogenone, and Vicenin2 with the CCHFV protein are shown in figures **(a & d)**, **(b & e)**, and **(c & f)**, respectively.

Molecular dynamic studies

The use of molecular dynamics (MD) simulation allows for real-time observation of ligand-protein binding interactions over a specified duration, enabling the prediction of the ligand's conformational stability within the protein's binding site. In this study, 2 ns MD simulations were performed to assess the stability of Diosgenin, Tigogenone, and Vicenin-2, key constituents of fenugreek, when docked into CCHFV protein binding pocket.

The simulation results indicated that these compounds maintained a stable conformation within the protein's binding site throughout the simulation. The analysis of the root mean square deviation (RMSD) of the protein backbone showed that the protein complexes formed with Diosgenin, Tigogenone, and Vicenin-2 reached a stable equilibrium at the same time, signifying that these ligands provide structural stability to the protein.

Moreover, the comparison of the protein-ligand complexes with the unbound protein revealed that the presence of these ligands increased the overall stability of the protein. This suggests that Diosgenin, Tigogenone, and Vicenin-2 not only fit well into the binding pocket but also interact effectively with the surrounding amino acids, enhancing the rigidity of the protein structure.

Hydrogen bond formation

The hydrogen bond formation between Diosgenin, Tigogenone, Vicenin-2, and the CCHFV protein was evaluated over the 4000 ps molecular dynamics trajectory (Fig. 5). The Diosgenin-CCHFV complex showed the formation of two hydrogen bonds, with one remaining stable throughout the simulation. In the case of the Tigogenone-CCHFV complex, a single hydrogen bond was observed, which was consistently maintained during the simulation period. For the Vicenin-2-CCHFV complex, four hydrogen bonds were formed, with two or three bonds remaining stable throughout the simulation. It can be inferred that the stability of these complexes is largely driven by persistent hydrogen bonding, especially for the Vicenin-2-CCHFV complex.

J. Mex. Chem. Soc. **2025**, *69*(4)
Regular Issue

ISSN-e 2594-0317

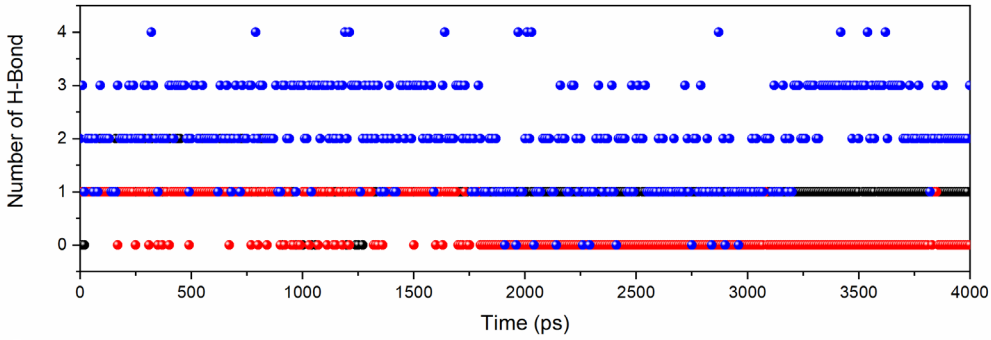

Fig. 5. Number of hydrogen bond formations of Diosgenin (Black), Tigogenone (Red), and Vicenin2 (Blue) with the CCHFV protein during a 4000 ps MD simulation.

Analysis of principal components

Fig. 6(a) shows the 2D projection of the first two eigenvectors. In the Diosgenin-CCHFV complex, it was observed that Diosgenin-CCHFV exhibited comparable diversity in conformations during the simulations (shown in black) with Tigogenone (red), and Vicenin2 (blue) in complex with the CCHFV protein. It was widely clustered in the range of −10 to 10. Fig. 6(b) shows that the eigenvalue of the Diosgenin (black), Tigogenone (red), and Vicenin2 (blue) in complex with the CCHFV protein are 18.75 nm2, 13.75 nm2 and 10 nm2, suggesting that the secondary structure of the Diosgenin-CCHFV complex underwent significant conformational changes throughout the 4 ns simulation, favouring the formation of a stable complex.

Gibbs free energy landscapes (FELs)

Fig. 7 illustrates the free energy landscapes (FELs) of the ligand-protein complexes involving (a) Diosgenin, (b) Tigogenone, and (c) Vicenin2 with the CCHFV protein, plotted as a function of two reaction coordinates or principal components (PCs). The FEL plots reveal distinct free energy distributions between the unbound and ligand-bound protein complexes. Despite these differences, the protein was still able to adopt energetically favorable and structurally stable conformations. The analysis of FELs indicates that the inclusion of small molecules influenced both the size and position of the sampled energy basins, contributing to stable equilibrium states.

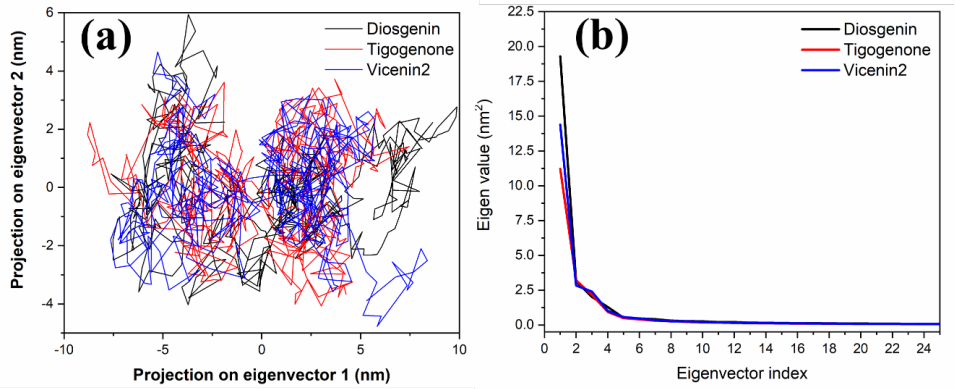

Fig. 6. (a) Principal component analysis (PCA) of the protein-ligand complexes: The collective motions of Diosgenin (black), Tigogenone (red), and Vicenin2 (blue) with the CCHFV protein were analyzed by projecting the MD trajectories onto two eigenvectors corresponding to the first two principal components. (b) The plot shows the first 25 eigenvectors versus their associated eigenvalues for Diosgenin (black), Tigogenone (red), and Vicenin2 (blue) in complex with the CCHFV protein.

J. Mex. Chem. Soc. **2025**, *69*(4)
Regular Issue

ISSN-e 2594-0317

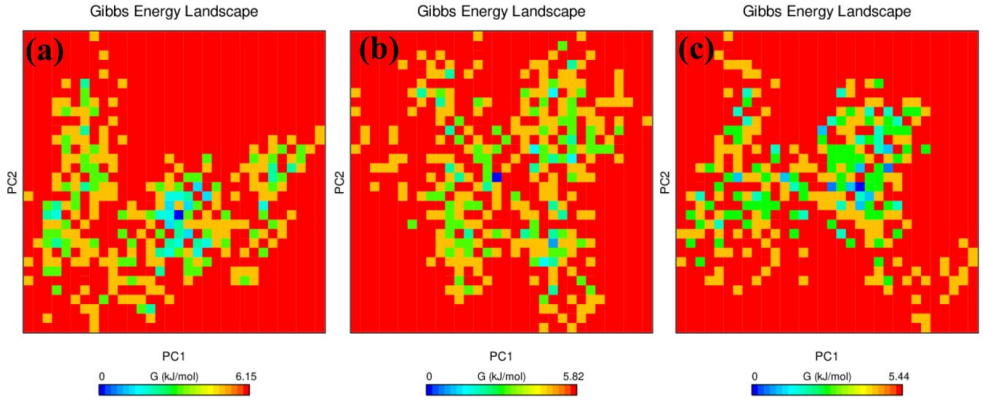

Fig. 7. Gibbs Free Energy Landscape for Ligand-Protein Complex of **(a)** Diosgenin, **(b)** Tigogenone and **(c)** Vicenin2 with CCHFV protein as a function of two reaction coordinates or principal components (PCs).

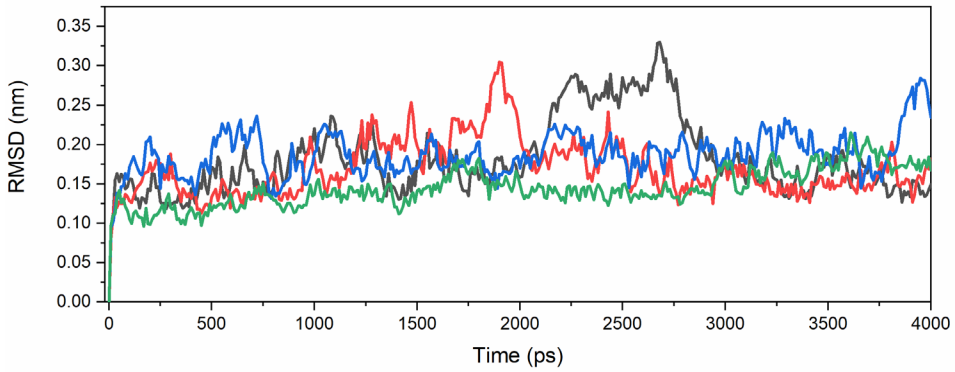

Fig. 8. RMSD Plot for Ligand-Protein Complex of Diosgenin (Black), Tigogenone (Red) and Vicenin2 (Blue) with CCHFV protein and separate protein (Green).

Root mean square deviation (RMSD) Plot

Fig. 8 presents the RMSD plot for the ligand-protein complexes of Diosgenin, Tigogenone, and Vicenin-2 with the CCHFV protein over a 4000 ps simulation. The CCHFV protein alone displayed an average backbone RMSD of approximately 1.25 Å. In comparison, the Diosgenin, Tigogenone, and Vicenin-2 complexes with the CCHFV protein exhibited average backbone RMSD values of around 1.5 Å, 1.4 Å, and 1.7 Å, respectively.

In summary, the MD simulations strongly indicate that Diosgenin, Tigogenone, and Vicenin-2 bind stably within the CCHFV protein's binding site. Their presence not only stabilizes the protein-ligand complexes but also imparts additional stability to the protein itself. These findings support the hypothesis that these fenugreek constituents could potentially serve as potential inhibitor and effectively interacting with the CCHFV protein.

Conclusions

Fenugreek is renowned for its medicinal and antiviral properties, which makes it a compelling candidate for combating viruses such as CCHFV. Due to the absence of approved treatments for CCHFV and the significant mortality associated with the virus, there is an urgent need for attention. The nucleoprotein of

J. Mex. Chem. Soc. **2025**, *69*(4)
Regular Issue

ISSN-e 2594-0317

CCHFV, which plays a key role in viral replication, has emerged as an attractive target for developing antiviral treatments. This research aimed to identify potential inhibitors of this nucleoprotein through virtual screening techniques. The study utilized a combination of docking and molecular dynamics (MD) simulations to evaluate seventeen active compounds derived from fenugreek for their ability to inhibit the nucleoprotein. Given that CCHFV is classified as a biosafety level-4 pathogen by WHO, which limits research in standard laboratories, in-silico approaches offer a safe and effective way to identify possible inhibitors. Based on the outcomes of the docking studies and MD simulations, Diosgenin, Tigogenone, and Vicenin-2 are suggested as potential inhibitors of the CCHFV nucleoprotein. These results indicate that compounds from fenugreek may serve as valuable candidates for the development of antiviral therapies targeting CCHFV.

Acknowledgments

SK thanks Magadh University, Bodh Gaya, Bihar, India for providing lab facility and SERB, Department of Science and Technology (DST), India (Grant No. SRG/2019/002284) for financial support.

References

1. Srinivasan, K. *Food Rev. Int.* **2006** *22*, 203. DOI: http://dx.doi.org/10.1080/87559120600586315.
2. Al-Habori, M.; Raman, A., in: *Phytotherapy Research: An International Journal Devoted to Pharmacological and Toxicological Evaluation of Natural Product Derivatives.* **1998** *12*, 233
3. Smith, M. *Alternative Medicine Review.* **2003** *8*, 20
4. Sun, W.; Shahrajabian, M. H.; Cheng, Q. *Mini Rev. Med. Chem.* **2021** *21*, 724. DOI: http://dx.doi.org/10.2174/1389557520666201127104907.
5. Singletary, K. W. *Nutr. Today.* **2017**, *52*, 93.
6. Aboubakr, H. A.; Nauertz, A.; Luong, N. T.; Agrawal, S.; El-Sohaimy, S. A.; Youssef, M. M.; Goyal, S. M. *J. Food Prot.* **2016**, *79*, 1001. DOI: http://dx.doi.org/10.4315/0362-028X.JFP-15-593.
7. Alu'datt, M. H.; Rababah, T.; Al-ali, S.; Tranchant, C. C.; Gammoh, S.; Alrosan, M.; Kubow, S.; Tan, T. C.; Ghatasheh, S. *J. Food Sci.* **2024**, *89*, 1835
8. Salam, S. G. A.; Rashed, M. M.; Ibrahim, N. A.; Rahim, E. A. A.; Aly, T. A. A.; Al-Farga, A. *Sci. Rep.* **2023**, *13*, 7032. DOI: http://dx.doi.org/10.1038/s41598-023-31888-y.
9. Haxhiraj, M.; White, K.; Terry, C. *Int. J. Mol. Sci.* **2024**, *25*, 6987. DOI: http://dx.doi.org/10.3390/ijms25136987.
10. Agrawal, S.; Sanap, S. N.; Bisen, A. C.; Biswas, A.; Choudhury, A. D.; Verma, S. K.; Jaiswal, S.; Narender, T.; Bhatta, R. S. *Bioanalysis.* **2023**, *15*, 711. DOI: http://dx.doi.org/10.4155/bio-2023-0074.
11. Ahmad, I.; Kuznetsov, A. E.; Pirzada, A. S.; Alsharif, K. F.; Daglia, M.; Khan, H. *Front. Chem.* **2023**, *11*, 1145974. DOI: http://dx.doi.org/10.3389/fchem.2023.1145974.
12. Konstantinidis, N.; Franke, H.; Schwarz, S.; Lachenmeier, D. W. *Molecules.* **2023**, *28*, 3460. DOI: http://dx.doi.org/10.3390/molecules28083460.
13. Arya, P.; Munshi, M.; Kumar, P. *Food Chemistry Advances.* **2023**, *2*, 100170.
14. Aghababaei, F.; Hadidi, M. *Pharmaceuticals.* **2023**, *16*, 1020. DOI: http://dx.doi.org/10.3390/ph16071020.
15. Whitehouse, C. A. *Antiviral Res.* **2004**, *64*, 145. DOI: http://dx.doi.org/10.1016/j.antiviral.2004.08.001.
16. Elaldi, N.; and Kaya, S. *J. Med. Microbiol. Infect. Dis.* **2014**, *4*, 1.
17. Swanepoel, R.; Gill, D. E.; Shepherd, A. J.; Leman, P. A.; Mynhardt, J. H.; Harvey, S. *Rev. Infect. Dis.* **1989**, *11, Suppl 4*, S794. DOI: http://dx.doi.org/10.1093/clinids/11.supplement_4.s794.

J. Mex. Chem. Soc. **2025**, *69*(4)
Regular Issue

ISSN-e 2594-0317

18. Deyde, V. M.; Khristova, M. L.; Rollin, P. E.; Ksiazek, T. G.; Nichol, S. T. *J. Virol.* **2006**, *80*, 8834. DOI: http://dx.doi.org/10.1128/JVI.00752-06.
19. Kumar Panja, S.; Kumar, S.; Fazal, A. D.; Bera, S. *J. Photochem. Photobiol. A Chem.* **2023**, *445*, 115084. DOI: http://dx.doi.org/10.1016/j.jphotochem.2023.115084.
20. Kumar Panja, S.; and Kumar, S. *J. Mol. Liq.* **2023**, *375*, 121354. DOI: http://dx.doi.org/10.1016/j.molliq.2023.121354.
21. Kumar, S.; Prajapat, A.; Panja, S. K.; Shukla, M., in: *Green Chemical Synthesis with Microwaves and Ultrasound*. **2024,** 1.
22. Kumar Sada, P.; Kaur Jassal, A.; Bar, A.; Kumar, P.; Srikrishna, S.; Kumar, S.; Kumar Singh, A.; Lee, Y.; Singh, L.; Rai, A. *Microchem. J.* **2024**, *207*, 111710. DOI: http://dx.doi.org/10.1016/j.microc.2024.111710.
23. Panja, S. K.; Kumar, S.; Haddad, B.; Patel, A. R.; Villemin, D.; Amine, H.-M.; Bera, S.; Debdab, M. *Physchem.* **2024**, *4*, 369. DOI: http://dx.doi.org/10.3390/physchem4040026.
24. Srivastava, S.; Kumar, S.; Sharma, P. K.; Rustagi, S.; Mohanty, A.; Donovan, S.; Henao-Martinez, A. F.; Sah, R.; Franco-Paredes, C. *Health Sci. Rep.* **2024**, *7*, e70053. DOI: http://dx.doi.org/10.1002/hsr2.70053.
25. Kiefer, F.; Arnold, K.; Kunzli, M.; Bordoli, L.; Schwede, T. *Nucleic Acids Res.* **2009** *37*, D387. DOI: http://dx.doi.org/10.1093/nar/gkn750.
26. Waterhouse, A.; Bertoni, M.; Bienert, S.; Studer, G.; Tauriello, G.; Gumienny, R.; Heer, F. T.; de Beer, T. A. P.; Rempfer, C.; Bordoli, L.; Lepore, R.; Schwede, T. *Nucleic Acids Res*. **2018**, *46,* W296. DOI: http://dx.doi.org/10.1093/nar/gky427.
27. Madeira, F.; Madhusoodanan, N.; Lee, J.; Eusebi, A.; Niewielska, A.; Tivey, A. R. N.; Lopez, R.; Butcher, S. *Nucleic Acids Res.* **2024**, *52*, W521. DOI: http://dx.doi.org/10.1093/nar/gkae241.
28. Muhamad, F.; Ahmad, R. B.; Asi, S.; Murad, M. N. *J. Phys. Conf. Ser.* **2018,** *1019*, 012085.
29. Kumar, S., J. Serb. Chem. Soc. 2023 88, 381 DOI: http://dx.doi.org/10.2298/jsc220921087k.
30. Kumar, S.; and Panja, S. K. *Theor. Chem. Acc.* **2023**, *142*, 126. DOI: http://dx.doi.org/10.1007/s00214-023-03073-x.
31. Trott, O.; and Olson, A. J. *J. Comput. Chem.* **2010**, *31*, 455. DOI: http://dx.doi.org/10.1002/jcc.21334.
32. Berendsen, H. J.; van der Spoel, D.; van Drunen, R. *Comput. Phys. Commun.* **1995**, *91*, 43.
33. Mark, P.; and Nilsson, L. *J. Phys. Chem. A.* **2001**, *105*, 9954.
34. Kumar, V.; Kumar, R.; Kumar, N.; Kumar, S. *Asian J. Chem.* **2023**, *35*, 991. DOI: http://dx.doi.org/10.14233/ajchem.2023.27594.
35. Ergonul, O. *Curr. Opin. Virol.* **2012**, *2*, 215. DOI: http://dx.doi.org/10.1016/j.coviro.2012.03.001.
36. Frank, M. G.; Weaver, G.; Raabe, V. *Emerg. Infect. Dis.* **2024**, *30*, 847. DOI: http://dx.doi.org/10.3201/eid3005.231646.
37. Tewari, A.; Singh, R.; Brar, J. K. *J. Phytopharm.* **2024**, *13*, 97. DOI: http://dx.doi.org/10.1016/j.sajb.2022.04.014.
38. Contreras-Garcia, J.; Johnson, E. R.; Keinan, S.; Chaudret, R.; Piquemal, J. P.; Beratan, D. N.; Yang, W. *J. Chem. Theory Comput.* **2011**, 7, 625. DOI: http://dx.doi.org/10.1021/ct100641a.

Article

J. Mex. Chem. Soc. **2025**, *69*(4)
Regular Issue

ISSN-e 2594-0317

Development and Validation of a Liquid Chromatographic Method for CasiopeinaIII-ia® in Rabbit Blood and its Application in Pre-clinical Pharmacokinetic Research

N. Vara-Gama[1], K. Rubio-Carrasco[2], J. Antonio-Jarquin[2], H. Rico-Morales[3†], L. Ruiz-Azuara[1], I. Fuentes-Noriega[2]*

[1]Inorganic Chemistry Department, Faculty of Chemistry, UNAM, Av. Universidad 3000, Circuito Exterior s/n, CU, Mexico City 04510.
[2]Pharmacy Department, UNAM, Av. Universidad 3000, Circuito Exterior s/n, CU, Mexico City 04510.
[3]Animal Experimentation and Preclinical Research Unit, Faculty of Chemistry, UNAM, Av. Universidad 3000, Circuito Exterior s/n, CU, Mexico City 04510, Mexico.

***Corresponding author:** I. Fuentes-Noriega, email: fuentesines16@gmail.com; Phone: +525554096198.

Received November 15th, 2024; Accepted March 11th, 2025.

DOI: http://dx.doi.org/10.29356/jmcs.v69i4.2397

Abstract. A rapid and simple high-performance liquid chromatography (HPLC) method using extraction with zinc sulfate was developed for determining Casiopeina III-ia (CasIII-ia) levels and then validated for the linear 10-120 µg/mL range in 200 µL of rabbit blood. An HPLC method for quantifying CasIII-ia in plasma has been previously reported; however, studies on its distribution found that CasIII-ia concentrations were higher in whole blood than in plasma. The analysis was performed using the following parameters: methanol-sodium phosphate buffer (pH 6.5; 0.01 M) (40:60 v/v) mobile phase, using a 250 x 4.6 mm I.D Symmetry® C_{18} column and a particle size of 5 µm (Waters Associates, Milford, MA, USA) with a C_{18} 5 µm guard column (Phenomenex®) was kept at a isocratic flow-rate of 0.8 ml/min, room temperature at a wavelength of 262 nm. Acetaminophen was used as the internal standard. The results showed that the assay is sensitive at 10 µg/mL. A linear relationship of r^2=0.9954 for Cass-III-ia was plotted against concentrations ranging from 10 to 120 µg/mL; the analytical method complies with linearity. The maximum intra-day relative standard deviation (RSD) was 5.10 %. An average 84.8 % intra-day (n=15) and 92.5 % inter-day (n=30) recovery % of CasIII-ia was recovered for the whole blood samples. The results demonstrated the applicability of this method for obtaining its *in vitro* distribution and also it´s for use in pharmacokinetic studies at the preclinical level on rabbits. The present study shows an assay rapid, simple, precise, and accurate for quantifying Cas III-ia in rabbit whole blood. The pharmacokinetic study, carried out in rabbits, obtained the following pharmacokinetic parameters: (kel) = 0.0150 min^{-1}; half-life time ($T_{1/2}$) = 53.9 min; with an apparent volume of distribution (Vd) = 202.8 mL; clearance (Cl) = 2.0 mL /mi; and area under the curve (AUC)=23163.8 µg/mL.min. The results contribute to the preclinical characterization of Cas III-ia.
Keywords: Antineoplastic; Casiopeína III-ia; validation HPLC-UV; pharmacokinetics; copper compound.

Resumen. Se desarrolló un método rápido y sencillo por cromatografía líquida de alta resolución (HPLC) utilizando la extracción por precipitación con sulfato de zinc para determinar los niveles de Casiopeína III-ia (CasIII-ia), se validó en un rango lineal de 10-120 mg/mL en 200 µL de sangre de conejo. Un método HPLC para cuantificar Cas III-ia en plasma ha sido reportado previamente; sin embargo, estudios realizados sobre su distribución encontraron que las concentraciones de Cas III-ia eran más altas en sangre total que en plasma. El análisis se realizó utilizando los siguientes parámetros: fase móvil fue metanol y solución amortiguadora de fosfato sódico (pH 6,5; 0,01 M) (40:60 v/v) a un flujo de 0,8 mL/min, temperatura ambiente a una longitud de onda de 262 nm. Se utilizó acetaminofén como estándar interno. Los resultados obtenidos mostraron que el ensayo es sensible a 10 µg/mL. Se encontró una relación lineal de r^2=0.9954 para CasIII-ia contra

J. Mex. Chem. Soc. **2025**, *69*(4)
Regular Issue

ISSN-e 2594-0317

concentraciones que van de 10 a 120 µg/mL; el método analítico cumple con la linealidad. La desviación relativa estándar (RSD) fue de 5.10 %. La media del recobro fue de 84.8 % intra-dia (n=15) y de 92.5 % inter-día (n=30) para Cas III-ia en muestras de sangre total. Los resultados demuestran la aplicabilidad de este método para la obtención de la distribución *in vitro* y para su uso en estudios farmacocinéticos a nivel preclínico en conejos. El presente estudio muestra un ensayo rápido, sencillo, preciso y exacto para cuantificar CasIII-ia en sangre total de conejo. El estudio farmacocinético, realizado en conejos se obtuvieron los siguientes parámetros farmacocinéticos: (kel) = 0,0150 min-1; tiempo de semivida ($T_{1/2}$) = 53,92 min; volumen aparente de distribución (Vd) = 202,8 mL; aclaramiento (Cl) = 2,0 mL /mi; y área bajo la curva (AUC)=23163,8 µg/mL.min. Los resultados contribuyen a la caracterización preclínica de Cas III-ia.
Palabras clave: Antineoplásico; Casiopeína III-ia; validación HPLC-UV; farmacocinética; compuestos de cobre.

Introduction

Several metal complexes have shown promising antineoplastic activity against cancer cells and tumors, both *in vitro* and *in vivo* [1]. One group of such complexes, which resulted from the search for new anticancer drugs based on endogenous (essential) metals that could have presented lower toxicity [2-4], Casiopeinas® have proven to be cytotoxic to cancer cells that are sensitive or resistant to cisplatin and to xenograft tumors in mice. [3]

Some Casiopeinas® have exhibited greater antineoplastic potency than cisplatin in both *in vitro* and *in vivo* studies on a variety of tumor cell lines [3,4] while also showing superoxide genomic instability due to intrachromosomal recombination [5] and a low potency in inducing genomic instability via intrachromosomal recombination [3]. These features suggest that these drugs are able to can diminish undesirable side effects [3], while stability constants and structural data have also been reported [6] CasIII-ia (Fig. 1) has shown, *in vitro*, both a pharmacological effect and selectivity towards tumor lines (MCF- 7, HCT-15, SK-N-SH neuroblastoma, HeLa, and SiHa) and healthy cells such as T lymphocytes and macrophages [3,24] In addition, pharmacokinetic studies on Cas III-ia have also been conducted on various species, including rats [3] and dogs [20]. It should be noted that Cas III-ia is the first drug with anticancer activity and developed at a Mexican university to reach Phase 1 for clinical studies in Mexico.

Some of the mechanisms reported for Casiopeinas® include DNA fragmentation and oxidation, which generate reactive oxygen species (ROS) and, thereby, cause copper reduction [3]. Reactive oxygen species also depolarize the mitochondrial membrane and cause mDNA damage by decreasing the levels of proteins involved in the respiratory chain, causing cell apoptosis via the caspase pathway. Casiopeinas® have been found to interact with the cytochrome p450 isoform CYP1A1 enzyme and present an affinity for adenine [15]. Additionally, it has been reported that Casiopeinas® interact with tubulins, integrins, and proteins such as fibronectin, there by producing changes in the cytoskeleton and, ultimately, cell death. [3]

The hemotoxicity observed in rats, points to a more complex *in vivo* cytotoxicity in the case of Casiopeinas®, as the administration of a single C_I (5 mg/kg) dose was found not to generate serious damage and was within the functional range [3,7]. Acute toxicological studies conducted for Casiopeinas® in different species at a preclinical level have reported the following results: for an LD_{50} dose of Cas III-Ea in NIH mice 12.47 mg/kg (females) and 6.67 mg/kg (males) via intraperitoneal administration and 7.12 mg/kg (females) and 10.15 mg/kg (males) via intravenous administration; and, for an LD_{50} dose of Cas III-Ea in Wistar rats 4.63 mg/kg (females) and 5.26 mg/kg (males) via intraperitoneal administration and 8.48 mg/kg for both (males and females) via intravenous administration. These findings show clear differences between the species, with a lower LD_{50} dose observed for the Wistar rats, indicating that they are more affected. Respective LD_{99} doses of 200 mg/m^2 for Cas III-ia and 160 mg/m^2 for Cas IIgly have been reported for their administration in dogs. The toxicity data found for the different Casiopeinas® can serve as a scientific basis for selecting, by extrapolating from allometric studies, a dose safe for use in future clinical studies. [3]

Studies on the pharmacokinetics of Cas III-ia in different animal species, such as rats and dogs, have the reported on its viability in terms of the corresponding pharmacokinetic parameters, as related to body weight and the physiological processes of each animal species. [3,14]

Cas III-ia (Fig. 1) is a potentially useful antineoplastic agent [13]. It is very active against L1210 leukemia cells, kills cells by inducing apoptosis [11], induces a weak recombinogenic action, and is able to degrade DNA

J. Mex. Chem. Soc. **2025**, *69*(4)
Regular Issue

ISSN-e 2594-0317

in vitro under a range of cultures. The use of high-performance liquid chromatography (HPLC) methods for the quantification of Cas III-ia® and Cas IIgly® in rat plasma has also been reported [8,9]. However, to determine both their preclinical pharmacokinetic parameters and *in vitro* distribution in rabbit blood, a sensitive and specific assay method is needed to measure the levels of these drugs in the blood. Therefore, the present study developed and validated a simple, inexpensive gradient reversed-phase HPLC. The method was validated according to procedures and acceptance criteria based on national (NOM-177-SSA1-2013) [18] and international (FDA,2001) [19] guidelines, as well as the recommendations made by other guides and authors related to the study of casiopeinas [10-12].

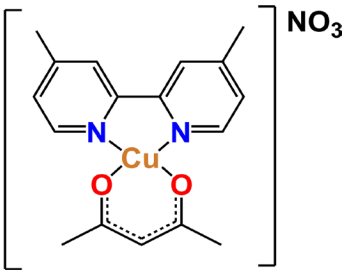

Fig. 1. Chemical structure of Cas III-ia,[Cu(4,4'-dimethyl-1,10-phenanthroline)(acetylacetonate)]NO_3.

Materials and reagents

The Cas III-ia was obtained by the present authors at their laboratory facilities, in accordance with the procedure reports set out in the corresponding patents [2,3]. The whole blood pool of rabbit samples was used for the validation method, while acetaminophen (2.5 µg/ml, USP reference standard) was used as an internal standard. It was added to the corresponding academic solutions (calibration samples stored in methanol and whole blood rabbit control samples), with the relative peak area (drug peak/internal standard peak) also analyzed.

The methanol used in the present study was HPLC grade. The water was produced by the Milli-Q water system (Millipore, Bedford, MA, USA), while the sodium phosphate and other reagents were commercially available and were of analytical grade.

Animals

Male New Zealand rabbits, weighing between 2.0 and 3.0 kg, were used in the present study. The animals were kept under clean conventional conditions and had access to food and water *at libitum*.

Methodology

Chromatographic conditions

The assay was performed using a high performance liquid chromatograph system with a Shimadzu pump (model LC10ADVP; Kyoto, Japan), a Shimadzu variable wave length UV absorbance detector (model SPD10ADVP), a Shimadzu automatic injector (model SIL10ADVP) fitted with a 50 µL sample loop (Cotati, CA, USA), a Shimadzu system controller (model SCL10AVP; Kyoto, Japan), and a chromatography data station, (Shidmadzu, Class VP, Version 5.0, Shimadzu, 1999). Chromatographic separation was carried out under the following conditions: 250 x 4.6 mm I.D Symmetry® C_{18} column and a particle size of 5 µm (Waters Associates, Milford, MA, USA) and a C_{18} 5 µm guard column (Phenomenex®). A system of methanol-sodium phosphate buffer (pH 6.5; 0.01 M) (40:60 v/v) as mobile phase and with an isocratic flow-rate of 0.8 ml/min. The analyses were performed at room temperature. The absorbance at 262 nm was recorded at a sensitivity of the detector expressed in mV (millivolts). The duration of the analytical run was 15 minutes.

Sample preparation

Two-hundred microliters of blood (Samples are collected in tubes containing heparin equivalent to 2 I.U. used as an anticoagulant.) was added to 0.6 µL of methanol and then shaken for 30 s in a vortex, with 50 µL of

J. Mex. Chem. Soc. **2025**, *69*(4)
Regular Issue

ISSN-e 2594-0317

zinc sulfate (10 % *w/w*) and 150 µL of acetaminophen (2.5 µg/mL concentration) added to the mixture, which was vigorously stirred for 30 s and centrifuged for 5 min at 5000 *g*. The supernatant was transferred to vials and a 50 µL then the aliquot was injected into the HPLC system.

Calibration curves in methanol

The stock Cas III-ia solution was prepared by dissolving 10 mg of Cas III-ia in methanol, which was then diluted to 10 mL with the same solvent (1000 µg/mL). Table 1 presents the preparation of the calibration curve in the system in a range of concentrations of 10–120 µg/mL were prepared in mobile phase and analyzed by chromatography.

Table 1. Preparation of calibration curve in system.

Aliquot of stock solution(mL)	Bring to capacity with mobile phase (mL)	Final concentration (µg/mL)
0.1	10	10
0.2	10	20
0.4	10	40
0.6	10	60
0.8	10	80
1.2	10	120

Calibration curves in whole rabbit blood

Four milligrams of Cas III-ia were diluted in 10 ml whole rabbit blood (400 µg/mL, stock solution), the Table 2 shows the preparation of the calibration curve in whole rabbit blood in a concentration range of 10 to 120 µg/mL. Three calibration curves were prepared, and each calibration curve was prepared from a stock solution of 400 µg/mL of CasIII-ia from an independent weighing. The calibration curves were subjected to the pretreatment of the samples indicated in section sample preparation, only the step of collecting the aliquot in a tube previously loaded with heparin was eliminated, since the collection of the aliquot (200 µL) was performed in a microtube without heparin because the pool of whole blood that was used to prepare the calibration curves was collected in falcon tubes of 50 mL previously loaded with heparin (containing heparin equivalent to 20 I.U. used as an anticoagulant) to avoid the formation of clots. The treated samples were injected and analyzed by chromatography.

Table 2. Preparation of calibration curve in whole rabbit blood.

Aliquot of stock solution (mL)	Bring to capacity with whole rabbit blood (mL)	Final concentration (µg/mL)
0.25	10	10
0.5	10	20
1.0	10	40
1.5	10	60
2	10	80
3	10	120

J. Mex. Chem. Soc. **2025**, *69*(4)
Regular Issue

ISSN-e 2594-0317

Limit of quantification and detection based on signal to noise

Limit of quantification (LOQ): the response of blanks (rabbit whole blood) and the response of analytical samples (rabbit whole blood spiked with Cas III-ia) were determined. The amount of the analyte (CasIII-ia) that generated a response with respect to the blank in a ratio of 10 to 1 was verified; this concentration corresponds to the limit of quantification since it was evaluated that it complied with precision and accuracy criteria.

Limit of detection (LOD): determination of the concentration that generated a response with respect to the response of blanks in a ratio of 3 to 1 was evaluated.

Intra-day and inter-day relative standard deviation (RSD)

The analysis was conducted in quintuplicate, at three concentrations high, medium, and low-quality (control points), corresponding to 15, 35, and 75 µg/mL.

Stability studies

For stability studies, the rabbit blood control and methanol solutions with Cas III-ia (1 mL) were added in Eppendorf tubes, at both 4 °C (for 96 h) and room temperature, both with and without light protection (for 96 h). Each determination was performed in duplicate, and the samples were treated in accordance with how they were prepared.

Preclinical pharmacokinetics

Healthy male New Zealand rabbits (n=10), weighing between 2.0 and 3.0 kg, were used in the study. A 10.0 mg/kg Cas III-ia dose was prepared in 30 ml of a saline solution and methanol mixture (10:1) and then administered via marginal ear vein for 60 minutes at slow infusion (0.5 mL/min). The blood samples were collected in microtubes through a cannula inserted into the marginal ear vein, first prior to administration (blanck sample) and then at 80, 90, 100, 110, 120, 140, 160, 180, 210, 240, 270, and 300 minutes post admin istration. At the end of the extraction of each sample (200 µL), the cannula was flushed with an equal volume of heparinized solution. The blood samples were then immediately stored at 4 °C until analysis.

Results and discussion

Representative chromatograms of the whole rabbit blood are shown as a blank chromatogram (Fig. 2), the chromatogram of total blood spiked with acetaminophen as internal standard (**a**), and heparin (**b**) (Fig. 3), and chromatogram for Cas III-ia with a retention time of 10.6 min (Fig. 4). No interfering peaks were detected in the blood during the retention time for Cas III-ia.

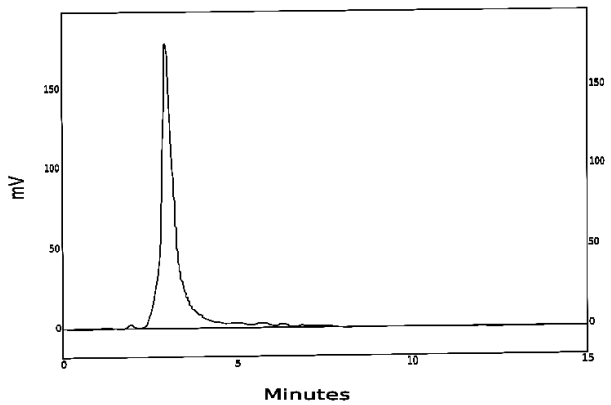

Fig. 2. Blank chromatogram in whole rabbit blood.

J. Mex. Chem. Soc. **2025**, *69*(4)
Regular Issue

ISSN-e 2594-0317

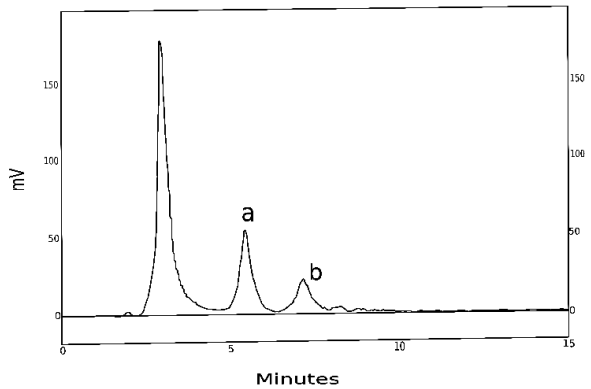

Fig. 3. Chromatogram of total blood spiked with acetaminophen as internal standard **(a)**, and heparin **(b)**.

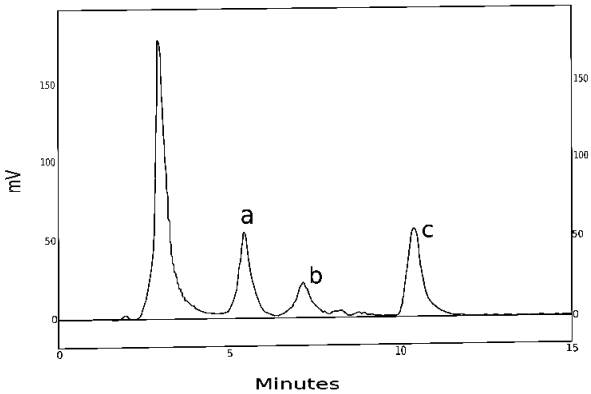

Fig. 4. Chromatogram of total blood spiked with internal standard **(a)**, heparin **(b)**, and Cas III-ia **(c)**, retention time 10.6 min.

The linearity system relationship (r^2=0.9996) was found when the relative peak area for Cas III-ia was plotted against concentrations ranging from 10 to 120 µg/mL (10.0, 20.0, 40.0, 60.0, 80.0, and 120.0 µg/mL), curves corresponding to triplicate assays (Table 3 and Fig. 5).

Table 3. Cas III-ia system linearity, corresponding to triplicate assays.

Theoretical con- centration (µg/mL)	**Relative peak area**	**Relative peak area**	**Relative peak area**	**Mean**	**SD**	**RSD%**
	Curve 1	**Curve 2**	**Curve 3**			
10	0.9	0.9	0.9	0.9	0.00	0
20	2.0	2.0	2.0	2.0	0.00	0
40	3.7	3.7	3.7	3.7	0.00	0.0
60	5.6	5.6	5.5	5.6	0.06	1.04
80	7.3	7.3	7.3	7.3	0.00	0
120	10.8	10.8	10.8	10.8	0.00	0

RSD: relative standard deviation, SD: standard deviation

J. Mex. Chem. Soc. **2025**, *69*(4)
Regular Issue

ISSN-e 2594-0317

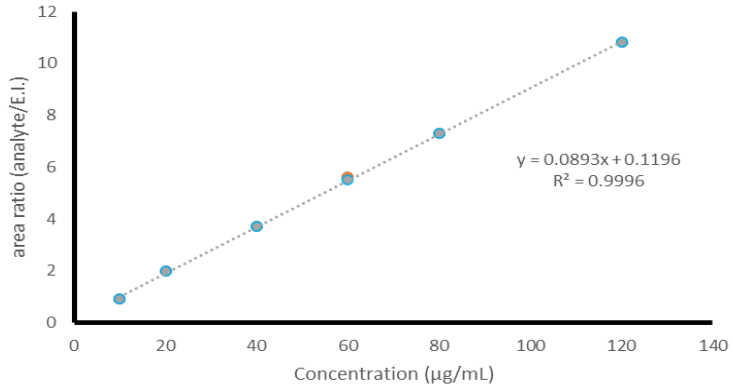

Fig. 5. Average-curve for CasIII-ia in the system, corresponding to triplicate assays.

A relationship (r^2=0.9954) was found when the relative peak area for Cas III-ia was plotted against concentrations ranging from 10 to 120 µg/mL (10.0, 20.0, 40.0, 60.0, 80.0, and 120.0 µg/mL) in 600 µL of rabbit blood, with the curves corresponding to triplicate assays (Table 4 and Fig. 6).

Table 4. Cas III-ia linearity in whole rabbit blood, corresponding to triplicate assays.

Theoretical con- centration (µg/mL)	Relative peak area	Relative peak area	Relative peak area	Mean	SD	RSD%
	Curve 1	Curve 2	Curve 3			
10	0.9	0.8	0.9	0.9	0.04	5.0
20	1.8	1.8	1.8	1.8	0.01	0.5
40	3.6	3.5	3.5	3.5	0.00	0.2
60	5.2	5.3	5.4	5.3	0.03	0.7
80	6.9	6.9	7.0	6.9	0.07	1.1
120	9.6	9.7	9.6	9.6	0.04	0.4

RSD: relative standard deviation, SD: standard deviation

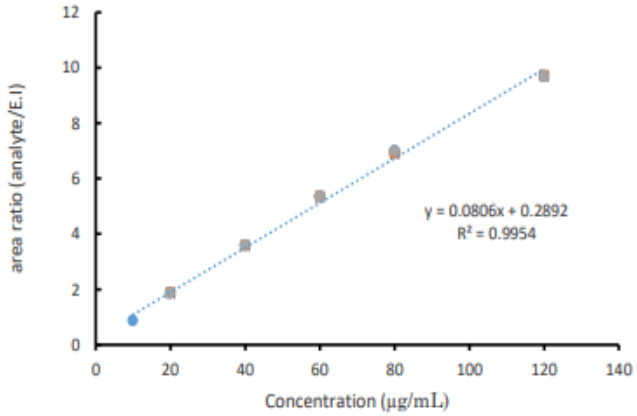

Fig. 6. Average-curve for CasIII-ia in whole rabbit blood, corresponding to triplicate assays.

J. Mex. Chem. Soc. **2025**, *69*(4)
Regular Issue

ISSN-e 2594-0317

Both the intra-day and inter-day precision of the method applied, obtained via the analysis conducted on the samples, are shown in Table 3. The precision was estimated based on the control curve samples prepared on both the same day (n=15) and subsequent days (n=30) using different stock solutions. The corresponding relative standard deviation (RSD) was below 15 %, meeting the acceptance criteria.

The level of Cas III-ia recovery was determined by first identifying the relative peak observed for the whole blood spiked with the different amounts of the compound (15, 35, and 75 µg/mL, control points) using the extraction procedure described and then comparing this peak with the relative peak observed for the same series when prepared in the mobile phase and injected into the HPLC. It is necessary to specify that to prepare the control points, a clean pool of whole rabbit blood is used, which is obtained from rabbits that were not administered any compound. The level of Cas III-ia recovered from each sample was determined in quintuplicate (Table 5), with an average of 84.8 % intra-day (n=15) and 92.5 % inter-day (n=30) recovery % from the blood. Previous reports describe Casiopeinas® in plasma protein having been observed, in binding assays, to present a significantly higher accumulation in whole blood than in plasma, which is due to the significant binding to blood cells reported in red blood cell/plasma ratios (Ke/p) of over 2 for human blood and Beagle dogs at concentrations of 1 µg/mL [13,14]. Therefore, performing the extraction process in whole blood was more efficient for comparing the pharmacokinetic parameters with those of rabbit plasma.

Table 5. Accuracy and precision of the use of the HPLC method in whole rabbit blood.

Theoretical concentration (µg/mL)	**Average experimental concentration (µg/mL) (n=5)**	**Recovery (%)**	**RSD(%)**
Intra-day (n=15)			
15	12.3	82.0	5.1
35	31.6	90.3	1.1
75	61.7	82.3	0.8
		Average recovery	
		84.8	
Inter-day (n=30)			
15	12.4	83.0	2.2
35	33.9	97.0	0.9
75	73.2	97.7	1.5
		Average recovery	
		92.5	

RSD (relative standard deviation); LQC (low-quality control, 15 µg/mL); MQC (mid-quality control, 35 µg/mL); and HQC (high-quality control, 75 µg/mL).

Defined as the sample concentration obtained from spiked blood and which presents a peak area of ten times the noise level, the LOQ was observed at 5.08 µg/mL.

Defined as the sample concentration presenting a peak of three times the noise level, the LOD was observed at 3.5 µg/mL.

The determination of the stability of Cas III-ia both before and after the sample pre- treatment revealed that, after 96 h at 4 °C, 99.85 % of the Cas III-ia was still present in the rabbit blood. At room temperature and

J. Mex. Chem. Soc. **2025**, *69*(4)
Regular Issue

ISSN-e 2594-0317

without light protection, 74.96 % of Cas III-ia was observed after 96 h, whereas, at room temperature and with light protection, 97.5 % of the blood was enriched with Cas III-ia after 96 h.

Pharmacokinetic results

No chromatographic interferences by any endogenous compounds were found. Fig. 7 shows the average pharmacokinetic profile of Cas III-ia terminal phase data, after administration by intravenous infusion in New Zealand rabbits (n=10), It was also found that the steady-state blood levels for Cas III-ia were 117.42± 3.26 µg/mL in a non-compartment model, was obtained by WINNOLIN software, while the half-life time was 53.92± 25.41 min.

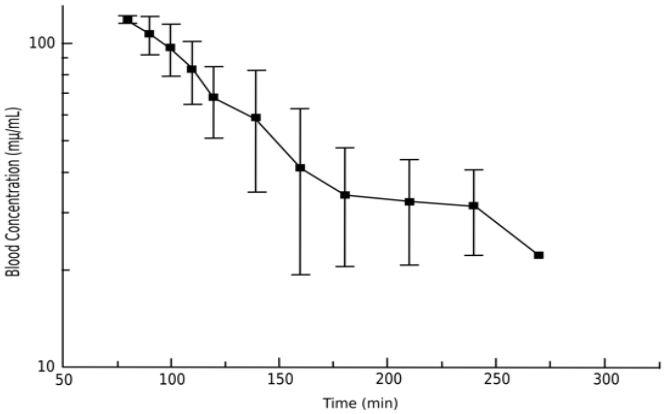

Fig. 7. Mean pharmacokinetic profile of Cas III-ia in whole blood (n= 10 New Zealand rabbit) after intravenous infusion.

The following pharmacokinetic parameters were obtained from the rabbit blood samples: (kel) = 0.0150 min-^{1}; half-life time ($T_{1/2}$) = 53.92 min; the apparent volume of distribution (Vd) = 202.81 mL; clearance (Cl) = 2.08 mL /min; and area under the curve (AUC)=23163.85 µg/mL.min. The results obtained reveal that the half-life time in rabbit blood (0.89 h) is shorter than that found in for rat blood (12.46 h) [3]. An elimination rate of 2.08 mL/min was observed for clearance in the rabbit blood samples, which was higher than that observed for rat blood (0.45 mL/min). According to the basic concepts of pharmacokinetics, the higher the elimination rate of a compound, the higher its clearance, and the smaller its distribution volume, the shorter its half-life. The volume of distribution data obtained for the different rabbits (202.81 mL), rats (0.462 L), and dogs (TMR= approximately 2 weeks) (data obtained from compartmental modeling program WINNOLIN) [3] species show that Cas III-ia presents a wide distribution in tissue. This suggests that, as reported for other Casiopeinas®, it has a wide distribution in tissues, such as blood, due to its high affinity with blood cells such as erythrocytes. [13] However, although different doses were administered intravenously in each species, the results obtained show that Cas III-ia presents low bioavailability across the three species of interest: 10 mg/kg administered to a rabbit sample=23163.85 µg/mL*.min; 10 mg/kg administered to a rat sample=22.27 µg/mL*min 3.5 mg/kg administered to a dog sample =40472.75 µg/mL.min [3]. Furthermore, a smaller distribution volume generates a higher concentration of the compound in the central circulatory system, and this is observed in the bioavailability data, since the rabbit presented a slightly higher bioavailability compared to that reported for the rat. (both species of rabbit and rat were administered the same dose of 10 mg/kg). These data indicate interspecies variability, due to both the body weight and physiological processes specific to each species. Perfusion is the flow of blood through blood vessels to multiple organs and tissues, therefore in rats, a greater perfusion could be related to their heart rate and blood pressure. Therefore, the greater the blood perfusion of multiple organs and tissues, the greater the volume of distribution of the compound in the organs of the rat, the lower the perfusion, the lower the volume of distribution of the compound in the rabbit [20]. In addition to perfusion, there is the pharmacokinetic parameter of binding to plasma proteins, with which it is known that only free drug can cross the membranes of tissues and organs. Depending on this binding will be the distribution in the different

J. Mex. Chem. Soc. **2025**, *69*(4)
Regular Issue

ISSN-e 2594-0317

species. Pharmacokinetic scaling between species is necessary to optimize test doses in humans via allometric equations, in which biochemical, anatomical, and physiological similarities between animals can be generalized and expressed in mathematical models [17].

Conclusions

The development of the method proved to be useful and reliable for determining Cas III-ia levels in whole rabbit blood. The pre-treatment procedure applied on to the sample, which involved direct precipitation with zinc sulphate, was found to be fast and simple. The method, validated for concentrations in the range of 10 to 120 µg/mL, presented a simple, repeatability, accuracy, and low limits for both: quantification and detection. The recovery % of Cas III-ia was adequate and reproducible and constant over the range of the calibration curve. This method is sufficiently sensitive for performing pharmacokinetic evaluations and can, therefore, be applied at in the future in preclinical pharmacokinetic studies. The pharmacokinetic data obtained by the present study, especially when compared with the data obtained for the different species reported [3], contributes to the characterization of Cas III-ia. At a preclinical level, this data enables the bases to be established for extrapolating an adequate dose, via allometric studies, for future clinical studies. The data also contributes to the adequate design of dosing intervals' safety for humans.

Acknowledgments

To the CONAHCYT 314819 project for financial support, to Adrián Espinoza Guillen thanks for technical support, and to all the students and collaborators who have participated in the development of this article on Casiopeinas® and the Dra. Hernández for reviewing English.

References

1. Mjos, K.D.; Orvig, C. *Chem. Rev.* **2014**, *114*, 4540–4563. DOI: https://doi.org/10.1021/cr400460s.
2. Serment-Guerrero J.; Bravo-Gomez M. E.; Lara-Rivera E.; Ruiz-Azuara L. *J. Inor. Biochem.* **2017**, *166*, 68-753. DOI: https://doi.org/10.1016/j.jinorgbio.2016.11.007.
3. Aguilar-Jiménez Z.; Espinoza-Guillén A.; Resendiz-Acevedo K.; Fuentes-Noriega I.; Carmen Mejía C.; Ruiz-Azuara L. *Review Inorganics*. **2023**, *11*, 1-23. DOI: https://doi.org/10.3390/inorganics11100394.
4. Anthony, E.J.; Bolitho, E.M.; Bridgewater, H.E.; Carter, O.W.L.; Donnelly, J.M.; Imberti, C.; Lant, E.C.; Lermyte, F.; Needham, R.J.; Palau, M.; et al. *Chem. Sci.* **2020**, *11*, 12888–12917. DOI: https://doi.org/10.1039/D0SC04082G.
5. Nayeem, N.; Contel, M. *Chem. Eur. J.* **2021**, *27*, 8891–8917. DOI: https://doi.org/10.1002/chem.202100438.
6. Ndagi, U.; Mhlongo, N.; Soliman, M.E. *Drug Des. Devel Ther.* **2017**, *11*, 599–616. DOI: https://doi.org/10.2147/DDDT.S119488.
7. Lucaciu, R.L.; Hangan, A.C.; Sevastre, B.; Oprean, L.S. *Molecules.* **2022**, *27*, 6485 DOI: https://doi.org/10.3390/molecules27196485.
8. Fuentes I.; L. Ruiz-Ramírez L.; Tovar A.; Rico H.; Gracia I. *J. Chrom. B Anal. Tech. Bio. Life Sci.* **2002**, *772*, 115-121. DOI: https://doi.org/10.1016/S1570-0232(02)00064-8.
9. Reyes, L.; Fuentes I.; Ruiz-Ramírez, L.; Macías, L. *J. Chrom. B Anal. Tech. Bio. Life Sci.* **2003**, *791*, 111-116. DOI: https://doi.org/10.1016/S1570-0232(03)00226-5.
10. https://www.ema.eu-ropa.eu/en/ich-m10-bioanalytical-method-validation-scientific-guideline, accessed in June 2022.

J. Mex. Chem. Soc. **2025**, *69*(4)
Regular Issue

ISSN-e 2594-0317

11. Vértiz, G.; García-Ortuño, L. E.; Bernal, J. P.; Bravo-Gómez, M. E.; Lounejeva, Elena.; Huerta, A.; Ruiz-Azuara, L. *Fund. & Clin. Pharm.* **2014**, *28*, 78-87. DOI: https://doi.org/10.1111/j.1472-8206.2012.01075.x.
12. García-Ramos, J. C.; Vértiz-Serrano,G.; Macías-Rosales, L.; Galindo-Murillo,R.; Toledano-Magaña, Y.; Bernal, J.P.; Fernando Cortés-Guzmán,F.; Ruiz-Azuara, L. *Eur, J. Inor. Chem*. **2017**, *12*, 1728-1736. DOI: https://doi.org/10.1002/ejic.201601199.
13. Cañas-Alonso, R. C.; Fuentes-Noriega, I.; Ruiz-Azuara, L. *J. Mex. Chem. Soc*. **2013**, *57*, 239-244. S1870-249X2013000300012.
14. Cañas-Alonso R.C.; Fuentes-Noriega, I.; Ruiz-Azuara, L. *J. Bioanal. Biomed*. **2010**, *2*, 28–34. DOI: https://doi.org/10.4172/1948-593X.1000018.
15. Campero, P. C.; Bravo, G. M. E.; Hernández, O. S. L.; Olguin, R. S. R.; Espinosa, A. J. J.; Ruiz-Azuara, L. *Toxicol. In Vitro*. **2016**, 33, 16–22. DOI: https://doi.org/10.1016/j.tiv.2016.02.008.
16. García-Ramos, J. C.; Toledano-Magaña, Y.; Gutiérrez, A. G.; Vázquez-Aguirre, A.; Alonso-Sáenz, L.; Gómez-Vidales, V.; Flores-Álamo, M.; Mejía, C.; Ruiz-Azuara, L. *BioMetals.* **2017**, *30*, 43–58. DOI: https://doi.org/10.1007/s10534-016-9983-8.
17. Paul, R. V.; Edginton, M.; Edginton A. N. *Cpt. Pharmacom. Syst Pharmacol.* **2019**, *8*, 835–844 DOI: https://doi.org/10.1002/psp4.12456.
18. https://www.dof.gob.mx/nota_detalle.php?codigo=5314833&fecha=20/09/2013#gsc.tab=0, accessed in June 2022.
19. https://www.fda.gov/media/70958/download, accessed in June 2022.
20. Gary, M.; Harkness, J. E.; Wagner, J.E, in: *The Biology and Medicine of Rabbits and Rodents*, 4th edn, 2015.

Review

J. Mex. Chem. Soc. **2025**, *69*(4)
Regular Issue

ISSN-e 2594-0317

Continuous Manufacturing in Pharmaceutical Industry: How it Thrives Green Chemistry Principles

Luis Alberto Aranda-Hernandez[1], Mariana Ortiz-Reynoso[1*], María Magdalena García-Fabila[1], Alfonso Durán[2]

[1]Faculty of Chemistry, Universidad Autónoma del Estado de México. Paseo Colón & Paseo Tollocan, s/n, Col. Residencial Colón, 50120, Toluca de Lerdo, Estado de México, México.
[2]Faculty of Chemistry, Unviersidad Nacional Autónoma de México. Circuito Escolar S/N, Coyoacán, Cd. Universitaria, 04510, Ciudad de México, México.

***Corresponding author:** Mariana Ortiz-Reynoso, email: mortizr@uaemex.mx

Received December 5th, 2023; Accepted October 17th, 2024.

DOI: http://dx.doi.org/10.29356/jmcs.v69i4.2326

Abstract. Green Chemistry is an approach that looks for a sustainable development, encouraging the industry to migrate towards cleaner and more efficient processes, reducing waste generation, and depleting carbon footprint. Continuous Manufacturing is an advanced production technology that has caught attention during the past decade because of its flexibility, agility and robustness; lately, some regulatory agencies have endorsed its implementation, but there are only a few cases of its actual applications in the manufacturing of drug substances and products. In the current paper, we review some examples available up to date in which continuous processes and green chemistry principles converge in the pharma-chemical & pharmaceutical industries in order to bring elements to understand the future of drug molecules and pharmaceutical products production.
Keywords: Continuous manufacturing; green chemistry; pharmaceutical industry; drug manufacturing; flow process.

Resumen. La Química Verde es un enfoque que busca un desarrollo sostenible, alentando a la industria a migrar hacia procesos más limpios y eficientes, reduciendo la generación de residuos y la huella de carbono. La Manufactura Continua es una tecnología de producción avanzada que ha llamado la atención durante la última década por su flexibilidad, agilidad y robustez; últimamente, algunas agencias reguladoras han avalado su implantación, pero sólo existen unos pocos casos de sus aplicaciones reales en la fabricación de fármacos y medicamentos. En el presente artículo, repasamos algunos ejemplos disponibles en los que convergen la manufacturas procesos continuos y los principios de la química verde en las industrias farmoquímica y farmacéutica, con el fin de aportar elementos para comprender el futuro de la producción de fármacos y productos farmacéuticos.
Palabras clave: Manufactura continua; química verde; industria farmacéutica; industria farmoquímica; procesos de flujo continuo.

Introduction

The pharmaceutical industry is one of the main manufacturing businesses that generates the greatest amount of waste mass with respect to the total mass of manufactured product. [1] This ratio is known as Environmental factor (E-factor), and according to this parameter, the production of pharmaceutical products can be considered as a pollutant industrial activity, as shown in Table 1. The E-Factor is calculated by the quotient of the Total waste (kg) and Total product (kg), so the better performing a process is, the lower is the E-Factor value.

J. Mex. Chem. Soc. **2025**, *69*(4)
Regular Issue

ISSN-e 2594-0317

Table 1. Current E-Factor values for different industrial sectors. [1]

Industrial sector	Production (Ton/year)	E-Factor (kg/kg)	Produced waste (Ton/year)
Petrochemical	10^6-10^8	0.1	10^6
Bulk chemicals	10^4-10^6	1-5	10^5
Fine chemicals	10^2-10^4	5-50	10^4
Pharmaceuticals	10-10^3	25-100	10^3

The pharmaceutical industry is also known for making multimillion-dollar investments in the research and development of new active pharmaceutical ingredients (API) and drugs to treat diseases or search for therapeutic solutions that improve the patients' quality of life; however, the traditional manufacturing process has changed very slowly over time, [2] and the pharmaceutical sector remains as a sector with little innovation. The traditional manufacturing process for API and drugs that are predominant in the pharmaceutical industry is known as batch manufacturing (BM), which can be summarized as a method where a predefined amount of material is processed for a certain time and then it is tested to be released as a single and unique batch. To carry it out, manufacturing conditions are previously established in compliance with current Good Manufacturing Practices (cGMP). The batch production cycle typically involves several consecutive unit operations, where the intermediate products are tested offline and stored before releasing them to move on to the next production stage. Only after the finished product is approved by the Quality Control department, the batch can be released.

BM is based on inspection and tests performed in order to demonstrate that a certain product meets its specifications. [3] Fig. 1 shows a traditional batch manufacturing process for hard gelatin capsules. In this example, BM is verified in each of the three manufacturing sites. Although usually there are only two sites involved in drug manufacturing (API and final drug production), for didactical purposes in this example the whole process requires three manufacturing sites, and each site's processes require to stop after each unit operation for sampling and testing. A three-site scenario is not exaggerated, but actually frequent for omeprazole oral capsules, to set an example. The API omeprazole is manufactured in one plant (let's say, a pharma-chemical site in Asia), then purchased by a pharmaceutical plant as raw material for pellets production (for instance, by extrusion and spheronization methods, in a European facility). Omeprazole pellets are then converted in the new raw material for the outsourced capsule-filling operation and final packaging in a Latin-American plant. So, the BM process is carried out in three locations.

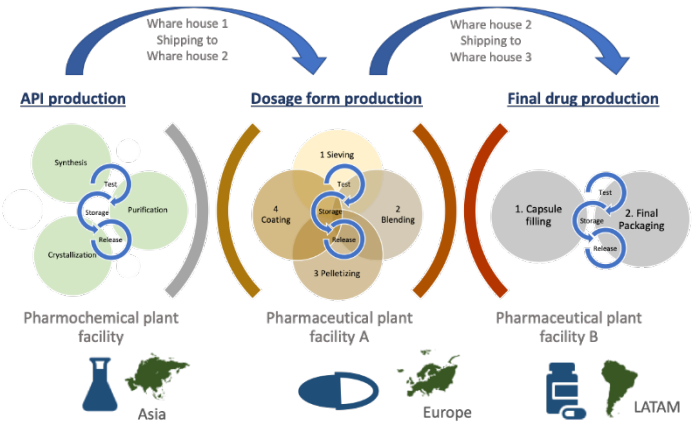

Fig. 1. Example of a hypothetical BM process for a solid dosage form, consisting on hard-gelatin capsules filled with pellets. Source: own elaboration.

J. Mex. Chem. Soc. **2025**, *69*(4)
Regular Issue

ISSN-e 2594-0317

Traditional BM has changed very little in the past five decades. This is partially explained over historical reasons. Being extremely regulated due to its direct impact in patients' health, over the years the pharmaceutical industry has adopted a position opposed to change, aimed to preserve the processes as they were first approved by federal agencies. Pharmaceutical companies have managed to avoid risks and stay in a comfort zone, knowing that any change will be examined with scrutiny by the regulators and may represent burdens, delays or fines to the companies. [2] This explains why this industrial sector deals with issues such as: being slow in regards of product supply chains, creating shortages for patients who require a product in time, and conserving pollutant and inefficient processes that not only generate waste but also represent high costs related to scale up and tech transfer between the Research and Development (R&D) stage and actual commercial manufacturing. [4]

In the last decade, greater interest has been shown in Continuous Manufacturing (CM) as an alternative that can strongly impact operations including synthesis reactions, which is a key player in the drug development process [5]; substantial research has been reported on reaction, crystallization and filtration using continuous processes. [6-11] MC has been used to produce several active pharmaceutical ingredients, either in a laboratory or on a commercial scale. Some examples are: aliskiren, artemisinin, ibuprofen, imatinib mesylate, quinolone derivatives (such as a 5HT1B antagonist), rufinamide, thioquinazolinone, hydroxypyrrolotriazine, 2,2-dimethylchromenes, fused-bycyclic isoxazolidines, 7-ethyltryptophol, 6-hydroxybuspirone. [12]

To introduce the GC concept, we need to acknowledge that one of the major challenges of humanity is the damage to the environment, which is reflected in events such as climate change, the dispersion of toxic elements and pollutants in land, air and water, the depletion of non-renewable resources, deforestation, the destruction of biodiversity and the ozone layer, among the most relevant, which have worsened in recent years. Most of these problems are generated by the implementation of chemical processes, the indiscriminate use of natural resources and the inadequate management of domestic and industrial waste. [13]

There is common consensus that these material practices are unsustainable; mankind is struggling to transition to an era of green awareness in favor of the environment with sustainable materials and processes. Part of this shift has been the emergence of Green Chemistry (GC), which refers to the study of the general methodology for the synthesis of chemical products and processes in a benign and environmentally safe manner. [14]

In 1990s, Anastas and Williamson presented the best-known definition of GC, being: "designing chemistry for the environment", emphasizing the role of science in this challenge. [15] In 1998 Anastas and Warner published the book *Green Chemistry: Theory and Practice*, where they defined GC as "the design of chemical products and processes that are more environmentally benign and that reduce negative impacts to human health and the environment". [16] Anastas and Warner's 12 principles of Green Chemistry, shown in Table 2, are still considered as guidelines on how to perform chemistry with environmental awareness.

Table 2. The 12 principles of the Green Chemistry approach. [15-16]

No.	Green Chemistry Principle
1	Prevention
2	Atom economy
3	Less hazardous chemical syntheses
4	Designing safer chemicals
5	Safer solvents and auxiliaries
6	Design for energy efficiency
7	Use of renewable feedstocks
8	Reduce derivative
9	Catalysis

J. Mex. Chem. Soc. **2025**, *69*(4)
Regular Issue

ISSN-e 2594-0317

No.	Green Chemistry Principle
10	Design for degradation
11	Real-time analysis for Pollution Prevention
12	Inherently safer chemistry for accident prevention

GC is involved in the optimization of materials synthesis, the use of renewable resources instead of non-renewable resources (both chemical and energy), and the qualitative and quantitative control of the man-made materials used and produced (as well as their waste). [17]. GC ushers scientists and engineers to rethink chemical reactions and processes, empowering them to "protect and benefit the economy, people, and the planet by finding creative solutions and innovative ways to reduce waste, conserve energy, and discover replacements for hazardous substances". [18]

Although the approach of efficient and low waste chemistry existed before the 1990s, it was from the 2000s onwards that GC started to be applied in research and development and manufacturing processes in the pharmaceutical industry. This has resulted in the discovery and publication of green syntheses of pharmaceuticals, such as sertraline hydrochloride [19], sildenafil citrate [20], paclitaxel [21], and sitagliptin phosphate monohydrate [22]. In 2022, WuXi STA, a manufacturer of active pharmaceutical ingredients and intermediates, opened a CM site in Changzhou, China [23]; that same year, Patheon, another reknown manufacturing leader, built a CM plant in Greenville, USA [24].

De Soete et al. assessed the potential implementation of a continuous production line at Janssen-Cilag SpA pharmaceutical manufacturing plant, and reported great decreases in exergetic resource consumption of electromechanical power, heating media, chemicals and cleaning agents and disposal when moving from a batch granulation to a continuous granulation process for several unit operations when manufacturing Tramacet®, a drug that was already in Teva's commercial portfolio and is produced in a facility located in Ulm, Germany. The return of investment resulting from moving from batch manufacturing to CM was verified in 3 years. [25] Also, back in 2019 in an internal conference held by Frank Streil, Chief Technical and Scientific Affairs Officer from Teva, he showed evidence of the implementation and validation of a CM platform for tablet manufacturing at the Ulm plant in Germany, and stated that a great advantage of this type of process is the consistency in the quality of the products; a smaller amount of labor required for manufacturing; and the reasonable investment cost according to the required production volumes, enhancing that CM has a high potential for savings in both manufacturing and quality costs.

The current review seeks for optimistic outcomes for implementing CM in terms of productivity and sustainability, and comes to the conclusion that CM can produce a positive impact regarding productivity, yields and financial indicators, and it is notable that it has proved to reduce the environmental impact, even helping in achieving the Sustainable Development Goals (SDG) settled by the World's Health Organization (WHO). For this reason, it is important to explore and disseminate how the CM can uphold the GC principles, and turn the pharmaceutical industry into a productive, agile, innovative, clean, green and socially responsible industry. For readers that have little knowledge of this technology, we begin with an introduction of the CM process and its intrinsic relationship with the 12 principles of GC. We also discuss the framework that is being constructed by regulatory agencies, academia, equipment suppliers, third party organizations and of course both pharma-chemical and pharmaceutical industries. Further on, we recover five examples to show some advantages related to the change from BM to CM, also describing the observed challenges. Throughout the document, we reference the principles of GC listed in Table 2. Ultimately, we plan to point out how CM endeavors overlap some of the GC principles, thus harvesting benefits both in productivity and economy, as result of the change from batch to continuous manufacturing.

Method

From a methodological point of view, we conducted a systematic review according to the Preferred Reporting Items for Systematic Reviews and Meta-Analyses (PRISMA) guidelines. [26] The search was

J. Mex. Chem. Soc. **2025**, *69*(4)
Regular Issue

ISSN-e 2594-0317

performed on articles' title, abstract, and keywords slots available in Scopus, using search terms for three terms: (1) "continuous manufacturing" OR "continuous process", (2) "Green chemistry" OR "flow chemistry" OR "Green engineering"; and (3) "pharmaceutical". Inclusion criteria were defined as follows: article published in a journal or conference proceedings, written in English or Spanish, original contribution and full text available. This search yielded 86 papers. From this group, articles that reported on the adoption of CM for the API or drug production processes were selected, yielding 37 publications from 2010 to 2023. We also reviewed the regulatory documents available on-line from WHO, ICH, FDA, PMDA, EMA, ChFDA regarding continuous manufacturing. With this information, we reviewed the state of the art in CM and GC applied to pharmaceutical processes and a master dissertation was elaborated. [12] For the current article, we selected five cases that best represent what has been achieved so far in this field; these are original articles with experimental evidence that depict CM and GC applications for API production and liquid and solid dosage forms, providing thorough description of the continuous production systems. Due to the nature of this investigation, there are several gaps in the available data, starting by the fact that pharmaceutical companies publish very few of their findings in order to protect their industrial property. Also, information varies from paper to paper, and pursuing a one-to-one comparison among processes was out of limits since the beginning; differences in size, operations, dosage forms and molecules are some of the difficulties when studying each process. Since the search method did not include biological terms or references to them, we may have ruled out some other findings from the biotechnological drugs. Given the fact that the production of biological drugs responds to completely different processes, often based on microorganisms, we hypothesize that CM applications has not yet raised enough awareness for this industry. Nonetheless, we did find scarce hints of the introduction of new biological and biosimilar products in CM approaches. [27] Lastly, underlying private interests may bias the available information and compromise the accuracy of the companies' success claims, in a context in which competence is central and the speed to achieve a market plays a major role.

Continuous manufacturing in the manufacture of API and pharmaceutical products

Continuous manufacturing: concept and utility

The essential characteristic of CM is that materials flow at a predefined rate through all the unit operations involved. Only a relatively small amount is processed in a certain time. During the manufacturing process, raw materials are continuously introduced, and the finished product is tested and released in real time, based on the results of the Process Analytical Technology (PAT) [3], which is recommended to improve the understanding and control of the manufacturing process. According to the FDA, CM "*is a process in which the input material(s) are continuously fed into and transformed within the process, and the processed output materials are continuously removed from the system. Although this description can be applied to individual unit operations or a manufacturing process consisting of a series of unit operations, as described in this guidance, continuous manufacturing is an integrated process that consists of a series of two or more unit operations*." [28, p. 1] CM uses closed-loop system controls, meaning that the process control systems (controllers) can adjust based on the real-time data. [29] CM is based on an integrated conceptual sequence, considering an end-to-end manufacturing process. Fig. 2 illustrates how former unit operations flow in to a whole process with in-time & in-site controls.

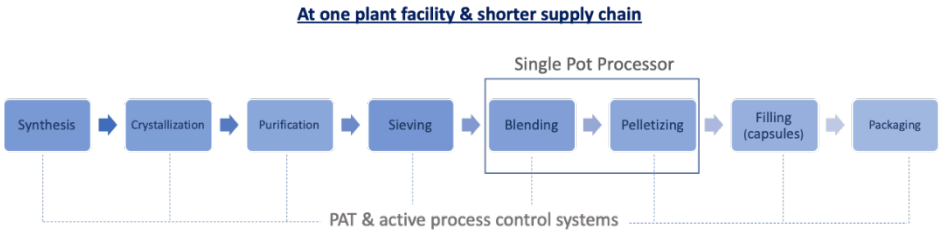

Fig. 2. A conceptual integrated CM process of a hypothetical oral solid dosage form, consisting on hard-gelatin capsules filled with pellets. Source: own elaboration.

J. Mex. Chem. Soc. **2025**, *69*(4)
Regular Issue

ISSN-e 2594-0317

Regulatory framework for CM of API and pharmaceutical products

As stated before, historically, pharmaceutical plants have been reluctant to adopting new production technologies, blaming the tight regulation to which they are subject to, and fearing that the introduction of new production technologies will bring heavy burdens and delays on the regulatory approval processes for new products. This is a complex situation; as on one hand, the pharmaceutical stakeholders expect significant regulatory challenges related to the implementation of continuous technologies, while on the other hand, regulators continue to encourage their development. [27]

One of the main obstacles pertaining to the implementation of CM in pharmaceutical products was the lack of a regulatory framework. Since the 2000s, however, the US Food and Drug Administration (FDA) has provided strong support to explore the possibilities of CM. [29] In 2002, the FDA launched an initiative titled *Current Good Manufacturing Practices (CGMP) for Pharmaceuticals for the 21st Century: A Risk-Based Approach* to encourage the implementation of a modern science and risk-based pharmaceutical quality assessment system. [30] This initiative was ground-breaking for the pharmaceutical industry. In November 2003, FDA agreed to work with the International Council for Harmonization (ICH) to develop a pharmaceutical quality system based on the integration of risk management strategies and scientific data. The ICH established several Expert Working Groups (EWG) in pharmaceutical development and these have published quality guidelines that are followed worldwide to design effective and efficient manufacturing processes in order to reach product quality, and define a "desired state" for manufacturing in the 21st century. [31] For instance, Guidelines ICH Q8 *Pharmaceutical Development* describes how to build Quality by Design (QbD), and ICH Q9 *Quality Risk Management* outlines how to take into account risks throughout the pharmaceutical product's life cycle. [32-33]

These regulatory agencies also stated that QbD and PAT are key elements to promote a vision of a flexible, agile and efficient manufacturing sector that reliably manufactures high-quality pharmaceutical products, based on the premise: "*quality cannot be tested in products; It must be built-in or it must be by design*." [34]

In March 2023, the FDA published the *Guidance for Industry Quality Considerations for Continuous Manufacturing*. In the introduction, FDA states: "*This guidance provides information regarding FDA's current thinking on the quality considerations for continuous manufacturing of small molecule, solid oral drug products that are regulated by the Center for Drug Evaluation and Research (CDER)*." [28, p. 1] Precisely, the manufacturing processes of solid oral drug products made with small molecules comprise the traditionally known unit operations that, although perfectible, have stayed still for decades, perhaps because companies perceive changes as a threat, as in a "*why fix it if it ain't broken?*" philosophy.

As observed, the FDA supports the adoption of modern manufacturing technologies that improve the quality of pharmaceutical products and their ready availability to patients, and recognizes that CM is an emerging technology that enables modernization and offer benefits to both the industry and patients. FDA indicates that: "*Continuous Manufacturing can improve pharmaceutical manufacturing, for example, by using an integrated process with fewer steps and shorter processing times; requiring smaller equipment footprint; supporting an enhanced development approach (e.g. quality by design (QbD) and the use of process analytical technology (PAT) and models); enabling real-time product quality monitoring; and providing flexible operation to allow scale-up, scale-down, and scale-out to accommodate changing supply demands. We also expect that this operational flexibility may decrease the need for some postapproval regulatory submissions. Therefore, FDA expects that adopting continuous manufacturing for pharmaceutical production will reduce drug product quality issues, lower manufacturing costs, and improve availability of quality medicines to patients.*" [28, p. 2]

In November 2022, the ICH published the Q13 Guideline: *Continuous Manufacturing for Drug Substances and Drug Products*, which describes the scientific and regulatory considerations for the development, implementation, operation and life cycle management of CM of API and drugs. [35]

Other international regulatory bodies such as the European Medicines Agency (EMA), the Japanese Pharmaceutical and Medical Devices Agency (PMDA). The China's Food and Drug Administration (ChFDA) have also issued a favorable position towards the implementation of CM, indicating that the principles established in the ICH Q13 Guideline are to be adopted. [4]

In this context, it is clear that trend-setting regulatory agencies have been recently active in establishing guides to help clarify whatever requirements are needed to implement CM and shift pharmaceutical industry practices.

J. Mex. Chem. Soc. **2025**, *69*(4)
Regular Issue

ISSN-e 2594-0317

Continuous manufacturing and the pharmaceutical industry

As per the guidance and direction given by the regulatory bodies, thrusting a QbD approach leads to new opportunities, such as process intensification, higher production rates in smaller manufacturing lines and facilities, but also at lower energy and materials consumption levels. The industry has explored CM not only for specific unit operations, but also to the complete manufacturing process.

In the continuous model, waiting times between stages can be eliminated. This represents an important advantage for drugs or intermediates susceptible to degrading over time or that are sensitive to environmental conditions, directly improving the product quality. Furthermore, one of the characteristics of CM is that it is carried out on a small scale. An example of a CM platform for research purposes installed at Rutgers University, New Jersey, USA, is shown in Figure 3. The model implies the reduction of safety risks associated with highly energetic or dangerous materials and allows for greater flexibility in the use of equipment and facilities; [3 & 5] These effects show the close association between CM and GC. In 2019 Continuous Pharmaceuticals reported the first fully automated, end-to-end integrated continuous manufacturing pilot plant yielding 4,800 tablets/h. [36]

In recent years, the pharmaceutical community has admitted that CM can be competitive compared to BM considering price and quality, also finding out that it can better meet the requirements set by regulatory authorities. This scenario has encouraged the competition of large companies that are leading the way in demonstrating the feasibility and benefits of this new manufacturing model. Until recently, there were only six pharmaceutical products on the market that include continuous technologies in their manufacturing processes: Pfizer's Daurismo (glasdegib), Vertex's Orkambi (lumacaftor/ivacaftor) and Symdeko (tezacaftor / ivacaftor), Janssen-Cilag's Prezista (darunavir), Eli Lilly's Verzenio (abemaciclib), and Johnson & Johnson's Tramacet (tramadol, acetaminophen). [27]

These products have paved the way for other competitors; for example, the leading company in the manufacturing of generic drugs Teva has implemented a CM platform in its Ulm, Germany site; WuXi STA has announced the opening of a CM plant at Changzhou site in China; and the CMO leading company Patheon has also built a CM site at Greenville, USA. Additionally, the equipment suppliers have taken important steps to develop innovative CM concepts demonstrating greater interest (GEA, Bosch, Glatt, Bohle, Hosokawa, Fette, Lodige, Gericke, Ktron, Schenk, among others). Recently, new suppliers of quality control equipment and solutions have entered the market, creating more competition and, consequently, better solutions for the industry. [29]

Examples of a readily commercialized CM product are the following. Orkambi, 200 mg lumacaftor plus 125 mg ivacaftor fixed-dose combination coated tablets manufactured by Vertex. Orkambi is manufactured by a two-stage process. In the first stage, ivacaftor crystal drug is dissolved with a polymer and a surfactant, then spray-dried into a powder which undergoes a second drying phase to remove the solvents to acceptable limits. This results in an amorphous intermediate, which is a free-flowing, compressible powder. The second stage, consists of seven steps, comprising a continuous wet granulation process: a) intragranular mixing, b) continuous granulation in a wet twin-screw, c) drying and grinding in a fluid bed, e) extra-granular mixing, f) compression, g) film coating, and h) impression. This process occurs in three different manufacturing sites with different PAT systems and capabilities and real-time release testing (RTRT).

Vertex's Symdeko (tezacaftor/ivacaftor), an orphan drug for cystic fibrosis, was developed by a Quality by Design (QbD) approach, and phase III batches were manufactured by a CM process, confirming equivalence as to the BM used in prior stages. Symdeko's CM system uses gravity feeding for material transfer between unit stages, along with a pneumatic conveying system to transfer granules, and a lift-container conveying system to move forward the tablet cores. The individual components are mixed and conveyed using a worm system (convective mixing) and the final mix is then fed into a roller compactor. The intragranular and extragranular mixtures are transported separately by a pneumatic transfer device to the granule conditioning unit for further grinding, where a segregation point device removes non-conforming material.

Prezista (600 mg darunavir tablets), a drug manufactured by Janssen-Cilag Prezista (JSC), is approved in more than a dozen countries, including the USA, Brazil, Canada and Australia. On 2016 the FDA approved the upgrade in the manufacture of Prezista, shifting to a CM production line at its facility in Gurabo, Puerto Rico. The replacement of the BM process came as a result of a 5-year partnership with Rutgers University and the University of Puerto Rico. This partnership made it possible to develop a process that integrates all manufacturing steps (weighing, grinding, mixing, compression, and coating) into a single line. JSC collaborated

J. Mex. Chem. Soc. **2025**, *69*(4)
Regular Issue

ISSN-e 2594-0317

with researchers at the Engineering Research Center for Structured Organic Particle Systems (C-SOPS) to develop a full-scale CM and direct compaction production line at the Rutgers facility for testing, and the CM line at the JSC facility was built using this design. By incorporating one of the first full-production-scale continuous direct compression solid oral dose manufacturing facilities in Puerto Rico, JSC reduced a two-week production led time to a one-day production lead time, allowing for continuous quality monitoring. [29] On Janssen's words posted at its website, "*This new technology allows us to shorten production and test cycle times, reduce waste and environmental impact, and reduce process risks. And all this while maintaining the quality of the existing product by offering innovative therapies to patients. In this way, the technology is of enormous importance for the future of pharmaceutical production, as it can reduce processing times and the footprint of manufacturing facilities*." [37] Lastly, Verzenio (abemaciclib) from Eli Lilly, an oncology drug for the treatment of hormone-receptor positive women, also developed by QbD principles, is currently manufactured by a near infra-red (NIR)-based PAT for drug concentration monitorization in a CM, followed by a traditional batch process film coating operation. [25]

The examples given above show that CM, although not being a fast, low-investment and easy method, is being conceived as a long-term, steady, robust, more sustainable and ultimately cheaper way of producing medicines. As this paper shows, CM is not being implemented by small local industries, but by strong global companies, who will lead the way in the future. The potential is huge, and will be used for competitiveness purposes, for sure. Currently several vendors offer integrated PAT monitoring and process control platforms balancing price affordability and ease of use. Furthermore, some advances in CM in pharmaceuticals and oral liquid medications are taking place. [38-40] Also, developments for injectables are occurring. [2]

As it was mentioned, academia players are actively involved in learning more about CM processes. [41 36] Since 2002, Rutgers University has focused on manufacturing solid dosage forms and operates the C-SOPS. The Massachusetts Institute of Technology (MIT) supports the Novartis Project on implementing end-to-end CM. In Austria, the Research Center for Pharmaceutical Engineering (RCPE) at Graz University of Technology, and the University of Graz have been doing research on Hot Melt Extrusion (HME) technologies in CM. The Ghent University at Belgium, has studied wet granulation CM. The Advanced Crystallization (CMAC) body in the United Kingdom has focused on CM applied to API and crystallization processes.

The most powerful force driving this transition is the new global competence in performance and quality. The equipment for freeze-drying operations, for instance, shows that despite the fact that the process has not changed over the past 80 years, its market value is expected to double to $ 4.8 billion. [25]

Results

CM and GC applied to pharmaceutical products

According to our data base search, 37 publications from 2010 to 2023 relate CM and GC topics. This number gave us a hint that GC activities converge with CM and that both approaches are suitable in the production of drug substances and pharmaceutical products. [42-48] The integration of GC into the early development stages of drugs also aligns to pharmaceutical Benign by Design (BbD) and QbD ideals, driving research towards opportunities in process improvements and added value throughout products' life cycle; for instance, greater production with less use of space, energy and raw materials, as well as the mitigation of additional costs associated with waste generation (i.e. reducing chemical substances that are not directly converted into a product, as well as costs derived from the treatment and/or disposal/destruction of waste). Given the fact that the environmental impact of pharmaceutical manufacturing has been greater than that of the rest of the chemical industries, [1] companies that comply with GC principles through CM, may strive for building up a better reputation while seizing a competitive advantage.

Although there are few examples, the review allowed us to realize that CM has started to be implemented in pharma-chemical and pharmaceutical processes, and that large companies have already spotted benefits with respect to BM. The pharmaceutical industry is exploring CM processes both in individual unit operations and in end-to-end manufacturing systems. With respect to GC, some pharmaceutical companies have sought to migrate towards sustainable manufacturing practices, having learned that these can broaden production portfolios and increase competitiveness. The implementation of continuous processes using PAT

J. Mex. Chem. Soc. **2025**, *69*(4)
Regular Issue

ISSN-e 2594-0317

tools helps to reduce waste by increasing the understanding of the process. Closed loop controls and online optimization, for instance, drive the first principle of GC: waste prevention. [42] In sum, combining CM with the GC principles can result in improved performance, additional capabilities and added efficiencies to products and processes, while addressing environmental, safety and security concerns.

Now at days, there are 6 drug products that incorporate continuous manufacturing in their manufacturing process: Vertex's Orkambi and Symdeko, Johnson & Johnson's Prezista, Eli Lilly's Verzenio, and Pfizer's Daurismo have been approved in the US; Vertex's Orkambi and Symkevi, Johnson & Johnson's Prezista, and Eli Lilly's Verzenio in the EU; and Johnson & Johnson's Tramacet and Eli Lilly's Verzenio in Japan. [38]

Manufacturers such as Pfizer and Johnson & Johnson, have reported advantages such as shortening the manufacturing process from weeks to minutes, shorter cycle times, faster technology transfer, reduction of the process variability, decrease of energy consumption and waste, as well as a lower environmental impact. [25]

Although companies still have to face the challenge of getting acquainted to PAT and process automation if they wish to succeed in the implementation of CM processes, the following appreciations have been reported already.

A. The implementation of flow chemistry through clean technologies such as electrochemistry, photochemistry, and microwave heating, are easy to scale up in a continuous mode.
B. CM technologies allow better control of the processes, and aid in reducing risky working conditions found in BM facilities, such as high pressures and temperatures and use of dangerous or explosive solvents.
C. CM permits to improve the purity and selectivity of the intermediate and final products to be obtained.
D. By using smaller equipment and modules as compared to traditional manufacturing, the equipment footprint and the environmental impact decrease.

According to Khinast, Kleinebudde & Rantanen, CM leads to economic success because it increases the overall equipment effectiveness level, and reduces inventory value of work in progress, cycle times (less downtime), operational costs, labor costs (direct and indirect), and quality analysis costs, but it also brings savings in capital investment and product transfer, not to mention the inherent space reduction for a CM site. [29]

In a 2015 press release, Pfizer company announced collaboration with Glaxo Smith Kline (GSK) on the so called "Next-Generation Design of Portable, Continuous, Miniature and Modular (PCMM) Oral Solid Dose Development and Manufacturing Units". According to this information, "A PCMM facility has 60 to 70% smaller footprint than a conventional production facility." This platform is being used for the development and launch of several products, shortening the manufacturing process from weeks to minutes, in Pfizer's Groton and Freiburg facilities, located in the USA and in Germany, respectively. The company estimates that 70% of its portfolio of small-molecule oral solid doses will be manufactured in PCMM, which will produce shorter cycle times, faster technology transfers, and reduced process variability, for which it estimates that this will occur within the next 10 years. In 2017 Pfizer joined the consortium CMAC (Continuous Manufacturing and Advanced Crystallisation), alongside with GSK, Astra Zeneca, Novartis, Bayer, Takeda, Lilly and Roche, led by the University of Strathclyde, to accelerate progress in pharmaceutical manufacturing. CMAC focuses on accelerating the adoption of CM for the production of medicines with a lower cost and improved sustainability. [49]

Pfizer's first PCMM platform for oral-dose solid delivery systems was used for the development and launch of *Daurismo*, which lead to shortening the manufacturing process from weeks to minutes. According to the European Medicines Agency (EMA) [50] evaluation report, the cores of Daurism (glasdegib maleate tablets) are in fact manufactured by direct compression using the PCMM. This CM process involves three first steps: continuous feeding, continuous mixing, and tablet compression using a conventional rotary tablet press, followed by one separate unit operation, consisting in film coating the cores, that is performed as a batch manufacturing process using conventional equipment. Interestingly, the process flow and equipment used to supply the European Union market is the same as that used in the manufacturing of clinical batches and batches for stability studies.

J. Mex. Chem. Soc. **2025**, *69*(4)
Regular Issue

ISSN-e 2594-0317

In the following lines, we show examples of how the CM of API and drugs can shift from a batch scheme to a continuous flow, overcoming typical limitations of the traditional scheme. These five examples denote the significant efforts that are being made to transit towards process designs, chemical reactions, and pharmacochemical and pharmaceutical engineering for CM models, while approaching the GC principles.

Example of plug-and-play factories for on-demand CM of API

In 2011 the kick-off of the pharmacy-on-demand (PoD) project verified as part of the *Defense Advanced Research Projects Agency* (DARPA), aiming to develop portable factories that integrated continuous manufacturing technologies to enable the production of drugs anywhere, any time. These factories, which occupy an environmental footprint the size of a commercial refrigerator, aim to solve drugs shortages in places that are difficult to access or that have political-social problems, such as war zones and pandemics. The whole idea is that in the future, when PoD initiative reaches a market phase, the manufacturing sites of pharmaceutical products will be located closer than ever to the point of use, and a distribution network having an *Amazon*-like storage system would be running. This production scheme would make possible to respond quickly to peaks in demand and depletes the need of drug storage rooms that have a great economic and environmental impact for its maintenance and replenishment. In the PoD approach, the drugs are expected to be fresher and have a longer shelf life. Thus, PoD promotes the GC principle: "Real-time analytics for pollution prevention" and the SDGs: "sustainable cities and communities" and "health and well-being". [39,51,52]

The development of the first generation of platforms with plug-and-play modules helped to obtain a purified stream of an API with a consistent solvent composition prior to the crystallization step. These platforms provided liquid doses of diphenhydramine hydrochloride, lidocaine hydrochloride, diazepam and fluoxetine hydrochloride, and ibuprofen and diazepam in solid forms. Platforms evolved into a second generation, where synthesis occurs in a continuous flow until drug crystals are dissolved in order to obtain liquid doses of nicardipine hydrochloride, ciprofloxacin hydrochloride, neostigmine methylsulfate, rufinamide, linezolid and lisinopril. Some systems aim to manufacture at least 1,000 doses/day of diazepam, diphenhydramine hydrochloride, ciprofloxacin hydrochloride, lidocaine hydrochloride, and atropine sulfate in a 3-week long manufacturing campaign. New production systems comprise new set of modules, including one for synthesis, two modules for the manufacture of the API and a module for solid dosages. Rogers and collaborators showed the ability of these production platforms to manufacture all the way from the API to oral tablets, and showed the manner for increasing production capacity. [42]

In 2021 Capellades and collaborators published the results of the first end-to-end continuous manufacturing campaign, showing that it is possible to synthetize a drug molecule that consistently meets quality specifications using a fully automated process and with a 4-fold increase in throughput. By switching to continuous integrated and miniaturized processes, capital and operational costs were significantly reduced, and at the same time product quality was improved. [39,53] This on-demand pharmacy initiative involved the development of equipment and processes for the manufacture of ciprofloxacin hydrochloride, and covered the implementation and development of control strategies.

The following phase developed by Capellades, called Good Manufacturing Practice (GMP), aimed to develop modules, platforms and processes for commercial purposes. To this end, it was important to introduce design considerations, process controls, and understanding of the system to prepare the manufacture of pharmaceutical products for human consumption. [39] Ciprofloxacin, a broad-spectrum antibiotic comprised in the WHO's list of essential medicines, was chosen as the first drug to be tested, due to its strategic value in medical emergencies and because this molecule was also the most challenging in the previous phases, presenting operational difficulties during several stages of the production: synthesis and purification of the drug molecule, full formulation of the final dosage form, and meeting of manufacturing performance demands. [54,55]

This integrated manufacture of ciprofloxacin tablets was carried out in four modules: a first one for the synthesis of the un-pure API. From there, the raw solution is transferred to a second processing module, where it is purified. The product obtained is transferred to the third module where the isolation of ciprofloxacin hydrochloride as a dry powder occurs. The pure molecule then reaches the fourth module, which is where the production of the dosage form (in this case an oral tablet) is carried out.

In addition to testing the performance of the four aforementioned modules, Capellades and collaborators defined the process parameters that have higher impact on process performance and in the Critical

J. Mex. Chem. Soc. **2025**, *69*(4)
Regular Issue

ISSN-e 2594-0317

Quality Attributes (CQA) of the product. Having the process parameters defined, two test production runs were performed, one with high flow (equivalent to 0.54 g/min of ciprofloxacin or 3,100 doses of 250 mg/day) and another with a low flow (equivalent to 0.30 g/min of ciprofloxacin or 1,750 doses of 250 mg/ day). As a result of these runs, tablets with essay test values of 96.83 $\pm$ 0.70% for high flow and 97.28 $\pm$ 0.28% for low flow were obtained. After these runs, a CM campaign of four cycles with stable conditions was carried out successfully. [39]

Due to the implementation of a closed-loop system for continuous operation in the purification and isolation modules, the drug output rate increased 390%, moving from 215 doses/day (obtained in the demonstration phase) to 839 doses/day in this GMP phase. Likewise, it was proven that 100% of the tablets manufactured with the GMP phase platform comply with the USP essay specification range of 98.0 to 102.0%, while meeting CQA such as crystal shape, particle size and water content.

According to the forementioned authors, there remain challenges to improve the continuous process and have more attractive commercial platforms, among these is the search for a higher product output rate (that is, more units or doses per day), which can be achieved by looking at other types of solvents and exploring more configurations for the process parameters. For now, it has been demonstrated that it is feasible to have a platform where the product is manufactured continuously, from the synthesis of the drug to the pharmaceutical dosage form. [39]

Example of 3D printed reactors for CM systems

We selected this paper as the latest example of how continuous manufacturing has evolved and to show the potential it has for the future. In this study, chemically resistant parts for a reactor for flow chemistry and CM were manufactured using the fused filament 3D-printing process, from polyetheretherketone (PEEK), a material that has higher chemical resistance than common fused filament manufacturing materials such as acrylonitrile, butadiene styrene, polypropylene or even high-performance plastics such as polyetherimide, in addition to having superior heat resistance it has excellent mechanical strength.

The 3D-printed PEEK reactors proved to be suitable for liquid-liquid extractions and flow chemistry as they were able to withstand pressures of at least 30 bar, which allowed the use of superhot solvents. With this, it has been shown that it is possible to design and use customizable and cost-effective reactors and flow equipment that can be manufactured on relatively inexpensive 3D-printers. [56] Some tests were even carried out at a pressure of 60 bar so that reactors with the capacity to operate at this pressure would be further designed.

Another innovative approach used in this study was the use of X-ray microcomputed tomography to obtain images of the 3D printed reactor. This method allowed to non-invasively verify the internal structure, to assume that it was manufactured according to specifications and served to the original design, which is a key for the qualification of the equipment as a part of the regulatory requirements that apply to the pharmaceutical industry. These results set the standard for how to manufacture mini and micro scale equipment for CM in the future. Using the same 3D-printing method, a micromixer was manufactured to complement the microreactor showing full functionality.

To test the system manufactured from PEEK 3D printing, the authors carried out a nucleophilic substitution reaction (SNAr) of 2,4-difluoronitrobenzene with morpholine, using methanol for solvent, at a reaction temperature of 80 °C and at a pressure of 100 psi.

Not all reaction products were necessarily observed, but the ortho and bis species predominated. In a second 3D-printed mixer, the product at the outlet of the reactor was met with a stream of ethyl acetate and water in equal parts, at a flow of 1 mL/min. After cooling the product down, a High-Performance Liquid Chromatography (HPLC) analysis was executed. As a result, a high extraction efficiency (97%) of the product in the organic phase was obtained, thus verifying the correct performance of the equipment designed and manufactured by 3D-printing of PEEK.

As a highlight of this example, there have been developed, manufactured and tested chemically resistant PEEK based flow reactors and mixers through 3D-printing, showing that these microreactors resist high pressures and temperatures. The ability to produce customized reactors with customized geometries and properties, similar to those of metal parts, is a valuable property in academia, research and industry for the pharmaceutical fields. This equipment could be in the short-medium term the basis for CM and on-demand pharmacy platforms that will help bring priority drug products to places that are difficult to access or where greater demands need to be met.

J. Mex. Chem. Soc. **2025**, *69*(4)
Regular Issue

ISSN-e 2594-0317

Example of a continuous system for the recovery of solvents in drugs production

Because the pharmaceutical industry uses relatively high amounts of solvents, solvent recovery is necessary to achieve a sustainable manufacturing and comply with GC principles: “less hazardous chemical syntheses”, “designing safer chemicals”, and “providing safer solvents and auxiliaries”.

Solvent recovery is defined as the process of extracting useful materials from waste or byproducts during a manufacturing process. These recovered chemicals can be reused in the manufacturing process, greatly reducing the need for new solvents and significantly reducing waste generation. This pursues the GC principles: safer solvents and auxiliaries, and prevention. Solvents that can be recovered are aliphatic and aromatic compounds, halogenated hydrocarbons, alcohols, ketones, and esters, among others. The most common methods for solvent recovery include distillation, membrane separation, liquid-liquid extraction, thin film evaporation, and chemical extraction. [36]

Between 90% and 95% of industrial separations are carried out by distillation because it is a fast, effective and efficient method. [57] This process is used to separate the components in a mixture by means of vaporization followed by condensation, thus taking advantage of the differences in concentration of the components in vapor and liquid phases.

In 2020 Shores and collaborators designed a simple vapor-liquid equilibrium (VLE) arrangement using a binary ethanol-cyclohexane system as the reference solvent. Process reliability was evaluated through the VLE measurement of a two polar-solvents system. With this information different columns were designed for distillation in a 30.7 m^2 CM pilot plant comprising dissolution & clarification bypass, reactive crystallization, filtration & resuspension, drying and separation, extrusion-molding-coating (of tablets), and solvent recovery. [36]

The purity of the recovered solvents was >99.9 % by weight for the first solvent and >99.8 % by weight for the second solvent, reaching recovery yields of 94.9 % and 98.3 %, respectively. According to the E-Factor analysis, approximately 30% waste saving was recorded in the CM implementation, as compared to the corresponding BM process. After integrating the solvent recovery system, the E-Factors for both the BM and CM processes decreased significantly, from 1.63 to 0.29 and from 0.77 to 0.21, respectively. [36]

As a conclusion to this example, the CM process coupled to the solvent recovery system allowed for a sustainable manufacturing process for the pharmaceutical industry. This proves that CM has greater impact and thrust on the GC principles than traditional BM: “less hazardous chemicals synthesis”, “design of safer chemicals”, and “safer solvents and auxiliaries”. Given that solvent recovery was carried out by distillation, which is an energy-consuming operation, there is an opportunity for optimization by testing different pressures or mechanical vapor recompression to reach a more efficient design.

Example of a portable continuous system for tablet manufacturing

In 2018 Azad and collaborators designed a portable, reconfigurable and automated system for the manufacture of tablets that included several unit operations: feeding, measuring, transporting, mixing, dispensing, tableting (compression) and weighing. This increased the scope of the previous results on liquid dosage forms. [58] A tablet production unit was designed with the capacity to produce hundreds to thousands of tablets per day, resulting in the opportunity to "manufacture to distribute" (make and ship), which could break the paradigm of the traditional industry scheme and could help limit drug overproduction. Overall, this approach reduces the use of chemical reactants, including organic solvents, and at the same time, depletes the waste volumes. The work of this research group supports GC principles of “Prevention” and stands for a responsible production / consumption approach.

The compact, portable, reconfigurable, and automated tablet manufacturing equipment was designed, built, and tested. The whole miniature system is the size of a household oven, 72.4 cm long × 53.3 cm wide × 134.6 cm high and upholds an on-demand and CM of tablets, going from drug crystals to oral tablets on scales of hundreds to thousands tablets per day. The drugs tested were ibuprofen, a popular over the counter analgesic, and diazepam, a controlled depressive of the central nervous system. Each API was manufactured using the miniature system with different drug loads, in compliance with quality standards set by the Pharmacopoeia of the United States of America. [58]

In summary, these miniature CM systems have the potential to aid in meeting the SDG 3 of “Good Health and well-being” and 11 “Sustainable Cities and Communities”, as they:

A. Help mitigate drugs shortages

J. Mex. Chem. Soc. **2025**, *69*(4)
Regular Issue

ISSN-e 2594-0317

B. Are a preferred option when manufacturing short shelf-life drugs
C. Produce drugs on-demand, thus avoiding storage costs and unnecessary inventories
D. Fast-respond to health emergencies, natural disasters and other catastrophic events
E. Improve access to medicines in underserved areas

The miniature platforms for drug manufacturing open a future possibility to address the need for personalized and on-demand medicines, through flexible production schemes in portable devices to treat diseases at the point of care in shorter timeframes.

Example of a continuous reconfigurable system of liquid pharmaceutical products

In 2016 faculties from the Department of Chemical Engineering at Massachusetts Institute of Technology (MIT) developed a continuous manufacturing platform that combined the processes of synthesis and formulation of a finished product in a single compact unit. [38] The use of continuous flow within the system allowed for the efficient heat and mass transfer, as well as the intensification and automation of the process.

The platform was initially developed to carry out a CM process for the entire production train for aliskiren hemifumarate, an API used for the treatment of hypertension, but the result was a reconfigurable platform, called "plug-and-play", having the size of a refrigerator (1.0 m width × 0.7 m length × 1.8 m height), and a weight of approximately 100 kg. This platform allows simple or complex synthesis reactions, multiple online purifications, post-synthesis processing and handling, crystallization, real-time process monitoring, and ultimately, the end-to-end formulation of high-purity active pharmaceutical ingredients.

To demonstrate the capacity and flexibility of this manufacturing platform, hundreds to thousands of doses of four different drugs were produced: diphenhydramine hydrochloride, an antihistamine used to treat common cold, reduce allergy symptoms and gentle sleep aid; lidocaine hydrochloride, a common local anesthetic also used for treating arrhythmias; diazepam, a controlled central nervous system depressant; and fluoxetine hydrochloride, used as an antidepressant. The reconfigurable modules were custom made for each API, varying reactors sizes (5 to 30 mL) and location of downstream units, waste collection sites, cartridges, heaters, solvent delivery key points, membrane-based separators, in-line pumps, etc. Having generic molecules from different chemical structures coming from diverse synthesis routes represented one of the main challenges for this platform, with respect to capacity and technical limits ever thought for a continuous flow system.

These trials carried out by the MIT showed that CM systems aid in having integrated processing and control, which in turn translates into safer processes aligned to GC principles. The plug-and-play platform inherently brought a safer chemistry for accident prevention, since it is carried out without manual handling and takes shorter process times. The use of smaller, highly adaptable equipment, with real-time monitoring, also results in reductions in production costs and improvements in product quality. The CM of the afore mentioned drugs demonstrated that it is feasible to carry out a continuous production on a small scale and on demand. CM offers other advantages, such as the potential to scale up processes with relative ease and in the right timing to satisfy the demand for product in the market. Interestingly, CM of drugs from beginning to end reduces the use of solvents and other waste. The MIT's research also proved to decrease energy consumption and enhance process intensification, driving the GC principles of: "prevention", "atomic economy", "safer solvents and auxiliaries", "efficient energy design", "reduction of derivatives", "catalysis", and "real-time analysis for pollution prevention". At the end, these principles stand for safer chemistry, but they also seek the prevention of accidents. [42]

Discussion

Having analyzed the information, it is clear that the conditions that can drive the adoption and implementation of CM have been created and are supported by new technologies, nurtured by an academic research and development framework collaborating hand by hand with the industry. The regulatory agenda is enabling to empathize with operational requirements, through issuing guides that facilitate learning and

J. Mex. Chem. Soc. **2025**, *69*(4)
Regular Issue

ISSN-e 2594-0317

understanding CM. With this landscape, the transition from batch operations to continuous operations is therefore the new challenge of pharmaceutical manufacturing. [27]

Yet, there are some key-points that need to be taken into account to facilitate CM implementation:

- Understand the product and the process
- Analyze the information and safeguard it
- Use tools as sensors, controllers, process simulators
- Implement tools in early development stages (design phase), or look for alternatives for efficiency and reduction of waste and pollutants to optimize current processes
- Seek for the integration of quality and sustainability into the process and the product, beginning from the design and following through real-time controls

There remain challenges to improve the continuous process at a commercial scale, such as meeting higher product output rates, choosing solvents and exploring new configurations for equipment and process parameters. Although the technologies are fully implemented, it is feasible to have a CM platform, either for API or dosage forms, and even for a merge of both activities: drug substances and drug product manufacturing. These groundbreaking results present the possibility of merging pharma-chemical (namely organic chemistry methods) and pharmaceutical processes (unit operations as mixing and powder compaction) in a single processing system rather than in two different manufacturing facilities.

As shown in this paper, new technologies such as 3D-printing microreactors with customized geometries could be in the short-medium term the basis for CM and on-demand pharmacy platforms to bring out priority drug products to hard-to-reach places or populations with the greatest demands. We also presented CM developments coupled to solvent recovery systems allowing for sustainable manufacturing processes for the pharmaceutical industry, proving to thrust on less hazardous chemicals synthesis, and safer solvents and auxiliaries. As stated, integrated processing, such as the plug-and-play platform, can aid in having safer chemistry practices for accident prevention, since they are carried out without manual handling and achieving shorter process times. As reviewed, it is feasible to carry out continuous production of drugs on a small scale and on demand. Some advances in CM in pharmaceuticals and oral liquid medications are also taking place, along with some developments for injectables.

The explicit support of regulatory agencies, such as the FDA in the United States of America, the European Medicines Agency in Europe and the Pharmaceutical and Medical Devices Agency in Japan has been crucial for promoting the growth of CM in diverse fields such as research, development and implementation. Global organizations, emphasizing the ICH, are also encouraging the implementation of advanced technologies for CM. In the USA, the FDA envisages pharmaceutical companies to adopt CM for drugs production, and declares confidence on the fact that it will reduce quality problems, lower manufacturing costs, and improve the availability of quality medications for patients. Likewise in the USA the Environmental Protection Agency has been a promoter of the implementation of GC, openly supporting the efforts of companies to mitigate their environmental impact. This national structure is nurtured by the academy and by the equipment and service suppliers, all working together to develop more and better machines, gears, and platforms. It should be noted that for now these efforts are taking place mainly in the USA, Europe and Japan, so it will be important for regulatory agencies in other regions, namely Asia and Latin America, to promptly work on guidelines for the approval of this type of technologies in order to set a clear regulatory framework and stimulate its adoption.

Particularly for the pharmaceutical industry, the CM-GC duo is powerful factor, for speed is the key to meet the market requirements. Most of the advantages of CM are a direct consequence of reduced operating volumes. A full-scale manufacturing process of an API, including synthesis, purification and formulation stages, can have an environmental footprint as small as that of the container used for its shipment. This drives the principles of GC: “prevention”, “synthesis of less hazardous chemicals” and “design of safer chemicals”; but also implies significant advantages with respect to temperature control, safety and simplified scaling [8], promoting the GC principles: “energy efficient design”, “intrinsically safer chemistry for accident prevention” (facilitating the integration of green chemistry into industry with a high environmental impact), and the sustainable development goals (SDGs): “affordable and clean energy”; “industry, innovation and infrastructure”, “responsible production and consumption”; “climate action”; and “life on land”. [42] Table 3 encloses how CM’s characteristics overlap some of the GC principles, which can be observed in Table 3.

J. Mex. Chem. Soc. **2025**, *69*(4)
Regular Issue

ISSN-e 2594-0317

Table 3. Features of CM processes and its benefits observed from different perspectives (Green Chemistry / Environmental, Economic and Productivity), adapted from: [42,43]. Numbers in parenthesis refer to GC principles.

CM's Characteristic	Environmental perspective	Economic perspective	Productivity perspective
Use of Mini and micro equipment, capable to perform the process of intensification and increase process efficiency	Minimal byproduct formation Atom economy (2) Reduced environmental burden and footprint	Incorporate total value of materials Reduced costs	Implementation of demanding separations (e.g., multistage extraction) Accelerated implementation (shorter lead times, facilitated scale-up) Reduced hold-ups Larger toolbox of reactions More efficient process
Solvent reduction	Less solvent required, less solvent waste. Reduced environmental burden / Prevention (1)	Reduced capacity requirements, less energy required. Reduced cost	Reduced solvent volumes through the elimination of large reactors
Reagent optimization	Catalytic, low stoichiometry, recyclable. Reduced environmental burden (9)	Higher efficiency, higher selectivity Reduced costs	Increased process understanding and thus, increased process performance
Chance to use disposable equipment for highly potent or cytotoxic reagents/ products	Fewer potential intermediate and/or product Isolations Reduced environmental burden (2, 9) related to the improved process efficiency	Higher efficiency, fewer operations Reduced cost	Reduced waste / treatment for waste Avoid unnecessary steps Direct processing of unstable intermediates/products
Improved reaction control for exothermic reactions	More efficient heating and cooling Reduced environmental burden. Design for energy efficiency (6) related to power generation, transport, and use.	Increased efficiency, shorter processes, milder conditions Reduced cost	Smaller energy requirements to run continuous platforms Energy reduction
Real time testing	Reduced potential for exposure or release to the environment (11)	Real time data increases throughput and efficiency, fewer reworks. Reduced cost	*In situ* analysis Large utilization of PAT for CM to ensure product quality and reduce burden for final product testing Reduction of variations between batches
Small volumes of hazardous materials being processed at any given time, increased control over process parameters	Nonhazardous materials and processes reduce risk of exposure, release, explosions, and fires Inherently safer chemistry for accident prevention (12)	Worker safety and reduced downtime Reduced special control measures. Reduced cost	Safety Smaller equipment

J. Mex. Chem. Soc. **2025**, *69*(4)
Regular Issue

ISSN-e 2594-0317

A few large pharmaceutical companies have already begun to implement CM and GC, proving that it is worthwhile to invest in flow technologies and qualified personnel to raise businesses' return of investment. Simply said: Innovation leads to economic benefits expressed as cut-offs in wastes, savings in resources, higher energy efficiencies, and greater productivity and competitiveness, but also aids in meeting higher safety standards. Another benefit is the improvement in the company's social/political reputation due to the reduction of polluting waste, since results to mitigate the environmental impact are noteworthy. Environmental care rewards not only consumers (patients) but the entire world and could assist in making employees feel a sense of pride to be part of the organization. Ultimately, embracing GC could also reduce taxes. The adoption of flow technologies by third-party manufacturers shows that there is a trend set to have more API and drugs continuously manufactured in the near future.

As shown in this paper, Pfizer's PCMM, the CMAC consortium and the joint ventures held with some institutions such as Purdue University, are actions that have aid in facilitating the transition; in other words, companies have already prepared to meet the evolving requirements, and regulatory agencies have supported this transition.

Conclusions

For now, the greatest co-development of CM and GC has been applied to the manufacturing of pharmaceuticals, especially solid oral pharmaceutical forms. In the short term, we visualize processes comprising continuous stages combined with batch operations; in the long term, though, the trend will be for the entire process to be continuous (depending on the cost-benefit evaluation).

The adoption of CM processes (and the GC intrinsic benefits) by the pharma-chemical and pharmaceutical industries is happening already. There is a natural synergy in merging CM and GC to test or implement both in the production of API or drugs. Academy set aside, large companies, technology suppliers and standard-setting authorities are interested in the advantages brought together by these two industrial approaches. CM and GC convergence has occurred naturally, since these two approaches promote innovation, efficiency, competitiveness and productivity, and both synergize by seeking cost reduction through a wiser use of resources. The CM-GC joint reduces variability and renders cleaner processes. The allure of this association spontaneously lies in the potential for economic, productive and sustainability improvements of processes and products.

Traditional BM operates around a supply chain that is subject to complex logistics and is vulnerable to demand spikes and unplanned disruptions. In this regard, CM is a promising solution with applications in medicine, pandemics and emergencies. To quote the FDA: "… *the need for innovation goes beyond drug discovery and approval – manufaturing processes and technologies must keep pace with advances in drug research and development*." [59, p.22] The transition from batch to continuous operations is the new challenge of pharmaceutical manufacturing.

Drug manufacturers need to implement strategies to achieve global supply, yet meet regional and local demands. Part of these strategies lays on strengthening their plant's capabilities and processes with optimal resource allocation and reduced complexity in manufacturing procedures. The most powerful force driving this transition is the new global competence in performance and quality. This context has driven pharmaceutical companies to explore the application of CM techniques in different pharmaceutical therapies, seeking to reduce the time to scale-up and commercialization of drugs. For now, focus is on aiming to manufacture a great amount of the highest volume products using CM within the next few years, but also in increasing processes' throughput, reducing wastes and testing cycle times significantly. As shown here, new investment is being allocated in new CM technology to produce medicines faster and to respond effectively to the demand for new medicines. Examples are Pfizer, GSK, Vertex, Teva, Janssen-Cilag, Eli Lilly, and Johnson & Johnson, who have heavily invested in CM processes, and noteworthy satellite industry (vendors) is doing so too, for instance GEA, Bosch, Glatt, Bohle, Hosokawa, Fette, Lodige, Gericke, Ktron, Schenk. Also, academy has shown up for the paradigm shattering, addressing a perfect convergence in science, technology and innovation.

Regulatory changes in the last years have paved the road for pharmaceutical companies to shift from BM to CM and benefit from greener processes. CM and GC converged approaches have proved to promote innovation, efficiency, competitiveness and productivity in some processes of the pharmaceutical industry. The

J. Mex. Chem. Soc. **2025**, *69*(4)
Regular Issue

ISSN-e 2594-0317

reviewed examples of plug-and-play factories for on-demand CM of API, 3D printed reactors for CM systems, continuous systems for the recovery of solvents in drugs production, portable continuous systems for tablet manufacturing, and continuous reconfigurable systems of liquid pharmaceutical products, point out the benefits brought by CM and GC, and show that this convergence will detonate different research angles in applied sciences. Likely, CM interest will eventually move away from high volume production of solid oral dosage forms to be applied in every other production line. As a final conclusion, it is expected that flow technologies will be developed in the future for other pharmaceutical products, such as biological or biotechnological products; yet, it is unclear now when will this happen.

Acknowledgments

This work was supported by the Faculty of Chemistry of the Autonomous University of the State of Mexico (*Universidad Autónoma del Estado de México*, UAEMéx).

References

1. Albini, A.; Protti, S., in: *Paradigms in Green Chemistry and Technology*. Springer, New York-London, **2016**. DOI: http://doi.org/10.1007/978-3-319-25895-9_2.
2. Pisano, R. *Am. Pharm. Rev*. **2020**, *23*, 1-4.
3. Lee, S. L., O'Connor, T. F., Yang, X., Cruz, C. N., Chatterjee, S., Madurawe, R. D., & … Woodcock, J. *J. Pharm. Innovation*. **2015**, *10*, 191–199. DOI: http://doi.org/10.1007/s12247-015-9215-8.
4. Muzzio, F., in: *Pharmaceutical Engineering Cycle*. Rutgers University. **2021**. Rutgers University. Retrieved from: https://youtu.be/ZBbCvE4QYLg?si=VjzCDVdduLpvzD_3
5. Malet-Sanz, L.; Susanne, F. *J. Med. Chem.* **2012**. *55*, 4062–4098. DOI: http://doi.org/10.1021/jm2006029.
6. Lawton, S.; Steele, G.; Shering, P.; Zhao, L.; Laird, I.; Ni, X. W. *Org. Process Res. Dev.* **2009**, *13*, 1357–1363. DOI: http://doi.org/10.1021/op900237x.
7. Ferguson, S.; Morris, G.; Hao, H.; Barrett, M.; Glennon, B. *Chem. Eng. Sci.* **2013**, *104*, 44–54. DOI: http://doi.org/10.1016/j.ces.2013.09.006.
8. Mascia, S.; P.L., H.; Zhang, H.; Lakerveld, R.; Benyahia, B.; Barton, P.; . . . B.L., T. *Angew. Chem. Int. Ed*. **2013**, *52*, 12359–12363. DOI: http://doi.org/10.1002/anie.201305429.
9. Gutmann, B.; Cantillo, D.; Kappe, C. *Angew. Chem. Int. Ed.* **2015**, *54*, 6688–6728. DOI: http://doi.org/10.1002/anie.201409318.
10. Besenhard, M.; Neugebauer, P.; Scheibelhofer, O.; Khinast, J. *Cryst. Growth Des*. **2017**, *17*, 6432-6444. DOI: http://doi.org/10.1021/acs.cgd.7b01096.
11. McLaughlin, A.; Robertson, J.; Ni, X. W. *Pharm. Dev. Technol*. **2019**, *25*, 1–28. DOI: https://doi.org/10.1080/10837450.2019.1685543.
12. Aranda, L. A., in: *Aplicaciones de la Manufactura Continua y la Química Verde en la producción de Fármacos y Medicamentos*. Mstr. D. Thesis, Universidad Autónoma del Estado de México, Toluca, México, **2024**.
13. Pájaro, N., Olivero, J. *Ciencia e Ingeniería Neogranadina*. **2011**. *21*,169-182.
14. Kulkarni, S.; Rawat, N.; Haghi, A., in: *Green chemistry and green engineering: processing, technologies, properties and applications*. Apple Academic Press, Palm Bay, **2021**.
15. Anastas, P.; Williamson, T. C., *Green Chemistry: An Overview. In: Green Chemistry: designing chemistry for the environment*, vol. 626. 1–17. Washington: ACS symposium series, Washington, D.C. **1996**.
16. Anastas, P.; Warner, J., in: *Green Chemistry: Theory and Practice*. New York: Oxford University Press, **1998**.

J. Mex. Chem. Soc. **2025**, *69*(4)
Regular Issue

ISSN-e 2594-0317

17. Cannon, A. S.; Pont, J. L.; Warner, J. C., in: *Green Techniques for Organic Synthesis and Medicinal Chemistry*. John Wiley & Sons, Ltd. **2012**. DOI: http://doi.org/10.1039/b312329d10.1002/9780470711828.ch2.
18. Linthorst, J. A. *Found. Chem.* **2009**, *12*, 55–68.
19. Cue, B. W.; Zhang, J. *Green Chem. Lett. Rev*. **2009**, *2*, 193–211. DOI: http://doi.org/10.1080/17518250903258150.
20. Dunn, P. J.; Galvin, S.; Hettenbach, K. *Green Chem*. **2004**, *6*, 43–48. DOI: http://doi.org/10.1039/b312329d.
21. Mountford, P. G. *Green Chem. Pharm. Ind*. **2010**, 145–160. DOI: http://doi.org/10.1002/9783527629688.ch7.
22. Hansen, K. B.; Hsiao, Y.; Xu, F.; Rivera, N.; Clausen, A.; Kubryk, M.; … Armstrong, J. D. Highly *J. Am. Chem. Soc*. **2009**, *131*, 8798–8804. DOI: http//doi.org/10.1021/ja902462q.
23. WuXi AppTech Flow Chemistry Page. https://sta.wuxiapptec.com/services-solutions/drug-substance/enabling-technology-platform/flow-chemistry/, accessed in December 2024.
24. Patheon Continuous Manufacturing Page. https://www.patheon.com/us/en/innovative-solutions/manufacturing.html, accessed in December 2024.
25. De Soete, W.; Dewulf, J.; Cappuyns, P.; Van der Vorst, G.; Heirman, B.; Aelterman, W.; ...; Van Langenhove, H. *Green Chem*. **2013**, *15*, 3039-3048.
26. Moher, D.; Liberati, A.; Tetzlaff, J.; Altman, D. G.; PRISMA Group*, T. *Ann. Intern. Med.* **2009**, *151*, 264-269. DOI: doi:10.7326/0003-4819-151-4-200908180-00135.
27. Badman, C.; Cooney, C. L.; Haslam, R. T.; Florence, A.; Konstantinov, K.; Krumme, M.; … Baddour, R. F. *J. Pharm. Sci.* **2019**, *108*, 3521-3523. DOI: http://doi.org/10.1016/j.xphs.2019.07.016.
28. Food and Drug Administration. Quality Considerations for Continuous Manufacturing Guidance for Industry. **2019**. Retrieved from https://www.gmp-compliance.org/files/guidemgr/UCM632033.pdf.
29. Khinast, J.; Kleinebudde, P.; Rantanen, J. in: *Continuous Manufacturing of Pharmaceuticals*. John Wiley & Sons Ltd., Hoboken, **2017**.
30. Food and Drug Administration. Pharmaceutical cGMPs for the 21st Century: A Risk-Based Approach. **2004**. Retrieved from https://www.fda.gov/media/77391/download.
31. Berridge, J. ICH Q8: Pharmaceutical Development. Pharmaceutical Quality Forum, November 2004. Amsterdam-The Netherlands. **2004**. Retrieved from http://www.nihs.go.jp/drug/PhForum/documents041122/Berridge041122.pdf.
32. International Conference on Harmonization. Pharmaceutical Development Guideline Q8(R2). **2009**. Retrieved from: https://database.ich.org/sites/default/files/Q8_R2_Guideline.pdf.
33. International Conference on Harmonization. Quality Risk Management Q9(R1). **2023**. Retrieved from: https://database.ich.org/sites/default/files/ICH_Q9%28R1%29_Guideline_Step4_2023_0126_0.pdf.
34. Food and Drug Administration. Guidance for Industry — PAT — A Framework for Innovative Pharmaceutical Development, Manufacturing, and Quality Assurance. Rockville, MD, EUA. **2004**. Retrieved from https://www.fda.gov/media/71012/download.
35. International Conference on Harmonization. Continuous Manufacturing of Drug Substances and Drug Products Guideline Q13. **2022**. Retrieved from: https://www.ich.org. Retrieved from https://database.ich.org/sites/default/files/ICH_Q13_Step4_Guideline_2022_1116.pdf.
36. Shores, B. T.; Sieg, P. E.; Nicosia, A. T.; Hu, C.; Born, S. C.; Shvedova, K.; Mascia, S. *Org. Process Res. Dev*. **2020**. *24*, 10, 1996–2003. DOI: http://doi.org/10.1021/acs.oprd.0c00092.
37. Johnson&Johnson Home Page. https://innovativemedicine.jnj.com/, accessed in December 2024.
38. Adamo, A.; Beingessner, R. L.; Behnam, M.; Chen, J.; Jamison, T. F.; Jensen, K. F.; … Zhang, P. *Science*. **2016**, *352*, 61–67. DOI: http://doi.org/10.1126/science.aaf1337.

J. Mex. Chem. Soc. **2025**, *69*(4)
Regular Issue

ISSN-e 2594-0317

39. Capellades, G.; Neurohr, C.; Briggs, N.; Rapp, K.; Hammersmith, G.; Brancazio, D.; … Myerson, A. S. *Org. Process Res. Dev.* **2021**, *25*, 1534–1546. DOI: http://doi.org/10.1039/b312329d10.1021/acs.oprd.1c00117.
40. Zhang, P.; Weeranoppanant, N.; Thomas, D. A.; Tahara, K.; Stelzer, T.; Russell, M. G.; …; Adamo, A. *Chem. – Eur. J.* **2018**, *24*, 2776–2784. DOI: http://doi.org/10.1002/chem.20.
41. Muzzio, F., in: *Continuous manufacturing of tablets and capsules - The Emerging Paradigm*. Oral Presentation. Rutgers University. **2016**. Retrieved from USP.org: https://www.usp.org/sites/default/files/usp/document/our-work/research-innovation/research-innovation-muzzio-presentation.pdf.
42. Rogers, L.; Jensen, K. F. *Green Chem.* **2019**, *13*, 3481-3498. DOI: http://doi.org/10.1039/c9gc00773c.
43. Falß, S.; Kloye, N.; Holtkamp, M.; Prokofyeva, A.; Bieringer, T.; Kockmann, N. *Handb. Green Chem*. 2019. 153–190. DOI: http://doi.org/10.1002/9783527628698.hgc139.
44. Martin, B.; Lehmann, H.; Yang, H.; Chen, L.; Tian, X.; Polenk, J.; Schenkel, B. *Curr. Opin. Green Sustainable Chem*. **2018**, *11*, 27-33. DOI: http://doi.org/10.1016/j.cogsc.2018.03.005.
45. Domokos, A.; Nagy, B.; Gyürkés, M.; Farkas, A.; Tacsi, K.; Pataki, H.; Kristóf Nagy, Z. *Int. J. Pharm*. **2020**, *581*, 1-11. DOI: http://doi.org/10.1016/j.ijpharm.2020.119297.
46. Bennett, J. A.; Campbell, Z. S.; Abolhasani, M. *Curr. Opin. Chem. Eng*. **2019**, *26*, 9–19. DOI: http://doi.org/10.1016/j.coche.2019.07.007.
47. May, S. A. *J. Flow Chem*. **2017**, 7, 137–145. DOI: http://doi.org/10.1556/1846.2017.00029.
48. Cole, K. P.; Groh, J. M.; Johnson, M. D.; Burcham, C. L.; Campbell, B. M.; Diseroad, W. D.; Gowran, O. *Science*. **2017**, ***356***, 1144–1150. DOI: http://doi.org/10.1039/b312329d10.1126/science.aan0745.
49. Pfizer Continuous Manufacturing Press Release Page. https://www.pfizer.com/news/press-release/press-release-detail/pfizer_announces_collaboration_with_gsk_on_next_generation_design_of_portable_continuous_miniature_and_modular_pcmm_oral_solid_dose_development_and_manufacturing_units, accessed in December 2024.
50. European Medicines Agency. Assessment report Daurismo. **2020**. Retrieved from: https://www.ema.europa.eu/en/documents/assessment-report/daurismo-epar-public-assessment-report_en.pdf.
51. Phuong, J. M.; Penm, J.; Chaar, B.; Oldfield, L. D.; Moles, R. *PLOS ONE*. **2019**, *14*, e0215837. DOI: https://doi.org/10.1371/journal.pone.0215837.
52. Armstrong, C. M. *Org. Process Res. Dev*. **2021**, *25*, 1524-1533. DOI: http://doi.org/10.1021/acs.oprd.1c00118.
53. Schaber, S. D.; Gerogiorgis, D. I.; Ramachandran, R.; Evans, J. M.; Barton, P. I.; Trout, B. L. *Ind. Eng. Chem. Res*. **2011**, *50*, 10083–10092. DOI: http://doi.org/10.1021/ie2006752.
54. World Health Organization. 19th WHO Model List of Essential Medicines. **2015**. Retrieved from http://www.who.int/medicines/publications/essentialmedicines/EML2015_8-May-15.pdf.
55. Rogers, L.; Briggs, N.; Achermann, R.; Adamo, A.; Azad, M.; Brancazio, D.; …; Jensen, K. F. *Org. Process Res. Dev*. **2020**, *24*, 2183–2196. DOI: http://doi.org/10.1021/acs.oprd.0c00208.
56. Harding, M. J.; Brady, S.; O'Connor, H.; Lopez-Rodriguez, R.; Edwards, M. D.; Tracy, S.; … Ferguson, S. *React. Chem. Eng*. **2020**, *5*, 728–735. DOI: http://doi.org/10.1039/c9re00408d.
57. Gorak, A.; Sorensen, E., in: *Distillation: Fundamentals and Principles*. Academic Press, Amsterdam, **2014**.
58. Azad, M. A.; Osorio, J. G.; Brancazio, D.; Hammersmith, G.; Klee, D. M.; Rapp, K.; Myerson, A. *Int. J. Pharm*. **2018**, *539*, 157–164. DOI: http://doi.org/10.1016/j.ijpharm.2018.01.027.
59. Food and Drug Administration. FDA's Strategic Plan for Preventing and Mitigating Drug Shortages. 2013. Retrieved from https://www.fda.gov/downloads/Drugs/DrugSafety/DrugShortages/UCM372566.pdf.

Journal of the Mexican Chemical Society* (*J. Mex. Chem. Soc.*) *Vol 69, No 4 (2025). Quarterly publication (October-December). Edited and distributed by ***Sociedad Química de México, A.C.***, Barranca del Muerto 26, Col. Crédito Constructor, Alc. Benito Juárez, Zip Code 03940, Mexico City. Phone: +5255 56626837; +5255 56626823 Contact: soquimex@sqm.org.mx, https://www.sqm.org.mx ***Editor-in-Chief: Prof. Alberto Vela***. Indexed Journal. Certificate of reserved rights granted by the Instituto Nacional del Derecho de Autor (INDAUTOR): 04-2005-052710530600-102. Certificate of lawful title and content: Under procedure. ISSN-e granted by the Instituto Nacional del Derecho de Autor (INDAUTOR): 2594-0317. ISSN granted by the Instituto Nacional del Derecho de Autor (INDAUTOR): 1870-249X. Postal registration of printed matter deposited by editors or agents granted by SEPOMEX: IM09-0312 Published online (***https://www.jmcs.org.mx/***) October 1st, 2025 by Adriana Vázquez and Alejandro Nava (editorial assistants, ***e-mail: jmcs@sqm.org.mx***), ***J. Mex. Chem. Soc., Sociedad Química de México, A.C.***

Journal of the Mexican Chemical Society* (*J. Mex. Chem. Soc.*) *Vol 69, No 4 (2025). Quarterly publication (October-December). Edited and distributed by ***Sociedad Química de México, A.C.***, Barranca del Muerto 26, Col. Crédito Constructor, Alc. Benito Juárez, Zip Code 03940, Mexico City. Phone: +5255 56626837; +5255 56626823 Contact: soquimex@sqm.org.mx, https://www.sqm.org.mx ***Editor-in-Chief: Prof. Alberto Vela***. Indexed Journal. Certificate of reserved rights granted by the Instituto Nacional del Derecho de Autor (INDAUTOR): 04-2005-052710530600-102. Certificate of lawful title and content: Under procedure. ISSN-e granted by the Instituto Nacional del Derecho de Autor (INDAUTOR): 2594-0317. ISSN granted by the Instituto Nacional del Derecho de Autor (INDAUTOR): 1870-249X. Postal registration of printed matter deposited by editors or agents granted by SEPOMEX: IM09-0312 Published online (***https://www.jmcs.org.mx/***) October 1st, 2025 by Adriana Vázquez and Alejandro Nava (editorial assistants, ***e-mail: jmcs@sqm.org.mx***), ***J. Mex. Chem. Soc., Sociedad Química de México, A.C.***